COMPUTATIONAL MODELING OF THERMAL AND SHRINKAGE-INDUCED
CRACKING IN CONCRETE

A THESIS SUBMITTED TO
THE GRADUATE SCHOOL OF NATURAL AND APPLIED SCIENCES
OF
MIDDLE EAST TECHNICAL UNIVERSITY

BY

MEHRAN GHASABEH

IN PARTIAL FULFILLMENT OF THE REQUIREMENTS
FOR
THE DEGREE OF DOCTOR OF PHILOSOPHY
IN
CIVIL ENGINEERING

MARCH 2021

Approval of the thesis:

COMPUTATIONAL MODELING OF THERMAL AND SHRINKAGE-INDUCED CRACKING IN CONCRETE

submitted by **MEHRAN GHASABEH** in partial fulfillment of the requirements for the degree of **Doctor of Philosophy in Civil Engineering Department, Middle East Technical University** by,

Prof. Dr. Halil Kalıpçılar
Dean, Graduate School of **Natural and Applied Sciences**   ———————

Prof. Dr. Ahmet Türer
Head of Department, **Civil Engineering**   ———————

Assoc. Prof. Dr. Serdar Göktepe
Supervisor, **Civil Engineering, METU**   ———————

Prof. Dr. İsmail Özgür Yaman
Co-supervisor, **Civil Engineering, METU**   ———————

Examining Committee Members:

Prof. Dr. Sinan Turhan Erdoğan
Civil Engineering Dept., METU   ———————

Assoc. Prof. Dr. Serdar Göktepe
Civil Engineering Dept., METU   ———————

Assoc. Prof. Dr. Ercan Gürses
Aerospace Engineering Dept., METU   ———————

Assoc. Prof. Dr. İzzet Özdemir
Civil Engineering Dept., İYTE   ———————

Assist. Prof. Dr. Ali Javili
Mechanical Engineering Dept., Bilkent University   ———————

Date: 03.03.2021

I hereby declare that all information in this document has been obtained and presented in accordance with academic rules and ethical conduct. I also declare that, as required by these rules and conduct, I have fully cited and referenced all material and results that are not original to this work.

Name, Surname: Mehran Ghasabeh

Signature   :

ABSTRACT

COMPUTATIONAL MODELING OF THERMAL AND SHRINKAGE-INDUCED CRACKING IN CONCRETE

Ghasabeh, Mehran

Ph.D., Department of Civil Engineering

Supervisor: Assoc. Prof. Dr. Serdar Göktepe

Co-Supervisor: Prof. Dr. İsmail Özgür Yaman

March 2021, 201 pages

This work is concerned with the computational modeling of thermal and shrinkage-induced cracking in concrete. Thermal and hygral gradients develop within concrete structures of varying sizes and aspect ratios due to the intrinsic physicochemical phenomena accompanied by adverse environmental effects. These spatio-temporal gradients invariably result in uneven volumetric deformations that can cause stress concentrations when the concrete is sufficiently rigid. Then, when the gained tensile strength is lower than the principal stresses generated by the non-uniform volume changes, cracks will occur and make concrete structures prone to deleterious environmental effects that can cause consequent destructive durability problems. Therefore, predictive computational models are crucial to conduct crack risk analyses not only during the design stage but also during and after the construction of important concrete structures. For this purpose, we develop multi-field computational models to simulate thermal and shrinkage-induced cracking separately. For the former, we developed a novel chemo-thermo-mechanical model coupled with a quasi-brittle phase-field model where the hydration, thermal, mechanical, and fracture problems

are solved in a coupled manner. For the drying shrinkage-induced cracking, we develop a new coupled chemo-hygro-mechanical model within the framework of poro-viscoelasticity to describe the basic and drying creep of concrete in short- and long-terms. The latter model is further supplemented by a cohesive phase-field model to simulate shrinkage-induced cracking. The capabilities of the proposed models are assessed through the benchmark problems and experimental results reported in the literature.

Keywords: Thermal Cracking, Chemo-Thermo-Mechanical Model, Phase-Field Model, Poroviscoelasticity, Shrinkage-Induced Cracking

ÖZ

BETONDA ISI VE RÖTREDEN KAYNAKLI ÇATLAMALARIN HESAPLAMALI MODELLENMESİ

Ghasabeh, Mehran

Doktora, İnşaat Mühendisliği Bölümü

Tez Yöneticisi: Doç. Dr. Serdar Göktepe

Ortak Tez Yöneticisi: Prof. Dr. İsmail Özgür Yaman

Mart 2021, 201 sayfa

Bu çalışma betonda ısı ve rötreden kaynaklanan çatlakların hesaplamalı modellemesini konu almaktadır. Değişken boyut ve en-boy oranlarına sahip beton yapılarında, olumsuz çevresel etkilerin de eşlik ettiği içsel fizikokimyasal olaylar nedeniyle sıcaklık ve bağıl nem değişimine bağlı gradyanlar gelişir. Bu uzamsal ve zamansal gradyanlar, genellikle beton yeterince rijitleştiğinde, gerilme yoğunlaşmaları oluşturabilecek düzensiz hacimsel şekil değişimlerine neden olur. Bu durumda, kazanılan gerilme dayanımı, düzensiz hacim değişiklikleri sonucunda oluşan asal gerilmelerden daha düşük olduğunda çatlaklar oluşup, beton yapıları bunu izleyen daha yıkıcı durabilite sorunlarına neden olabilecek zararlı çevresel etkilere daha açık hale getirecektir. Bu nedenle kestirime dayalı hesaplamalı modeller, önemli beton yapıların çatlak riski analizlerini sadece tasarım aşamasında değil, inşası sırasında ve sonrasında da yapabilmek için kritik önemdedir. Bu amaçla, ısı ve rötre kaynaklı çatlamayı ayrı ayrı modellemek için çok alanlı hesaplamalı modeller geliştirildi. İlki için, hidratasyon, ısıl, mekanik ve kırılma problemlerinin bağlaşık bir şekilde çözüldüğü yarı kırılgan

bir faz alanı modeliyle birleştirilmiş yeni bir kemo-termo-mekanik model önerilmektedir. Kuruma rötresine bağlı çatlama için, betonda temel ve kuruma sünmesini kısa ve uzun vadede tanımlamak için poroviskoelastisite kuramı kullanılarak yeni bir bağlaşık kemo-higro-mekanik model sunulmaktadır. İkinci model ayrıca rötre kaynaklı çatlamayı dikkate almak için kohezif bir faz-alan modeli ile birleştirilmiştir. Önerilen modellerin yeterlikleri, bu modellerin kullanımı ile elde edilen sonuçların literatürde bildirilen kıyaslama problemleri ve deneysel sonuçlarla karşılaştırılarak değerlendirilmiştir.

Anahtar Kelimeler: Isıl Çatlama, Kemo-Termo-Mekanik Model, Faz Alanı Modeli, Poroviskoelastisite, Rötreye Bağlı Çatlama

To Angle of My Life Noras, Hero of My Life Rahim
and Spring of My Life Bahar

ACKNOWLEDGMENTS

The Revelations of Devout and Learn'd
Who rose before us, and as Prophets burn'd,
Are all but Stories, which, awoke from Sleep
They told their comrades, and to Sleep return'd.
"*Omar Khayyam*"

TABLE OF CONTENTS

LIST OF TABLES

TABLES

FIGURES

xxiii

CHAPTER 1

INTRODUCTION

1.1 Concrete and Hydration

Concrete is a widely used construction material in the world. For millennia, it has been used in constructing the pioneering architectural achievements at least as far back as the Egyptian times and Roman empire. Concrete owes this remarkable popularity to its several advantages. It is known for its high compressive strength so that it can be easily adopted to meet the requirements related to the specific degree of strength and the deformability needed in a specific design by modifying the water, cement and aggregate ratio. Concrete gains it strength and stiffness over time. Therefore, it will be a durable construction material if its production process is followed by providing correct specifications dictated by the specific requirements for the desired service life. The accelerated construction times of the concrete structures, the limited maintenance requirements and the consequent reduction in life-cycle costs distinguish the economical benefits of concrete among other alternative construction materials [1]. Higher thermal mass characteristic of concrete causes thermal stability as its main benefit optimizes the energy performance of concrete constructions [2]. The versatility is another benefit of concrete which makes it applicable in constructing different types of structures such as buildings, roads, infrastructures, dams, and nuclear power plants.

Conventional concrete is produced by mixing Portland cement with sand, crushed rock, and water. Hence, concrete is considered as a composite material that consists fundamentally of a binding medium (cement paste) and fragments of aggregate embedded within the medium. Concrete has a highly heterogeneous and complex

microstructure, due to numerous capillary porosities, nonhydrate granules, and crystalline solids at the microscale. For engineering applications, however, it is convenient to consider concrete as a homogeneous material of the macroscale with smeared inhomogeneities. The properties of concrete such as strength, rigidity, dimensional stability, and durability are determined by the characteristics of hydrated cement paste, aggregates, and the interfacial transition zone between the cement paste and aggregates.

Concrete gains its physical characteristics such as rigidity, strength and durability through a set of exothermic chemical reactions that is collectively referred as hydration. To understand the physicochemical mechanisms controlling the mechanical properties of cementitious materials such as the stiffness, strength, deformability, and durability, predictive modeling and characterization of the hydration process and heat development are of primary concerns. The hydration of cement is a quite complex set of competing chemical reactions of different kinetics and amplitudes, and is related to complex physico-chemical phenomena at the microlevel of material description. As concrete is composed of water phases, layers of hydrates, unhydrated cement and gel porosities, it can be considered as a porous medium.

During the hydration process, water diffuses through the layers of recently formed hydrates to reach the unhydarated cement, then new hydrates are produced within the time scale of micro-diffusion process. This water is physically or chemically combined [3, 4]. The microdiffusion of free water though the layers of hydrates are schematically represented in Figure 1.1. To this end, the aformentioned microdiffusion may be evaluated as a predominant mechanism controlling the hydration reaction at the microlevel of the porous medium. From this point of view, it is observed that the water content in terms of the moisture distribution within cementitious materials is an important factor. This field primarily dominates the hydration process of cementitious materials so the physico-chemical properties of concrete are dependent mainly on the moisture distribution. The driving force of the free water microdiffusion is known as affinity. The affinity is specified in terms of Gibbs free energy and the hydration extent at constant pressure and temperature [5]. In reality, the affinity of a chemical potential describes the imbalance between the chemical potentials of the free water and the water combined in the solid phase [6].
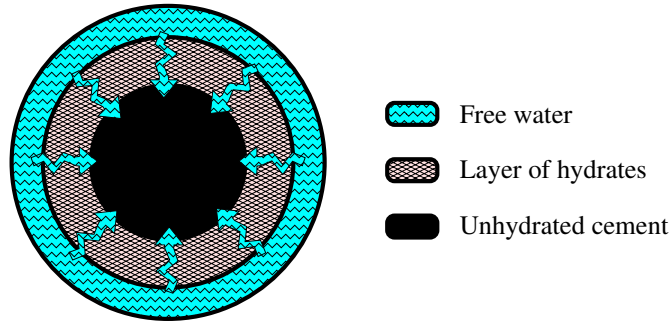
Figure 1.1: The demonstration of micro-diffusion of free water through layers of hydrates to reach unhydrated cement during course of hydration [3].

The hydration of cement compounds is an exothermic chemical reaction, which is accompanied by the release of energy in the form of heat. At early age, during the hardening of young concrete, the process of heat liberation leads to remarkable temperature increase and volume changes in concrete. In the first day after casting, the generated heat may produce a temperature rise up to $50-60°$C under adiabatic conditions. In this duration, the viscous effects are significant and due to quite low stiffness of concrete, the temperature increase is primarily accompanied by moderate compressive stresses. The concrete initiates to cool down later on, while the stiffness is significantly continuing to increase [7].

The hydration process instantly begins when the cement ingredients come into contact with free water, and heat is consequently liberated at every moment until the hydration is accomplished. As a matter of fact, this chemical process does not reach 100% level of accomplishment, the heat generation and the strength gain also continue in a mature concrete. At the microscopic level of concrete, there are five main mineral components forming Portland cement. These major components are aluminates, including tricalcium aluminate (C_3A) and tetracalcium aluminoferrite (C_4AF), silicates, including tricalcium silicate (C_3S) and dicalcium silicate (C_2S), and calcium sulfate ($C\bar{S}$), also known as gypsum, sometimes hydrated ($C\bar{S}H_2$). Calcium silicates constitute about 75% of cement, therefore, the primary compounds during the hydration process are produced as a result of the reactions between silicates and water. The dissolution of hydrates is a slow process so the silicates do not have immediate, but have major effect on concrete strength and durability in the long term. The hydra-

3

tion process can be described in five stages, according to the rate of heat of hydration evolution [5], see Figure 1.2.
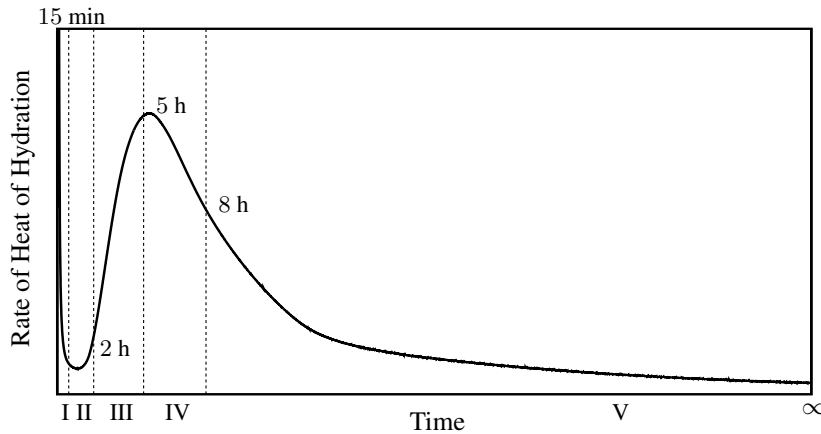
Figure 1.2: Cement hydration process in terms of the evolution of rate of heat of hydration.

In the first stage, also known as the mixing stage, when water gets contact with cement particles C_3A and gypsum ($C\bar{S}$) dissolve at once. Then, solid compounds are produced from these materials within a short time of about 15 minutes. The process results in the significant heat generation that increases at a high speed. In this period, a substance coating the cement grains is produced from the reaction between fast-dissolving gypsum, dissolved C_3A and water. The hydration product is solid without a specific composition or crystalline form. In general, it is referred to as gel-like ettringite (C-A-$\bar{S}$-H). It decreases the speed of the aluminate reactions so the amount of generated heat is reduced by the end of the mixing stage [1].

The second stage is subsequently observed $1 - 3$ hours after mixing. As a general rule, in this period the aluminate reactions are controlled by C-A-$\bar{S}$-H gel so it is accompanied by the almost complete deceleration of heat generation, and concrete is mainly in the plastic state. The second stage is also called as the dormant period [8]. During dormancy, the cement dissolution is extending so the water is getting saturated with dissolved calcium and hydroxyl (OH) ions, but silicates (C_2S and C_3S) dissolve at a slow rate. Finally, the water becomes fully saturated with calcium ions, and the hardening process initiates [1].

A few hours after mixing, concrete begins to set. This period is accompanied by the

4

third stage in which, the rate of heat of hydration development increases. The third stage is strongly governed by C_3S and as a result of the reaction between silicates and water, calcium silicate hydrate (C-S-H) and calcium hydroxide (CH) form. C-S-H is the primary desirable hydration product, resulting form the reaction and silicate, both C_3S and C_2S, with water. This product contributes to rigidity and strength gain of concrete ant its low permeability [1]. When the setting of concrete is ceased, it starts to gain strength. The solid concrete is characterized by its strength, elastic, plastic and viscous properties. In the third stage, thermal and drying effects induce development of tensile stress after final set. The solidifying concrete in this stage is considered as early-age concrete. The period is the followed by the fourth stage, in which the hydration decelerates again.

In the fourth stage, the chemical reactions between remaining water and undissolved cement grains are continuing, also the rate of C_3S reactions begins to slow down. Therefore, the rate of heat generation first increases then it begins to slow down. Moreover, after the temperature reaches a peak point, $C\bar{S}$ continuously reacts with aluminates so it will be consumed. The remaining aluminates reacts with ettringite to produce monosulfate. However, monosulfate does not have any significant affect on the properties of concrete [1].

In the fifth stage, the hydration reaches almost a steady state so the concrete continues to gains its strength and mechanical properties, although with a slow rate. This stage corresponds to the hardened state of concrete. If there are any remaining C_3S and water in concrete, they will keep on the hydration reaction to produce C-S-H. During the fifth stage, C_2S reacts with water but more slowly than C_3S. After several days, C_3S will mostly react and the rate of C_2S hydration starts to be remarkable.

1.2   Concrete as a Porous Medium

The governing equations, derived within the thermodynamically consistent theory of Reactive Porous Media, deal with the description of response of the porous media to the physio-chemical phenomena. A porous medium, also designated as a fluid-solid mixture consists of a solid matrix and a variety of connected pores saturated by fluid,

5

see Figure 1.4. According to this definition, a cement paste or concrete is regarded as a hydrophilic porous medium whose solid skeleton is composed of uhydrated cement and hydrates, and the pores completely filled with water and randomly distributed within the cement paste. In general, water can be found in concrete in several phases, as capillary water, water vapor, free adsorbed water and hindered adsorbed water [9, 10, 11, 12].

In Figure 1.3, the different water phases coming across between two cement gel surfaces are demonstrated. The capillary water in the form of liquid, filling the vacancies between the cement particles, which are known as capillary pores. The state of capillary water is thermodynamically expressed through the capillary pressure. As an assumption, the capillary water can behave as incompressible gas if the capillary pores are not fully saturated and an equilibrium is constructed between the capillary water, air and water vapor. In the vicinity of pore walls, the van der Waals forces hold the adjacent molecules of water vapor at the solid surface where they form thin adsorbed water layers. The specific mass of the adsorbed layer per unit solid surface and its average thickness $\bar{\delta}_a$ are determined as a function of relative humidity φ. It is fairly assumed that the layer reaches its maximum thickness about 5 molecules, i.e. about 13 Å for $\varphi \to 1$. Under high relative humidity conditions, in small micro-pores also known as gel pores with the sizes of a few Å, the hindered adsorbed water layers form due to the incomplete development of adsorbed water layers [10]. The existence of the hindered adsorbed water will appear in terms of the large local pressure, well-known as the disjoining pressure. It may have the magnitude of up to 300 MPa. Moreover, the capillary tension develops in a water filled pore due to the presence of capillary menisci formed between the pores [11]. The capillary pressure in a pore with a radius of 10 μm is about 30 MPa [13]. As the pores inside the cement gel have the enormous internal surface area about 500×10^5 mm^2 per mm^3, the capillary tension and disjoining pressure govern the stress level in the microstructure of concrete [14].

The largest portion of the pores includes micropores ($d < 2.5$nm) and mesopores ($2.5 \leq d < 50$ nm). However, the small portions of the pores are formed by the macropores whose diameters are of about 50 nm to 10 μm. The structure and size of the pores strongly dominate the diffusion mechanism of concrete [15]. The diameter
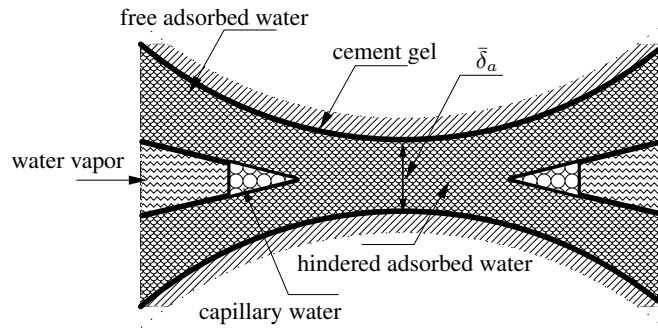
Figure 1.3: The demonstration of different water phases between the cement gel surface with average thickness of the adsorbed water layer of $\bar{\delta}_a$ [10].

of the pores varies over a very wide range. Also, their structures change with age. To this end, the process of the moisture diffusion within the concrete is more complex, also the determination of the diffusion parameters such as diffusivity and moisture capacity is not straightforward. Three particular diffusion mechanisms are defined in concrete. These mechanism which may occur individually or simultaneously are known as molecular diffusion, Knudsen and surface diffusion [15].
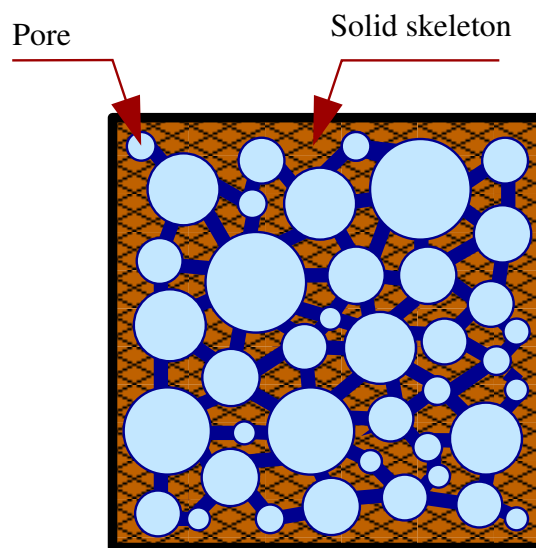
Figure 1.4: Schematic demonstration of a porous medium including solid skeleton and fluid-saturated pores.

The molecular diffusion, also known as the ordinary diffusion takes place inside the macropores (capillary pores) of concrete. The field force of the pore in terms of

adsorption attracts the water molecules to the pore wall. At low relative humidity, the first layer of waters molecules is formed on the wall of a pore. As the relative humidity increases, more water molecules adhere to the wall so the number of layers of the water molecules covering the pore wall increases. Thus, there exits not enough free space for vapor inside the macropores. As a result, the mean free path of water molecules surrounded by the water-adsorbed pore wall get narrower, because of the increase in the thickness of the water molecular layers. This path is smaller than one surrounded just by the solid wall of the pore. This treatment decreases the resistance against the diffusion process [15].

At higher pore humidity, menisci completely filled by the adsorbed water forms on both sides of the necks which narrowly connect the large pores together. At one end of the neck the water molecules are condensed while at the other end, they evaporate. These condensation and evaporation processes effectively characterize the diffusion process. This ordinary diffusion process is dominant when the mean free path of vapor, of 80 nm at 25°C is small relative to the size of the macropore. As the macropores constitute a small portion of the pores in concrete, the ordinary diffusion process is less dominant mechanism. Knudsen diffusion process is defined as a resistance occurring in the mesopores where the water molecules strike together and collide with the pore walls. In the Knudsen diffusion, the pore size defines the resistance against the diffusion process. Also, pore connection and turtuosity are necessary to consider in the description of Knudsen diffusion mechanism. Therefore, smaller pores present larger resistance, thus the diffusivity becomes smaller [15].

The surface diffusion mainly occurs in some mesopores and micropores, such as the pores belong to the parallel wall. The adsorption force holds the water molecules on the wall. The mass transport related to the surface diffusion is thermally activated that there exist jumps between the adsorption site of the water molecules. Thus, this process represents higher resistance than Knudsen diffusion process. The significance of the surface diffusion is featured when a greater volume of the water adsorbed to the pore wall. It occasionally happens at low relative humidity [15].

1.3   Thermal and Hygral Phenomena in Concrete

Thermally Induced Volume Changes and Cracking in Concrete. In the case of thermal effects, the main causes for volume changes are due to the nonuniform temperature distribution during the construction process and the existence of thermal gradients near the surface of the structure owing to convection phenomena arising from interaction. Therefore, the risk of cracking due to thermal variation may be observed in two main different patterns in concrete structures. The first one is cracking in the interior part of the body due to the cooling process as a result of the nonuniform distribution of maximum temperature getting down to the mean annual temperature several years after completion of the dam. The second one is cracking near the surface of the body as a consequence of the thermal gradient development through the fast surface cooling due to the ambient temperature [16]. The second process has a key role in occurrence of critical durability problems in the first week after placing concrete. In the literature, the thermally induced cracking in concrete structures have been investigated by developing couplings in terms of the cross-effects between the hydration process, the temperature evolution and the corresponding deformation [3]. The studies have been generally conducted within the framework of the theory of Reactive Porous Media [17]. This theory contributes to derive the governing relations and constitutive equations dealing with the continuum mechanical problems.

Shrinkage Phenomenon in Concrete. The water content variation and the related moisture diffusion process at the micro-structure of the cementitious material may lead to the early-age durability phenomena by inducing volume changes in concrete. In the presence of the hygral gradients near the surface of concrete elements, the stresses generated in concrete, when the stresses reach the tensile strength, micro-cracks may occur. In the literature, the mechanism related to the autogenous shrinkage leads to (i) an increase of capillary tension in pore fluids due to the formation of menisci, (ii) an increase of surface tension causing reduction of thickness of water adsorbed on solid surface, and (iii) a decrease in disjoining pressure in hindered adsorption area [18]. All these mechanisms result in autogenous shrinkage. When the concrete is subjected to the environment with a lower humidity than the initial one in the pore system of concrete, the hygral gradients are constructed between the interior

and the exterior of concrete. These gradients act as the driving force for the moisture transport to the environment. This phenomenon is referred to the drying shrinkage. It is accompanied by the volume reduction and consequently stresses are generated in concrete, if the body is mechanically restrained and the stresses reach the maximum critical stress of concrete, cracking is initiated.

Creep Response in Concrete. Creep is an other time- and stress-dependent phenomenon that occurs in cementitious materials. In general, creep behavior classified into three common types, according to the hygral and thermal effects. These creep types Basic creep, drying creep and thermal creep. The basic creep occurs under constant temperature, when the concrete is completely sealed and there is no moisture exchange between the interior of concrete and the environment. Drying creep, the so-called Pickett effect is observed in concrete when it is exposed to the environment with relative humidity lower than that in the interior of concrete. Thermal transient creep occurs in concrete under varying temperature conditions.

As a matter of fact, creep in concrete originates from its response to the mechanical, hygral and thermal effects at the microlevel that its structure is discussed in Section 1.2. In the microstructure of concrete, there are highly localized sites which treat like bridges connecting opposite walls of micropores to each other. These bridges contain hindered adsorbed water. The atomic bonds within these bridges are under very high tensile micro-pre-stresses. These micro-pre-stresses are produced by the disjoining pressure of the hindered adsorbed water in the gel pores and by very large volume changes induced by the hydration and the drying effects localized within the gel pores bonds. The deviatoric and volumetric creep at the macroscopic scale is believed to be caused by the viscous shear slip due to the frequent interatomic bond breakage and reformation. The kinetic energy of random vibrations of atoms induced by thermal effects and the magnitude of the activation energy barrier determine the bond breakage. Indeed, the interatomic bond breakage increases by the reduction in the activation energy barrier owing to the increase of the tensile microprestress. [19].

1.4 Modeling Aspects

The reaction of cement hydration, as any other chemical reaction is strongly dependent on the variation of water content and temperature evolution in cementitious materials. To model the temperature-dependency of the hydration reaction, the Arrhenius law [20] is employed. This law is widely used to numerically formulate the evolution of hydration process, thereby determining the development of the mechanical properties of concrete. In the literature, there are several other methods applied to model hydration reaction. These methods are mainly based on the equivalent time and the affinity laws. The concept of equivalent time was first introduced in the work of Rastrup [21] as an alternative method to maturity. The equivalent age is defined as a time duration in which the concrete undergoing curing at a constant temperature reaches the same maturity as the concrete subjected to the actual curing history [5].

The affinity laws are constructed on a Arrhenius law by defining the affinity as the driving force of the hydration process within the framework of thermodynamics. To numerically formulate these model, it is required to consider a variable quantifying the extent of the hydration. This variable is called the degree of hydration [22]. It is defined as the ratio of the mass of the hydrated products to the mass of the hydrated products when the hydration reaches its ultimate state [23]. This definition is also proportional to the ratio of cumulative liberated heat at a certain time to the cumulative heat released by the almost complete cement hydration [24].

The evolution of the mechanical characteristics of concrete such as the elastic and viscous properties, the strength and its deformability, is determined by developing a realistic aging model [22]. It is introduced as a substitute for the concept of maturity. The latter does not sufficiently describe the degree of hydration with a thermodynamically consistent framework. Moreover, it does not consider the hydration kinetics [22]. Therefore, a realistic aging model describes the evolution of mechanical properties through the degree of hydration and the temperature. The definition of the hydration and heat development based on the degree of hydration and aging model can help us investigate the durability phenomena when early-age concrete is subjected to thermal or hygral effects.

Investigating the durability phenomena in concrete under thermal and hygral effects using the computational methods provides robust prediction and knowledge of concrete response to the external factors such as the mechanical loading and environmentally induced thermal and hygral effects at early age and beyond. Beside, the fracture mechanism of concrete is studied by considering all these effects and the couplings between them to precisely model the fracture in concrete and conduct a crack risk analysis. It is of primary concern in understanding behavior of concrete at early ages and beyond, because the existence of the crack accelerate the ingress of the external deteriorative substances which may cause the additional durability problems in the long term.

In the literature, there exist several works dealing with the modeling of durability of problem in concrete. In the work of Cervera *et al.* [7] a coupled chemo-thermo-mechanical model is proposed for concrete to investigate the hydration process and the aging effects on development of the mechanical properties of concrete, also the evolution of temperature at the early-age of concrete is studied. This chemo-thermo-mechanical model within the framework of viscoelasticity is applied to simulate the constructions of roller-compacted dams by investigating the aging effect, the temperature evolution, the stress distribution and the risk of tensile damage in [25, 16].

Lackner and Mang [23] develops a three-dimensional chemo-plastic material model for the simulation of early-age damage in the roller-compacted concrete. The hydration model in this study is developed within a multisurface chemoplasticity model to determine the evolution of the intrinsic material properties. The temperature evolution during the construction of the roller-compacted concrete is studied by incorporating the thermomechanical model. Then, the crack risk analysis is performed based on determination of a correlation between distribution of the maximum stress and the instant tensile strength without explicit account for the crack initiation and propagation.

To investigate the fracture mechanism in concrete, the phase-field models [26, 27] have attracted remarkable prevalence among the researchers who deal with the computational modeling of fracture in concrete over the recent years. Although, this approach is widely used to model cracking under the mechanical loading, there exist few recent works incorporate the computational chemo-thermo-mechanics along

12

with the phase-field model to simulate the brittle fracture caused by the early-age shrinkage and hydration heat [28, 29, 30].

In the case of modeling of the hygral effects in concrete, a microprestress-solidification theory has been developed to investigate the aging and drying effects along with the creep response in concrete [19, 31]. This model has been widely applied in the literature to model transitional thermal creep of early-age concrete [11], also it is coupled with the microplane model to investigate the primary aspect of concrete behavior, such as creep, shrinkage, thermal deformation and cracking in [32]. The microprestress-solidification theory is then modified in [33], and applied to model the thermal and moisture effects on creep response of concrete. Cervera *et. al* [34] extends the chemo-thermo-mechanical models to examine the short- and long-term creep response of concrete and damage by considering a viscoelastic model that is motivated by the microprestress-solidification theory.

1.5 Objective of the Thesis

In this study we aim at modeling the thermal and shrinkage-induced cracking in concrete structures. We develop a phenomenological model to consider the effect of hydration process and the environmental conditions on the temperature evolution in massive concrete structures and cracking. This model is founded on a basis of an approach which includes a coupling between the thermo-chemo-mechanical model and the cohesive zone phase-field model.

Apart from the modeling approaches suggested in the literature, the shrinkage strain is not obtained by using an empirical expression including the hygromechanical expansion coefficient and the change in humidity, we aim to develop a physically motivated coupled constitutive modeling approach. This model is furnished by a robust computational framework to address the durability problems that arise from drying shrinkage and creep within the three-dimensional framework of poro-viscoelasticity. Furthermore, we couple this model with the cohesive zone phase-field model to investigate the shrinkage-induced cracking.

13

1.6 Scope and Outline of the Thesis

The thesis is concerned with the development of a phenomenological model to be used for analyzing the short- and log-term behavior of concrete structures under mechanical loads and environmental conditions such as varying states of temperature and humidity. The effects of environmental conditions will be considered for thermal and shrinkage-induced cracking observed respectively in massive concrete structures such as dams and the structures which have relatively low ratios of volume-to-surface areas.

The basic ideas and the novel aspects of this thesis are

- Developing a robust numerical modeling of thermally induced cracking in massive concrete structures accounting for the effect of temperature evolution, autogenous shrinkage and the thermal transient creep at early ages.

- Formulate the stress-strain response of hardening concrete within the incremental scheme.

- Extending the cohesive phase-field model to simulate for the first time the quasi-brittle thermal fracture in roller-compacted concrete.

- Developing novel multi-field interface elements between the lifts of the concrete dam.

- Developing a robust numerical modeling of creep and drying shrinkage in a concrete structure with a higher ratio of surface-area-to-thickness within the framework of poro-viscoelasticity.

- Applying the microprestress theory to model the viscoelastic behavior of concrete in the long-term accounting for the hygral effects.

- Proposing a physically motivated approach to model the drying shrinkage and creep response in concrete.

- Extending the cohesive phase-field model to simulate shrinkage induced-cracking in concrete.

To this end, we adopt a thermodynamically consistent cohesive zone phase field-model, also known as the unified phase-field model to investigate the mechanical and environmentally-induced fracture mechanism of concrete. In Chapter 2, we present the formulations associated with the phase-field models including the approximation and regularization of the crack topology, the dissipation function, the energetic degradation function, and general softening laws adopted for different types of fracture, governing and constitutive equations. We then represent the finite element discretization of the phase-field equation. Furthermore, the representative numerical examples are demonstrated to validate the numerical modeling capabilities of the phase-field method and the current implementation.

Chapter 3 is devoted to numerical modeling of early-age cracking in roller-compacted concrete (RCC) dam in the presence of the varying environmental temperature conditions. To this end, coupled chemo-thermo-mechanical approach is numerically developed to investigate the cross-effect of evolution of both temperature and the degree of hydration, and consequent cracking on the durability and mechanical properties of concrete structures. This the first chemo-thermo-mechanical model coupled with the cohesive zone phase-field model for an aging concrete.

In Chapter 4, we develop a coupled constitutive modeling approach that is furnished by robust computational framework to address the durability problems that arise from drying shrinkage within the three-dimensional framework of poro-viscoelasticity. In this chapter, the adsorption-desorption isotherm model and the microprestress theory are applied within the general framework of poroelasticity to numerically model the variation of the evaporable water content of concrete in terms of the relative humidity change, and account for the viscoelastic behavior of concrete in terms of creep response. In contrast to the existing models of poromechanics where the pressure is a primary field, here we construct the model base on relative humidity. The results obtained using the proposed method have been constructed with a broad spectrum of experiments reported in the literature that cover various types of creep in concrete.

Chapter 5 is dedicated to the numerical model of shrinkage-induced cracking in concrete structures by applying the cohesive-zone phase-field model coupled with the constitutive modeling approach presented in Chapter 4.

The thesis closes with Chapter 6 where the concluding remarks and the outlook are presented.

CHAPTER 2

PHASE-FIELD MODELING OF MECHANICAL FRACTURE IN BRITTLE AND QUASI-BRITTLE MATERIALS

2.1 Introduction

In engineering applications, the prediction of crack initiation and propagation in structures made up of different materials under mechanical loading and environmental conditions is greatly important. Therefore, in the field of solid mechanics the investigation of failure mechanisms can contribute to explain the origination of failure processes in many materials such as concrete, rock, ceramics, metals, polymers, and biological soft and hard tissues. For many years, the numerical methods have been developed in the literature to quantitatively render the relationship between the crack length, the intrinsic resistance to crack growth, and the crack propagation criterion. The classical theory of brittle fracture has been theoretically pioneered in the work of Griffith [35] and Irwin [36]. They founded the theory of linear elastic fracture mechanics for brittle fracture, in which a global energy approach was developed to predict the crack initiation and propagation. Accordingly, the crack growth is observed when the elastic stored energy in the bulk material reaches a critical value. This critical value is defined as the surface energy dissipated for crack propagation.

The numerical modeling of fracture in concrete structures dates back to the late 1960s by Ngo and Scordelis [37], and Rashid [38] who presented discrete crack and smeared crack models, respectively. In the literature, the computational approaches that have been developed to simulate the fracture of cementitious materials are specifically categorized in three general classes: discrete crack models, lattice models, and continuum damage models. The classical discrete crack approaches [39, 40] require specific

techniques, which introduce discontinuities fields. According to this approach, cracks are modeled as a surface of discontinuities with explicit or implicit geometric modeling. The basic drawback of the classical discrete crack methods is that in a situation with complex crack topologies, they suffer from the issues of severe dependency on mesh-alignment and spurious stress locking [41]. These deficiencies have been avoided by proposing new discrete advanced approaches, which include the extended finite element model (XFEM) with the enriched displacement field with discontinuities [42, 43, 44]. However, the implementation of this approach is troublesome in the three-dimensional framework to predict the special cases of crack topology such as crack branching and merging [45, 27]. As another approach, the so-called cohesive zone modeling technique, pioneered by Barenblatt [46], is developed by introducing the traction-separation laws at the interface elements between the predefined crack surfaces [47, 48, 49]. This approach also requires sufficient degree of mesh refinement to circumvent the oscillation due to element-wise failure. Also, this method is inapplicable to the mesh without the predefined crack paths.

In the classical lattice model, the solid is discretized by trusses or beam elements. A fracture criterion which can be a threshold quantity such as stress or energy is specified. This quantity is calculated for each element. When its value exceeds the fracture limit, the elements are removed from the current mesh [50]. The results of simulations are dependent invariantly on the element type and the fracture criterion. In the literature, there are some works applied this technique to study the fracture mechanism in concrete [51, 52, 53]

Continuum damage models constitute another class of methods used to simulate fracture in cementitious materials, first proposed by Kachanov [54]. In these methods, there are one or several variables, which determine the degradation of material stiffness. The main disadvantage of this method is that this technique is highly dependent on the spatial discretization (mesh size and orientation), which results in an ill-posed mathematical description at a certain level of accumulated damage [55, 56]. To circumvent the ill-posedness of classical local continuum damage models associated with spatial dicretization in the finite element simulations, non-local damage models have been developed by introducing an internal length scale. The purpose of introducing the internal length scale is to regularize the localization of damage, thereby

overcoming the mesh sensitivity of the damage models [55].

Furthermore, the deficiencies of the classical damage methods have been suppressed by introducing variational methods based on energy minimization as proposed by Francfort and Marigo [57], Bourdin, Francfort an Marigo [58], Dal Maso and Toador [59] and Buliga [60]. Overcoming the difficulties associated with the computational modeling of fracture on the basis of the sharp crack discontinuities especially in the case of the complex crack topologies is motivated by the Γ-convergence theorem [61]. Adoption of the Γ-convergence approximations in the regularization setting of the variational methods established on the energy minimization is primarily motivated by image segmentation functional proposed in the work of Mumford and Shah [62]. The application of Γ-convergence approximations on the free discontinuity problems is explained in detail in the work of Ambrosio and Tortorelli [63], Dal Maso and Toador [59], and Braides *et al.* [61, 64]. The approximation provides regularization of a sharp crack surface topology based on a concept of diffuse crack zone. This zone is featured by a scalar auxiliary variable the so-called crack phase-field that characterizes the smooth transition between the intact solid and the fractured domain. These approaches to brittle fracture designated as the phase-field methods. The governing equation expressing the phase-field method has been principally founded on the classical Ginzburg-Landau-type evolution equation, which is also mentioned in Hakim and Karma [65], Karma *et al.* [66], and Estigate *et al.* [67]. The theories of energy minimization are mainly expressed in the rate-independent setting in the precedent studies. However, the time-dependent viscous regularizations may also be applied to these phase-field models, as in the work outlined in Hakim and Karma [65].

In general, the aforementioned studies are exclusively applicable in the special circumstance, where the monotonous loading applied to an arbitrary sub-domain of a fracturing solid, and they are not described in a thermodynamically consistent framework. Also, the energy-release driving force does not differentiate the fracture in tension and compression. Miehe *et al.* [26] extended the variationally-based phase-field approach to fracture within the thermodynamically consistent framework. They implemented this method straightforwardly as a multi-field finite element problem without explicitly modeling discontinuities. The main features which promote the work of Miehe *et al.* [26] are determining the fracture in tension, characterizing the

dissipation, and introducing the viscosity as a regularization of the rate-independent formulation. Furthermore, this formulation was modified in [68] to overcome some of the difficulties by supplementing anisotropic formulation in terms of the asymmetric tension-compression split to capture crack initiation only in tension by introducing an operator split algorithm for a staggered update of the history field associated with the energetic driving force. They also extended the phase-field model within the multi-field finite element solver to the multi-physics problems such as the crack propagation in thermo-elastic solids [69, 70] and the hydrualic fracturing in fluid-saturated porous media based on the coupled problem of Darcy-Biot-type fluid transport [71, 72, 73].

In the literature, the existing phase-field approaches have been widely applied to brittle fracture, however there exist few works [74, 75, 76], in which a phase-field model was proposed for cohesive fracture. Recently, a unified phase-field model of quasi-brittle failure was developed in the work of Wu [27]. Accordingly, in contrast to the existing phase-field models, this model adopts a novel constitutive functions optimal for quasi-brittle failure. The proposed phase-field theory converges to a cohesive zone model as the internal length scale vanishes. In addition, several general softening laws, e.g., linear, exponential, hyperbolic and Cornelissen [77], which is typically used for quasi-brittle solids have been incorporated to improve the accuracy of the model. There exist some works that have implemented the unified phase-field model to model both brittle and quasi-brittle fracture under the purely mechanical loading [78, 79, 80, 81]. The failure of a quasi-brittle material such as concrete whose post-cracking response is accompanied by softening can be modeled by the phase-field regularized cohesive zone model. Apart from this fact, this model avoids the troubles associated with the length scale and consequently the mesh-dependency of the global response of the fracturing solid.

In the phase-field model the regularization of diffuse crack topology is principally governed by the length scale parameter, such that Γ-convergence approaches to a sharp crack topology for a vanishing length scale parameter. The regularized crack surface is resolved by designating a definite minimum element size with respect to the length scale parameter [26, 68]. Moreover, a precise prediction of the behavior of fracturing solid is obtained by determining the length scale as a function of the mechanical properties of the material [82, 69, 83, 84]. Nevertheless, in the phase-field

regularized cohesive model, the length scale parameter has insignificant effect on the overall response of the material. This parameter at most changes the localization bandwidth. Nevertheless, it is required to be sufficiently resolved by the mesh size within the localization bandwidth to obtain the numerical results converging to the analytical ones [27].

This chapter is organized as follows. We first demonstrate the phase-field approximation of crack topology and express the formulations related to the crack surface functional and the corresponding crack surface density function in the one-dimensional setting. These formulations are then extended to the multi-dimensional case. To describe the homogeneous evolution of the crack phase-field and its regularization, the geometric crack function is introduced. Then, the energetic degradation function for the brittle and cohesive fracture is presented to investigate the effect of the crack evolution on the mechanical response of the material. Furthermore, the formulations of the dissipation function are demonstrated to derive the evolution equation of damage field. The common types of softening laws and the associated optimal parameters are demonstrated. The implementation of these laws in the phase-field model allows us to have a robust prediction of the structural response of the material without requiring the length scale parameter as a function of mechanical properties.

The description of a constitutive framework of the phase-field model is given by deriving the variational equation and the associated constitutive relations which determine the mechanical behavior and the evolution equation of the crack phase-field. Then we continue with the representative numerical examples related to the convergence of the crack surface functional Γ_ℓ to the sharp crack topology in both brittle and quasi-brittle fracture. Moreover, the capability of the phase-field models in predicting the crack patterns and the behavior of the fracturing material is exhibited by the several numerical examples. In particular, the brittle and quasi-brittle fracture under mechanical loading in different representative numerical examples are demonstrated in terms of the evolution of crack pattern and the overall structural response. In addition, the results obtained in this study are compared with the numerical and the experimental findings reported in the literature, to verify our current implementation of the phase-field models.

2.2 Phase-Field Approximation of Crack Topology

We motivate the theoretical aspects of the phase-field approach by considering a one-dimensional bar of cross-section Γ and of infinite length, $L \in [-\infty, +\infty]$ occupying the domain $\mathcal{B} = \Gamma \times L$ with a material point positioned at $x \in L$ of its axis. The bar is assumed to contain a crack at the axial position $x = 0$ where Γ quantifies the fully broken crack surface [26]. To approximate this sharp crack topology, an auxiliary field variable $d(x) \in [0, 1]$, also known in the literature as the crack phase-field is introduced as

$$d(x) = \begin{cases} 1 & \text{for } x = 0. \\ 0 & \text{otherwise.} \end{cases} \tag{2.1}$$

where this variable characterizes for $d = 0$ and $d = 1$ the unbroken and the fully broken state of the material, respectively. Therefore, consistent with the continuum theory of damage, in a homogenized macroscopic scheme, the description of micro-cracks growth is related to the scalar damage field d. The diffuse and sharp crack topologies along the axis of the bar are demonstrated in Figure 2.1. As is depicted, the sharp crack topology is regularized by the internal length scale parameter ℓ. As ℓ approaches to 0, $\ell \to 0$, a diffuse crack, demonstrated in Figure 2.1a converges to a sharp crack shown in Figure 2.1b. It represents the characteristic effect of the length scale parameter ℓ on the spatial distribution of the crack phase-field.
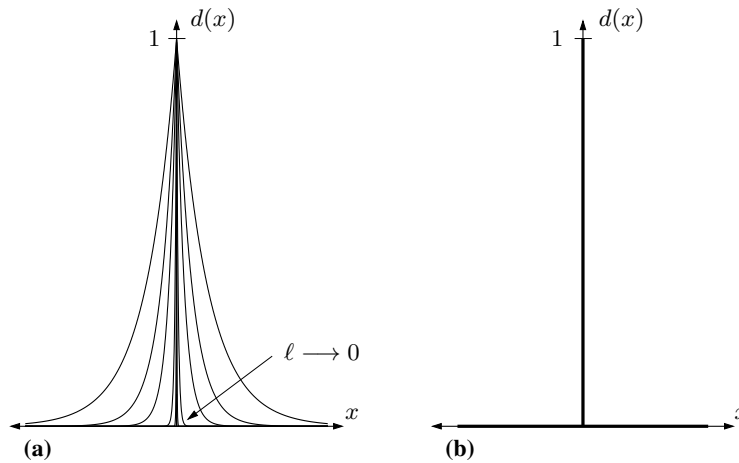
Figure 2.1: Diffuse and sharp crack topology. **(a)** A diffuse crack at $x = 0$ versus **(b)** a sharp crack at $x = 0$ modeled with the length-scale parameter ℓ.

In the one-dimensional bar, the crack phase-field $d(x)$ can be mathematically represented by the following homogeneous differential equation

$$\alpha'(d) - 2\ell^2 d_{,xx} = 0 \qquad (2.2)$$

where $\alpha(d)$ is the geometric crack function which represents the homogeneous evolution of the crack phase-field. This equation is subjected to the Dirichlet-type boundary conditions of $d(0) = 1$ and $d(\pm D_u) = 0$ where D_u indicates the ultimate half bandwidth of localization band. It can be shown that, the differential equation presented in (2.2) is the Euler equation of the variational principle

$$d = \mathrm{Arg}\left\{\inf_{d \in W} I(d)\right\} \quad \text{with} \quad W = \{d \,|\, d(0) = 1, d(\pm D_u) = 0\}. \qquad (2.3)$$

The functional $I(d)$ is established, by integrating Galerkin-type weak form of the homogeneous differential equation (2.2)

$$I(d) = \frac{1}{c_0} \int_{\mathcal{B}} \left\{\alpha(d) + \ell^2(d_{,x})^2\right\} \, dV \qquad (2.4)$$

where $c_0 > 0$ is a scaling parameter. It will be defined for the the brittle and quasi-brittle fracture in the following subsection. Using $dV = \Gamma \, dx$ and approximating the ultimate solution of the non-smooth crack phase-field $d(x) = d_u(x)$, we obtain $I(d = d_u) = \Gamma\ell$, which relates the functional I to the crack surface Γ. To this end, the crack surface functional is introduced in the following form [26, 27]

$$\Gamma_\ell(d) := \frac{1}{\ell} I(d) = \frac{1}{c_0\ell} \int_{\mathcal{B}} \left\{\alpha(d) + \ell^2(d_{,x})^2\right\} \, dV. \qquad (2.5)$$

Indeed, the crack surface functional is calculated by integrating the crack surface density function per unit volume of the solid body $\gamma(d; d_{,x})$, this function is given by

$$\gamma(d; d_{,x}) = \frac{1}{c_0\ell} \left\{\alpha(d) + \ell^2(d_{,x})^2\right\}, \qquad (2.6)$$

which represents the area of the crack surface per unit volume within the solid body domain. The scaling parameter c_0 normalizes the crack surface functional Γ that converges to Γ_ℓ for the sharp crack topology when the body is fully degraded.

2.2.1 Regularization of Phase-Field for Crack Topology

In this section, the geometric crack function $\alpha(d)$ is introduced [27]. This function governs the distribution of the crack phase-field and characterizes the crack surface

density function $\gamma(d; \nabla_x d)$, and governs the value of the scaling parameter c_0. In the literature, the following generic quadratic form is used

$$\alpha(d) = zd + (1 - z)d^2 \geq 0 \quad \forall d \in [0, 1] \tag{2.7}$$

where z is a positive parameter $z \in [0, 2]$. As the crack phase-field bounded between 0 and 1, the geometric crack function $\alpha(d) \in [0, 1]$ is expected to fulfill the characteristics of $\alpha(0) = 0$ for the intact state ($d = 0$) and $\alpha(1) = 1$ for the fully broken state ($d = 1$). The geometric crack function versus the crack phase-field curves for varying values of z are depicted in Figure 2.2. The crack geometric function for the classical brittle fracture mechanism is expressed by setting $z = 0$ and $z = 1$, likewise it is set to $z = 2$ for the quasi-brittle fracture.
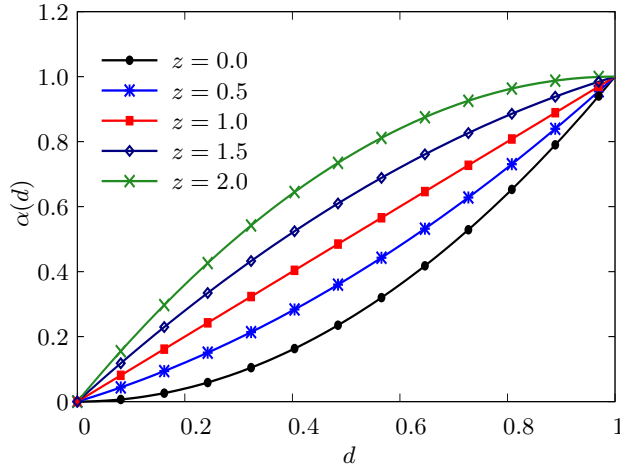
Figure 2.2: The geometric crack function $\alpha(d)$ versus the crack phase-field for different values of the parameter z.

The description of a diffuse crack topology in the one-dimensional space can be simply extended to the multi-dimensional setting. Let $\mathcal{B} \subset \mathbb{R}^\delta$ be the reference configuration of a material body with dimension $\delta \in \{1, 2, 3\}$ in space and $\partial \mathcal{B} \subset \mathbb{R}^{\delta-1}$ its surface as demonstrated in Figure 2.3. In addition, $\mathcal{L}$ represents the localization zone, as $\partial \mathcal{L}$ demonstrates its surface. In the following, the time-dependent crack phase-field is represented to study crack propagation for $\mathcal{T} \subset \mathbb{R}$ of time as follows

$$d : \begin{cases} \mathcal{B} \times \mathcal{T} \to [0, 1], \\ (\boldsymbol{x}, t) \mapsto d(\boldsymbol{x}, t). \end{cases} \tag{2.8}$$

24

Next, in the multi-dimensional setting the regularized crack functional $\Gamma_\ell(d)$ is introduced in terms of the crack surface density function $\gamma(d; \nabla_x d)$

$$\Gamma_\ell(d) = \int_{\mathcal{B}} \gamma(d; \nabla_x d) \, dV \quad \text{with} \quad \gamma(d; \nabla_x d) = \frac{1}{c_0} \left(\frac{1}{\ell} \alpha(d) + \ell |\nabla_x d|^2 \right). \quad (2.9)$$
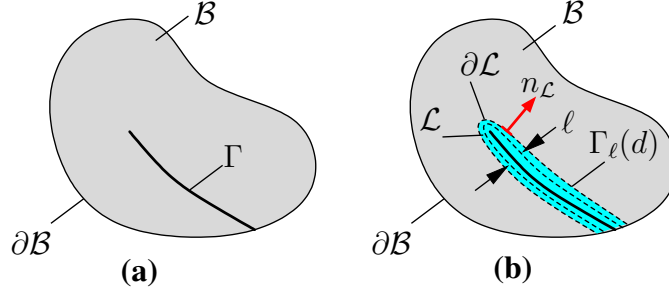
Figure 2.3: Sharp and diffuse crack topologies. **(a)** Sharp crack surface Γ embedded into the solid $\mathcal{B}$ and **(b)** the regularized crack surface $\Gamma_\ell(d)$ is a functional of the crack phase-field d over the crack phase-field localization zone $\mathcal{L}$.

The crack surface density function $\gamma(d; \nabla_x d)$ is described per unit volume of the solid and depends on the crack phase-field d and its spatial gradient $\nabla_x d$. The crack surface density function represents the density of the crack surface area. It has decisive role in the modeling of crack propagation. As demonstrated in Figure 2.3a, a given sharp crack topology $\Gamma(t) \subset \mathbb{R}^{\delta-1}$ is assumed inside the body $\mathcal{B}$ at time t. The regularized crack phase-field $d(\boldsymbol{x}, t)$, see Figure 2.3b is obtained from the minimization principle

$$d(\boldsymbol{x}, t) = \text{Arg} \left\{ \inf_{d \in W_{\Gamma(t)}} \Gamma_\ell(d) \right\} \quad (2.10)$$

subjected to the Dirichlet-type constraints

$$W_{\Gamma(t)} = \{ d \mid d(\boldsymbol{x}, t) = 1 \quad \text{at} \quad \boldsymbol{x} \in \Gamma(t) \}. \quad (2.11)$$

The variational principle in (2.10) is represented in the form of the Euler equations as follows

$$\alpha'(d) - 2\ell \Delta d(x) = 0 \quad \text{in} \quad \mathcal{B} \quad \text{and} \quad \nabla_x d \cdot \boldsymbol{n}_{\mathcal{L}} = 0 \quad \text{on} \quad \partial\mathcal{L} \quad (2.12)$$

where Δd is the Laplacian of the crack phase-field ($\Delta d := \text{div}(\nabla_x d)$) and $\boldsymbol{n}_{\mathcal{L}}$ presents the outward unit normal on $\partial\mathcal{L}$. Moreover, the length scale parameter ℓ controls the diffuse crack phase field topology. In particular, the length scale parameter ℓ characterizes the width of the localization band. In order to show the numerical solution

converging to the original problem, we let $\ell \to 0$ according to the convergence theorem presented in [61], as it will be presented in Subsections 2.5.2 and 2.5.6 for the brittle and the quasi-brittle phase-field models, respectively.

It is represented in the work of Miehe *et al.* [26], that the regularized crack surface $\Gamma_\ell(d)$ is resolved, i.e. $\Gamma_\ell(d) \approx \Gamma$ by choosing the element size smaller than the length scale parameter as $h < \ell/2$ for the brittle type of the fracture. In the case of the phase-field regularized cohesive zone model, Wu [27] recommends that for providing a robust prediction of the fracture, the solid domain should be discretized with a element size much smaller than the length scale parameter as $h \leq (0.1 \sim 0.2)\ell$. The length scale and mesh dependency of the phase-field model will be discussed in Subsection 2.2.3.

The scaling parameter c_0 in (2.4) and (2.5) is derived for the fully developed crack referring to (2.12). At first, (2.12) is multiplied by $d_{,x}$ and then integrated with respect to the coordinate $x_n = (\boldsymbol{x} - \boldsymbol{x}_\mathcal{S}) \cdot \boldsymbol{n}_\mathcal{S}$ where $\boldsymbol{x}_\mathcal{S}$ represents the closest point along the crack path $\mathcal{S}$, we obtain

$$\alpha(d) - \ell^2 |\nabla_n d| = 0 \tag{2.13a}$$

$$\text{yielding} \quad \gamma = \frac{2\alpha(d)}{c_0 \ell} \quad \text{and} \quad |\nabla_n d| := \frac{dd}{dx_n} = \frac{\sqrt{\alpha(d)}}{\ell}. \tag{2.13b}$$

We can define the scaling parameter c_0 by inserting (2.13b) and $dV = 2|dx_n|\Gamma$ in (2.9), and substituting $dd\,\ell/\sqrt{\alpha(d)}$ for $|dx_n|$ as

$$c_0 = 4 \int_0^1 \sqrt{\alpha(\beta)} d\beta. \tag{2.14}$$

2.2.2 Energetic Degradation Function and Associated Softening Laws

According to the theory of elasticity, the reference energy storage function Ψ_0 represents the elastic strain energy stored in the bulk of an isotropic solid per unit volume. While the crack is growing, the degradation acts on the reference energy storage function in a multiplicative manner. Therefore, the degradation of the reference energy is given by

$$\hat{\Psi}(\boldsymbol{\varepsilon}, d) = [g(d) + \kappa]\, \hat{\Psi}_0(\boldsymbol{\varepsilon}) \tag{2.15}$$

where $\kappa\hat{\Psi}(\varepsilon)$ with $\kappa \approx 0$ is the artificial elastic residual energy at a fully broken state $d = 1$ to avoid the complete degradation of the stored energy [26]. When the degradation functions treat on Ψ, it affects the overall response of the body. This treatment may not result in the physically realistic results, such as the occurrence of cracking in both tension and compression states. To this end, an asymmetric tension-compression split energy storage function is introduced by additively decomposing Ψ_0 into a positive part Ψ_0^+, due to tension and a negative part Ψ_0^- due to compression. In brittle and quasi-brittle, the degradation function affects only the positive part

$$\hat{\Psi}(\boldsymbol{\varepsilon}, d) = [g(d) + \kappa]\,\hat{\Psi}_0^+(\boldsymbol{\varepsilon}) + \hat{\Psi}_0^-(\boldsymbol{\varepsilon}). \tag{2.16}$$

The definition of the energy storage function and derivation of the stress response of the degrading material will be described in detail in Section 2.3.

In the literature there are several degradation functions adopted in simulating the various types of fracture in solid material. These functions are respectively represented for linear, quadratic and rational generic form (2.17) in Figure 2.4. In this work, to model the bulk response of a fracturing solid undergoing the energy degradation, the following generic form of the energetic degradation function is adopted [27]

$$g(d) := \frac{1}{1 + \phi(d)} = \frac{(1-d)^p}{(1-d)^p + Q(d)} \quad \text{with} \quad \phi(d) = \frac{Q(d)}{(1-d)^p} \tag{2.17}$$

for the exponent $p = 2$ and the continuous function $Q(d) > 0$, which is defined in the form of a polynomial expression as follows

$$Q(d) = a_1 d + a_1 a_2 d^2 + a_1 a_2 a_3 d^3 = a_1 d P(d)$$
$$\text{with} \quad P(d) = 1 + a_2 d + a_2 a_3 d^2 \tag{2.18}$$

where the material constants a_1, a_2, and a_3 are calibrated from the standard material properties for different softening laws.

The material constants a_1, a_2 and a_3 are specified for the constitutive function $g(d)$ optimal for brittle and quasi-brittle fracture. At first, the equivalent cohesive zone model is designated by applying the proposed phase-field theory to a one-dimensional problem. Let us assume a sufficiently long bar with $x \in [-L, L]$ in which the crack evolution is not affected by the outer boundary conditions. The loads are applied at both ends of the bar by increasing displacements u^* in the opposite directions. In this
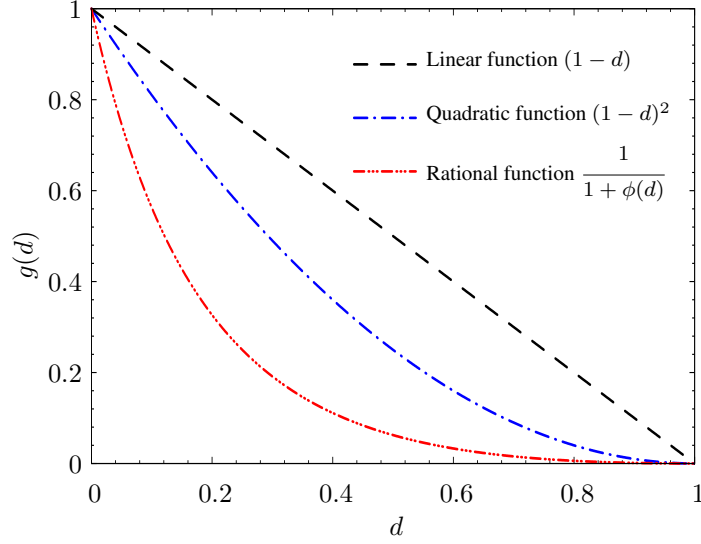
Figure 2.4: Different types of the energetic degradation function $g(d)$ adopted widely in the literature.

case, the distributed body forces are neglected. The crack is assumed to be initiated at the axial position $x = 0$ and the localization band is lumped in the definite domain $[-D_u, D_u]$, which is dependent on deformation. During the displacement-controlled loading, the homogeneous stress field $\sigma(x)$ along the bar is described by the following constitutive equation

$$\sigma(x, d) = g(d)E_0\varepsilon(x) \tag{2.19}$$

where d represents the crack phase-field, E_0 is the elastic modulus and $\varepsilon(x)$ denotes the strain field along the bar. The imposed displacement u^* at the free end is determined by integrating the strain

$$u^* = \frac{\sigma(x)}{E_0} \int_0^L g^{-1}(d)\, dx = \frac{\sigma(x)}{E_0} \left[L + \int_0^D \phi(d)\, dx \right] = \frac{\sigma(x)}{E_0} L + \frac{1}{2} w(\sigma(x)) \tag{2.20}$$

where the function $\phi(d)$ is specified as $\phi(d) := g^{-1}(d) - 1$ according to (2.18) and $w(\sigma)$ is designated as the apparent displacement jump defined through the following expression

$$w(\sigma) := \frac{2\sigma}{E_0} \int_0^D \phi(d)\, dx. \tag{2.21}$$

The governing equations for the one-dimensional bar subjected to loading at both

28

ends by increasing the displacement in the opposite directions are given by

$$\sigma' = 0, \tag{2.22a}$$

$$\frac{G_c}{c_0}\left[\frac{1}{\ell}\alpha'(d) - 2\ell d_{,xx}\right] = -\frac{1}{2}g'(d)E_0\varepsilon^2(x) \tag{2.22b}$$

where the distributed body forces are neglected for the simplicity. As a consequence, (2.22b) is simply reformulated as

$$\sigma^2\phi'(d) - \frac{2E_0G_c}{c_0\ell}\left[\alpha'(d) - 2\ell^2 d_{,xx}\right] = 0. \tag{2.23}$$

In (2.22) and (2.23), G_c indicates the critical energy release rate. When the crack phase-field initiates within the localization zone, we focus on the localizated solution to the homogeneous differential equation (2.23) which is obtained in terms of the ultimate inverse crack phase-field $x(d; d_u)$ and the half width of localization band $D(d_u)$. The ultimate inverse crack phase-field pivoting at the most on the crack geometric function in (2.7) is respectively defined as follows [27]

$$x(d_u, z) = \begin{cases} \dfrac{\ell}{\sqrt{(1-z)}}\hat{\mathcal{F}}(d_u, z) & z \in [0, 1] \\[4mm] \dfrac{\ell}{\sqrt{(1-z)}}\hat{\mathcal{G}}(d_u, z) & z \in [1, 2] \end{cases} \tag{2.24}$$

where the auxiliary functions $\hat{\mathcal{F}}(d_u, z)$ and $\hat{\mathcal{G}}(d_u, z)$ are presented as

$$\hat{\mathcal{F}}(d_u, z) = \ln\left[\frac{2\sqrt{(1-z)} + 2 - z}{2\sqrt{(1-\xi)\left[zd_u + (1-\xi)d_u^2\right]} + 2(1-\xi)d_u + z}\right], \tag{2.25a}$$

$$\hat{\mathcal{G}}(d_u, \xi) = \ln\left[\arcsin\frac{z - 2(z-1)d_u}{z} - \arcsin\frac{2 - z}{z}\right]. \tag{2.25b}$$

Likewise, the localization bandwidth is defined by

$$D_u(z) = \begin{cases} \dfrac{\ell}{\sqrt{(1-z)}}\ln\left[\dfrac{2\sqrt{(1-z)} + 2 - z}{z}\right] & z \in [0, 1] \\[5mm] \dfrac{\ell}{\sqrt{(1-z)}}\left[\dfrac{\pi}{2} - \arcsin\dfrac{2 - z}{z}\right] & z \in [1, 2] \end{cases} \tag{2.26}$$

The following typical cases are described in detail to comprehend the above results:

- $z = 0$: This case results in geometric crack function $\alpha(d) = d^2$ that has been widely adopted in the classical phase-field models for brittle fracture [26, 68,

29

85]. The scaling parameter c_0, the half bandwidth D_u, and the ultimate crack phase-field $d_u(x)$ are respectively given by

$$c_0 = 2, \quad D_u = +\infty, \quad d_u(x) = \exp(-\frac{|x|}{\ell}). \tag{2.27}$$

- $z = \frac{1}{2}$: This case is considered to develop a variational approach to fracture [86] and gradient damage models [58]. It results in $\alpha(d) = \frac{1}{2}(d + d^2)$ where the scaling parameter c_0, the half bandwidth D_u and the ultimate crack phase-field $d_u(x)$ are respectively given by

$$c_0 = 3 - \frac{\sqrt{2}}{4}\ln(3 + 2\sqrt{2}), \quad D_u = \sqrt{2}\ell\ln(3 + 2\sqrt{2}),$$
$$d_u(x) = \frac{3 - 2\sqrt{2}}{4}\exp(\frac{\sqrt{2}x}{2\ell}) + \frac{3 + 2\sqrt{2}}{4}\exp(\frac{-\sqrt{2}x}{2\ell}) - \frac{1}{2}. \tag{2.28}$$

- $z = 1$: This case with the geometric crack function $\alpha(d) = d$ is adopted in [82, 87] to develop a gradient-based damage model applied to brittle fracture. The corresponding geometric parameters including the scaling parameter c_0, the half bandwidth D_u and the ultimate crack phase-field $d_u(x)$ then become

$$c_0 = \frac{8}{3}, \quad D_u = 2\ell, \quad d_u(x) = \left(1 - \frac{|x|}{2\ell}\right)^2. \tag{2.29}$$

- $z = 2$: This case is introduced in [27] and adopted in [78, 88, 80] to simulate the quasi-brittle failure in solid material especially concrete with the geometric crack function $\alpha(d) = 2d - d^2$. The scaling parameter c_0, the half bandwidth D_u and the ultimate crack phase-field $d_u(x)$ are respectively determined as

$$c_0 = \pi, \quad D_u = \frac{\pi}{2}\ell \quad d_u(x) = 1 - \left(\sin\frac{|x|}{\ell}\right). \tag{2.30}$$

The ultimate crack phase-field $d_u(x)$ with $d_u(x = 0) = 1$ for the aforementioned values of parameter z is demonstrated in Figure 2.5. It can be simply seen that, in the end a localized crack phase-field evolves within the finite domain $x \in [-D_u, D_u]$.

The localized solution to the homogeneous equation (2.23) is determined by multiplying (2.23) by $d_{,x}$ and integrating over x. Doing so, the following expression is obtained as

$$\sigma^2\phi(d) - \frac{2E_0 G_c}{c_0\ell}\left[\alpha(d) - 2\ell^2(d_{,x})^2\right] = 0. \tag{2.31}$$

30
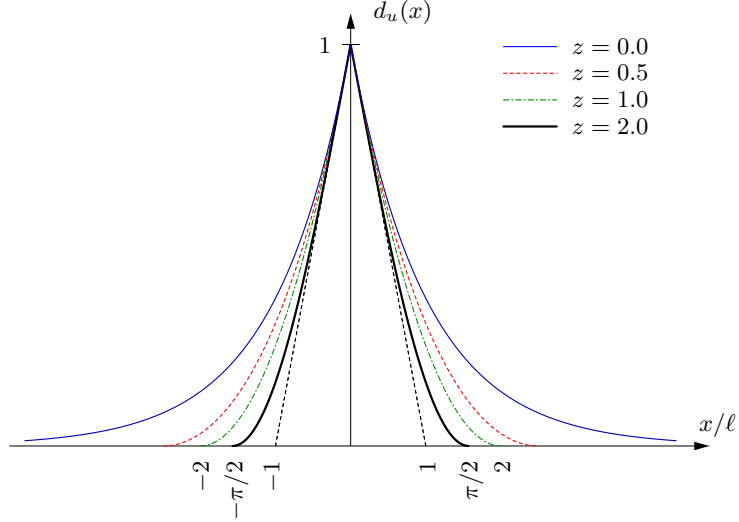
Figure 2.5: Ultimate crack phase-field $d_u(x)$ for various values of z adopted in geometric crack function $\alpha(d)$

As a result, the stress field σ is analytically computed at the point $x = 0$ where the crack phase-field reaches its maximum value d^* as

$$\sigma(d^*) := \sqrt{\frac{2E_0 G_c}{c_0 \ell} \frac{\alpha(d^*)}{\phi(d^*)}} = f_t \sqrt{\frac{[z + (1-z)d^*](1-d^*)^p}{z P(d^*)}}. \qquad (2.32)$$

where f_t the failure strength is defined as

$$f_t := \lim_{d^* \to 0} \sigma(d^*) := \sqrt{\frac{2E_0 G_c}{c_0 \ell} \cdot \frac{\alpha'(0)}{\phi'(0)}}, \quad \text{then} \quad f_t = \sqrt{\frac{2E_0 G_c}{c_0 \ell} \frac{z}{a_1}} \qquad (2.33)$$

For the `AT1`-type brittle phase-field model [89] with $z = 0$, the geometric crack function at $d = 0$ is $\alpha(0) = 0$ so the tensile strength in (2.33) is $f_t = 0$. It means that we can not define any initial elastic stage, therefore, the failure criterion is activated when the loading is started to be applied. But, for the `AT2`-type brittle phase-field model [63] with $z = 1$, and the cohesive zone phase-field model (`PF-CZM`) with $z = 2$, the value of the tensile strength in (2.33) is $f_t > 0$ so there is an initial elastic stage in which the material remains intact with $d = 0$. For characterization of the different types of the phase-field model are presented in Table 2.1.

As the stress field $\sigma = \sqrt{\dfrac{2E_0 G_c}{c_0 \ell} \cdot \dfrac{\alpha(d)}{\phi(d)}}$ as a solution to the differential equation (2.23) is inserted into (2.21) and the apparent displacement jump across the localiza-

31

tion band is analytically given by

$$w(d^*) = \mathcal{C}_0 \int_0^{d^*} \left[\frac{P(d^*)}{(1-d^*)^p} \cdot \frac{z + (1-z)\beta_d}{z + (1-z)d^*} - \frac{P(\beta_d)}{(1-\beta)^p} \right]^{-\frac{1}{2}} \frac{\sqrt{\beta_d} \cdot P(\beta_d)}{(1-\beta_d)^p} d\beta_d$$
(2.34)

where $\mathcal{C}_0 = \dfrac{4G_c\sqrt{z}}{c_0 f_t}$ reflects the effects of the physical properties of the solid material on the apparent displacement jump. The ultimate crack opening w_∞ with vanishing stress is defined by

$$w_\infty = \frac{2\pi G_c}{c_0 f_t} \sqrt{z P(1)} \lim_{d^* \to 1} (1-d^*)^{1-p/2}.$$
(2.35)

For the different value of p it is equivalently represented by

$$w_\infty = \begin{cases} 0 & p < 2, \\ \dfrac{2\pi G_c}{c_0 f_t} \sqrt{z P(1)} & p = 2, \\ +\infty & p > 2. \end{cases}$$
(2.36)

The derivation of the aforementioned equivalent cohesive zone model allows to predict the typical softening laws and determine the associated material constants in the energetic degradation function (2.17). The softening curves for the various types of the material behavior are defined through the relation between the stress field $\sigma(d^*)$ and the apparent displacement jump $w(d^*)$ presented in (2.32) and (2.34), respectively. The initial slope of the softening curve $k_0 < 0$ is determined by

$$k_0 = -\frac{c_0}{4\pi} \frac{f_t^2}{G_c} \frac{[z(a_2 + p + 1) - 1]^{3/2}}{z^2}$$
(2.37)

Referring to (2.33), (2.36) and (2.37), the constants a_1, a_2, and a_3 are defined through the following expressions [27]

$$a_1 = \frac{2z}{c_0} \frac{\ell_{\text{ch}}}{\ell} \quad \text{with} \quad \ell_{\text{ch}} := \frac{E_0 G_c}{f_t^2},$$
(2.38a)

$$a_2 = \frac{1}{z} \left[\left(-\frac{4\pi z^2}{c_0} \frac{G_c}{f_t^2} k_0 \right)^{2/3} + 1 \right] - (p+1),$$
(2.38b)

$$a_3 = \begin{cases} 0 & p > 0, \\ \dfrac{1}{a_2} \left[\dfrac{1}{z} \left(\dfrac{c_0 w_\infty f_t}{2\pi G_c} \right)^2 - (1 + a_2) \right] & p = 2. \end{cases}$$
(2.38c)

32

There exist several general softening laws in the literature, such as linear, exponential, hyperbolic and Cornelissen's laws. A generic traction-separation curve is demonstrated in Figure 2.6. In this curve, the filled area under the traction-separation $\sigma - w$ curve denotes the critical fracture energy release rate G_c. Also, the initial slope, shown with the slope of the red line is defined as $k_0 = -\dfrac{f_t}{w_0}$.

The softening laws frequently applied to model the brittle and quasi-brittle fracture are described in terms of the model parameters a_1, a_2 and a_3, and the initial slope of the softening curve k_0 and the ultimate crack opening w_∞ as follows
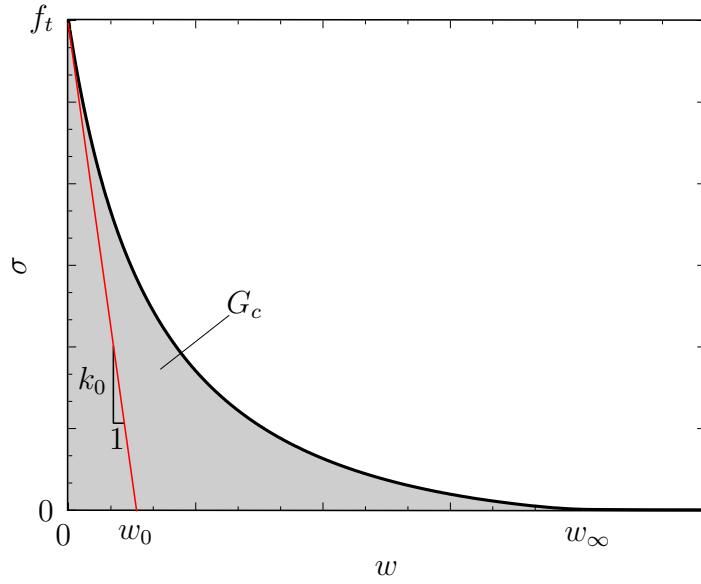
Figure 2.6: A generic traction-separation $\sigma - w$ curve with the critical fracture energy release rate G_c, and the initial slope of $k_0 = -\dfrac{f_t}{w_0}$.

- Linear softening curve: $z = 2$, $p = 2$, $a_2 = -\dfrac{1}{2}$ and $a_3 = 0$

$$\sigma(w) = f_t \max\left(1 - \frac{f_t}{2G_c}w, 0\right), \quad k_0 = -\frac{f_t^2}{2G_c}, \quad w_\infty = \frac{2G_c}{f_t} \quad (2.39)$$

- Exponential softening curve: $z = 2$, $p = \dfrac{5}{2}$, $a_2 = 2^{5/3} - 3 \approx 0.1748$ and $a_3 = 0$

$$\sigma(w) = f_t\left(-\frac{f_t}{G_c}w\right), \quad k_0 = -\frac{f_t^2}{G_c}, \quad w_\infty = +\infty \quad (2.40)$$

- Hyperbolic softening curve: $z = 2$, $p = 4$, $a_2 = 2^{7/3} - \dfrac{9}{2} \approx 0.5397$ and $a_3 = 0$

$$\sigma(w) = f_t\left(1 + \frac{f_t}{G_c}w\right)^{-2}, \quad k_0 = -\frac{2f_t^2}{G_c}, \quad w_\infty = +\infty \quad (2.41)$$

33

- Cornelissen's softening curve [77]: $z = 2$, $p = 2$, $a_1 = 1.3868$, $a_3 = 0.6567$

$$\sigma(w) = f_t \left[(1 + \eta_1^3 r^3) \exp(-\eta_2 r) - r(1 + \eta_1^3) \exp(-\eta_2) \right] \tag{2.42a}$$

$$k_0 = -6.9574 \frac{f_t}{w_c} = -1.3546 \frac{f_t^2}{G_c} \tag{2.42b}$$

$$w_\infty = 5.1361 \frac{G_c}{f_t} \quad \text{with} \quad r = \frac{w}{w_\infty} \tag{2.42c}$$

where r denotes the normalized crack opening and the typical constants for normal concrete are set as $\eta_1 = 0.3$ and $\eta_2 = 6.93$. This softening curve is mainly used to model fracture mechanism in concrete [27].

The comparison between the analytical and the approximated formulations of the general softening curves are demonstrated in Figure 2.7. It shows that there is a good agreement between the analytical and the approximated results.

2.2.3 Length Scale and Mesh Dependency of the Phase-Field Models

Based on the specific form of the geometric crack function $\alpha(d)$ and the degradation function $g(d)$ described above, we can classify the phase-field approaches for brittle and quasi-brittle fracture into three common models [90]. These models are AT1 [89] model developed in the work of Pham *et al.* [82], also see [87], AT2 [63] model pioneered by the work of Bourdin *et al.* [91] and extended in the work of Miehe *et al.* [26, 68], and the phase-field regularized cohesive zone model (PF-CZM) proposed in the work of Wu [27] as distinguished and presented in Table 2.1. As AT1 and AT2 models are typically applied to the brittle fracture, PF-CZM is applicable to both brittle and quasi-brittle fracture while AT1 and PF-CZM have an elastic domain, that is the cracking initiates when the crack driving force reaches a critical value, AT2 model does not possess an elastic domain. Furthermore, in AT1 and AT2 models, the length scale parameter ℓ is defined in terms of the mechanical properties of the material. This parameter, however, is just a numerical one in PF-CZM. In the literature, although the length scale parameter ℓ is initially considered as a numerical parameter as shown in [26, 68], it is regarded as a material parameter depending on the other

34
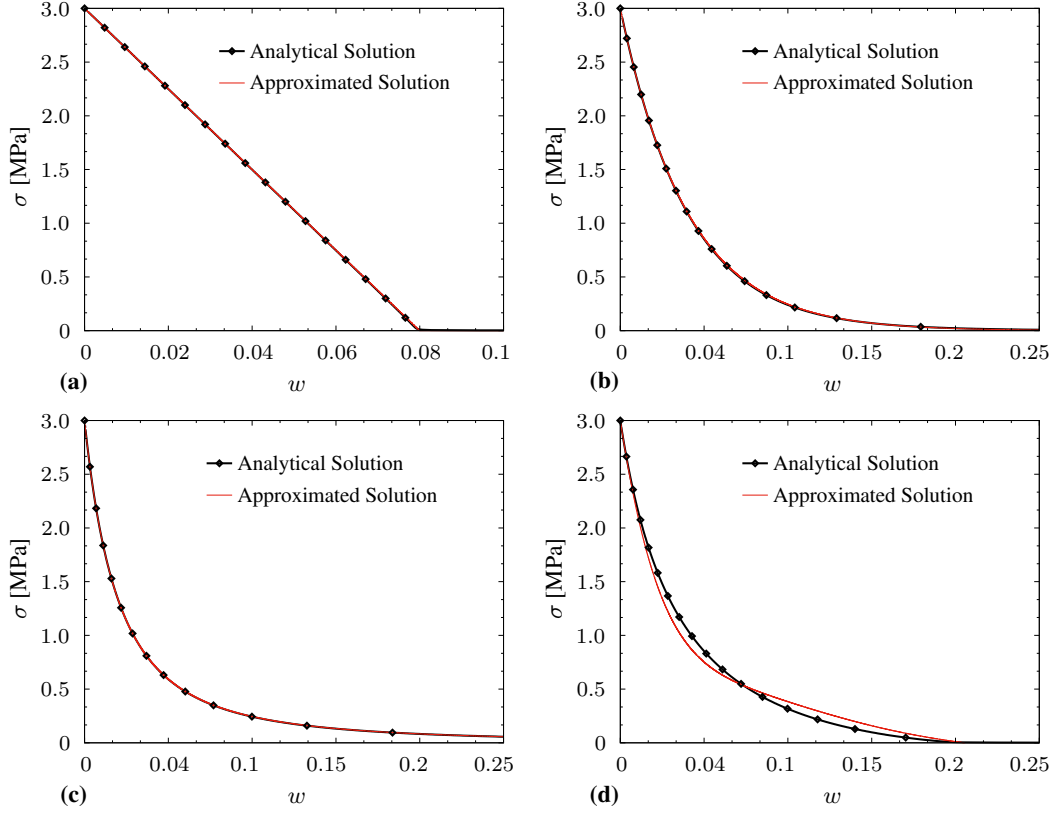
Figure 2.7: Softening laws. **(a)** Linear softening law, **(b)** Exponential softening law, **(c)** Hyperbolic softening law, and **(d)** Cornelissen's softening law ($f_t = 3.0$ MPa and $G_c = 0.12$ N/mm).

mechanical properties [69, 79, 92, 83]. The numerical length scale parameter is computed in terms of the Griffith's characteristic $\ell_{\text{ch}} = EG_c/\sigma_c^2$ where σ_c is the critical strength of material.

Comparison of the existing phase-field models [90] indicates that `PF-CZM` predicts the structural response and the crack pattern in a good agreement with the experimental findings. When the length scale is chosen as much smaller than the problem dimensions and with an element size $h \leq (0.1 \sim 0.2)\ell$, the crack-phase-field is resolved to an adequate degree. Then the results converge without any dependency on mesh discretization. However, the results obtained by using `AT1` and `AT2` models are dependent strongly on the length scale parameter determined as a function of material properties. If the length scale parameter is chosen smaller than the value dictated by the material parameters, `AT1` and `AT2` models overestimate the structural response, however a good match is observed in terms of the crack pattern between the numeri-

cal results and experiments. When the length scale as a constant parameter is chosen according to the material parameters, the structural response is acceptably predicted, whereas the crack path diffuses highly, which is numerically meaningless [90]. The geometrical characteristics of these phase-field models are summarized in Table 2.1

Table 2.1: Geometrical parameters for three common phase-field approach to brittle and quasi-brittle fracture

Model	$\alpha(d)$	$g(d)$	ℓ	D_u
AT1	d	$(1-d)^2$	$\dfrac{3}{8}\ell_{\mathrm{ch}}$	2ℓ
AT2	d^2	$(1-d)^2$	$\dfrac{27}{256}\ell_{\mathrm{ch}}$	∞
PF-CZM	$2d-d^2$	$\dfrac{(1-d)^p}{((1-d)^p)+Q(d)}$	numerical parameter	$\dfrac{\pi}{2}\ell$

2.3 Variational Equations and Associated Governing Equations

In this section, we develop a constitutive framework for brittle and quasi-brittle phase-field model of fracture. A coupled problem of fracture under the mechanical loading is formulated in terms of the two primary field variables, the total strain tensor $\boldsymbol{\varepsilon}(\boldsymbol{x},t)$ and the crack phase-field $d(\boldsymbol{x},t)$. Therefore, the state of a material point $\boldsymbol{x}$ for the coupled crack phase-field problem in a solid body is defined by

$$\text{State}(\boldsymbol{x},t) := \{\boldsymbol{\varepsilon}(\boldsymbol{x},t), d(\boldsymbol{x},t)\}. \tag{2.43}$$

The displacement field $\boldsymbol{u}(\boldsymbol{x},t)$ of the material point $\boldsymbol{x} \in \mathcal{B}$ at time $t \in \mathcal{T}$ is determined as

$$\boldsymbol{u} : \begin{cases} \mathcal{B} \times \mathcal{T} \to \mathbb{R}^\delta \\ (\boldsymbol{x},t) \mapsto \boldsymbol{u}(\boldsymbol{x},t) \end{cases} \tag{2.44}$$

As a consequence, the small strain tensor is defined as the symmetric displacement gradient

$$\boldsymbol{\varepsilon}(\boldsymbol{u}) := \nabla_s \boldsymbol{u} = \frac{1}{2} \left[\nabla_x^T \boldsymbol{u} + \nabla_x \boldsymbol{u} \right]. \tag{2.45}$$

The general formulation of this coupled problem begins through the introduction of the total energy functional of a degraded body in terms of the displacement field $\boldsymbol{u}$

and the crack phase-field d. The energy storage functional of an isotropic solid and defined by

$$\mathcal{E}(\boldsymbol{u}, d) = \int_{\mathcal{B}} \hat{\Psi}(\boldsymbol{\varepsilon}(\boldsymbol{u}), d) \, dV, \tag{2.46a}$$

$$\text{with} \quad \hat{\Psi}(\boldsymbol{\varepsilon}(\boldsymbol{u}), d) = [g(d) + \kappa] \, \hat{\Psi}_0^+(\boldsymbol{\varepsilon}) + \hat{\Psi}_0^-(\boldsymbol{\varepsilon}) \tag{2.46b}$$

$$\text{and} \quad \hat{\Psi}_0(\boldsymbol{\varepsilon}) := \hat{\Psi}_0^+(\boldsymbol{\varepsilon}) + \hat{\Psi}_0^-(\boldsymbol{\varepsilon}) = \frac{\lambda}{2} \operatorname{tr}[\boldsymbol{\varepsilon}]^2 + \mu \operatorname{tr}[\boldsymbol{\varepsilon}^2]. \tag{2.46c}$$

In (2.46c) the energy storage function Ψ is written in an additively decomposed form as a function of elastic constants, Lamé constant λ and shear modulus μ where Ψ^+ and Ψ^- are the positive and negative parts of the energy storage function associated with the tensile and compressive deformations, respectively. The positive and negative parts of the energy storage function are respectively defined as

$$\hat{\Psi}_0^+(\boldsymbol{\varepsilon}) = \frac{\lambda}{2} \langle \operatorname{tr}[\boldsymbol{\varepsilon}] \rangle_+^2 + \mu \operatorname{tr}[\boldsymbol{\varepsilon}_+^2] \quad \text{and} \quad \hat{\Psi}_0^-(\boldsymbol{\varepsilon}) = \frac{\lambda}{2} \langle \operatorname{tr}[\boldsymbol{\varepsilon}] \rangle_-^2 + \mu \operatorname{tr}[\boldsymbol{\varepsilon}_-^2] \tag{2.47}$$

In (2.47), the negative and positive parts of the strain tensor representing the tensile and compressive modes, respectively. They are determined by using the spectral decomposition of the strain tensor $\boldsymbol{\varepsilon} = \sum_{i=1}^3 \varepsilon_i \boldsymbol{n}_i \otimes \boldsymbol{n}_i$, where $\{\varepsilon_i\}_{i=1,2,3}$ are the principal strains and $\{\boldsymbol{n}_i\}_{i=1,2,3}$ are the principal strain directions. Therefore, $\boldsymbol{\varepsilon}_+$ and $\boldsymbol{\varepsilon}_-$ are defined as

$$\boldsymbol{\varepsilon}_+ = \sum_{i=1}^3 \langle \varepsilon_i \rangle_+ \boldsymbol{n}_i \otimes \boldsymbol{n}_i \quad \text{and} \quad \boldsymbol{\varepsilon}_- = \sum_{i=1}^3 \langle \varepsilon_i \rangle_- \boldsymbol{n}_i \otimes \boldsymbol{n}_i. \tag{2.48}$$

Note that the bracket operators $\langle x \rangle_+ := (x + |x|)/2$ and $\langle x \rangle_- := (x - |x|)/2$ are used in (2.47) and (2.48).

The macro- and micro-balance equations are derived from the standard argument of virtual work.

$$\dot{\mathcal{E}}(\dot{\boldsymbol{u}}, \dot{d}) + \mathcal{D}(\dot{d}, d) - \mathcal{P}(\dot{\boldsymbol{u}}) = 0 \tag{2.49}$$

where $\dot{\mathcal{E}}(\dot{\boldsymbol{u}})$, the rate of energy storage functional, is defined as follows

$$\dot{\mathcal{E}}(\dot{\boldsymbol{u}}, \dot{d}) = \int_{\mathcal{B}} [\partial_d \Psi \dot{d} + \partial_{\boldsymbol{\varepsilon}} \Psi : \dot{\boldsymbol{\varepsilon}}] \, dV, \tag{2.50}$$

$\mathcal{P}(\dot{\boldsymbol{u}})$ represents the external power functional as

$$\mathcal{P}(\dot{\boldsymbol{u}}) = \int_{\mathcal{B}} \bar{\boldsymbol{b}}(\boldsymbol{x}, t) \cdot \dot{\boldsymbol{u}} \, dV + \int_{\partial \mathcal{B}_t} \bar{\boldsymbol{t}}(\boldsymbol{x}, t) \cdot \dot{\boldsymbol{u}} \, dA \tag{2.51}$$

where $\bar{b}$ denotes the prescribed volume-specific body force in $\mathcal{B}$ and $\bar{t}$ indicates the surface traction on $\partial \mathcal{B}_t$. In (2.49), $\mathcal{D}(\dot{d}, d)$ indicates the dissipation functional.

Dissipation Function for Crack Phase-Field Evolution. Cracking is an irreversible and an inherently fully dissipative process. This fact allows us to derive the time-dependent evolution of cracking by the means of the regularized crack surface [26]. Thus, the temporal growth of regularized crack surface evolution reads

$$\dot{\Gamma}_\ell(d) = \int_{\mathcal{B}} \dot{\gamma}(d; \nabla_x d) \, dV = \int_{\mathcal{L}} (\delta_d \gamma) \dot{d} \, dV \geq 0 \tag{2.52}$$

where the variational derivative of the crack surface density function is defined as

$$\delta_d \gamma := \partial_d \gamma - \mathrm{div}[\partial_{\nabla_x d} \gamma] = \frac{1}{c_0} \left[\frac{1}{\ell} \alpha'(d) - 2\ell \Delta d \right]. \tag{2.53}$$

A diffuse fracture topology is created by the work for a given regularized crack surface functional $\Gamma_\ell(d)$

$$\hat{W}_c(d) = \int_{\mathcal{L}} G_c \gamma(d; \nabla_x d) \, dV, \tag{2.54}$$

where G_c is the critical energy release rate. The crack dissipation is determined by the rate of work functional

$$\mathcal{D} := \dot{W}(d; \dot{d}) = \int_{\mathcal{L}} \Phi(d, \nabla_x d, \dot{d}, \nabla_x \dot{d}) \, dV \tag{2.55}$$

where $\Phi(d, \nabla_x d, \dot{d}, \nabla_x \dot{d})$ denotes the constitutive dissipation function per unit volume

$$\Phi(d, \nabla_x d, \dot{d}, \nabla_x \dot{d}) := G_c \dot{\gamma}(d; \nabla_x d) = G_c (\delta_d \gamma) \dot{d}. \tag{2.56}$$

According to the second law of thermodynamics, the crack dissipation is required to be positive $\mathcal{D} \geq 0$. The global irreversibility constraint of crack evolution is locally conformed by a positive variational derivative of the crack surface function $\delta_d \gamma \geq 0$ and a positive evolution of the crack phase-field $\dot{d} \geq 0$. These local constraints for the rate-independent evolution of crack phase-field can be fulfilled by introducing the local threshold function [26]

$$f(\beta_d; d) = \beta_d - G_c \delta_d \gamma(d) \leq 0 \tag{2.57}$$

in terms of the variable β_d, representing the driving force field dual to the crack phase-field d. This expression designates a range without crack accumulation for $f < 0$.

Therefore, the dissipation function can be defined by the constrained optimization problem

$$\Phi(d, \nabla_x d; \dot{d}, \nabla_x \dot{d}) = \sup_{\beta_d, \lambda_L \geq 0} \left[\beta_d \dot{d} - \lambda_L \left(\beta - G_c \delta_d \gamma(d) \right) \right] \tag{2.58}$$

where λ_L is a Lagrange multiplier field. This field is set to $\lambda_L = \dot{d}$ by considering the necessary conditions of the constrained optimization problem in (2.58). Hence, the local evolution of the phase-field $\dot{d}$ is determined in terms of the local driving force β_d and the phase-field itself through the following conditions, also known as the Karush-Kuhn-Tucker optimality conditions

$$\dot{d} \geq 0, \quad \beta_d \leq G_c \delta_d \gamma(d), \quad \dot{d}(\beta_d - G_c \delta_d \gamma(d)) = 0. \tag{2.59}$$

The numerical treatment of the phase-field model is stabilized by a viscous regularization of the rate-independent formulation. To this end, the constitutive dissipation function is rewritten in terms of the viscous regularization setting [26]

$$\Phi(d, \nabla_x d; \dot{d}, \nabla_x \dot{d}) = \sup_{\beta, \lambda_L \geq 0} \left[\beta_d \dot{d} - \frac{1}{2\eta_d} \langle \beta_d - G_c \delta_d \gamma(d) \rangle_+ \right] \tag{2.60}$$

The necessary conditions of this optimization problem ensure

$$\partial_{\beta_d} \left(\beta_d \dot{d} - \frac{1}{2\eta_d} \langle \beta_d - G_c \delta_d \gamma(d) \rangle_+ \right) = 0 \quad \text{then} \quad \dot{d} = \frac{1}{\eta_d} \langle \beta_d - G_c \delta_d \gamma(d) \rangle_+ \tag{2.61}$$

where $\eta_d \geq 0$ is a viscosity parameter determines the rate-dependency of the model. In fact, it stabilizes the numerical treatment especially at the post-cracking steps where the brutal crack propagation is observed. For the rate-independent formulation with $\eta_d \rightarrow 0$, a steeper descent is observed in the structural response for brittle fracture. However, by applying a viscous regularization with $\eta_d > 0$, this wicked behavior of the material is smoothed out [68].

Insertion of the functionals and application of Gauss theorem, (2.49) is explicitly represented as

$$\int_{\mathcal{B}} -[-\text{div}[\partial_{\varepsilon}\Psi] + \bar{\boldsymbol{b}}] \cdot \dot{\boldsymbol{u}} + [\partial_d \Psi + \partial_{\dot{d}}\Phi - \text{div}[\partial_{\nabla_x \dot{d}}\dot{\Phi}]] \dot{d} \, dV$$
$$+ \int_{\partial \mathcal{B}_t} [\partial_{\varepsilon}\Psi \cdot \boldsymbol{n} - \bar{\boldsymbol{t}}] \cdot \boldsymbol{u} \, dA + \int_{\partial \mathcal{L}} [\partial_{\nabla_x \dot{d}}\Phi \cdot \boldsymbol{n}] \dot{d} \, dA = 0 \tag{2.62}$$

Then, the two coupled balance equations are obtained for the phase-field model of fracture as

$$\text{div}[\partial_\varepsilon \Psi] + \bar{b} = 0,$$

$$\text{div}[\partial_{\nabla_x d} \Phi] - [\partial_d \Psi + \partial_{\dot{d}} \Phi] = 0 \qquad (2.63)$$

considering the Neumann-type boundary conditions

$$\boldsymbol{\sigma} \boldsymbol{n} = \bar{t} \quad \text{on} \quad \partial \mathcal{B}_t \quad \text{and} \quad \partial_{\nabla_x d} \cdot \boldsymbol{n} = 0 \quad \text{on} \quad \partial \mathcal{L} \qquad (2.64)$$

The asymmetric tension-compression split degrading energy storage function $\hat{\Psi}(\boldsymbol{\varepsilon}, d)$ in (2.46) acts as the potential to derive the constitutive equations for the stress tensor $\boldsymbol{\sigma}$ and the crack energetic driving force β_d. These aforementioned constitutive equations are given by

$$\hat{\boldsymbol{\sigma}}(\boldsymbol{\varepsilon}, d) := \frac{\partial \hat{\Psi}(\boldsymbol{\varepsilon}, d)}{\partial \boldsymbol{\varepsilon}} = [g(d) + \kappa_d] \, \hat{\boldsymbol{\sigma}}_0^+(\boldsymbol{\varepsilon}) - \hat{\boldsymbol{\sigma}}_0^-(\boldsymbol{\varepsilon}) \qquad (2.65a)$$

$$\hat{\beta}_d(\boldsymbol{\varepsilon}, d) := -\frac{\partial \hat{\Psi}(\boldsymbol{\varepsilon}, d)}{\partial d} = -g'(d) \hat{\Psi}_0^+(\boldsymbol{\varepsilon}) \qquad (2.65b)$$

In (2.65), $\boldsymbol{\sigma}_0^+$ and $\boldsymbol{\sigma}_0^-$ express respectively the positive and negative parts of the stress tensor of a fictitious intact solid body. These compressive and tensile stresses are determined in terms of the principal strains and their directions as follows

$$\boldsymbol{\sigma}_0^\pm := \frac{\partial \Psi_0^\pm}{\partial \boldsymbol{\varepsilon}} = \sum_{i=1}^3 \left[\lambda \langle \varepsilon_1 + \varepsilon_2 + \varepsilon_3 \rangle_\pm + 2\mu \langle \varepsilon_i \rangle_\pm \right] \boldsymbol{n}_i \otimes \boldsymbol{n}_i \qquad (2.66)$$

where the Lamé constants λ and μ can be expressed in terms of the elastic modulus E and the Poisson's ratio ν

$$\lambda = \frac{E\nu}{(1+\nu)(1-2\nu)} \quad \text{and} \quad \mu = \frac{E}{2(1+\nu)} \qquad (2.67)$$

By using (2.49) and applying the Neumann-type boundary (2.64) conditions the specific form of the balance equations of the coupled problems are derived. These balance equations, namely the conservation of linear momentum and the non-local crack phase-field evolution equation are represented as

$$\text{div}\left[\hat{\boldsymbol{\sigma}}(\boldsymbol{\varepsilon}, d)\right] + \bar{b} = 0, \qquad (2.68a)$$

$$\left[\frac{G_c}{c_0 \ell} \left(\alpha'(d) - 2\ell^2 \Delta d \right) + \eta \dot{d} + g'(d) \mathcal{H} \right] = 0 \qquad (2.68b)$$

The evolution equation of the crack phase-field in (2.68b) is reformulated in terms of the local history field $\mathcal{H}$ in (2.68b) to enforce the damage evolution according to the thermodynamic principle of $\dot{d} > 0$. The positive part of the reference free energy function Ψ_0^+ in (2.68a) is used to compute the local history field $\mathcal{H}$. This field represents the maximum local history field of positive reference energy required to derive the crack phase-field d

$$\mathcal{H}_{n+1}(\boldsymbol{x}, t) := \max_{s \in [0,t]} \Psi_0^+(\boldsymbol{\varepsilon}_n(\boldsymbol{x}, s)). \tag{2.69}$$

The history field $\mathcal{H}$ is updated within the typical time step $[t_n, t_{n+1}]$ according to the operator split algorithm which uses a staggered scheme to update the crack phase-field and the displacement field [68]. Therefore, the current history field $\mathcal{H}_{n+1} := \mathcal{H}(\boldsymbol{x}, t_{n+1})$ is defined in terms of the displacement field $\boldsymbol{u}_n$ at time t_n. The initial condition for the history field is set as $\mathcal{H}_0 := \mathcal{H}(\boldsymbol{x}, t = t_0) = 0$ so the current value of maximum reference energy obtained in history is given by [68]

$$\mathcal{H} = \begin{cases} \mathcal{H}_{n+1} & \text{for } \mathcal{H}_{n+1} > \mathcal{H}_n, \\ \mathcal{H}_n & \text{otherwise.} \end{cases} \tag{2.70}$$

This expression indicates that the energy $\mathcal{H}$ drives the current crack phase-field d at time t_{n+1}. This energetic driving force is defined in the case of damage loading dependent on the displacement $\boldsymbol{u}_n$ at time t_n. On this account, the non-local equation of crack phase-field evolution, (2.68b) is rewritten as

$$\text{div}\, \hat{\boldsymbol{q}}_d(d; \nabla_x d) - \hat{\beta}_d(d; \dot{d}) + \hat{f}_d(\boldsymbol{\varepsilon}, d) = 0. \tag{2.71}$$

The functions related to the spatial and temporal evolution of crack phase-field $\hat{\beta}_d(d; \dot{d})$, $\hat{\boldsymbol{q}}_d(d; \nabla_x d)$ and $\hat{f}_d(\boldsymbol{\varepsilon}, d)$ are respectively defined as

$$\hat{f}_d(d; \dot{d}) = \frac{G_c}{c_0 \ell} \alpha'(d) + \eta_d \dot{d} \tag{2.72a}$$

$$\hat{\boldsymbol{q}}_d(d; \nabla_x d) = -\frac{2 G_c \ell}{c_0} \nabla_x d, \tag{2.72b}$$

$$\hat{\beta}_d(\boldsymbol{\varepsilon}, d) = -g'(d) \hat{\mathcal{H}}(\boldsymbol{\varepsilon}). \tag{2.72c}$$

In general, this non-local (gradient-enriched) equation is used to calculate the temporal and spatial variation of the crack phase-field. The aforementioned softening laws are simply used by adopting the regularized material parameters for different type of

41

fracture in a solid material. It should be noted that the phase-field damage model for the quasi-brittle fracture is implemented by imposing the damage boundedness $0 \leq d \leq 1$ and the irreversibility condition $\dot{d} \geq 0$. We deal with this matter by applying a general scheme referred to as the constrained optimization problem that is associated with variational inequalities with box constraints and solved by the Scalable Nonlinear Equations Solver (SNES) [93]. The SNES library of PETSc provides a powerful suite of data-structure-neutral routines for solving the large-scale nonlinear and general constrained problems.

2.4   Finite Element Formulation

In this section, we apply the conventional Galerkin method to derive the weak form of the conservation of linear momentum and the evolution equation of the crack phase-field in (2.68). To this end, the square integrable weight functions $\delta \boldsymbol{u} \in \mathscr{U}_0$ and $\delta d \in \mathscr{V}_0$, which satisfy the homogeneous Dirichlet-type boundary conditions ($\delta \boldsymbol{u} = \boldsymbol{0}$ on $\partial \mathcal{B}_{\boldsymbol{u}}$ and $\delta d = 0$ on $\partial \mathcal{L}_d$), are multiplied with the local residual differential equations, presented in (2.68). Then the weighted residual equations are integrated over the solid volume by explicitly applying the integration by parts to obtain the following weighted residual expressions for the balance of linear momentum

$$G^u(\delta \boldsymbol{u}, \boldsymbol{u}, d) = G^u_{\text{int}}(\delta \boldsymbol{u}, \boldsymbol{u}, d) - G^u_{\text{ext}}(\delta \boldsymbol{u}) = 0 \qquad (2.73)$$

and the succeeding expression for the evolution equation of the crack phase-field

$$G^d(\delta d, \boldsymbol{u}, d) = G^d_{\text{int}}(\delta d, \boldsymbol{u}, d) - G^d_{\text{ext}}(\delta d, \boldsymbol{u}, d) = 0. \qquad (2.74)$$

The specific forms of the internal G^u_{int} and external G^u_{ext} terms in (2.73) are separately defined as

$$G^u_{\text{int}}(\delta \boldsymbol{u}, \boldsymbol{u}, d) := \int_{\mathcal{B}} \hat{\boldsymbol{\sigma}} : \delta \boldsymbol{\varepsilon} \ dV \,,$$

$$G^u_{\text{ext}}(\delta \boldsymbol{u}) := \int_{\mathcal{B}} \bar{\boldsymbol{b}} \cdot \delta \boldsymbol{u} \ dV + \int_{\partial \mathcal{B}_t} \bar{\boldsymbol{t}} \cdot \delta \boldsymbol{u} \ dA \,. \qquad (2.75)$$

In the same fashion, the following expressions represent the specific forms of the internal G^d_{int} and external G^d_{ext} terms associated with the evolution of crack phase-field

problem

$$G_{\text{int}}^d(\delta d, \boldsymbol{u}, d) \quad := \quad \int_{\mathcal{B}} -\nabla_x(\delta d) \cdot \hat{\boldsymbol{q}} \ dV \,,$$

$$G_{\text{ext}}^d(\delta d, \boldsymbol{u}, d) \quad := \quad -\int_{\mathcal{L}} \delta d \, (\hat{\beta}_d + \hat{f}_d) \ dV \qquad (2.76)$$

where the functions related to the spatial and temporal evolution of crack phase-field $\hat{\beta}_d(d; \dot{d})$, $\hat{\boldsymbol{q}}_d(d; \nabla_x d)$ and $\hat{f}_d(\boldsymbol{\varepsilon}, d)$ already are given in (2.72c).

Owing to the nonlinear constitutive equations, the weighted residual equations (2.73) and (2.74) are nonlinear functions of the state variables. Thus monolithic or staggered treatment of the these equations requires the adoption of Newton-type iterative solution schemes within the framework of the implicit finite element method. Although we use the staggered scheme to solve the coupled problems, the constraint linearization is derived for the monolithic scheme. In the former, the off-diagonal terms of the global tangent vanish identically. As a consequence, the consistent linearization of the weighted residuals are conducted with respect the state variables at an intermediate iteration step at which the variables are assumed to take the respective values $\tilde{\boldsymbol{u}}$ and $\tilde{d}$

$$\text{Lin} \, G^u(\delta \boldsymbol{u}, \boldsymbol{u}, d)|_{\tilde{\boldsymbol{u}}, \tilde{d}} \quad := \quad G^u(\delta \boldsymbol{u}, \tilde{\boldsymbol{u}}, \tilde{d}) + \Delta G^u(\delta \boldsymbol{u}, \tilde{\boldsymbol{u}}, \tilde{d}; \Delta \boldsymbol{u}, \Delta d) = 0 \,,$$

$$\qquad (2.77)$$

$$\text{Lin} \, G^d(\delta d, \boldsymbol{u}, d)|_{\tilde{\boldsymbol{u}}, \tilde{d}} \quad := \quad G^d(\delta d, \tilde{\boldsymbol{u}}, \tilde{d}) + \Delta G^d(\delta d, \tilde{\boldsymbol{u}}, \tilde{d}; \Delta \boldsymbol{u}, \Delta d) = 0$$

where the incremental terms $\Delta G^{\boldsymbol{u}}$ and ΔG^d are obtained through the Gâteaux derivative and represented in the following forms

$$\Delta G^\gamma = \Delta G_{\text{int}}^\gamma - \Delta G_{\text{ext}}^\gamma \quad \text{with} \quad \gamma = u, d \,. \qquad (2.78)$$

Then, the incremental terms are defined with respect to the related equations. At first, the increment $\Delta G_{\text{int}}^{\boldsymbol{u}}$ is expressed in the specific form as

$$\Delta G_{\text{int}}^u = \int_{\mathcal{B}} \delta \boldsymbol{\varepsilon} : \Delta \hat{\boldsymbol{\sigma}} \ dV \qquad (2.79)$$

where the increment of the stress tensor $\Delta \hat{\boldsymbol{\sigma}}$ is given by

$$\Delta \hat{\boldsymbol{\sigma}} = \mathbb{C}^{uu} : \Delta \boldsymbol{\varepsilon} + \boldsymbol{C}^{ud} \Delta d \,. \qquad (2.80)$$

In this expression, $\mathbb{C}^{uu}$ is the fourth-order tangent moduli tensor defined as the derivative of the stress tensor with respect to the strain tensor and $\boldsymbol{C}^{ud}$ is the second-order

tensor, which is the derivative of the stress tensor with respect to the crack phase-field. The fourth order $\mathbb{C}^{uu}$ is defined through the following expression

$$\mathbb{C}^{uu} := \partial_{\varepsilon}\hat{\sigma} = g(d)\left[\lambda\frac{\langle\mathrm{tr}(\varepsilon)\rangle_+}{\mathrm{tr}(\varepsilon)}\mathbf{1}\otimes\mathbf{1} + 2\mu\mathbb{P}^+\right] + \left[\lambda\frac{\langle\mathrm{tr}(\varepsilon)\rangle_-}{\mathrm{tr}(\varepsilon)}\mathbf{1}\otimes\mathbf{1} + 2\mu\mathbb{P}^-\right]$$

(2.81)

where $\mathbb{P}^+ := \partial_{\varepsilon}[\varepsilon_+(\varepsilon)]$ and $\mathbb{P}^- := \partial_{\varepsilon}[\varepsilon_-(\varepsilon)]$ are introduced as the fourth-order tensors projecting the total strains onto their positive and negative parts, that is $\varepsilon_+ = \mathbb{P}^+ : \varepsilon$ and $\varepsilon_- = \mathbb{P}^- : \varepsilon$. These fourth-order tensors are given by [68]

$$\begin{aligned}
\mathbb{P}^+ &= \sum_{i=1}^{3}\sum_{j=1}^{3}\frac{\partial\langle\varepsilon_i\rangle_+}{\partial\varepsilon_i}\boldsymbol{n}_i\otimes\boldsymbol{n}_i\otimes\boldsymbol{n}_j\otimes\boldsymbol{n}_j \\
&+ \sum_{i=1}^{3}\sum_{i\neq j}^{3}\frac{1}{2}\frac{\langle\varepsilon_i\rangle_+ - \langle\varepsilon_j\rangle_+}{\varepsilon_i - \varepsilon_j}\boldsymbol{n}_i\otimes\boldsymbol{n}_j\otimes(\boldsymbol{n}_i\otimes\boldsymbol{n}_j + \boldsymbol{n}_j\otimes\boldsymbol{n}_i), \\
\mathbb{P}^- &= \mathbb{I} - \mathbb{P}^+.
\end{aligned}$$

(2.82)

Also the second order tensor $\boldsymbol{C}^{ud}$ is determined as

$$\boldsymbol{C}^{ud} := \partial_d\hat{\sigma} = g'(d)\left[\lambda\langle\mathrm{tr}(\varepsilon)\rangle_+\mathbf{1} + 2\mu\varepsilon_+\right]$$

(2.83)

The incremental term ΔG^d is determined through the following formulation

$$\begin{aligned}
\Delta G^d &:= \Delta_u G^d + \Delta_d G^d \\
&= \int_{\mathcal{B}}\left[\delta d\boldsymbol{C}^{du}\right] : \Delta\varepsilon\ dV + \int_{\mathcal{B}}\left[-\nabla_x(\delta d)\cdot\Delta\hat{\boldsymbol{q}}\right]\ dV \\
&+ \int_{\mathcal{B}}\left[\partial_d\hat{\beta}_d + \partial_d\hat{f}\right]\Delta d\ dV
\end{aligned}$$

(2.84)

where the increment of the crack phase-field flux $\Delta\hat{\boldsymbol{q}}_d$

$$\Delta\hat{\boldsymbol{q}} = -\hat{\boldsymbol{D}}\nabla_x(\Delta d) \quad\text{with}\quad \hat{\boldsymbol{D}} := -\partial_{\nabla_x d}\hat{\boldsymbol{q}} = \frac{2G_c l}{c_0}\mathbf{1},$$

(2.85)

and the second order tensor is $\boldsymbol{C}^{du} = \dfrac{\partial\hat{\beta}_d}{\partial\varepsilon}$

Now, the isoparametric Galerkin Finite Element approach is applied to numerically evaluate the weak form of the governing equations. To this end, we use the spatial dicretization of the coupled problem within the solid domain $\mathcal{B}$ by dividing it into finite elements of domain $\mathcal{B}_e^h$, i.e. $\mathcal{B} \approx \mathcal{B}^h = \bigcup_{e=1}^{n_{el}}\mathcal{B}_e^h$ where n_{el} denotes the total

44

number of elements within the domain $\mathcal{B}$. The displacement field $\boldsymbol{u}(\boldsymbol{x}, t)$, the crack phase-field $d(\boldsymbol{x}, t)$, and their associated weight functions, $\delta \boldsymbol{u}$ and δd, are expressed by using the shape functions within an element domain $\mathcal{B}_e^h$

$$
\begin{aligned}
\delta \boldsymbol{u}_e^h &= \sum_{i=1}^{n_{en}} N^i \delta \boldsymbol{U}_i^e, \quad \delta d_e^h = \sum_{k=1}^{n_{en}} N^k \delta D_k^e, \\
\boldsymbol{u}_e^h &= \sum_{j=1}^{n_{en}} N^j \boldsymbol{U}_j^e, \quad d_e^h = \sum_{l=1}^{n_{en}} N^l D_l^e.
\end{aligned}
\tag{2.86}
$$

In this expression, n_{en} demonstrates the number of nodes per element within the domain $\mathcal{B}_e^h$. $\boldsymbol{U}_i^e$ and $\delta \boldsymbol{U}_i^e$ are the vectors of the nodal displacements and displacement weight functions. Also, D_l^e and δD_k^e indicate the nodal crack phase-field variables and its weight functions. Moreover, N^i presents the shape function associated with node i. In the following, the gradient of the weight functions of the displacement field and crack phase-field with element e are defined as

$$
\begin{aligned}
\nabla_x(\delta \boldsymbol{u}_e^h) &= \sum_{i=1}^{n_{en}} \delta \boldsymbol{U}_i^e \otimes \nabla_x N^i, \\
\nabla_x(\delta d_e^h) &= \sum_{k=1}^{n_{en}} \delta D_k^e \otimes \nabla_x N^k.
\end{aligned}
\tag{2.87}
$$

Likewise, the spatial gradient of the incremental fields with element e are specified as

$$
\begin{aligned}
\nabla_x(\Delta \boldsymbol{u}_e^h) &= \sum_{j=1}^{n_{en}} \Delta \boldsymbol{U}_j^e \otimes \nabla_x N^j, \\
\nabla_x(\Delta d_e^h) &= \sum_{l=1}^{n_{en}} \Delta D_l^e \otimes \nabla_x N^l.
\end{aligned}
\tag{2.88}
$$

The discrete residual vectors are obtained by incorporating the dicretized representation (2.86) and (2.87) in (2.73) and (2.74) along with (2.75) and (2.76)

$$
\begin{aligned}
\boldsymbol{R}_I^u &= \underset{e=1}{\overset{n_{el}}{\mathbf{A}}} \left\{ \int_{\mathcal{B}_e^h} \nabla_x N^i \cdot \hat{\boldsymbol{\sigma}} \ dV - \int_{\mathcal{B}_e^h} N^i \boldsymbol{b} \ dV - \int_{\partial \mathcal{B}_t^e} N^i \bar{\boldsymbol{t}} \ dA \right\} = \boldsymbol{0}, \\
R_K^d &= \underset{e=1}{\overset{n_{el}}{\mathbf{A}}} \left\{ -\int_{\mathcal{B}_e^h} \nabla_x N^k \cdot \hat{\boldsymbol{q}} \ dV + \int_{\mathcal{B}_e^h} N^k (\hat{H} + \hat{f}) \ dV \right\} = 0
\end{aligned}
\tag{2.89}
$$

where the assembly operator $\mathbf{A}$ operates the standard assembly of element contributions at the local element nodes $i, k = 1, 2, \ldots, n_{en}$ to the global residuals at the

45

global nodes $I, K = 1, 2, \ldots, \mathrm{n_{nd}}$. Likewise, the tangent matrix of the coupled problem is obtained by inserting (2.86), (2.87) and (2.88) into (2.79) and (2.84) through the following expressions

$$
\begin{aligned}
\boldsymbol{K}_{IJ}^{uu} &= \mathop{\textsf{A}}_{e=1}^{\mathrm{n_{el}}} \left\{ \int_{\mathcal{B}_e^h} \nabla_x N^i \cdot \hat{\mathbb{C}}^{uu} \cdot \nabla_x N^j \ dV \right\}, \\
\boldsymbol{K}_{IL}^{ud} &= \mathop{\textsf{A}}_{e=1}^{\mathrm{n_{el}}} \left\{ \int_{\mathcal{B}_e^h} (\nabla_x N^i \cdot \hat{\boldsymbol{C}}^{ud}) N^k \ dV \right\}, \\
\boldsymbol{K}_{KI}^{du} &= \mathop{\textsf{A}}_{e=1}^{\mathrm{n_{el}}} \left\{ \int_{\mathcal{B}_e^h} (N^k \boldsymbol{C}^{du} \nabla_x N^i) \ dV \right\}, \\
K_{KL}^{dd} &= \mathop{\textsf{A}}_{e=1}^{\mathrm{n_{el}}} \left\{ \int_{\mathcal{B}_e^h} \nabla_x N^k \cdot \hat{\boldsymbol{D}} \nabla_x N^l \ dV + \int_{\mathcal{B}_e^h} N^k (\partial_d \hat{H} + \partial_d \hat{f}) N^l \ dV \right\}
\end{aligned}
\tag{2.90}
$$

In these expressions, $\textsf{A}$ denotes the assembly operator of the element contribution at the local element nodes $i, j, k, l = 1, \ldots, \mathrm{n_{en}}$ to the global tangent moduli at the global nodes $I, J, K, L = 1, \ldots, \mathrm{n_{nd}}$ of the mesh with $\mathrm{n_{nd}}$ nodes. As a consequence, the global form of the tangent matrix for the specific coupled problems is written as

$$
\mathcal{K} := \begin{bmatrix} \boldsymbol{K}^{uu} & \boldsymbol{K}^{ud} \\ \boldsymbol{K}^{du} & \boldsymbol{K}^{dd} \end{bmatrix}.
\tag{2.91}
$$

The solutions related to mechanical and crack phase-field DOFs are calculated at time $t = t_{n+1}$ for an intermediate iterative values $\bar{\mathcal{D}}$. To this end, the global residual vectors and the global coupled tangent matrices separately defined as $\bar{\mathcal{R}} := \mathcal{R}(\bar{\mathcal{D}})$ and $\bar{\mathcal{K}} := \mathcal{K}(\bar{\mathcal{D}})$ with the global unknown vector including the mechanical and crack phase-field DOFs as $\mathcal{D} := [\boldsymbol{U} \ \boldsymbol{D}]^T$ are used to calculate the iterative solutions of the mechanical and crack phase-field DOFs at the global nodes of a finite element mesh

$$
\mathcal{D} = \bar{\mathcal{D}} - \bar{\mathcal{K}}^{-1} \cdot \bar{\mathcal{R}}.
\tag{2.92}
$$

We us the Finite Elements Analysis Program (FEAP) [94] to implement our user material (UMAT) and user element (UEL) codes. The finite element meshes are constructed for the numerical examples using the ABAQUS/CAE software [95]. The common solvers that are used by the Finite Element Analysis Program (FEAP) is not capable of solving non-standard phase-field fracture model (PF-CZM), in which the boundedness condition of crack phase-field degree of freedom d is not guaranteed.

Therefore, it is required to solve a bound-constrained optimization problem regarding R_K^d in (2.89) as an optimization bounded by the following condition

$$0 \leq \bar{d}_{K,n} \leq \bar{d}_{K,n+1} \leq 1 \tag{2.93}$$

For this purpose, we have used the nonlinear solver (SNES) to deal with the afore-mentioned boundedness and irreversibility conditions as suggested in [80]

$$\begin{cases} \bar{d}_{K,n} < \bar{d}_{K,n+1} < 1 & R_K^d = 1 \\ \bar{d}_{K,n+1} = \bar{d}_{K,n} & R_K^d < 1 \\ \bar{d}_{K,n+1} = 1 & R_K^d > 1 \end{cases} \tag{2.94}$$

2.5 Representative Numerical Examples

In this section, the modeling capacity of the phase-field approach with respect to the brittle and quasi-brittle fracture is demonstrated by means of representative numerical examples. At first, the numerical solution of the variational problem of diffuse crack topology introduced in this chapter is presented to investigate the effect of the length scale parameter on the regularized crack functional $\Gamma_\ell(d)$ in (2.9) associated with the brittle [68] and quasi-brittle [27] fracture. We then apply the phase-field approach to a variety of the problems to simulate the brittle and quasi-brittle fracture in solids under the mechanical loading. These examples are selected from the bench-mark problems widely employed in the literature. In the case of the brittle fracture, crack propagation is simulated in the single notched square plate under pure tension and pure shear, and in the three-point bending test [68]. The quasi-brittle fracture is investigated by modeling a Mode-I failure of bending concrete beam [27], mixed mode failure of L-shaped panel [27], and the crack evolution in the Brazilian split tension test of concrete. The material parameters and the geometric crack function used in the representative numerical examples are given in Table 2.2. In addition to the mechanical parameters, the value of the length scale parameter value will be given in the units of mm, for each numerical example.

Table 2.2: Material properties, degradation, and geometric crack functions used in the representative numerical examples

Parameter/Function	Description	Unit	EX1-EX4	EX5	EX6	EX7	EX8
E	Elastic modulus	[GPa]	210	0.1	20	25.85	20
ν	Poisson's ratio	[–]	0.375	0	0.2	0.18	0.2
f_t	Tensile strength	[MPa]	–	1	2.4	2.7	2.7
G_c	Critical fracture energy release rate	[kJ/m^2]	2.7	0.1	0.113	0.09	0.113
$g(d)$	Degradation function	[–]	$(1-d)^2$	$\dfrac{1}{1+\phi(d)}$	$\dfrac{1}{1+\phi(d)}$	$\dfrac{1}{1+\phi(d)}$	$\dfrac{1}{1+\phi(d)}$
$\alpha(d)$	Geometric crack function	[–]	d^2	$2d-d^2$	$2d-d^2$	$2d-d^2$	$2d-d^2$

2.5.1 A Square Plate with a Notch

In this example, the Γ_ℓ-convergence to sharp crack topology, i.e. $\Gamma_\ell \to \Gamma$ referring to Figure 2.3 is represented by a notched unit-square plate with the edge length of 1 mm. This plate has a pre-cracked path with a length of 0.5 mm at the mid of the plate, along which the Dirichlet boundary condition $d = 1$ is prescribed [26]. The geometry and dimensions of the square plate are illustrated in Figure 2.11a. The related finite element simulations are carried out for different length scales based on a very fine mesh with constant mesh size $h \approx 0.00082$, consisting of $1,488,400$ four-node quadrilaterals. In Figure 2.8, the results of the finite element simulations of the regularization of a crack topology of the brittle failure with the geometric crack function $\alpha(d) = d^2$ are depicted. Accordingly, the large length scale $\ell = 0.2$ yields the approximated regularized in (2.9) $\Gamma_\ell = 0.55013$ and the smaller value of the length scale parameter $\ell = 0.007$ yields $\Gamma_\ell = 0.50400 \approx \Gamma = 0.5$.

In Figure 2.9 the results of regularization of a crack topology for the geometric crack function $\alpha(d) = 2d - d^2$, obtained through the finite element simulations are demonstrated [27]. In comparison with the brittle failure, the regularized crack functional Γ_ℓ of the quasi-brittle failure has smaller values. For the largest and the smallest values of the length scale selected here, we obtain $\Gamma_\ell = 0.58734$ and $\Gamma_\ell = 0.50350 \approx \Gamma = 0.5$, respectively. The results represent that the Γ-convergence of the regularized crack surface functional $\Gamma_\ell(d)$ can reach its sharp crack counterpart by resolving the in-
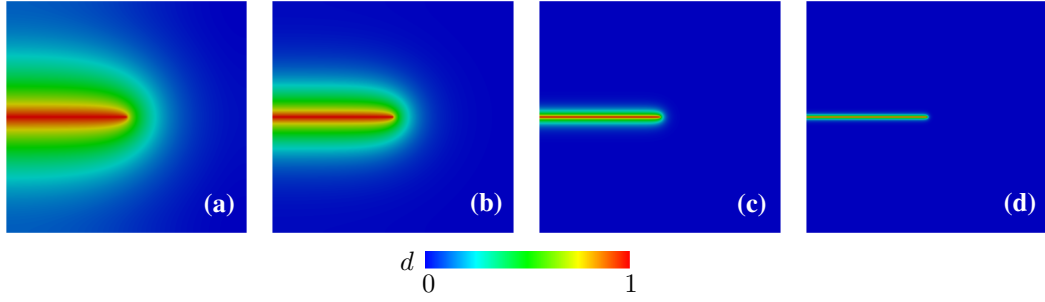
Figure 2.8: Regularized crack surface Γ_ℓ characterized by the crack phase-field d for different values of the length scale ℓ with $\alpha(d) = d^2$: **(a)** $\ell = 0.2$ with $\Gamma_\ell = 0.59388$, **(b)** $\ell = 0.1$ with $\Gamma_\ell = 0.55013$, **(c)** $\ell = 0.02$ with $\Gamma_\ell = 0.51020$, **(d)** $\ell = 0.007$ with $\Gamma_\ell = 0.50400$.

corporated length scale with sufficiently fine mesh. The evaluated crack phase-field localized within a narrow band whose width is scaled by the internal length scale.
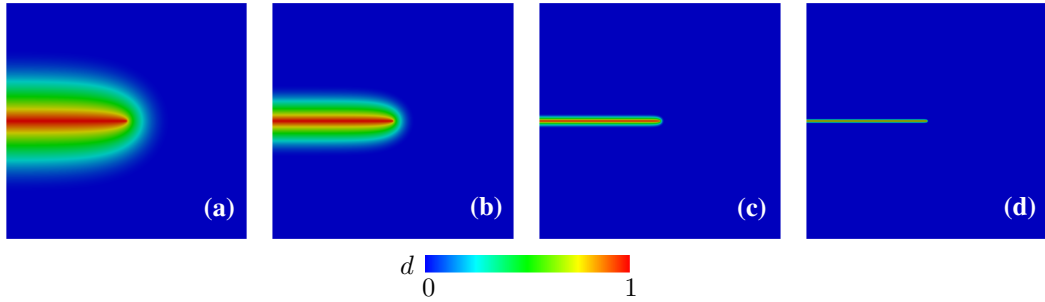
Figure 2.9: Regularized crack surface Γ_ℓ characterized by the crack phase-field d for different values of the length scale with $\alpha(d) = 2d - d^2$ ℓ: **(a)** $\ell = 0.2$ with $\Gamma_\ell = 0.58734$, **(b)** $\ell = 0.1$ with $\Gamma_\ell = 0.54355$, **(c)** $\ell = 0.02$ with $\Gamma_\ell = 0.50888$, **(d)** $\ell = 0.007$ with $\Gamma_\ell = 0.50350$.

2.5.2 Convergence Study on the Brittle Phase-Field Model (`EX1`)

Before representing the numerical examples related to the fracture under the mechanical loading, we conduct a convergence study on the mesh-dependency of the numerical results. For this purpose, a single edge notched tension test is considered. The geometry and dimensions of the plate are demonstrated in Figure 2.11. The domain

is discretized with a structured mesh consisting of four-node quadrilateral elements with different element sizes. The length scale parameter is chosen as a constant value of $\ell = 0.05$, and the element size in each analysis is set to $h \leq 0.5\ell$, in order to regularize the crack surface functional Γ_ℓ. The material parameters used in this study and the related geometric crack function for this type of brittle fracture are given in Table 2.2.
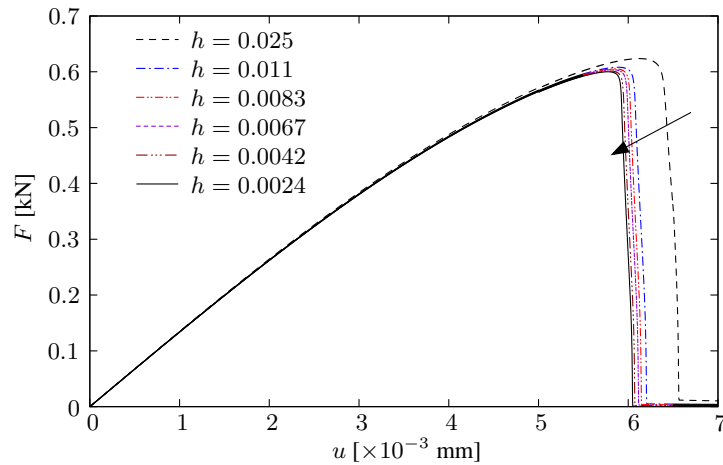
Figure 2.10: Load-displacement curve of the single edge notched tension test obtained by the convergence study.

The displacement-driven loading is computationally performed by monotonically increasing displacement on the surface of the top surface of the specimen with constant displacement increment of $\Delta u = 10^{-5}$ mm in the first 500 time steps and with $\Delta u = 10^{-6}$ mm in the remaining time steps because of the brutal character of the crack propagation.

The structural response in terms of the load-displacements curves are shown in Figure 2.10 for different element sizes. The results indicate that the structural response of a fracturing material modeled by the brittle phase-field model is mainly independent of the element size, as by decreasing the element size to sufficiently refine the plate domain, the structural response becomes independent of the element size.

2.5.3 Single Edge Notched Tension Test (`EX2`)

The brittle failure is investigated in a square plate with a notch horizontally placed at middle height from the left outer surface to the center of the specimen [68]. The geometry of the specimen, its boundary conditions, boundary conditions, and the finite element model are shown in Figure 2.11. The mesh is sufficiently refined in the center strip of the specimen where the crack is predicted to propagate. The domain of the specimen is discretized with $64,556$ four-node quadrilateral elements with the effective size of $h = 0.001$ mm. In order to regularize the crack surface Γ_ℓ, the maximum mesh size is chosen to be one half of the length scale, which is set to $\ell = 0.015$ mm. The mechanical properties of the material, the geometric crack function, and the displacement-driven loading condition are the same as the previous example in Subsection 2.5.3. The further simulations are performed to clarify the effect of the length scale parameter ℓ and the viscosity η_d.

Figure 2.11: Single edge notched compact tension test **(a)** Geometry, dimensions and boundary conditions (All dimensions in mm), **(b)** Finite element mesh with the effective element size $h = 0.001$ mm in the center strip of the specimen.

The patterns of the crack propagation at different displacement stages predicted by the brittle phase-field theory [68] for the rate-independent case are illustrated in Figure 2.12. The load-deflection curves for single edge notched tension test and the comparison with the results reported in [68] are depicted for $\ell = 0.015$ mm and $\ell = 0.075$ mm in Figure 2.13 and Figure 2.14, respectively. The results are represented for the

51
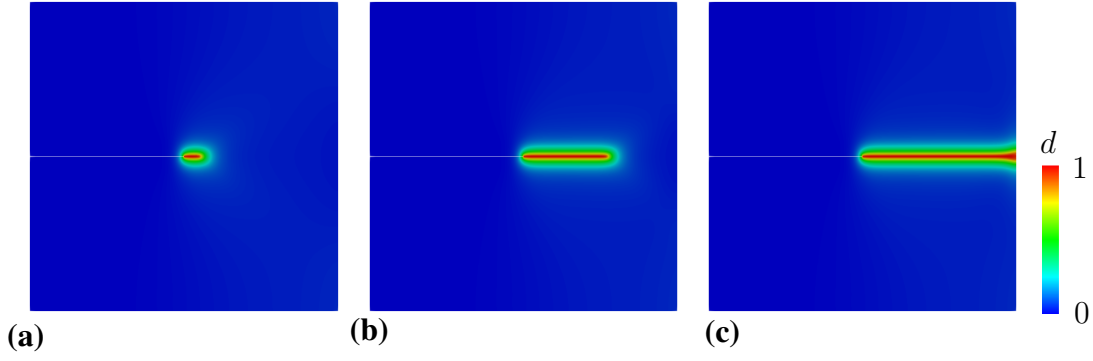
Figure 2.12: Single edge notched tension test. Crack propagation path for $\eta_d = 0$ kNs/mm^2 and $\ell = 0.015$ mm at a displacement of **(a)** $u = 5.71 \times 10^{-3}$ mm, **(b)** $u = 5.83 \times 10^{-3}$ mm, and **(c)** $u = 5.91 \times 10^{-3}$ mm.

different values of the length scale parameter and the viscosity.
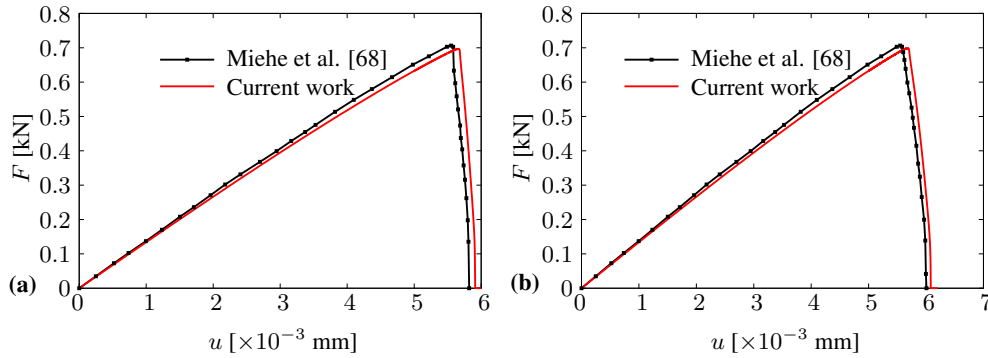
Figure 2.13: Load-deflection curve of the Single edge notched tension test for **(a)** $\ell = 0.015$ mm and $\eta_d = 0$ kNs/mm^2 and **(b)** $\ell = 0.015$ mm and $\eta_d = 1 \times 10^{-3}$ kNs/mm^2.

By comparing the structural response in terms of the load-displacement curve, see Figure 2.13a and Figure 2.14a, it is observed that for the rate-independent case with $\eta_d = 0$ kNs/mm^2 the load-displacement curves abruptly descends in the post-cracking regime. Whereas this brutal crack propagation is smoothened by the viscous model with $\eta_d = 1 \times 10^{-3}$ kNs/mm^2 as it is visualized in Figure 2.13a and Figure 2.14b.
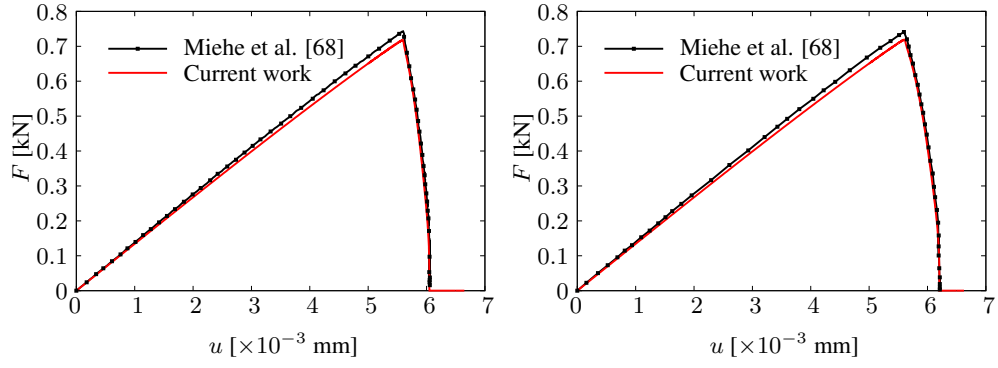
Figure 2.14: Load-deflection curve of the Single edge notched tension test for **(a)** $\ell = 0.0075$ mm and $\eta_d = 0$ Ns/mm^2 and **(b)** $\ell = 0.0075$ mm and $\eta_d = 1 \times 10^{-3}$ Ns/mm^2.

2.5.4 Single Edge Notched Shear Test (`EX3`)

In this example, as the previous one the same square plate with a horizontal notch is used for a shear test [68]. The geometric setup of the specimen, the dimensions, the boundary conditions, and the finite element model are illustrated in Figure 2.15. Also, the plate is prevented from the vertical deformation at its right and left edges. The crack pattern is captured satisfactorily by refining the mesh in the lower right diagonal strip of the specimen where the crack is expected to propagate. The domain of the specimen is discretized with $64,556$ four-node quadrilateral elements with the effective element size of $h = 0.002$ mm. The length scale parameter is set to $\ell = 0.0075$. For the material parameters and the geometric crack function adopted in this example, we refer to Table 2.2. The viscosity is set to $\eta = 0$ Ns/mm^2 for the rate-independent case. The displacement-driven loading is computationally performed by monotonically increasing the displacement on the top face with a constant displacement increment of $\Delta u = 1 \times 10^{-5}$ mm.

The patterns of crack propagation at different displacement stages are illustrated in Figure 2.16. Moreover, the load-displacement curves for the single edge notched shear test and the comparison with the result in [68] are depicted in Figure 2.17
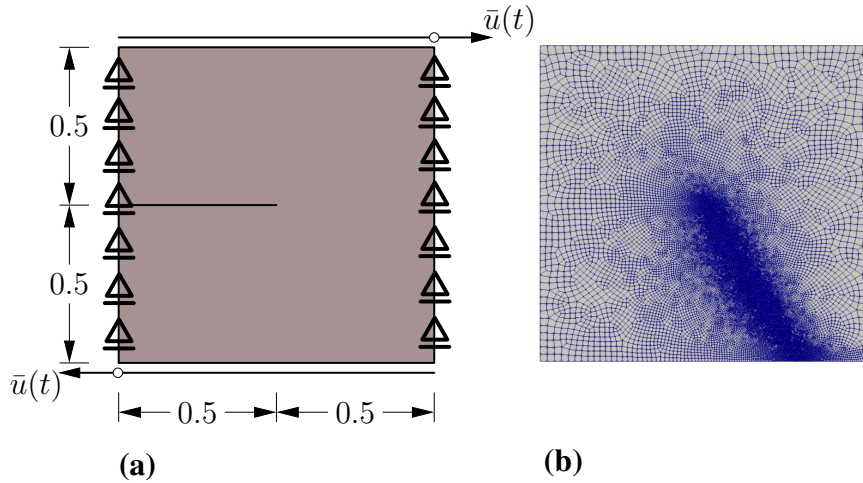
Figure 2.15: Single edge notched pure shear test **(a)** Geometry,dimensions and boundary conditions (All dimensions in mm), **(b)** Finite element meshes with the effective element size $h = 0.002$ mm in along the right diagonal strip.

(a)   **(b)**   **(c)**
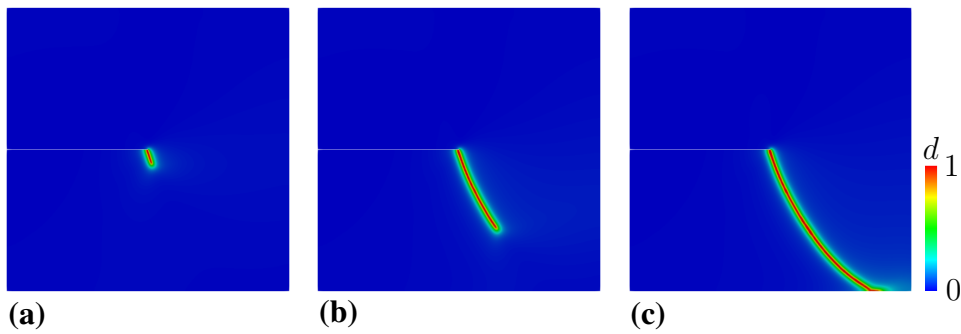
Figure 2.16: Single edge notched pure shear test. Crack propagation path for $\eta = 0$ kNs/mm^2 at a displacement of **(a)** $u = 6.02 \times 10^{-3}$ mm, **(b)** $u = 6.52 \times 10^{-3}$ mm, and **(c)** $u = 7.04 \times 10^{-3}$ mm.

2.5.5   Asymmetric Notched Three-Point Bending Test (`EX4`)

In this example, we apply the brittle phase-field model to simulate the growth of the curvelinear crack in an asymmetric notched three-point bending test. The numerical and experimental results associated with this problem are given in the work of Bittencourt *et al.* [96]. It is also simulated in the work of Miehe *et al.* [68] by implementing the phase-field model. The geometry of the beam, its boundary and loading conditions are depicted in Figure 2.18a. The beam domain is discretized by the linear
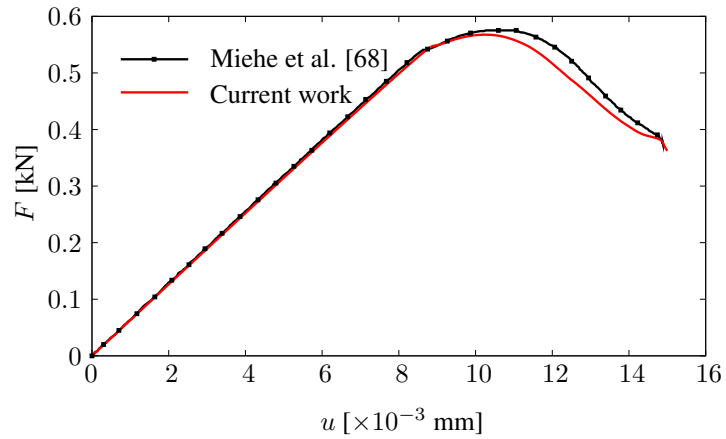
Figure 2.17: Load-deflection curve of the single edge notched shear test for $\ell = 0.0075$ mm and $\eta_d = 0$ kNs/mm^2

triangular elements with a refined zone around the expected crack path as shown in 2.18b. The effective elements size is $h = 0.01$ mm, which is set to $\ell = 0.1$ mm for the remaining domain which yields $66,556$ elements. The length scale parameter is set to $\ell = 0.02$ mm.
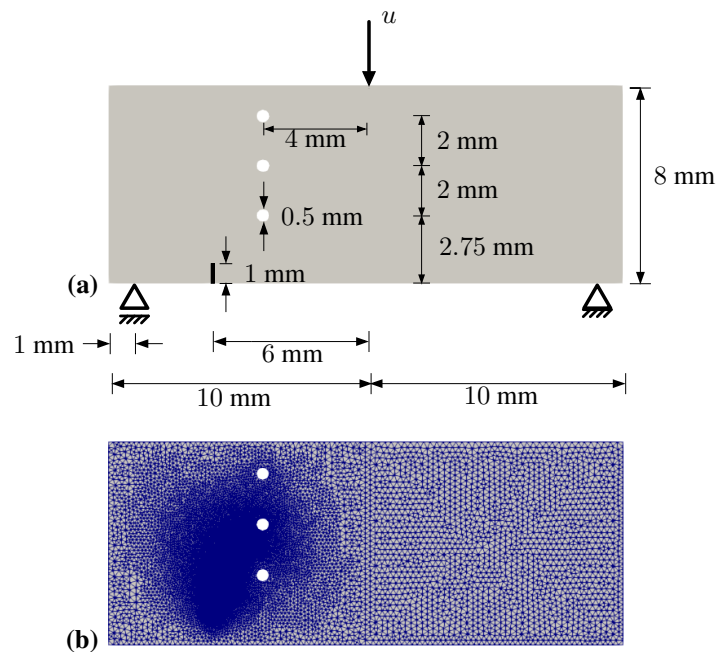
Figure 2.18: Asymmetric notched three-point bending beam. **(a)** geometry, dimensions, loading and boundary conditions, and **(a)** finite element mesh with the effective element size $h = 0.01$ mm in the damage critical zone.

The mechanical parameters are taken from [68]. These parameters and the geometric crack function for this type of brittle fracture are given in Table 2.2. The viscosity is set to $\eta_d = 0$ kNs/mm^2 for the rate-independent fracture model. The displacement-driven loading is computationally applied by increasing the displacement monotonically at the center of the top surface with a constant incremental value of $\Delta u = 10^{-5}$ mm.

In Figure 2.19, the visualization of the numerical result of the crack trajectory in the current work is compared with ones experimentally investigated in [96]. It represents that the phase-field model is capable of capturing such a curvelinear crack pattern, which cannot be easily simulated by the classical damage models.

(a)   (b)

Figure 2.19: Crack trajectory of the assymetric notched three point bending test obtained by **(a)** the current work, and **(b)** the experimental work by Bittencourt *et al.* [96]

2.5.6 Convergence Study on the Cohesive Zone Phase-Field Model (`EX5`)

In the first step, we conduct two convergence studies in this part, to investigate the mesh size and the length scale dependency of the cohesive zone phase-field model. For this purpose, a three point bending beam, reported in [97], is considered. The geometry of the beam, its dimensions, and the loading and boundary conditions of the three-point bending test are shown in Figure 2.20. The displacement-controlled loading is monotonically imposed at the midpoint of the top surface with a constant displacement increment of $\Delta u = 10^{-4}$ mm.

The solid domain is discretized with the linear triangular elements, refined along
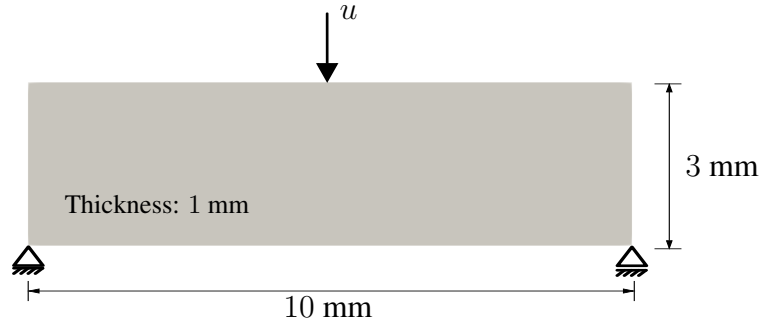
Figure 2.20: Geometry, dimensions, loading and boundary conditions of a symmetric three point bending test
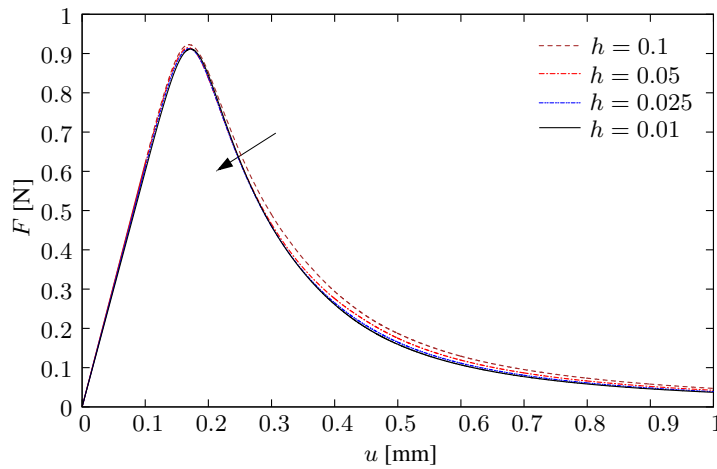
Figure 2.21: Load-displacement of the symmetric three-point bending test obtained by the convergence study.

the path where the crack is expected to propagate. However, the element size in remaining domain has the constant value of $h = 0.1$ mm as shown in Figure 2.22. The corresponding mechanical properties, taken from [97], and the geometric crack function adopted for this type of quasi-brittle fracture are presented in Table 2.2. We choose a constant value of $\ell = 0.25$ mm. The Griffith's characteristic length scale parameter is calculated as $\ell_{\mathrm{ch}} = 10$ mm. The corresponding material parameters of Cornelissen's softening low are $a_1 = 50.93$, $a_2 = 1.3868$ and $a_2 = 0.6567$.

We conduct the analyses with different element size along the critical path. The resulting load-displacement curves for different values of the element size are demonstrated in Figure 2.21. The results indicate that when the mesh is sufficiently resolved

within the critical zone with the critical mesh size, chosen smaller than the length scale parameter $h \leq (0.1 \sim 0.2)\ell$, the results become mesh-independent.
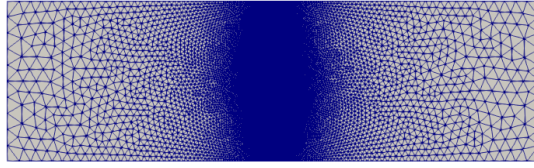
Figure 2.22: Finite element discretization of the three-point bending beam test with the effective element size $h = 0.01$ mm.
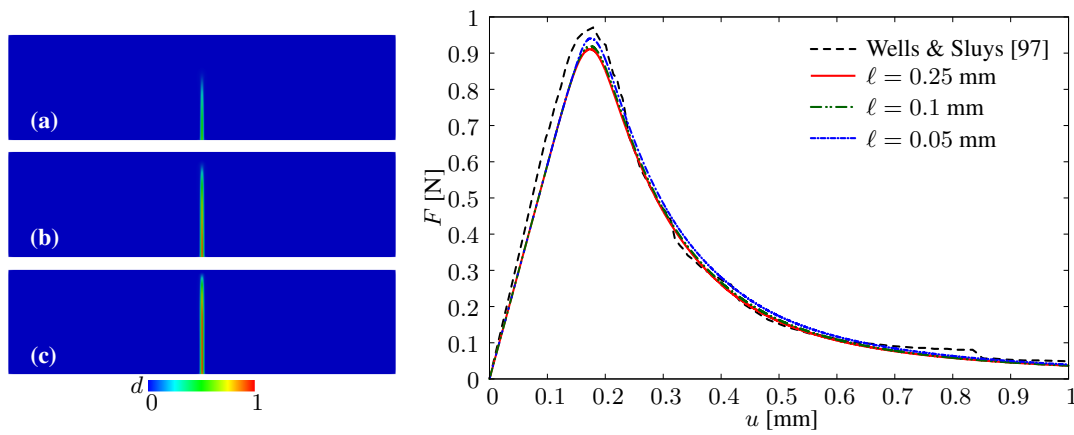
Figure 2.23: Three-point bending test. Crack pattern at **(a)** $u = 0.25$ mm, **(b)** $u = 0.5$ mm, **(c)** $u = 1$ mm, and **(d)** results obtained from the convergence study on the length scale dependency.

In the second step, we perform analyses to validate the length scale independency of the structural response. To this end, we repeat the three-point bending beam test as presented in the first step of the convergence study with the constant element size, but the length scale parameter is different for each analysis. The domain is discretized by $59, 132$ elements with the effective element size $h = 0.01$ mm around the centroid of the beam. The crack patterns at three different loading steps are demonstrated in Figure 2.23a for the length scale parameter $\ell = 0.05$. The load-displacements curves for different values of the length scale parameter along with one obtained in [97], are presented in Figure 2.23b. The load-deflections curves for distinct length scale parameter values are nearly equal to each other. The results indicate that the length scale parameter has a negligible effect on the structural response when it is sufficiently

small.

2.5.7 Mode-I Failure of a Three Point Bending Beam (`EX6`)

We validate the capability of the unified phase-field model in predicting the crack path in a concrete notched beam under the three-point bending test reported in [98]. The geometry of the test specimen, its dimensions, the loading and boundary conditions are demonstrated in Figure 2.24. The discretization is refined in the expected crack propagation zone (around the centroid of the beam), rendering a discretization with 54,498 elements with the effective element size of $h = 0.25$ mm being used in the critical zone, as demonstrated in Figure 2.24.
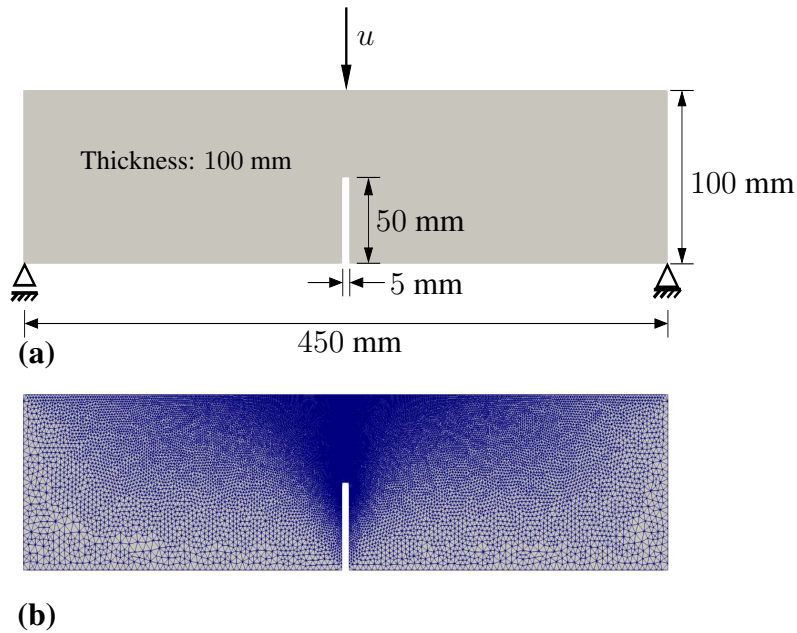
Figure 2.24: Three-point bending test. **(a)** Geometry, loading and boundary conditions of a notched concrete beam **(b)** Finite element discretization with the effective element size $h = 0.25$ mm.

The material parameters, taken from [98], and the corresponding geometric crack function for this type of quasi-brittle fracture are represented in Table 2.2. The internal length scale $\ell = 1.25$ mm as represented in [27]. As regards the material properties, the Griffith's characteristic length scale is determined $\ell_{ch} \approx 392.36$ mm.

The model parameters, used in formulation of the softening law according to Cornelissen's approach are chosen to be $a_1 = 399.65$, $a_2 = 1.3868$, and $a_3 = 0.6567$. The displacement-driven loading is imposed at the midpoint of the top surface of the beam. The loading is monotonically increased with a constant incremental value of $\Delta u = 10^{-4}$ mm.

In Figure 2.25, the numerical results are presented in terms of the crack path topology. Beside, the comparison between the experimentally and numerically obtained load-deflection curves are depicted in Figure 2.26.
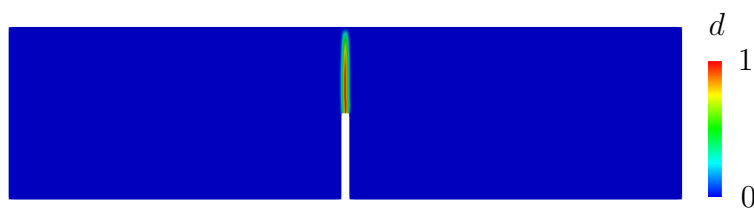
Figure 2.25: Prediction of crack pattern for three-point bending of a notched concrete beam.
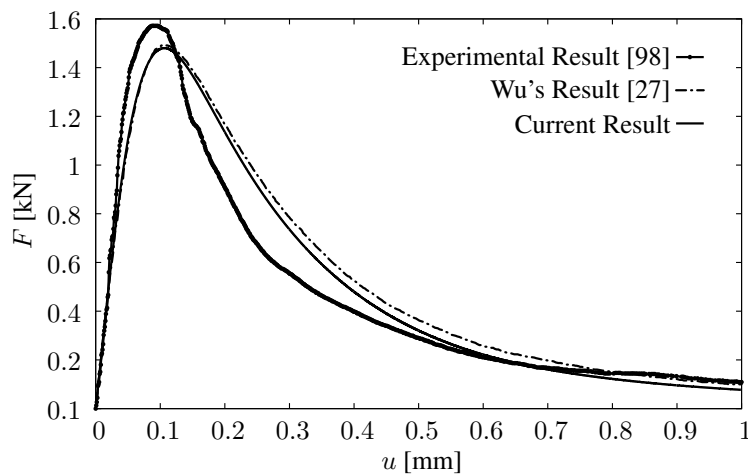
Figure 2.26: Load-deflection curves for three-point bending of a notched concrete beam.

2.5.8 Mixed-Mode Failure of a L-Shaped Panel (EX7)

As another example, the mixed mode failure test of a L-shaped panel is presented [99]. The geometry, the loading and boundary conditions of the related specimen are represented in Figure 2.27a. The discretization is refined in a region where the crack propagation is expected to be observed, yielding $53,579$ linear triangular elements with the effective mesh size as $h = 0.5$ mm. In Figure 2.27b, the finite element mesh is illustrated. The material constants, reported in [99], and the geometric crack function are shown in Table 2.2. The internal length scale is set to $\ell = 2.5$ mm. The Griffith's characteristic length scale is calculated $\ell_{\text{ch}} \approx 319.14$ mm. The corresponding material parameters of Cornelissen's softening low are $a_1 = 81.27$, $a_2 = 1.3868$ and $a_2 = 0.6567$. The displacement-driven loading is imposed at a point located 30 mm towards left form the right edge of the specimen. The loading is monotonically increased with a constant value of $\Delta u = 10^{-4}$ mm.
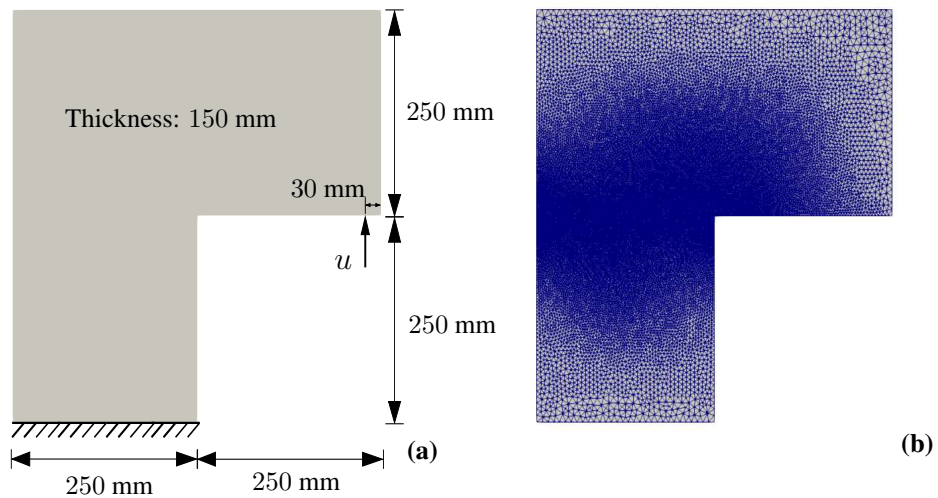
Figure 2.27: L-shaped panel. **(a)** Geometry, dimensions, loading and boundary conditions, **(b)** finite element discretization with the effective element size $h = 0.5$ mm.

Figure 2.28 represents the crack path topology, respectively obtained by the phase-field cohesive zone model and experiments. Furthermore, the load-deflection curves obtained numerically and experiment are compared in Figure 2.29.
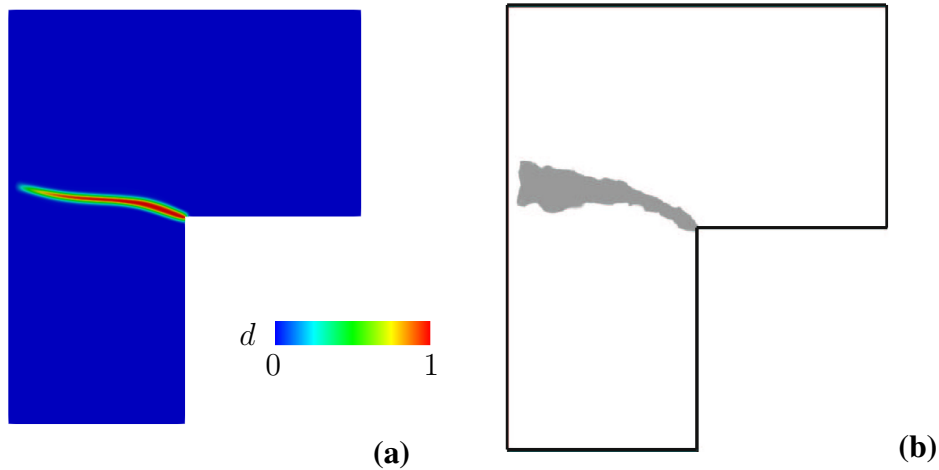
Figure 2.28: L-shaped panel. Crack patterns obtained by **(a)** the cohesive zone phase field model in the current work and **(b)** the experiment reported in [99].
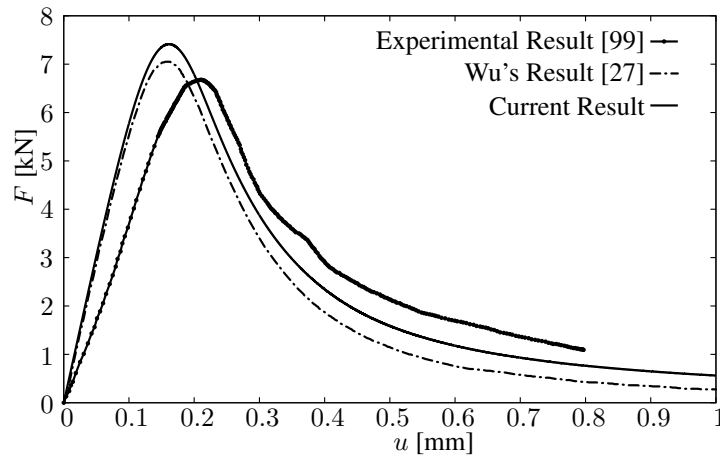
Figure 2.29: Load-deflection curves for the L-shaped panel.

2.5.9 Crack Evaluation in Brazilian Split Tensile Test of Concrete (`EX8`)

The tensile strength is one of the primary properties of concrete, so its definition is of great importance for engineers to determine the load at which the concrete members may crack. Due to the difficulties related to conducting the direct tension test, an indirect test method has been developed by means of a tensile splitting experiment (Brazilian test). These difficulties correspond to holding the test specimen properly in the testing machine without introducing stress concentration and application of a pure tensile load on the plain concrete specimen, which is free from eccentricity to

the specimen. The Brazilian test is conducted by subjecting a standard cylindrical concrete specimen to compressive loads applied along two diametrically opposite lines. Figure 2.30 illustrates the geometry, the boundary and loading conditions, and the finite element model. The domain is discretized by totally $28,321$ quadrilateral elements with the constant element size of $h = 0.8$ mm.

Figure 2.31 visualizes the crack propagation obtained by the phase-field cohesive zone model. Likewise Figure 2.32 demonstrates maximum principal stress along the diameter of the cylindrical specimen. It can be observed that the maximum principal stress yields in the concrete specimen are approximately equal to the tensile strength of the concrete.

Tensile stress occurs perpendicular to the direction of loading and almost uniformly distributed over the diameter of the cylindrical specimen, however, near the loading points local compressive stresses are generated and tensile stresses are not observed at all. Eventually, these tensile stresses cause the splitting of the cylinder by cracking along the diameter. The brittle crack propagation in Brazilian disk test conducted on rocks is investigated in [100] by adopting brittle phase-field model. Moreover, the failure mechanism of the sandstone under Brazilian test with different loading geometries is studied by means of the brittle phase-field model in [101].

The material parameters, and geometric crack function associated with the quasi-brittle fracture are given in Table 2.2. The internal length scale is chosen to be $\ell = 4$ mm. The Griffith's characteristic length scale is calculated $\ell_{\text{ch}} \approx 319.14$ mm regarding the material constants. The corresponding material parameters of Cornelissen's softening low are $a_1 = 101.59$ mm, $a_2 = 1.3868$ and $a_2 = 0.6567$. The displacement-driven loading is performed on a bearing strip whose width is about 50 mm, and placed at the top of the specimen. The loading is monotonically increased with a constant value of $\Delta u = 10^{-4}$ mm.

The tensile stress, perpendicular to the direction of loading is distributed over the diameter and induce the splitting of the cylindrical concrete specimen so cracking occurs parallel to the loading path. As it is known the direct and the split tensile strength of concrete are calculated as the function of the compressive strength as $f_{dt} = 0.35\sqrt{f_c}$ and $f_{st} = 0.5\sqrt{f_c}$, respectively [102]. Therefore, we can determine
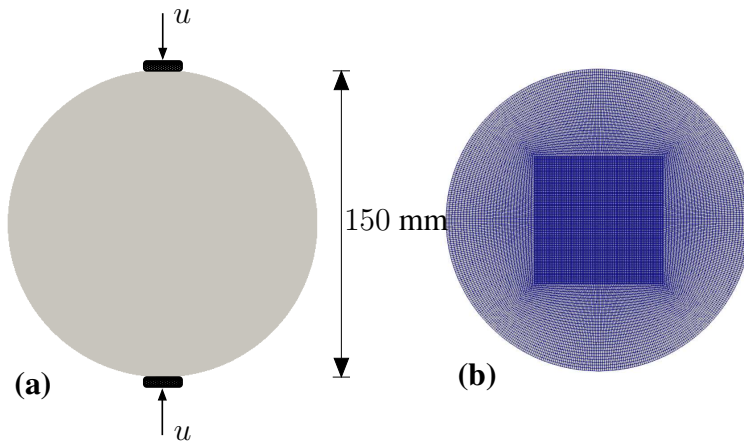
Figure 2.30: Brazilian test of concrete: **(a)** Geometry, loading and boundary conditions, and **(b)** finite element discretization with $h = 0.8$ mm.
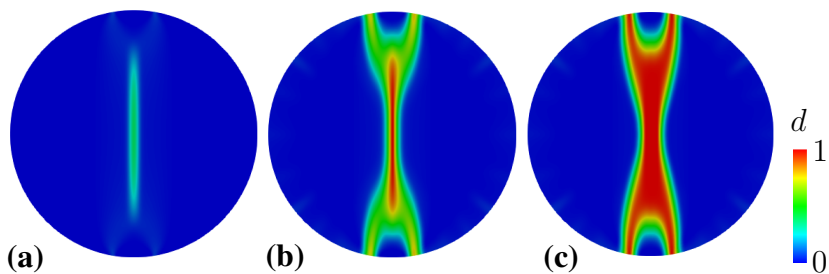
Figure 2.31: Prediction of crack pattern in concrete specimen under Brazilian tensile test at **(a)** $u = 0.102$ mm, **(b)** $u = 0.212$ mm and **(c)** $u = 0.24$ mm.
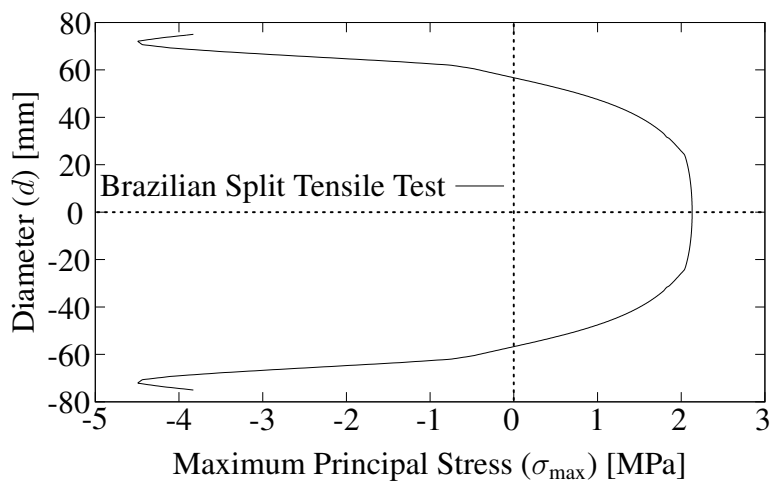
Figure 2.32: Distribution of the maximum principal stress along the diameter of the specimen at displacement $u = 0.238$ mm.

the split tensile strength of concrete as $f_{st} = 1.429 f_{dt}$. The split tensile strength can also be determined using the following expression [103]

$$f_{st} = \frac{2 P_{max}}{\pi\, l\, D} \tag{2.95}$$

where P_{max} indicates the maximum load at the onset of cracking, l and D represent the length and the diameter of the cylindrical specimen, respectively. These are $l = 300$ mm and $D = 150$ mm. As the direct tensile strength is $f_{dt} = 2.7$ MPa in this example, the split tensile strength is computed as $f_{st} = 3.86$ MPa. Then the maximum load in (2.95) is theoretically calculated as $P_{max} = 272.65$ kN. We obtain the maximum load from the numerical results as $F_{max} = 271$ kN, which is in good agreement with the theoretical value, see Figure 2.33.

Referring to Figure 2.32, it is observed that there is a difference between the calculated maximum principal stress, that its distribution is demonstrated in Figure 2.32 is different from the direct tensile strength computed form the analytical expression as $f_{dt} = 2.7$ MPa. This originates from the basic principles and the derivation of the cohesive zone phase-field model. In this study, the crack driving force β_d is calculated as a function of the tensile strains, that are calculated differently for the non-identical mechanical displacements. In addition, within the framework of the cohesive zone phase-field model, the formulation is predominantly derived for the Mode I fracture, but in this example there exist a mixed-mode fracture.
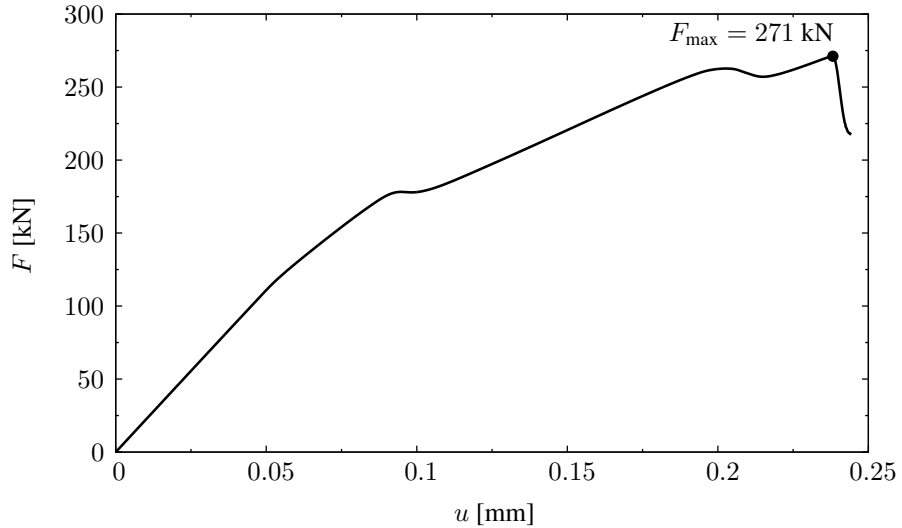
Figure 2.33: Load-deflection curve for Brazilian split tensile test.

2.6 Concluding Remarks

In this chapter, a thermodynamically consistent framework for the phase-field model is presented and used to simulate the brittle and quasi-brittle fracture in solid bodies by using Finite Element Method. At first, we have derived the general form of a regularized crack surface functional in terms of the crack geometric function. Then, we have introduced the dissipation function for crack phase-field evolution which is also dependent on the geometric crack function. Furthermore, the energetic degradation function based on the optimal constitutive functions associated with the specific form of the softening law has been represented. To this end, we solve a crack phase-field problem over a one-dimensional bar to obtain the inverse crack phase-field an half with of localization band which contributes to relate the optimal parameters for the softening laws.

Contrary to the classical phase-field model, which has been widely applied to model the brittle fracture in the solid bodies, the cohesive-zone phase-field model is presented in this study to predict the quasi-brittle fracture in a solid body especially in concrete. This approach allows us to predict the post-cracking response of the material which is accompanied by softening. In the traditional phase-field models, the response of the material strongly depends on the length scale parameter. This parameter is defined as a function of the mechanical properties of the material which also governs the spatial discretization of the solid body. However, the cohesive-zone phase-field approach overcomes this drawback where the length scale parameter has a negligible effect on the global response of the material so that it no longer depends on the mesh size and bias. It just affects the localization bandwith so by sufficiently refining the mesh size the crack phase-field is resolved within the localization band and, the results converge to the analytical ones [27].

The cohesive-zone phase-field model is implemented by using the Scalable Nonlinear Equations Solvers (SNES) to solve a bounded-constrained optimization problem in which the crack irreversibility is enforced. The presented numerical results represent the capabilities of the phase-field model in predicting the fracture in solid bodies especially for the case of materials which exhibit the quasi-brittle behavior under the mechanical loading.

In the following chapter, the cohesive-zone phase-field model will be used to simulate thermally-induced cracking in hardening concrete and its response is investigated the varying environmental temperature conditions.

CHAPTER 3

PHASE-FIELD MODELING OF THERMAL CRACKING IN MASS CONCRETE

3.1 Introduction

In massive concrete structures, the volumetric deformation due to temperature changes is of great importance since it may induce cracking. In the concrete technology of massive structures construction, the cracks resulting from the volume changes due to the thermal gradient between the interior and exterior of the structures are a primary concern. It has also a considerable effect on the stress state of massive structures. The variation of temperature is related to the amount of heat generated in the course of the hydration process of cement. This heat generation also influences the behavior of concrete at the early ages [25, 16].

The behavior of concrete at the early ages is the cross-effect between the hydration reactions, temperature evolution, and deformation, which can lead to cracking. The risk of cracking due to temperature variations in a massive structure such as a concrete dam is required to differentiate two primary patterns. It is concerned with cracking due to the cooling process that may take several years after the completion of the dam, and cracking near the surface as a result of the surface cooling due to the ambient air temperature. The latter process may become an essential issue during the first week after concreting [16]. The increasing number of massive concrete structures constructed around the world and the importance of their serviceability require detailed methodologies to estimate practically the risk of thermally induced cracking in the massive concrete constructions. As a consequence, the failure mechanics of massive concrete structures is appealed great significance in the field of the prediction of

fracture in engineering applications.

In the literature, there exist studies investigating the fracture mechanism to develop convincing methodologies for the realistic assessment of the risk of thermally induced cracking in the massive concrete structures.

The more relevant features of the concrete behavior at early ages, e.g. the cement hydration, the aging effects, temperature variation, creep and damage are studied in [25, 16]. In the latter study, the numerical approach is proposed within the framework of chemo-thermo-elasticity to predict the temporal evolution of the degree of hydration and the production of the heat of hydration. Moreover, a damage model based on the theory of continuum damage mechanics is presented to perform the stress analysis of the evolutionary construction process of RCC dams, and the consequent cracking in the interior of the dam body due to the cooling process, in which the nonuniform distribution of maximum temperature decreases down to the mean annual temperature, and cracking near the surface as a consequence of the thermal gradient in concrete is induced by environmental conditions. The thermally induced stress in a massive concrete structure can be classified in two general types: (i) self-stress which may develop as a result of the non-linear distribution of the internal temperature without any external constraint and (ii) the restraint-stress, which is produced by external boundary constraints so the solid body cannot deform freely as temperature varies.

De Schutter has conducted finite element simulation to investigate the occurrence of thermal cracking in massive hardening concrete elements using the degree of hydration based parameter laws [104]. Moreover, in the study, the crack initiation and propagation are simulated through a smeared cracking approach with non-linear softening behavior. Furthermore, a three-dimensional material model based on the Rankine criterion is presented in [23] to simulate the early-age cracking of concrete. The proposed model is employed for the chemo-thermo-mechanical analysis of RCC dam. In addition, crack risk analysis is conducted to capture the potentially cracking paths.

Over the recent years, the phase-field model has been more favored by several researchers to simulate cracking under thermal effects. This method has been widely applied to simulate the brittle fracture. In the work of Miehe *et al.* [69], it is developed to model the brittle fracture in thermo-elastic solids and then it is extended

to model crack propagation in a thermo-elastic-plastic solid by developing a generalization of continuum phase-field model from brittle to ductile fracture coupled with thermo-plasticity [70].

The phase-field model is applied in [28], to computationally modeling the brittle fracture caused by the heat generated during the hydration process and autogenous shrinkage in concrete at early ages. In addition to the thermal and early-age shrinkage effect, response of a degrading concrete to the basic and transient thermal creep effects are also investigated in [29, 30].

The existing phase-field approaches have been applied mainly to brittle fracture, except for few works [74, 75, 76], in which the phase field-model was proposed for cohesive fracture. Recently, a unified phase-field model of quasi-brittle failure was developed in [27]. Accordingly, in contrast to the existing phase-field models, this present model adopts a novel constitutive functions optimal for quasi-brittle failure. The proposed phase-field theory converges to a cohesive zone model as the internal length scale vanishes. Moreover, several softening laws, e.g., linear, exponential, hyperbolic and Cornelissen's ones [77] were incorporated for quasi-brittle solid, to improve the accuracy of the model. This unified phase-field model was used to model the quasi-brittle failure in the solids under the different mechanical loading [78, 79, 80, 81]. In reality however, there are other factors affect the materialistic behavior of concrete especially at its both short- and long-term serviceability such as thermal and hygral effects originating from the various environmental conditions. To computationally predict the behavior of massive concrete structures under these environmental effects, especially potential crack topology, the phase-field regularized cohesive zone model can be favorable.

In this study, a coupled constitutive modeling approach through the robust computational framework is developed to address the thermally induced cracking in massive concrete dams. In the literature, there are limited studies which explicitly account for the fracture under coupled chemo-thermo-mechanical effects by implementing the phase-field model. To a large extent, the existing phase-field models have been applied to brittle fracture. In this study, a phase-field regularized cohesive zone model, the so-called unified phase-field model by means of an associated softening law is

71

used to simulate the approximately actual behavior of hardening concrete subjected to thermally induced cracking. In contrast to the current phase-field model in which a hybrid formulation is used, we apply an anisotropic formulation with tension/compression split, described in [105, 26, 106]. However, this split causes non-linearity in the displacement subproblem and increases the computational costs. In the case of mixed-mode cracking, on the other hand, it improves the precision of the solutions.

The performance of the present coupled chemo-thermo-mechanical cohesive zone phase-field model is validated by regarding the multiphysics problem in the roller-compacted concrete. To this end, the temperature distribution, the crack initiation and propagation under the effects of the ambient temperature and the latent heat of hydration are investigated. Moreover, we examine the effect of cracking on the temperature distribution by performing additional analyses.

3.2   Theory

In this section, we introduce the governing equations of the multi-field boundary-value problem of chemo-thermo-mechanics along with the phase field approximation of quasi-brittle fracture.

3.2.1   Geometry and Kinematics

Let $\mathcal{B} \subset \mathbb{R}^\delta$ be a solid body with the boundary $\partial \mathcal{B} \subset \mathbb{R}^{\delta-1}$ within the δ-dimensional space where $\delta \in \{2, 3\}$ as depicted in Figure 3.1. The position change of the material point $\mathcal{P} \in \mathcal{B}$, initially situated at point $\boldsymbol{x}$, at time t is represented by the displacement field $\boldsymbol{u}(\boldsymbol{x}, t)$. Within the geometrically linear framework, the strain tensor $\boldsymbol{\varepsilon}$ is defined as the symmetric displacement gradient $\boldsymbol{\varepsilon}(\boldsymbol{x}, t) := \frac{1}{2} \left(\nabla \boldsymbol{u} + \nabla^T \boldsymbol{u} \right)$.

Moreover, we approximate the sharp crack Γ present in the body $\mathcal{B}$, Figure 3.1a, by the crack phase field d smeared over the localization zone $\mathcal{L}$, bounded by $\partial \mathcal{L}$, as shown in Figure 3.1b. The value of the crack phase field d varies within the interval $d \in [0, 1]$ where the lower bound $d = 0$ and the upper $d = 1$ bound represent the intact state and the fully broken state of the material, respectively. Within the framework of
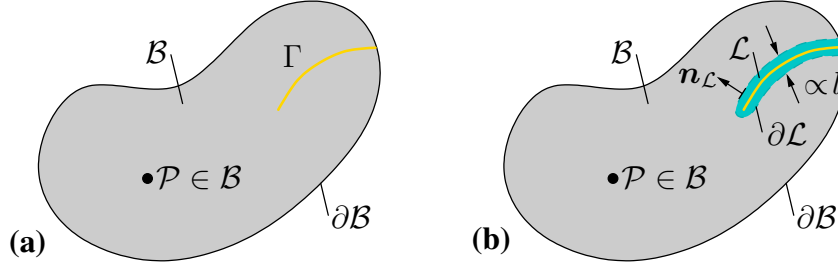
Figure 3.1: Schematic representations of fracture in a solid body $\mathcal{B}$ through **(a)** a sharp crack topology Γ and **(b)** as a diffuse crack smeared in the localization zone $\mathcal{L}$ described by the crack phase field d.

phase field fracture models, the total surface area of the sharp crack is approximated by

$$\mathcal{S} := \int_{\Gamma} dA \approx \int_{\mathcal{B}} \gamma_l(d; \nabla d) \, dV \tag{3.1}$$

see e.g. Francfort & Marigo [57]. Following Miehe *et al.* [26], we refer to the function $\gamma_l(d; \nabla d)$ as the crack surface (area) density function that depends on the crack phase field d, its gradient ∇d, and the length scale parameter l. The latter controls the width of the localization zone $\mathcal{L}$ where the intensity of the crack phase field d decays from the central line of the localization zone $\mathcal{L}$ along the crack in the transverse direction towards $\partial\mathcal{L}$ as depicted in Figure 3.1b. In other words, the smaller the length scale parameter l is, the sharper the gradient of the crack phase field $\nabla_n d$ in the lateral direction $\boldsymbol{n}_{\mathcal{L}}$ becomes.

Following Wu [27], the majority of various kinds of the crack surface density function used in the phase field fracture models can be expressed in a unified manner through the expression

$$\gamma_l(d; \nabla d) := \frac{1}{c_0 \, l} \left[\hat{\alpha}(d) + l^2 |\nabla d|^2 \right] \quad \text{with} \quad c_0 := 4 \int_0^1 \sqrt{\alpha(y)} \, dy \tag{3.2}$$

where the so-called the geometric crack function $\hat{\alpha}(d)$ represents the local geometric crack resistance and governs the homogeneous evolution of the crack phase field d. The scaling factor c_0 is introduced to make the phase field models capture the area of the sharp crack Γ, shown in Figure 3.1.

73

3.2.2 Thermodynamic State

The overall behavior of mass hardening concrete is considered to be controlled by chemical, thermal, mechanical, and fracture phenomena that are generally coupled at different scales. Although the water transport-related hygral phenomena are equivalently important in early ages of concrete structures especially with high surface area-thickness ratio, we leave out the hygral effects from the scope of the present work that focuses solely on the thermal cracking in mass concrete. Therefore, we construct a chemo-thermo-mechanical model at macro scale within the framework of the theory of reactive porous media, originally proposed by Ulm & Coussy [17, 3, 4, 6]. To this end, the local thermodynamic state of hardening concrete possibly undergoing thermal quasi-brittle fracture is described by the following four state variables

$$\text{State}(\boldsymbol{x}, t) := \{\boldsymbol{\varepsilon}(\boldsymbol{x}, t), d(\boldsymbol{x}, t), \theta(\boldsymbol{x}, t), \xi(\boldsymbol{x}, t)\}. \tag{3.3}$$

The strain tensor $\boldsymbol{\varepsilon}(\boldsymbol{x}, t)$ and the crack phase field $d(\boldsymbol{x}, t)$ have already been introduced in the preceding section. In addition to the latter, we have the temperature field $\theta(\boldsymbol{x}, t)$ and the degree of hydration $\xi(\boldsymbol{x}, t)$ that characterize the thermal state and the chemical state of hardening concrete, respectively. A fundamental state function governing the coupled chemo-thermo-mechanical behavior of hardening concrete exhibiting thermal cracking is the Helmholtz free energy function

$$\Psi = \hat{\Psi}(\boldsymbol{\varepsilon}, d, \theta, \xi). \tag{3.4}$$

formulated in terms of the state variables (4.1).

According to the theory of reactive porous media, the hardening concrete is considered as a closed thermodynamic system where the boundaries are impermeable to any mass transfer. Apparently, this assumption simplifies the process of hydration greatly and allows one to quantify the hydration extent through a single variable, namely the degree of hydration ξ. The latter can be conceived as the molar mass ratio of the chemically bonded water through hydration reactions to the total amount of initially free water. Therefore, the degree of hydration ξ is an essential field variable representing the growth of rigidity and strength of hardening concrete [24, 107, 108]. Owing to the closed system assumption, the degree of hydration ξ is considered as an internal state variable whose thermally activated evolution is governed by an Arrhenius-type

ordinary differential equation as suggested in Ulm & Coussy [4], Cervera *et al.* [7], Lackner & Mang [23].

3.2.3 Governing Differential Equations

In this section, we introduce the differential equations that govern the evolution of the state variables, given in (4.1). In particular, the balance of linear momentum and the conservation of energy, through the transient heat conduction equation, describe the spatio-temporal evolution of external state variables, the displacement field $\boldsymbol{u}(\boldsymbol{x}, t)$ and the temperature field $\theta(\boldsymbol{x}, t)$, respectively. To obtain the evolution equations for the crack phase field $d(\boldsymbol{x}, t)$ and the degree of hydration $\xi(\boldsymbol{x}, t)$, associated with the intrinsically dissipative phenomena of fracture and highly exothermic hydration reactions, respectively, we extend the energy equivalence principle, recently proposed by Wu [78], towards chemo-thermo-mechanics incorporating phase field fracture.
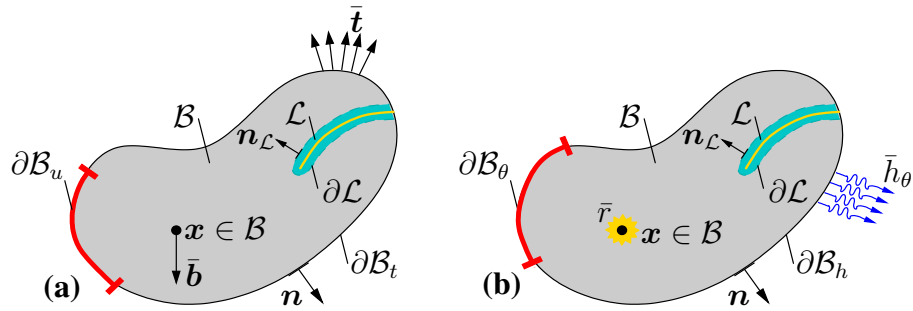
Figure 3.2: Schematic representations of the Dirichlet and Neumann boundary conditions for the **(a)** mechanical and **(b)** thermal problems.

The balance of linear momentum representing the quasi-static stress equilibrium

$$\operatorname{div} \hat{\boldsymbol{\sigma}} + \bar{\boldsymbol{b}} = \boldsymbol{0} \tag{3.5}$$

in terms of the stress tensor $\hat{\boldsymbol{\sigma}}$ and the given volume-specific body forces $\bar{\boldsymbol{b}}$ governs the evolution of the displacement field $\boldsymbol{u}(\boldsymbol{x}, t)$ along with the Dirichlet $\boldsymbol{u} = \bar{\boldsymbol{u}}$ on $\partial \mathcal{B}_u$ and the Neumann $\boldsymbol{\sigma} \boldsymbol{n} = \bar{\boldsymbol{t}}$ on $\partial \mathcal{B}_t$ boundary conditions where $\boldsymbol{n}$ is the outward unit surface normal on $\partial \mathcal{B}$. Clearly, the respective parts of the boundary $\partial \mathcal{B}_u$ and $\partial \mathcal{B}_t$ satisfy $\partial \mathcal{B} = \partial \mathcal{B}_u \cup \partial \mathcal{B}_t$ and $\partial \mathcal{B}_u \cap \partial \mathcal{B}_t = \emptyset$ as shown in Figure 3.2a.

The first law of thermodynamics $\dot{e} = \boldsymbol{\sigma} : \dot{\boldsymbol{\varepsilon}} + Q_{\text{ext}}$ describes the rate of energy balance in terms of the volume-specific internal energy e, the internal stress power $\boldsymbol{\sigma} : \dot{\boldsymbol{\varepsilon}}$, and the externally supplied thermal power $Q_{\text{ext}} := -\operatorname{div} \boldsymbol{q}_\theta + \bar{r}$ where $\boldsymbol{q}_\theta$ denotes the outward heat flux vector and $\bar{r}$ is the given volume-specific external heat source. Substituting the Legendre transformation $e = \Psi + \theta\eta$ between the internal energy and the Helmholtz free energy, we arrive at the following version of the first law

$$\theta\dot{\eta} = \mathcal{D}_{\text{loc}} + Q_{\text{ext}} \tag{3.6}$$

where $\mathcal{D}_{\text{loc}} := \boldsymbol{\sigma} : \dot{\boldsymbol{\varepsilon}} - \dot{\Psi} - \eta\dot{\theta} \geq 0$ denotes the intrinsic dissipation due to the internal dissipative mechanisms. The non-negativeness of $\mathcal{D}_{\text{loc}}$ is dictated by the second law of thermodynamics. Expanding the rate of the free energy $\hat{\Psi}(\boldsymbol{\varepsilon}, d, \theta, \xi)$ in (3.4) in terms of its partial derivatives with respect to the state variables (4.1) and their rates, we obtain the Clausius-Planck inequality

$$\mathcal{D}_{\text{loc}} := [\boldsymbol{\sigma} - \partial_{\boldsymbol{\varepsilon}}\hat{\Psi}] : \dot{\boldsymbol{\varepsilon}} - [\partial_\theta\hat{\Psi} + \eta]\,\dot{\theta} - \partial_d\hat{\Psi}\dot{d} - \partial_\xi\hat{\Psi}\dot{\xi} \geq 0\,.$$

Based on the Coleman's exploitation method, see e.g. Coleman & Gurtin [109], we demand that the non-negativeness of $\mathcal{D}_{\text{loc}}$ must be fulfilled for arbitrary rates of the controllable external variables $\boldsymbol{\varepsilon}$ and θ. Based on this argument, the expressions within the brackets vanish identically to yield the well-known constitutive definitions of the stress tensor $\boldsymbol{\sigma}$ and the entropy η through

$$\hat{\boldsymbol{\sigma}} = \partial_{\boldsymbol{\varepsilon}}\hat{\Psi}(\boldsymbol{\varepsilon}, d, \theta, \xi) \quad \text{and} \quad \hat{\eta} = -\partial_\theta\hat{\Psi}(\boldsymbol{\varepsilon}, d, \theta, \xi)\,. \tag{3.7}$$

The local dissipation expression then reduces to the following form

$$\mathcal{D}_{\text{loc}} := -\partial_d\hat{\Psi}\dot{d} - \partial_\xi\hat{\Psi}\dot{\xi} \geq 0\,,$$

from which it is clear that the chemical hydration and fracture processes are the main dissipative mechanisms of the chemo-thermo-mechanical phase field fracture model. Within the framework of the phase field modeling of brittle and quasi-brittle fracture, the local dissipation arising from fracture $\mathcal{D}_{\text{loc}}^d := -\partial_d\hat{\Psi}\dot{d} \geq 0$ can be alternatively expressed as a product of the rate of crack surface density function $\dot{\gamma}_l(d; \nabla d)$, introduced in (3.1,3.2), and the critical energy release rate G_c representing the amount of energy needed to advance a crack by unit area; that is,

$$\mathcal{D}_{\text{loc}}^d = Y\dot{d} = G_c\,\dot{\gamma}_l(d; \nabla d) \geq 0\,. \tag{3.8}$$

76

where $Y := -\partial_d \hat{\Psi}$ is the local driving force of the crack phase field d. Moreover, the rate of the crack surface density function can be expressed through the variational derivative of $\gamma_l(d; \nabla d)$

$$\dot{\gamma}_l(d; \nabla d) = \delta_d \gamma_l \, \dot{d} \quad \text{with} \quad \delta_d \gamma_l := \partial_d \gamma_l - \text{div}(\partial_{\nabla d} \gamma_l) \,. \tag{3.9}$$

Clearly, this equality holds for homogeneous Neumann boundary conditions, i.e. $\partial_{\nabla d} \gamma_l \cdot \boldsymbol{n}_{\mathcal{L}} = 0$ on $\partial \mathcal{L}$ where $\boldsymbol{n}_{\mathcal{L}}$ denotes the outward unit normal defined on the boundary $\partial \mathcal{L}$ of the crack phase field localization zone $\mathcal{L}$ as shown in Figures 3.1 and 3.2. For the specific form of $\gamma_l(d; \nabla d)$, given in (3.2), the variational derivative can be expressed as

$$\delta_d \gamma_l(d; \nabla d) = \frac{1}{c_0 \, l} \left[\hat{\alpha}'(d) - 2l^2 \, \text{div}(\nabla d) \right] \,.$$

Substituting the representation (3.9) into (3.8), we obtain

$$g(Y, d) \, \dot{d} = 0 \quad \text{with} \quad g(Y, d) := Y - G_c \delta_d \gamma_l \,. \tag{3.10}$$

Owing to the irreversibility constraint $\dot{d} \geq 0$, this equality can be written in the form of a Karush-Kuhn-Tucker-type conditional evolution equation

$$\begin{cases} g(Y, d) < 0 \quad \text{for} \quad \dot{d} = 0 \,, \\[2mm] g(Y, d) = 0 \quad \text{for} \quad \dot{d} > 0 \end{cases} \tag{3.11}$$

where $g(Y, d) \leq 0$ can be conceived as the fracture criterion. When the rate of crack phase field is positive ($\dot{d} > 0$), the differential equality $g(Y, d) = 0$ describes the spatial evolution of the crack phase field d within $\mathcal{L}$. The nonlocal damage evolution $(3.11)_2$ can then be recast into the form, analogous to (3.5)

$$\text{div} \, \hat{\boldsymbol{q}}_d - \hat{\mathcal{H}}_d + \hat{f}_d = 0 \tag{3.12}$$

where $\hat{\mathcal{H}}_d \equiv Y$ indicates the crack driving force, while the remainder terms $\hat{\boldsymbol{q}}_d := -\frac{2l}{c_0} \hat{G}_f(\xi) \nabla d$ with $\boldsymbol{q}_d \cdot \boldsymbol{n}_{\mathcal{L}} = 0$ on $\partial \mathcal{L}$ and $\hat{f}_d := \frac{\hat{G}_c(\xi)}{c_0 \, l} \hat{\alpha}'(d)$ characterize the resistance to the crack phase field evolution and diffusion. In brittle and quasi-brittle fracture, the crack driving force $\hat{\mathcal{H}}_d$ is alternatively identified often with the highest tensile deformation energy generated locally, thereby allowing the crack initiation and propagation in a thermodynamically consistent manner. In the numerical implementation, we account for the fact that the crack phase field remains bounded within $d \in [0, 1]$

through the bound-constrained optimization solver provided by the PETSc package [93] as suggested in Wu [80].

The local dissipation $\mathcal{D}_{\text{loc}}^{\xi} := -\partial_{\xi}\hat{\Psi}\dot{\xi} \geq 0$ due to the hydration reactions, responsible for the growth of concrete in strength and rigidity, can be expressed as a product of the chemical driving force $\tilde{A}_{\xi}$ and the rate of the degree of hydration $\dot{\xi}$; that is,

$$\mathcal{D}_{\text{loc}}^{\xi} = \tilde{A}_{\xi}\dot{\xi} = -\partial_{\xi}\hat{\Psi}\dot{\xi} \geq 0\,.$$

The latter energetic equivalence identifies the chemical driving force, often referred to as the normalized chemical affinity, $\tilde{A}_{\xi} := -\partial_{\xi}\hat{\Psi}$ as the energy conjugate variable to the degree of hydration. Within the context of the theory of reactive porous media, the chemical affinity $\tilde{A}_{\xi}$ represents the imbalance between the free water and the bonded water in hydrates. Since hydration is a thermally activated process, the evolution of the degree of hydration is assumed to be described by the thermodynamically consistent, Arrhenius-type first-order kinetics activated by temperature, see e.g. Ulm & Coussy [4], Lackner & Mang [23],

$$\dot{\xi} = \tilde{A}_{\xi} \exp\left(-\frac{E_{\text{a}}}{R\theta}\right) \quad \text{with} \quad \xi_0(\boldsymbol{x}) = \xi(\boldsymbol{x}, t = 0) \tag{3.13}$$

where the parameters E_a and R denote the activation energy and the universal gas constant with $R = 8.315$ J/(mol K), respectively. The ratio E_a/R, which can be experimentally determined, ranges from 3000 to 8000 K for concrete. According to van Breugel [110] for many practical purposes at least for Portland cement, $E_a = 33500$ J/mol for $\theta \geq 293$ K.

Expanding the rate of entropy using the constitutive expression for entropy (3.7) and inserting the result into the energy balance expression (3.6), we arrive at the transient heat conduction equation

$$c\dot{\theta} = \hat{\mathcal{H}}_{\xi} + \hat{\mathcal{H}}_{\varepsilon} + \hat{\mathcal{H}}_{d}^{\theta} + Q_{\text{ext}}$$

where $c := \theta\partial_{\theta}\eta = -\theta\partial_{\theta\theta}\hat{\Psi}$ is the volume-specific heat capacity, $\hat{\mathcal{H}}_{\xi} := (\tilde{A}_{\xi} - \theta\partial_{\theta}\tilde{A}_{\xi})\dot{\xi}$ stands for the chemical heating, and $\hat{\mathcal{H}}_{\varepsilon} := \theta\partial_{\theta}\boldsymbol{\sigma} : \dot{\boldsymbol{\varepsilon}}$ and $\hat{\mathcal{H}}_{d}^{\theta} := (Y - \theta\partial_{\theta}Y)\dot{d}$ denote the thermoelastic heating and the heating due to irreversible evolution of crack phase field, respectively. Compared to the chemical heating $\hat{\mathcal{H}}_{\xi}$, the latter two types

78

$(\hat{\mathcal{H}}_\varepsilon, \hat{\mathcal{H}}_d^\theta)$ of heating are assumed to be negligible under moderate rates of chemo-thermo-mechanical cracking processes. Moreover, in the chemical dissipation expression the hydration dissipation $\tilde{A}_\xi \dot{\xi}$ is negligible compared to the exothermic heating $-\theta \partial_\theta \tilde{A}_\xi \dot{\xi}$, see Ulm & Coussy [4], Lackner & Mang [23]. In the absence of any deformation and cracking, the heat of hydration L_ξ can be measured through calorimetric measurements under nearly adiabatic conditions per unit mass. Therefore, the chemical heating can be approximated by $\hat{\mathcal{H}}_\xi \approx L_\xi \dot{\xi}$. This, along with the above simplifying asssumptions, leads us to the following transient heat conduction equation

$$\text{div}\, \hat{\boldsymbol{q}}_\theta - \hat{\mathcal{H}}_\theta + \hat{f}_\theta = 0\,, \tag{3.14}$$

analogous to the evolution equation for the crack phase field (3.12). Here, $\hat{\mathcal{H}}_\theta := L_\xi \dot{\xi}$ indicates the heating due to hydration and $\hat{f}_\theta := c\dot{\theta} - \bar{r}$ accounts for the thermal energy storage and external heat supply. The spatio-temporal evolution of the temperature field $\theta(\boldsymbol{x}, t)$ is described by the transient heat conduction equation that is complemented by the Dirichlet $\theta = \bar{\theta}$ on $\partial\mathcal{B}_\theta$ and the Neumann $\boldsymbol{q}_\theta \cdot \boldsymbol{n} = \bar{h}_\theta$ on $\partial\mathcal{B}_h$ boundary conditions and the initial condition $\theta_o(\boldsymbol{x}) = \theta(\boldsymbol{x}, t = 0)$ in $\mathcal{B}$. The parts of the boundary, $\partial\mathcal{B}_\theta$ and $\partial\mathcal{B}_h$, are complementary $\partial\mathcal{B} = \partial\mathcal{B}_\theta \cup \partial\mathcal{B}_h$ and disjoint $\partial\mathcal{B}_\theta \cap \partial\mathcal{B}_h = \emptyset$ as shown in Figure 3.2b.

The governing differential equations (3.5,3.12,3.14,3.13) along with the associated boundary and initial conditions are summarized in Table 3.1.

3.2.4 Constitutive Equations

The governing differential equations of the chemo-thermomechanical phase field fracture model, given in Table 3.1, are coupled through the constitutive equations for the stress tensor $\hat{\boldsymbol{\sigma}}$ in (3.5), the crack-driving force $\hat{\mathcal{H}}_d$ in (3.12), and the hydration power $\hat{\mathcal{H}}_\theta$ in (3.14). Besides these coupling terms, the geometric crack function $\hat{\alpha}(d)$ in (3.2) contributing to the crack resistance term $\hat{f}_d$, the normalized chemical affinity $\tilde{A}(\xi)$ in (3.13), and the heat flux vector $\hat{\boldsymbol{q}}_\theta$ in (3.14) need to be specified for hardening concrete to complete the theoretical description of the model. Hence, this subsection is devoted to the constitutive equations.

Table 3.1: Governing equations of the chemo-thermo-mechanical phase field fracture model

Field	Problem	Equation	#	BC's / IC's
$\boldsymbol{u}(\boldsymbol{x}, t)$	Mechanical	$\operatorname{div} \boldsymbol{\sigma} + \bar{\boldsymbol{b}} = \boldsymbol{0}$	(3.5)	$\boldsymbol{u} = \bar{\boldsymbol{u}}$ on $\partial \mathcal{B}_u$
				$\boldsymbol{\sigma} \boldsymbol{n} = \bar{\boldsymbol{t}}$ on $\partial \mathcal{B}_t$
$d(\boldsymbol{x}, t)$	Phase Field Fracture	$\operatorname{div} \hat{\boldsymbol{q}}_d - \hat{\mathcal{H}}_d + \hat{f}_d = 0$	(3.12)	$\boldsymbol{q}_d \cdot \boldsymbol{n} = 0$ on $\partial \mathcal{L}$
$\theta(\boldsymbol{x}, t)$	Thermal	$\operatorname{div} \hat{\boldsymbol{q}}_\theta - \hat{\mathcal{H}}_\theta + \hat{f}_\theta = 0$	(3.14)	$\theta = \bar{\theta}$ on $\partial \mathcal{B}_\theta$
				$\boldsymbol{q}_\theta \cdot \boldsymbol{n} = \bar{h}_\theta$ on $\partial \mathcal{B}_h$
				$\theta_o(\boldsymbol{x}) = \theta(\boldsymbol{x}, t = 0)$ in $\mathcal{B}$
$\xi(\boldsymbol{x}, t)$	Hydration	$\dot{\xi} = \tilde{A}_\xi \exp\left(-\dfrac{E_\mathrm{a}}{R\theta}\right)$	(3.13)	$\xi_o(\boldsymbol{x}) = \xi(\boldsymbol{x}, t = 0)$ in $\mathcal{B}$

Stress Response. To account for the tension-compression asymmetry in the failure behavior of concrete, as suggested in Miehe *et al.* [68], we decompose the total stress response into the tensile and compressive parts

$$\boldsymbol{\sigma} = \hat{\boldsymbol{\sigma}}(\boldsymbol{\varepsilon}, d, \theta, \xi) = \hat{g}(d)\, \hat{\boldsymbol{\sigma}}_0^+(\boldsymbol{\varepsilon}, \theta, \xi) - \hat{\boldsymbol{\sigma}}_0^-(\boldsymbol{\varepsilon}, \theta, \xi) \tag{3.15}$$

where only the tensile part of the stress tensor is affected by damage through the monotonically decreasing degradation function

$$\hat{g}(d) := \frac{(1-d)^p}{(1-d)^p + Q(d)} \tag{3.16}$$

where following cubic polynomial is assumed for the rigorously positive function $Q(d)$

$$Q(d) = a_1 d + a_1 a_2 d^2 + a_1 a_2 a_3 d^3 \tag{3.17}$$

with $p > 0$ and $Q(d) > 0$ as suggested in Wu [27] being inspired by Lorentz & Godard [86]. The degradation function $g(d) \in [0, 1]$, a monotonically decreasing function of the crack phase field d, is required to fulfill the following conditions

$$g'(d) < 0\,,\ g(0) = 1\,,\ g(1) = 0\,, \quad \text{and} \quad g'(1) = 0 \quad \text{for all} \quad d \in [0, 1]\,. \tag{3.18}$$

Since the material model is constructed for hardening concrete that continuously gains strength and rigidity, the current non-degraded stress response is formulated in the following incremental form

$$\hat{\boldsymbol{\sigma}}_0^{\pm} = \hat{\boldsymbol{\sigma}}_{0n}^{\pm} + \Delta\hat{\boldsymbol{\sigma}}_0^{\pm} \tag{3.19}$$

in terms of the non-degraded stress tensor $\hat{\boldsymbol{\sigma}}_{0n}^{\pm}$ at time t_n and the incremental stress tensor $\Delta\hat{\boldsymbol{\sigma}}_0^{\pm}$ introduced for a typical time step $[t_n, t_{n+1}]$. This incremental form accounts for the fact that new products of hydration begin to contribute to the stiffness of hardening concrete from the onset of their hydration as suggested in Bažant [111], Ulm & Coussy [4], Cervera *et al.* [7], Lackner & Mang [23] among others. The incremental undamaged stress response is then specified as

$$\Delta\hat{\boldsymbol{\sigma}}_0^{\pm} = \hat{\lambda}(\xi)\Delta\langle\operatorname{tr}\boldsymbol{\varepsilon}^e\rangle_{\pm}\mathbf{1} + 2\hat{\mu}(\xi)\Delta\boldsymbol{\varepsilon}_{\pm}^e \tag{3.20}$$

where $\hat{\lambda}(\xi) > 0, \hat{\mu}(\xi) > 0$ denote the Lamé constants that grow as a function of the degree of hydration, as specified in (3.36). The chemo-thermomechanical coupling has been incorporated in the stress response through the stress-producing elastic part of the strain tensor $\boldsymbol{\varepsilon}^e$ that is defined as

$$\boldsymbol{\varepsilon}^e := \boldsymbol{\varepsilon} - \boldsymbol{\varepsilon}^{\text{th}} - \boldsymbol{\varepsilon}^{\text{au}} - \boldsymbol{\varepsilon}^{\text{ttc}} \tag{3.21}$$

where the thermal strain tensor $\boldsymbol{\varepsilon}^{\theta}$, the autogenous shrinkage strain tensor $\boldsymbol{\varepsilon}^{\text{au}}$, and the rate of the transitional thermal creep strain tensor $\boldsymbol{\varepsilon}^{\text{ttc}}$ are described by

$$\boldsymbol{\varepsilon}^{\theta} := \alpha_{\theta}\Delta\theta\,\mathbf{1}\,, \qquad \boldsymbol{\varepsilon}^{\text{au}} := -\kappa\left\langle\frac{\xi - \xi_0}{1 - \xi}\right\rangle_+ \mathbf{1}\,, \quad \text{and} \quad \dot{\boldsymbol{\varepsilon}}^{\text{ttc}} := \lambda^{\text{ttc}}\,|\,\dot{\theta}\,|\,\hat{\boldsymbol{\sigma}}_0\,, \tag{3.22}$$

respectively. The thermal strain $\boldsymbol{\varepsilon}^{\theta}$ accounts for the temperature-induced expansion through the thermal expansion coefficient α_{θ} and the change in temperature $\Delta\theta :=\theta - \theta_0$ relative to the reference temperature θ_0. Likewise, the autogenous shrinkage strain $\boldsymbol{\varepsilon}^{\text{au}}$ accounts for the self-dessication phenomenon caused by the consumption of water by the hydration process, see e.g. Tokyay [112], through the autogenous shrinkage coefficient κ as suggested in Briffaut *et al.* [113]. Moreover, the transitional thermal creep $\boldsymbol{\varepsilon}^{\text{ttc}}$ has been incorporated in the model to take into account the stress-induced thermal strain due to the transient temperature history in terms of the the transitional thermal creep coefficient λ^{ttc}, see Thelandersson [114].

The tensile and compressive parts of the elastic strain tensor $\boldsymbol{\varepsilon}^e$ are defined as

$$\boldsymbol{\varepsilon}^e_\pm := \sum_{i=1}^{\delta} \langle \epsilon_i \rangle_\pm \, \boldsymbol{m}_i \tag{3.23}$$

where $\langle \epsilon_i \rangle_\pm := (|\epsilon_i| \pm \epsilon_i)/2$ designate the Macaulay brackets, also used in $(3.22)_2$. In this definition, we use the principal values ϵ_i and the principal tensors $\boldsymbol{m}_i := \boldsymbol{n}_i \otimes \boldsymbol{n}_i$ for $i = 1, \ldots, \delta$ of the elastic strain tensor based on the spectral decomposition of the elastic strain tensor $\boldsymbol{\varepsilon}^e = \sum_{i=1}^{\delta} \epsilon_i \, \boldsymbol{n}_i \otimes \boldsymbol{n}_i$. The tensile and compressive parts of the incremental elastic strain tensor entering the incremental stress expression (3.20) can then be obtained as

$$\Delta \boldsymbol{\varepsilon}^e_\pm := \boldsymbol{\varepsilon}^e_\pm - \Delta \boldsymbol{\varepsilon}^e_{\pm n} \, . \tag{3.24}$$

Crack Driving Force. The irreversibility of the crack evolution can be accounted for in the model by replacing the the definition of the crack phase field driving force, which is originally derived in a thermodynamically consistent manner as $\hat{\mathcal{H}}_d = Y = -\partial_d \hat{\Psi} = -\hat{g}'(d)\hat{\Psi}_0^+$, with

$$\mathcal{H}_d := -\hat{g}'(d)\mathcal{H}_{\max} \tag{3.25}$$

where $\mathcal{H}_{\max}$ represents the crack driving force

$$\mathcal{H}_{\max}(\boldsymbol{x}, t) := \max_{s \in [0,t]} \left(\hat{\Psi}_0^+ (\, \boldsymbol{\varepsilon}(\boldsymbol{x}, s), \theta(\boldsymbol{x}, s), \xi(\boldsymbol{x}, s) \,) \right) \tag{3.26}$$

as suggested in Miehe *et al.* [68]. The positive part of the energy due to tension is defined as

$$\hat{\Psi}_0^+(\boldsymbol{\varepsilon}, \theta, \xi) := \hat{\Psi}_{0n}^+ + \Delta \hat{\Psi}_0^+(\boldsymbol{\varepsilon}, \theta, \xi) \tag{3.27}$$

where the incremental positive part of the free energy can be computed as

$$\Delta \hat{\Psi}_0^+(\boldsymbol{\varepsilon}, \theta, \xi) := \hat{\boldsymbol{\sigma}}_0^+ : \Delta \langle \boldsymbol{\varepsilon} \rangle_+ \, . \tag{3.28}$$

Crack Resistance. As mentioned in Section 3.2.3, the resistance to the spatial evolution of the crack phase field is governed by

$$\hat{\boldsymbol{q}}_d(d, \xi) := -\frac{2l}{c_0} \hat{G}_c(\xi) \nabla_x d \quad \text{and} \quad \hat{f}_d(d, \xi) = \frac{\hat{G}_c(\xi)}{c_0 \ell} \hat{\alpha}'(d) \tag{3.29}$$

where the geometric crack function $\hat{\alpha}_d(d)$ governing the homogeneous evolution of the crack phase field is assumed to be expressed as a quadratic function of d

$$\hat{\alpha}(d) = zd + (1 - z)d^2 \geq 0 \qquad \text{for} \qquad z \in [0, 2] \, . \tag{3.30}$$

82

Depending up on the value of z, different phase field fracture formulations can be recovered. In particular, the phase field fracture models developed, for example, by Miehe *et al.* [68], Bourdin *et al.* [91] employs $\hat{\alpha}(d)|_{z=0} = d^2$, the gradient damage model of Pham *et al.* [82] utilizes $\hat{\alpha}(d)|_{z=1} = d$, and the quasi-brittle phase field model proposed by Wu [27] uses $\hat{\alpha}(d)|_{z=2} = 2d - d^2$. These phase field models have been referred to as `AT1`, `AT2`, and `PF-CZM`, respectively, in the recently published studies, see e.g. Mandal *et al.* [115]. While `AT1` and `AT2` are limited to brittle fracture, `PF-CZM` can be used to model brittle and quasi-brittle fracture. Since we model thermal cracking in hardening mass concrete by using `PF-CZM`, we set $z = 2$.

Thermal Heating. While the heating due to hydration $\hat{\mathcal{H}}_\theta(\dot{\xi}) := L_\xi \dot{\xi}$ has already been introduced in Section 3.2.3, we extend the definition of the term $\hat{f}_\theta$ in (3.14) towards

$$f_\theta = \hat{f}_\theta(\theta, d, ; \dot{\theta}) = c\dot{\theta} - \bar{r} + \hat{\mathcal{R}}_\theta^c(\theta, d) \tag{3.31}$$

to incorporate the convective heat exchange at crack faces through the additional heat sink $\hat{\mathcal{R}}_\theta^c(\theta, d)$. This phenomenon is numerically motivated by presuming that the deformed crack surfaces are in contact with an ambient temperature θ_∞ inside the free space induced by the crack opening and shown to be modeled approximately by

$$\hat{\mathcal{R}}_\theta^c(\theta, d) := -2\frac{h_c}{\ell}(\theta - \theta_\infty)d^2 \tag{3.32}$$

in terms of the convective heat exchange parameter h_c in Miehe et al. [69].

Heat Conduction. In this study, besides the degrading stress-strain response, the damage-dependent growth of non-mechanical effects in damaged zone is examined [70]. To this end, the thermal conductivity is formulated as a function of crack phase field d; that is,

$$\boldsymbol{q}_\theta = \hat{\boldsymbol{q}}_\theta(\theta, d) := -\hat{k}_\theta(d)\nabla\theta \quad \text{with} \quad \hat{k}_\theta(d) = (1 - d)^2 k_\theta^s + d^2 k_\theta^c. \tag{3.33}$$

Here, $k_\theta^s \geq 0$ and $k_\theta^c \geq 0$ stand for the coefficients of thermal conductivity differentiating the thermal conduction response of concrete between non-degraded case ($k_\theta = k_\theta^s$) and fully degraded case ($k_\theta = k_\theta^c$).

Chemical Hydration and Growth in Rigidity and Strength. The normalized chemical affinity $\tilde{A}_\xi$, the driving force of the evolution of the degree of hydration ξ, is

assumed to be described by

$$\tilde{A}_\xi(\xi) := a\xi^b(1-\xi)^c \tag{3.34}$$

in terms of the degree of hydration ξ and the constants a, b, and c that can be favorably fitted to experimental data as shown in Lackner & Mang [23].

The hydration-induced growth of concrete in rigidity and strength is modeled through aging expressions that specify the mechanical properties such as the modulus of elasticity E, the compressive strength f_c, the tensile strength f_t, and the critical energy release rate G_c in terms of ξ. As we focus primarily on the thermal cracking of roller-compacted concrete dam benchmark, borrowed from [23], we consider the following growth equations

$$\hat{E}(\xi) = E_\infty\sqrt{\xi}, \quad \hat{f}_c(\xi) = \frac{\xi - \xi_0}{1 - \xi_0}f_c^\infty, \quad \hat{f}_t(\xi) = 0.1\hat{f}_c(\xi), \quad \text{and} \quad \hat{G}_c(\xi) = \xi G_c^\infty \tag{3.35}$$

where E_∞, f_c^∞, and G_c^∞ denote the values of the modulus of elasticity, the compressive strength, and the critical energy release rate of concrete when the hydration process is completed with $\xi = 1$. As a consequence, by assuming a constant value for Poisson's ratio, the Lamé constants in the incremental stress expression (3.20)

$$\hat{\lambda}(\xi) := \frac{\nu}{(1+\nu)(1-2\nu)}\hat{E}(\xi) \quad \text{and} \quad \hat{\mu}(\xi) := \frac{\hat{E}(\xi)}{2(1+\nu)}. \tag{3.36}$$

Having the theoretical description of the coupled chemo-thermomechanics along with the phase field fracture, we now proceed with the numerical solution procedures that are used to solve inital boundary-value problems.

3.3 Finite Element Formulation

In this section, we construct the corresponding weak forms of the governing differential equations, whose strong forms are summarized in Table 3.1, and discretize them both in space and time by using finite element and finite difference methods for the respective cases. Moreover, the system of nonlinear equations obtained through discretization is linearized consistently for the iterative Newton-type solvers.

For the spatial discretization, we employ the conventional Galerkin method to derive the weak forms of the governing differential equation by multiplying each of them

with the associated weight function $\delta\boldsymbol{u} \in \mathscr{U}_0$, $\delta d \in \mathscr{V}_0$ and $\delta\theta \in \mathscr{W}_0$ whose square of integrals remain finite-valued and they meet the conditions of the homogeneous boundary conditions; that is, $\delta\boldsymbol{u} = \boldsymbol{0}$ over $\partial\mathcal{B}_{\boldsymbol{u}}$, $\delta d = 0$ over $\partial\mathcal{B}_d$, and $\delta\theta = 0$ over $\partial\mathcal{B}_\theta$). The weighted residual equations, integrated over the body, take the following form

$$
\begin{aligned}
G^u(\delta\boldsymbol{u}; \boldsymbol{u}, d, \theta) &= G^u_{\text{int}}(\delta\boldsymbol{u}; \boldsymbol{u}, d, \theta) &-& G^u_{\text{ext}}(\delta\boldsymbol{u}) = 0\,, \\
G^d(\delta d; \boldsymbol{u}, d, \theta) &= G^d_{\text{int}}(\delta d; \boldsymbol{u}, d, \theta) &-& G^d_{\text{ext}}(\delta d; \boldsymbol{u}, d, \theta) = 0\,, \\
G^\theta(\delta\theta; d, \theta) &= G^\theta_{\text{int}}(\delta\theta; d, \theta) &-& G^\theta_{\text{ext}}(\delta\theta; d, \theta) = 0\,.
\end{aligned}
\tag{3.37}
$$

for the mechanical, phase field fracture, and thermal problems after the integration by parts of the terms that involve second-order spatial derivatives. Note that as the transient evolution of the degree of hydration ξ is expressed as a function of the temperature, (3.13) locally at a quadrature point, it is solved numerically only by discretizing the evolution equation in time. Therefore, in the above equations, the degree of hydration does not appear as an additional independent field but treated as a local history (internal) variable.

The specific forms of the internal and external functionals of the mechanical problem $(3.37)_1$ are given by

$$
\begin{aligned}
G^u_{\text{int}}(\delta\boldsymbol{u}; \boldsymbol{u}, d, \theta) &:= \int_{\mathcal{B}} \delta\boldsymbol{\varepsilon} : \hat{\boldsymbol{\sigma}}\ dV\,, \\
G^u_{\text{ext}}(\delta\boldsymbol{u}) &:= \int_{\mathcal{B}} \delta\boldsymbol{u} \cdot \bar{\boldsymbol{b}}\ dV + \int_{\partial\mathcal{B}_t} \delta\boldsymbol{u} \cdot \bar{\boldsymbol{t}}\ dA\,.
\end{aligned}
\tag{3.38}
$$

where $\bar{\boldsymbol{b}}$ and $\bar{\boldsymbol{t}}$ are the volume-specific body force and the surface traction vector, respectively. In the case of the crack phase-field fracture, the internal end external Galerkin functionals are defined as

$$
\begin{aligned}
G^d_{\text{int}}(\delta d; d, \theta) &:= \int_{\mathcal{B}} -\nabla_x(\delta d) \cdot \hat{\boldsymbol{q}}_d\ dV\,, \\
G^d_{\text{ext}}(\delta d; \boldsymbol{u}, d, \theta) &:= \int_{\mathcal{B}} \delta d\,(\hat{\mathcal{H}}_d - \hat{f}_d)\ dV\,.
\end{aligned}
\tag{3.39}
$$

Analogously, for the thermal problem, we have

$$
\begin{aligned}
G_{\text{int}}^{\theta}(\delta\theta;\theta) &:= \int_{\mathcal{B}} -\nabla_x(\delta\theta) \cdot \hat{\boldsymbol{q}}_\theta \ dV\,, \\[2mm]
G_{\text{ext}}^{\theta}(\delta\theta;\theta) &:= \int_{\mathcal{B}} \delta\theta \,(\hat{\mathcal{H}}_\theta - \hat{f}_\theta)\ dV - \int_{\partial\mathcal{B}_h} \delta\theta\ \bar{h}_\theta\ dA\,.
\end{aligned}
\tag{3.40}
$$

The weighted Galerkin functionals are consistently linearized with respect to the field variables about their intermediate values $\tilde{\boldsymbol{u}}$, $\tilde{d}$, and $\tilde{\theta}$ to arrive at

$$
\begin{aligned}
\operatorname{Lin} G^u(\delta\boldsymbol{u};\boldsymbol{u},d,\theta)\big|_{\tilde{\boldsymbol{u}},\tilde{d},\tilde{\theta}} &:= G^u(\delta\boldsymbol{u};\tilde{\boldsymbol{u}},\tilde{d},\tilde{\theta}) \;+\; \Delta G^u = 0\,, \\[2mm]
\operatorname{Lin} G^d\big|_{\tilde{\boldsymbol{u}},\tilde{d},\tilde{\theta}} &:= G^d(\delta d,\tilde{\boldsymbol{u}},\tilde{d},\tilde{\theta}) \;+\; \Delta G^d = 0\,, \\[2mm]
\operatorname{Lin} G^\theta(\delta\theta;\theta)\big|_{\tilde{\theta}} &:= G^\theta(\delta\theta,\tilde{\theta}) \qquad\;+\; \Delta G^\theta = 0\,.
\end{aligned}
\tag{3.41}
$$

The incremental terms

$$
\begin{aligned}
\Delta G^u &:= \Delta G^u(\delta\boldsymbol{u};\tilde{\boldsymbol{u}},\tilde{d},\tilde{\theta};\Delta\boldsymbol{u},\Delta d,\Delta\theta) \\[2mm]
\Delta G^d &:= \Delta G^d(\delta d,\tilde{\boldsymbol{u}},\tilde{d},\tilde{\theta};\Delta\boldsymbol{u},\Delta d,\Delta\theta) \\[2mm]
\Delta G^\theta &:= \Delta G^\theta(\delta\theta,\tilde{\theta};\Delta\theta),
\end{aligned}
$$

derived through the Gâteaux derivative, can be expressed in terms of the external and internal functionals according to (3.37); that is,

$$
\Delta G^\gamma = \Delta G_{\text{int}}^\gamma - \Delta G_{\text{ext}}^\gamma \quad \text{with} \quad \gamma = u, d, \theta\,.
\tag{3.42}
$$

As stated in $(3.38)_1$, ΔG_{int}^u is obtained as

$$
\Delta G_{\text{int}}^u = \int_{\mathcal{B}} \delta\boldsymbol{\varepsilon} : \Delta\hat{\boldsymbol{\sigma}}\ dV
\tag{3.43}
$$

where the total stress increment can be expressed as

$$
\Delta\hat{\boldsymbol{\sigma}} = \mathbb{C}^{uu} : \Delta\boldsymbol{\varepsilon} + \boldsymbol{C}^{ud}\Delta d + \boldsymbol{C}^{u\theta}\Delta\theta\,,
\tag{3.44}
$$

where the fourth order tensor $\mathbb{C}^{uu}$ denotes the derivative of the total stress tensor with respect to the strain tensor $\boldsymbol{\varepsilon}$, and the second order tensors $\boldsymbol{C}^{u\theta}$ and $\boldsymbol{C}^{ud}$ are defined as the derivatives of the stress tensor with respect to the temperature and the crack phase-field, respectively,

$$
\mathbb{C}^{uu} := \partial_{\boldsymbol{\varepsilon}}\hat{\boldsymbol{\sigma}}\,, \quad \boldsymbol{C}^{ud} := \partial_d\hat{\boldsymbol{\sigma}} \quad \text{and} \quad \boldsymbol{C}^{u\theta} := \partial_\theta\hat{\boldsymbol{\sigma}}\,.
\tag{3.45}
$$

Based on these definitions, (3.43) can be recast into

$$\Delta G^{ru}_{\text{int}} \;=\; \int_{\mathcal{B}} \delta\boldsymbol{\varepsilon} : \mathbb{C}^{uu} : \Delta\boldsymbol{\varepsilon} \; dV + \int_{\mathcal{B}} \delta\boldsymbol{\varepsilon} : \boldsymbol{C}^{ud}\Delta d \; dV + \int_{\mathcal{B}} \delta\boldsymbol{\varepsilon} : \boldsymbol{C}^{u\theta}\Delta\theta \; dV \,.$$
(3.46)

Regarding the thermal part of the coupled problem, the increment of the internal functional is expressed as

$$\Delta G^{\theta}_{\text{int}} = \int_{\mathcal{B}} -\nabla_x(\delta\theta) \cdot \Delta\hat{\boldsymbol{q}}_{\theta} \; dV$$
(3.47)

where the increment of the heat flux vector can be written as

$$\Delta\hat{\boldsymbol{q}}_{\theta} = -\hat{\boldsymbol{K}} \cdot \nabla_x(\Delta\theta) \quad \text{where} \quad \hat{\boldsymbol{K}} := -\partial_{\nabla_x\theta}\hat{\boldsymbol{q}}_{\theta} = k_{\theta}\,\boldsymbol{1} \,.$$
(3.48)

In the latter the dependency of the heat flux on the crack phase field has been suppressed for the sake of conciseness. Moreover, the increment of the external thermal functional in terms of the temperature field comes out to be

$$\Delta G^{\theta}_{\text{ext}} := \int_{\mathcal{B}} \delta\theta \, (\Delta\hat{\mathcal{H}}_{\theta} - \Delta\hat{f}_{\theta}) \; dV$$
(3.49)

with the increment of the heating and viscous thermal resistance being

$$\Delta\hat{\mathcal{H}}_{\theta} = \underbrace{\partial_{\theta}\hat{\mathcal{H}}_{\theta}}_{T_{\theta}} \Delta\theta \quad \text{and} \quad \Delta\hat{f}_{\theta} = \underbrace{\partial_{\theta}\hat{f}_{\theta}}_{t_{\theta}} \Delta\theta \,.$$
(3.50)

In the case of the crack phase field, the increment of the corresponding functional is expressed as

$$\Delta G^{d}_{\text{int}} = \int_{\mathcal{B}} -\nabla_x(\delta d) \cdot \Delta\hat{\boldsymbol{q}}_{d} \; dV$$
(3.51)

where

$$\begin{aligned} \Delta\hat{\boldsymbol{q}}_{d} &= -\hat{\boldsymbol{D}} \cdot \nabla_x(\Delta d) - \hat{\boldsymbol{d}}\Delta\theta \\ \text{with} \quad \hat{\boldsymbol{D}} &:= -\partial_{\nabla_x d}\hat{\boldsymbol{q}}_{d} = G_c\, l\, \boldsymbol{1} \\ \text{and} \quad \hat{\boldsymbol{d}} &:= -\partial_{\theta}\hat{\boldsymbol{q}}_{d} = \partial_{\theta}G_c\, l\, \nabla_x d \,. \end{aligned}$$
(3.52)

Similarly, the increment of the external functional for the phase field fracture is given by

$$\Delta G^{d}_{\text{ext}} := \int_{\mathcal{B}} \delta d \, (\Delta\hat{\mathcal{H}}_{d} - \Delta\hat{f}_{d}) \; dV$$
(3.53)

where the increment of the crack driving force and the viscous crack resistance are introduced in the following form

$$\Delta\hat{\mathcal{H}}_{d} = -\boldsymbol{C}^{ud} : \Delta\boldsymbol{\varepsilon} + H_{\theta}\, \Delta\theta \quad \text{and} \quad \Delta\hat{f}_{d} = h_d\, \Delta d + h_{\theta}\, \Delta\theta$$
(3.54)

along with the tangent tensors

$$\boldsymbol{C}^{ud} := -\partial_{\boldsymbol{\varepsilon}} \hat{\mathcal{H}}_d = \partial_d \hat{\boldsymbol{\sigma}} \, , \ \ H_\theta := \partial_\theta \hat{\mathcal{H}}_d \ \ \text{and} \ \ h_d := \partial_d \hat{f}_d \, , \ h_\theta := \partial_\theta \hat{f}_d \, . \qquad (3.55)$$

The isoparametric finite element method is used to discretize the unknown fields in space to transform the integral-type weak forms (3.37) into a system of equations. The field variables of the coupled problem, the displacement $\boldsymbol{u}(\boldsymbol{x}, t)$, the temperature $\theta(\boldsymbol{x}, t)$, the crack phase field $d(\boldsymbol{x}, t)$ and the weight functions associated with these fields are interpolated over each finite element through

$$
\begin{aligned}
\delta \boldsymbol{u}_e^h &= \sum_{i=1}^{n_{en}} N^i \delta \boldsymbol{d}_i^e \, , \quad \delta d_e^h = \sum_{j=1}^{n_{en}} N^j \delta D_j^e \, , \quad \delta \theta_e^h = \sum_{k=1}^{n_{en}} N^k \delta T_k^e \, , \\
\boldsymbol{u}_e^h &= \sum_{l=1}^{n_{en}} N^l \boldsymbol{d}_l^e \, , \qquad d_e^h = \sum_{m=1}^{n_{en}} N^m D_m^e \, , \quad \theta_e^h = \sum_{n=1}^{n_{en}} N^n T_n^e \, .
\end{aligned}
\qquad (3.56)
$$

where n_{en} represents the number of nodes in each finite element. The spatial gradients of the weight functions can then be expressed as

$$
\begin{aligned}
\nabla_x(\delta \boldsymbol{u}_e^h) &= \sum_{i=1}^{n_{en}} \delta \boldsymbol{d}_i^e \otimes \nabla_x N^i \, , \\
\nabla_x(\delta d_e^h) &= \sum_{j=1}^{n_{en}} \delta D_j^e \otimes \nabla_x N^j \, , \\
\nabla_x(\delta \theta_e^h) &= \sum_{k=1}^{n_{en}} \delta T_k^e \otimes \nabla_x N^k \, .
\end{aligned}
\qquad (3.57)
$$

Likewise, the spatial gradient of the increment of the generalized displacement vector, the crack phase field, and the temperature field are given as

$$
\begin{aligned}
\nabla_x(\Delta \boldsymbol{u}_e^h) &= \sum_{l=1}^{n_{en}} \Delta \boldsymbol{d}_l^e \otimes \nabla_x N^l \, , \\
\nabla_x(\Delta d_e^h) &= \sum_{m=1}^{n_{en}} \Delta D_m^e \otimes \nabla_x N^m \, , \\
\nabla_x(\Delta \theta_e^h) &= \sum_{n=1}^{n_{en}} \Delta T_n^e \otimes \nabla_x N^n \, .
\end{aligned}
\qquad (3.58)
$$

Incorporating the discretized representations (3.56,3.57) in the integral expressions of

88

the weak form (3.37-3.40), we end up with the discrete residual vectors

$$\boldsymbol{R}_I^u = \mathop{\textbf{A}}_{e=1}^{n_{el}} \left\{ \int_{\mathcal{B}_e^h} \nabla_x N^i \cdot \hat{\boldsymbol{\sigma}} \ dV \ - \int_{\mathcal{B}_e^h} N^i \boldsymbol{b} \ dV - \int_{\partial \mathcal{B}_t^e} N^i \bar{\boldsymbol{t}} \ dA \right\} = \boldsymbol{0} \,,$$

$$R_J^d = \mathop{\textbf{A}}_{e=1}^{n_{el}} \left\{ - \int_{\mathcal{B}_e^h} \nabla_x N^j \cdot \hat{\boldsymbol{q}}_d \ dV \ - \int_{\mathcal{B}_e^h} N^j (\hat{\mathcal{H}}_d - \hat{f}_d) \ dV \right\} = 0 \,,$$

$$R_K^\theta = \mathop{\textbf{A}}_{e=1}^{n_{el}} \left\{ - \int_{\mathcal{B}_e^h} \nabla_x N^k \cdot \hat{\boldsymbol{q}}_\theta \ dV \ - \int_{\mathcal{B}_e^h} N^k (\hat{\mathcal{H}}_\theta - \hat{f}_\theta) \ dV \right\} = 0 \,,$$

$$(3.59)$$

where the operator $\textbf{A}$ designates the standard assembly of element contributions at the local element nodes $i, j, k = 1, ..., n_{en}$ to the global residuals at the global nodes $I, J, K = 1, ..., n_{nd}$ of a mesh with n_{nd} nodes. Likewise, the tangent matrices arising from the linearization of the residual vectors can be expressed as

$$\boldsymbol{K}_{IL}^{uu} = \mathop{\textbf{A}}_{e=1}^{n_{el}} \left\{ \int_{\mathcal{B}_e^h} \nabla_x N^i \cdot \hat{\mathbb{C}}^{uu} \cdot \nabla_x N^l \ dV \right\} \,,$$

$$\boldsymbol{K}_{IM}^{ud} = \mathop{\textbf{A}}_{e=1}^{n_{el}} \left\{ \int_{\mathcal{B}_e^h} (\nabla_x N^i \cdot \hat{\boldsymbol{C}}^{ud}) N^m \ dV \right\} \,,$$

$$\boldsymbol{K}_{IN}^{u\theta} = \mathop{\textbf{A}}_{e=1}^{n_{el}} \left\{ \int_{\mathcal{B}_e^h} (\nabla_x N^i \cdot \hat{\boldsymbol{C}}^{u\theta}) N^N \ dV \right\} \,,$$

$$\boldsymbol{K}_{JL}^{du} = \mathop{\textbf{A}}_{e=1}^{n_{el}} \left\{ \int_{\mathcal{B}_e^h} N^j (\boldsymbol{C}^{ud} \cdot \nabla_x N^l) \ dV \right\} \,,$$

$$K_{JM}^{dd} = \mathop{\textbf{A}}_{e=1}^{n_{el}} \left\{ \int_{\mathcal{B}_e^h} \nabla_x N^j \cdot \hat{\boldsymbol{D}} \nabla_x N^m \ dV - \int_{\mathcal{B}_e^h} N^j (H_d - h_d) N^m \ dV \right\} \,,$$

$$K_{JN}^{d\theta} = \mathop{\textbf{A}}_{e=1}^{n_{el}} \left\{ \int_{\mathcal{B}_e^h} \nabla_x N^j \cdot \hat{\boldsymbol{d}} N^n \ dV - \int_{\mathcal{B}_e^h} N^j (H_\theta - h_\theta) N^n \ dV \right\} \,,$$

$$K_{KN}^{\theta\theta} = \mathop{\textbf{A}}_{e=1}^{n_{el}} \left\{ \int_{\mathcal{B}_e^h} \nabla_x N^k \cdot \hat{\boldsymbol{K}} \nabla_x N^n \ dV - \int_{\mathcal{B}_e^h} N^k (T_\theta - t_\theta) N^n \ dV \right\} \,.$$

$$(3.60)$$

Denoting the overall residual vector as a combination of the residual vectors of the

associated sub-problems as $\boldsymbol{\mathcal{R}} := [\boldsymbol{R}^u \ \boldsymbol{R}^d \ \boldsymbol{R}^\theta]^T$ and the nodal unknowns as $\boldsymbol{\mathcal{D}} :=$ $[\boldsymbol{d} \ \boldsymbol{D} \ \boldsymbol{T}]^T$, the Newton update equation for the nodal degrees of freedom can be expressed as

$$\boldsymbol{\mathcal{D}} = \bar{\boldsymbol{\mathcal{D}}} - \bar{\boldsymbol{\mathcal{K}}}^{-1} \cdot \bar{\boldsymbol{\mathcal{R}}} \tag{3.61}$$

where $\bar{\boldsymbol{\mathcal{R}}} := \boldsymbol{\mathcal{R}}(\bar{\boldsymbol{\mathcal{D}}})$, $\bar{\boldsymbol{\mathcal{K}}} := \boldsymbol{\mathcal{K}}(\bar{\boldsymbol{\mathcal{D}}})$ indicate the global residual vector and the global coupled tangent matrix, respectively. The global coupled tangent matrix in terms of the sub-tangent matrices is expressed as

$$\boldsymbol{\mathcal{K}} := \begin{bmatrix} \boldsymbol{K}^{uu} & \boldsymbol{K}^{ud} & \boldsymbol{K}^{u\theta} \\ \boldsymbol{K}^{du} & \boldsymbol{K}^{dd} & \boldsymbol{K}^{d\theta} \\ \boldsymbol{0} & \boldsymbol{0} & \boldsymbol{K}^{\theta\theta} \end{bmatrix}.$$

3.4 Representative Numerical Examples

In this section, the illustrative numerical examples are demonstrated to validate the primary properties and capabilities of the proposed formulation. The numerical examples are devoted to the unified phase-field damage model with the anisotropic formulation to simulate the quasi-brittle failure in concrete specimens, under coupled chemo-thermomechanical effects. In the illustrated numerical examples, unstructured piece-wise linear triangular and quadrilateral elements are employed to discretize the computational domain. Only the sub-domains close to the crack surface require a specific minimum element size to resolve the length scale (ℓ) in the finite element approximation. Indeed, the uniformity of meshes affects the approximation quality of the surface energy. Therefore, a posteriori re-meshing domain will enhance the precision of the energy estimation. For that reason, the length scale (ℓ) affects the materialistic response and the solution convergence strongly so the element sizes are chosen inevitably much smaller than the internal length scale (ℓ).

We employ the proposed material model to investigate the crack initiation and propagation in the Roller-Compacted-Concrete (RCC) dam under thermal loading. In this case, the effect of the material constants corresponding the hydration process and the environmental temperature on the thermally-induced cohesive fracture is investigated.

The staggered scheme is employed to solve the discretized governing equations related to the mechanical, thermal and phase-field part of the boundary-value problem.

In massive concrete structures, excessive cement content generates comparatively high heat of hydration. Indeed, the lower thermal conductivity of concrete causes thermal gradients near the surfaces ascribed to heat convection phenomena between the interior and the exterior side of the structure.

In this example, we exceptionally focus on the case for RCC dams. In contrast to the conventional concrete dams, the RCC dams require simple design and construction concepts, and they are economically competitive. The simplicity of the RCC dam construction leads to a reduction in the construction time and allow for a higher production rate. However, the primary difference between RCC and conventional concrete is the low cement content and the no-slump consistency of the former which considerably reduce the latent heat of hydration, up to approximately one-third conventional types of concrete. Nevertheless, a remarkable temperature rise may be still observed due to the high concreting rate practiced in RCC dams.

In the current examples, we first conduct a chemo-thermo-mechanical analysis to capture the temperature evolution in RCC dams under the various ambient temperatures at early ages. In [23], a three-dimensional chemoplastic material model was implemented to simulate early-age cracking in the RCC dam. The crack risk analyses are conducted in the framework of chemoplasticity model for concrete. On the other hand, we here apply the proposed approaches to capture the risk of early-age cracking in the RCC dam; however, the plastic strains are neglected in the current analyses as we explicitly account for cracking. However, the effects related to the autogenous shrinkage and transitional thermal creep are considered. The geometry, the dimensions and the boundary conditions of the RCC dam are represented in Figure 3.3.

The total height of the dam is 37.8 m and its width at the bottom is 29 m. The construction phases contain the bottom, middle, and top parts whose construction takes 42 days, 21 days, and 14 days, respectively. The dam is discretized by means of totally 80,250 four-node quadrilateral plain strain elements. The material properties, taken from [23, 116] are presented in Table 3.2. To model the connection between the
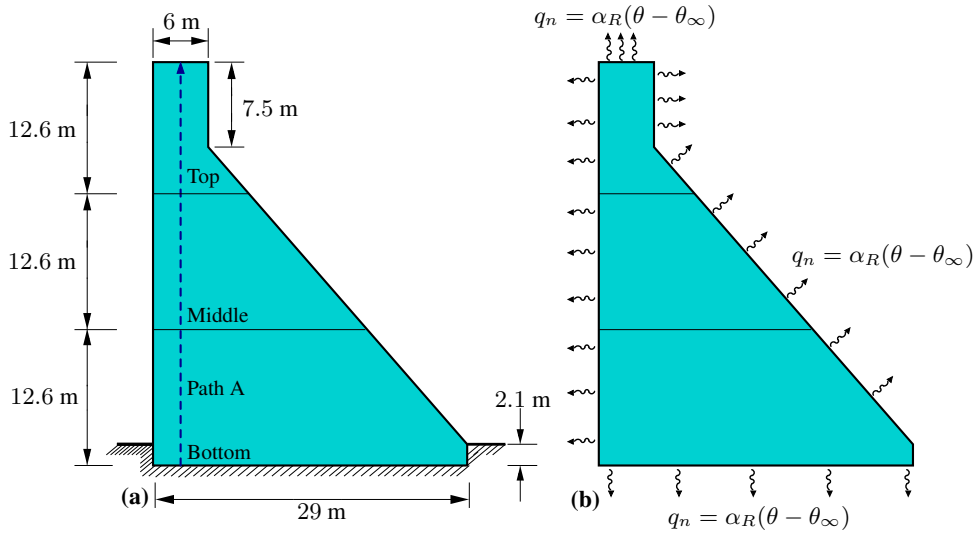
Figure 3.3: RCC dam. **(a)** Geometry, dimensions and mechanical boundary conditions and **(b)** thermal boundary conditions.

interior and exterior of the dam at the RCC-air and the rock-air the boundary of the finite element model, the convective heat flux is defined as $q_n = \alpha_R(\theta - \theta_\infty)$, with α_R is the corresponding surface conductance calculated as a function of wind speed and depends on either roughness or smoothness of surface at solid-air interfaces. In this case, this coefficient is taken as $\alpha_R = 4$ J/(s m^2 K) for the RCC-air interfaces and as $\alpha_R = 20$ J/(s m^2 K) for the RCC-rock interfaces [117].

In this study, totally five representative numerical examples are presented. In the first three examples, RCC1, RCC2, RCC3, the existence of the convective heat exchange at the crack faces is not considered. However, in comparison with RCC1, the ambient temperature is dropped by 10°C in RCC2 and the latent heat of hydration is kept constant, and in RCC3, in addition to ambient temperature dropped by 10°C, the latent heat of hydration is increased by 50%. In the succeeding two examples, RCC4, RCC5, the examples RCC2 and RCC3 are repeated by incorporating the convective heat exchange at crack faces.

In the current study, to prevent the sudden cracking of the middle and the top lifts of the dams at the onset of their analyses during the construction process, a novel multifield interface element is developed between the concrete lifts. This element provides a contact between the nodes located at the discontinuities between the lifts

Table 3.2: Material properties of RCC used in the coupled phase-field chomo-thermo-mechanical analysis [23, 116]

Parameter	Unit	Definition	Equation	Value
Hydration				
ξ_0	[–]	Percolation threshold	(3.13)	0.01
E_a/R	[K]	Normalized activation energy	(3.13)	4×10^3
a, b, c	[–]	Chemical affinity parameters	(3.34)	$57.0, 0.75, 7.05$
Mechanical				
E_∞	[N/mm^2]	Final Young's modulus	(3.35)	22×10^3
ν	[–]	Poisson's ratio	(3.36)	0.15
f_c^∞	[N/mm]	Final compressive strength	(3.35)	13.6
Phase-Field				
G_c^∞	[N/mm]	Final critical energy release rate	(3.29)	0.06
ℓ	[mm]	Internal length scale	(3.29)	275
c_0	[-]	Scaling parameter	(3.29)	π
Thermal				
c	[kJ/(K kg)]	Specific heat capacity	(3.31)	2500
k_θ	[J/(K m s)]	Thermal conductivity	(3.33)	1.679
α	[1/K]	Thermal expansion coefficient	(3.22)	8.33×10^{-6}
L_ξ	[J/m^3]	Latent heat of hydration	(3.14)	45×10^3
h_c	[J/(s m^2 K)]	Convective heat exchange coefficient	(3.32)	0.0
Creep and shrinkage				
κ	[-]	Autogenous shrinkage coefficient	(3.22)	45×10^{-6}
λ^{ttc}	[-]	Transitional thermal creep coefficient	(3.22)	0.08

of the dam, Figure 3.3 to enforce the displacement field and the temperature field to be transferred across these discontinuities. However, the interface element ensures debonding between the crack phase-field of the nodes across the discontinuities.

In the first example (RCC1), the ambient temperature is set to $\theta_\infty = 15$ °C. The initial temperatures of RCC and rock are $\theta_0 = 20$ °C and $\theta_0 = 10$ °C. The latent heat of hydration per unit volume of low-paste RCC referred to as RCC 90 is defined

Figure 3.4: `RCC1`: The crack phase-field, the temperature field, and the maximum principal stress distribution without convective heat exchange at the cracks in RCC dam.

as the amount of latent heat of an RCC material with a cementitious content of 90 kg/m^3, so $Q_\xi = 90 \times 500 = 45 \times 10^3$ kJ/m^3, where 500 kJ/kg declares the latent heat of 1 kg cementitious material. Figure 3.4 illustrates the results associated with the distributions of the crack phase-field, the temperature and the maximum principal stress at the end of the construction phase of each part of the RCC dam without considering a convective heat exchange at the free crack surfaces.
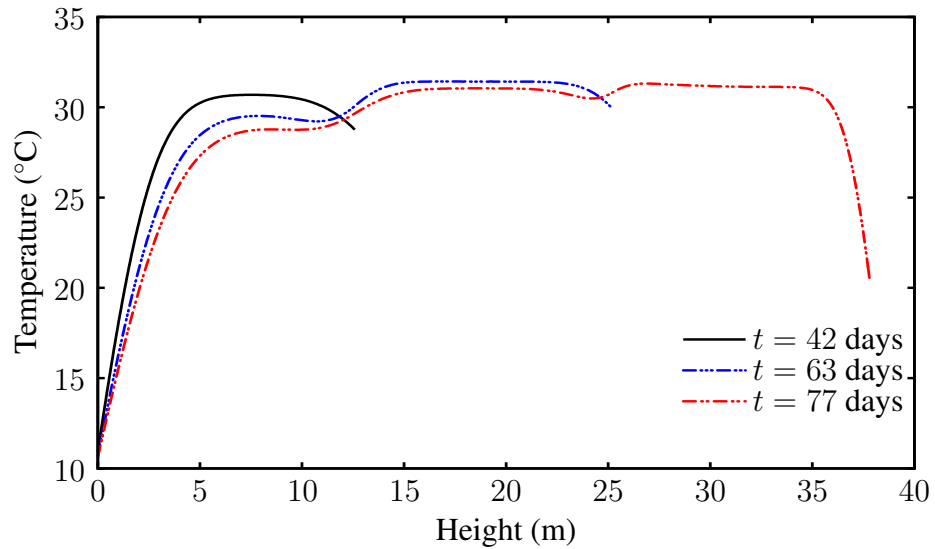
Figure 3.5: RCC1: Temperature evolution along Path A at the end of the construction of each part.

The maximum principal stress under the coupled chemo-thermo-mechanical effects at the end of the construction is bounded by the tensile strength at complete hydration, $\xi = 1$. Regarding the results obtained, the thermally-induced cracking is observed at the bottom and along the downstream side faces of the dam when the maximum principal stress reaches the tensile strength of concrete at that moment. According to the results obtained in the literature, due to the geometric properties of the RCC dam, it leans towards its upstream face. The placing speed is another factor affects the temperature distribution and evolution. At a faster of speed placing, the loss of hydration heat may decrease due to less time allowed for thermal conduction on the boundaries of the dam. By comparing the temperature distribution among the three different parts of the dam, it may be deduced that a greater area is cooled down in the bottom part than the other parts at the end of 77 days.

Also, the evolution of the temperature field during the construction process along Path A, see Figure 3.3, is represented in Figure 3.5 at the end of the construction of each part. The results show that the maximum temperature, evolved in each part decreases by passing the time until the end the construction.

In the second example (RCC2), the effect of the ambient temperature θ_∞ is investigated, so it is dropped by $10°$C. The results regarding the distribution of the temper-
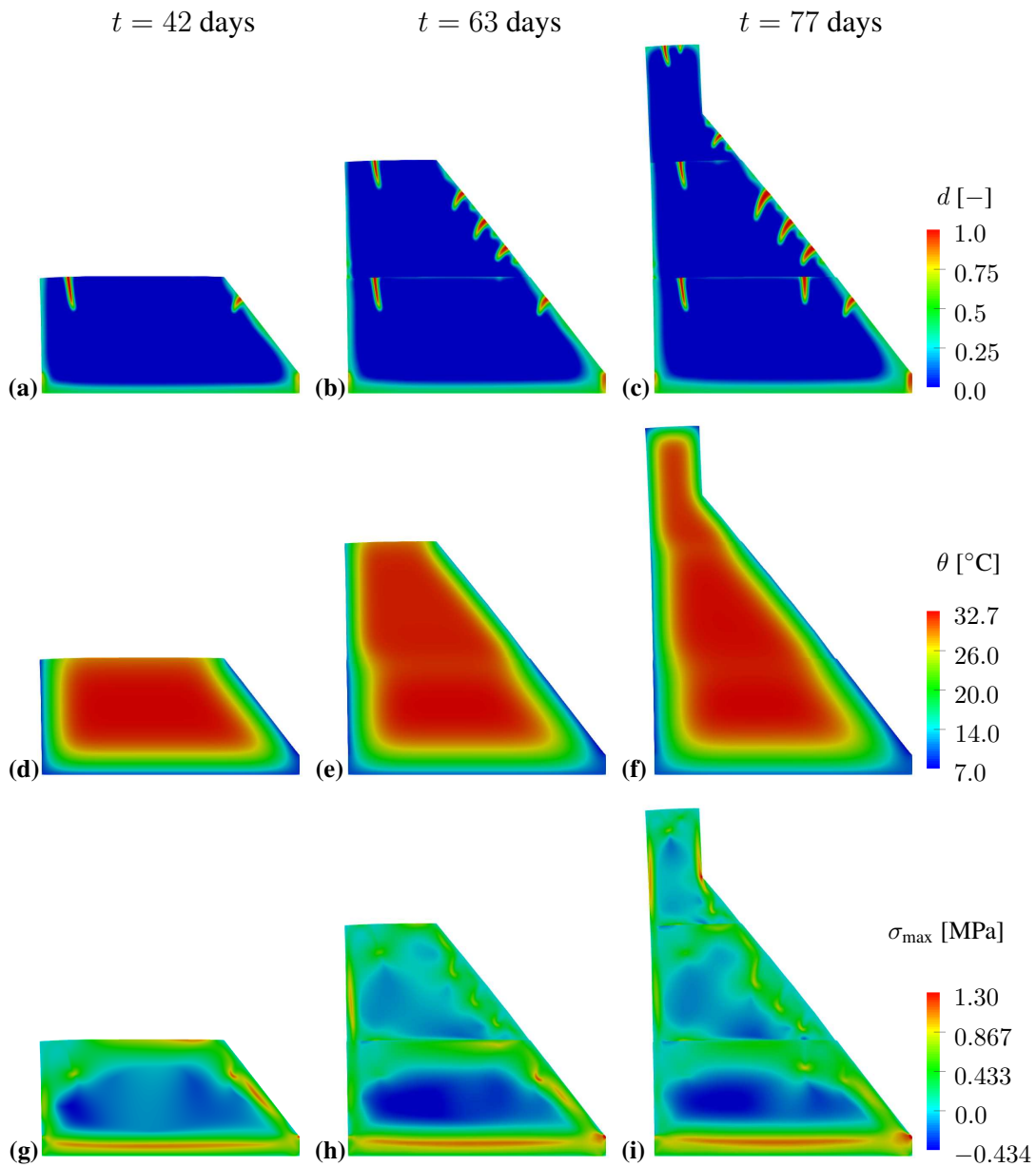
Figure 3.6: `RCC2`: The crack phase-field, the temperature field, and the maximum principal stress distribution without convective heat exchange at the cracks in RCC dam

ature field, the crack phase-field and the maximum principal stress is represented in Figure 3.6. The results describe that by decreasing the ambient temperature a higher temperature gradient is established between the interior and exterior of the dam, and in comparison with `RCC1` a greater part of the internal area is cooled down. These effects consequently induce higher stresses that are greater than the instant tensile strength of concrete at the RCC-air boundaries so a greater region of the dam experi-
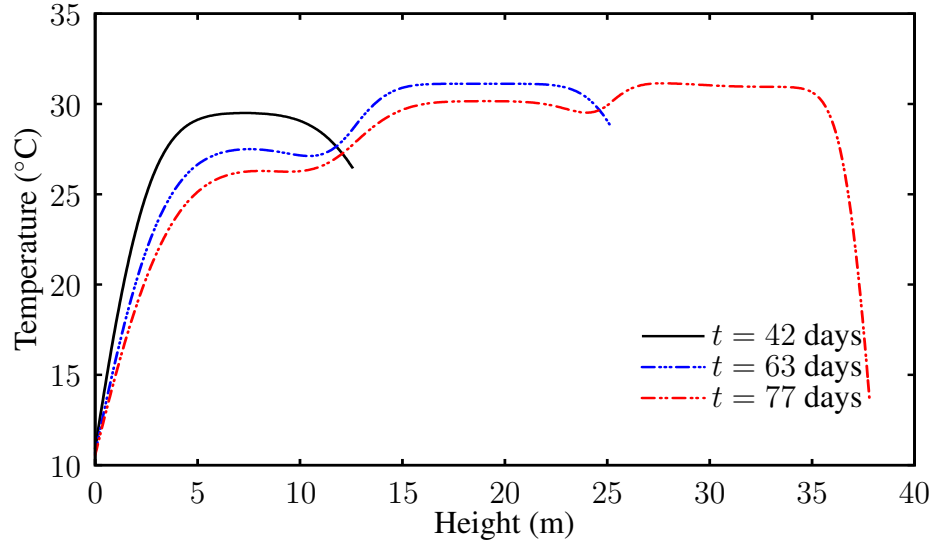
Figure 3.7: `RCC2`: Temperature evolution along Path A at the end of the construction of each part.

ences cracking.

Moreover, the evolution of the temperature field during the construction process along Path A, see Figure 3.3, are represented in Figure 3.7 at the end of the construction of each part. The results represent that by decreasing the ambient temperature by $10°C$ i.e. $\theta_\infty = 5°C$ comparing to the previous example `RCC1`, the maximum temperature within the parts decreased by about $5°C$. Also, the maximum temperature evolved within the dam decreases during the construction process. This decrease is a little bit grater than that obtained in the previous example.

Additional analysis is conducted to investigate simultaneously the effect of the ambient temperature θ_∞ and latent heat of hydration Q_ξ (`RCC3`). For this purpose, The ambient temperatures decreased by $10°C$ i.e. $\theta_\infty = 5°C$, and the latent heat of hydration is increased by 50% ($Q_\xi = 67.5$ kJ/m^3). The higher latent heat of hydration increases the internal temperature at the end of the dam construction. The higher temperature, on the other hand, and the lower ambient temperature cause higher temperature gradient in comparison to the first and second examples (`RCC1` and `RCC2`). The maximum principal stress reaches the instant tensile strength of concrete, so a greater area near to the boundaries, especially at the downstream, is subjected to cracking. In Figure 3.8, the distributions of the crack phase-field, the temperature field, and the

97
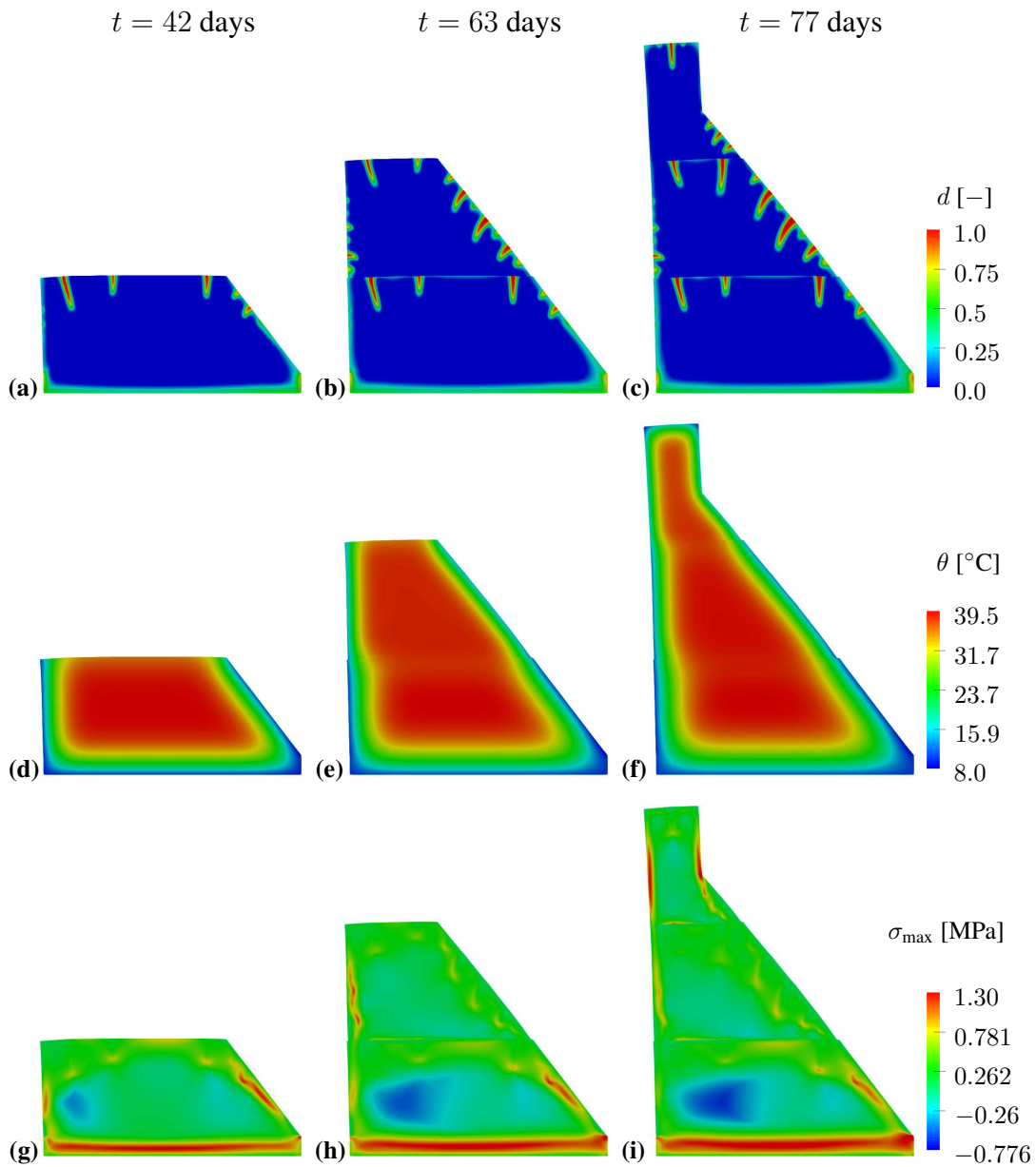
Figure 3.8: RCC3: The crack phase-field, the temperature field, and the maximum principal stress distribution without convective heat exchange at the cracks in RCC dam.

maximum principal stress are respectively depicted.

Furthermore, the evolution of the temperature field during the construction process along Path A, see Figure 3.3, are represented in Figure 3.9 at the end of the construction of each part. The results demonstrate that by increasing the latent heat of hydration, the maximum temperature reached within the dam increases in comparison
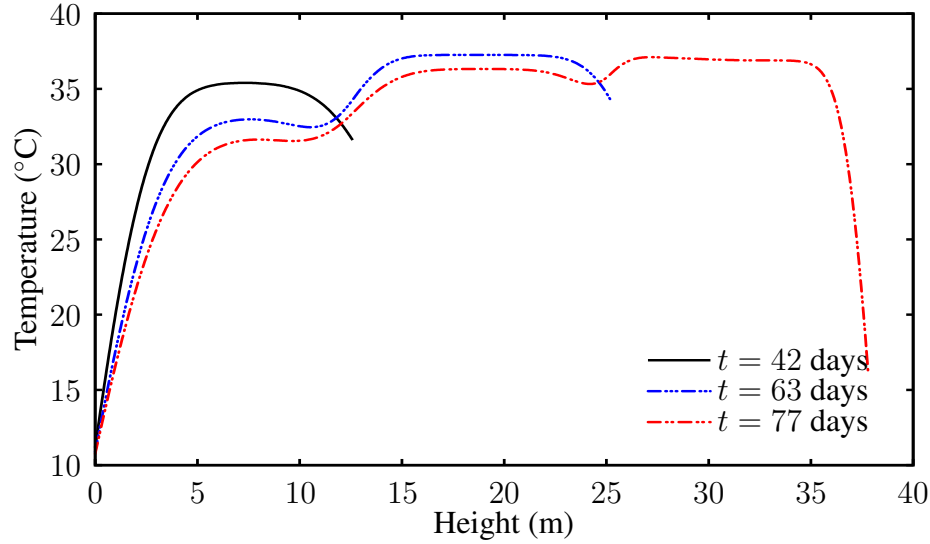
Figure 3.9: `RCC3`: Temperature evolution along Path A at the end of the construction of each part.

to the first (`RCC1`) and second (`RCC2`) examples. Also, the maximum temperature evolved at the end of the construction of each part decreases by about 1 and the temperature is decreased by $3°C$ at the boundaries by passing the time until the end of the construction process.

In the following, the effect of the crack phase-field on the temperature evolution through a convective heat exchange at crack faces, and the thermal conductivity are investigated by conducting additional analyses. For this purpose, in the fourth example (`RCC4`) the convection is activated by setting a convective heat exchange coefficient $h_c = 2.5$ J/(sm^{2}K) in (3.32), and the second example (`RCC2`) is reanalyzed, where the ambient temperature is dropped by $10°C$ i.e. $\theta_\infty = 5°C$. The results associated with the distributions of the crack phase-field, the temperature and maximum principal stress are presented respectively in Figure 3.10.

In Figure 3.11 the evolution of the temperature field during the construction process along Path A, see Figure 3.3, is depicted. The results validate that by considering a convective heat exchange, the body initiates to be cooled down along the crack path, and this sever reduction in the temperature is observed along the specified path on the height of the dam.

In the last example (`RCC5`), we repeat the third example (`RCC3`) by considering the
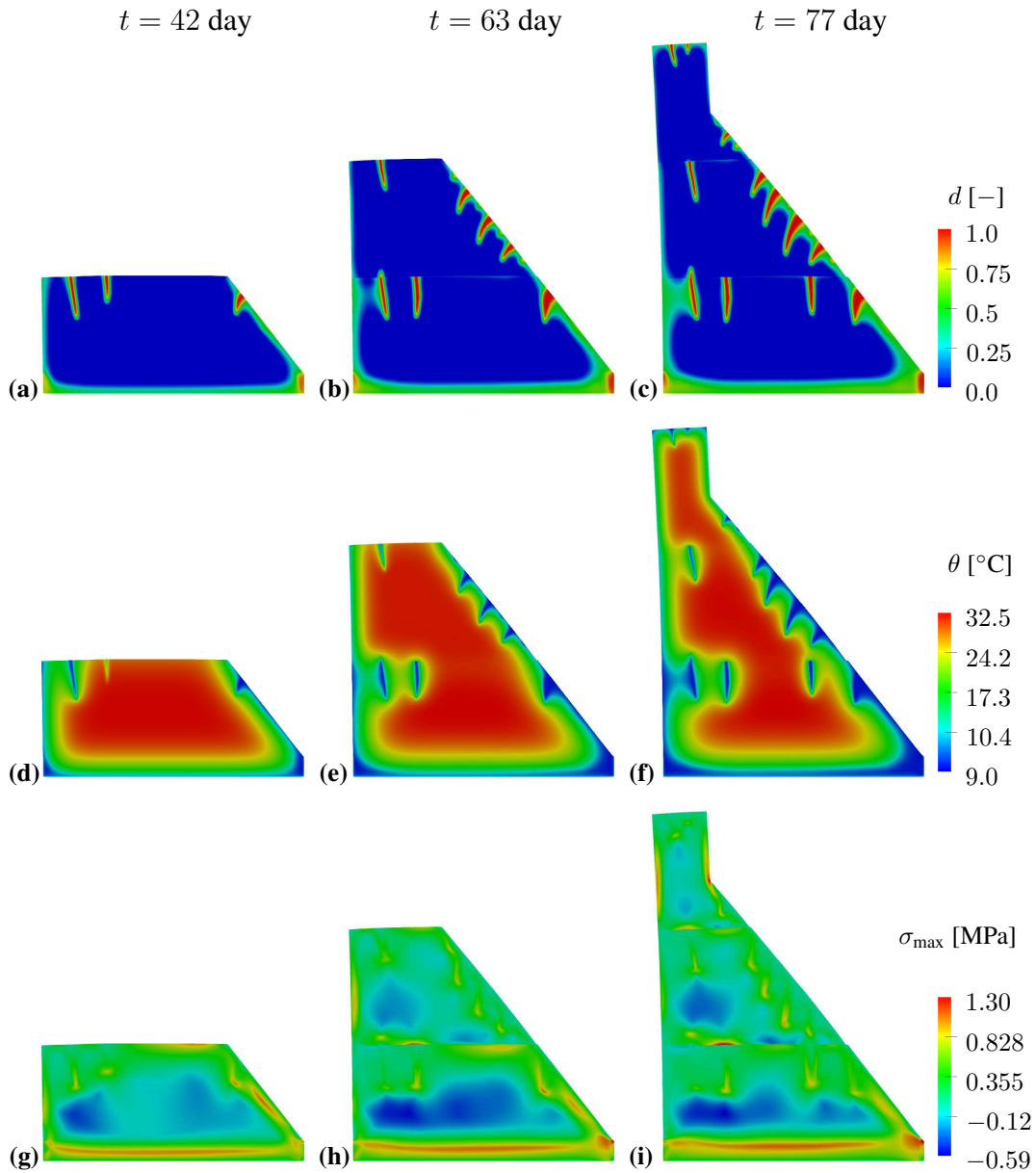
Figure 3.10: `RCC4`: The crack phase-field, the temperature field, and the maximum principal stress distribution with convective heat exchange at the cracks in RCC dam.

convective heat exchange at crack faces $h_c = 2.5 \text{ J/(s m}^2 \text{ K)}$ in (3.32) and degrading thermal conductivity to investigate the coupled effects of the ambient temperature and latent heat of hydration on the distribution and evolution of the temperature and crack phase-field also their mutual effect on each other. In Figure 3.12 the results relating to the distributions of the crack phase-field, the temperature field and the maximum principal stress are shown.
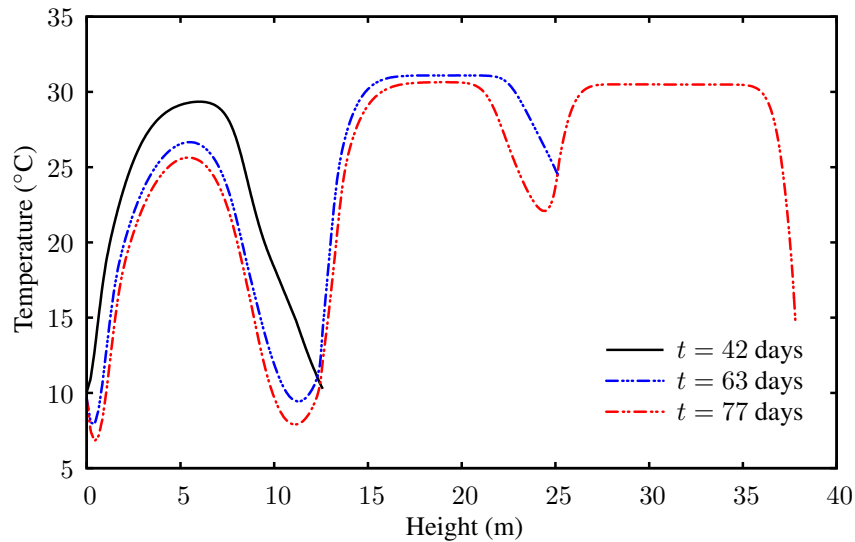
Figure 3.11: `RCC4`: Temperature evolution along Path A at the end of the construction of each part.

In Figure 3.13 the evolution of the temperature field during the construction process along Path A, see Figure 3.3, are visualized. By applying a convective heat exchange along the crack surfaces, decreasing the ambient temperature, and increasing the latent heat of hydration, although the maximum temperature within the dam increases, the temperature is severely decreases at the boundary and along the crack surfaces.

Concerning the results obtained through the chemo-thermo-mechanical framework coupled with the cohesive zone phase-field approach, it is observed that the increase in the latent heat of hydration by 50% leads to increase the internal temperature up to $39.5°$C in comparison with `RCC1` state at which it is up to $32.8°$C. On the other hand, the decrease in the ambient temperature by $10°$C causes a greater part of the dam's internal area to be cooled down. These effects increase the temperature gradient between the interior and exterior parts of the dam. A more significant temperature gradient induces higher tensile stresses at the RCC-air boundaries, so cracking initiates when these stresses reach the instant tensile strength of concrete. Cracking at the dam boundaries may justify a convective heat exchange at crack faces and affect the thermal conductivity. Therefore, additional analyses are conducted on this purpose. The results show that by considering the convection and degrading thermal conductivity, the body of the dam is cooled down through the crack faces. By comparing the results of `RCC2` and `RCC3` with the results of `RCC4` and `RCC5`, it can be easily

101

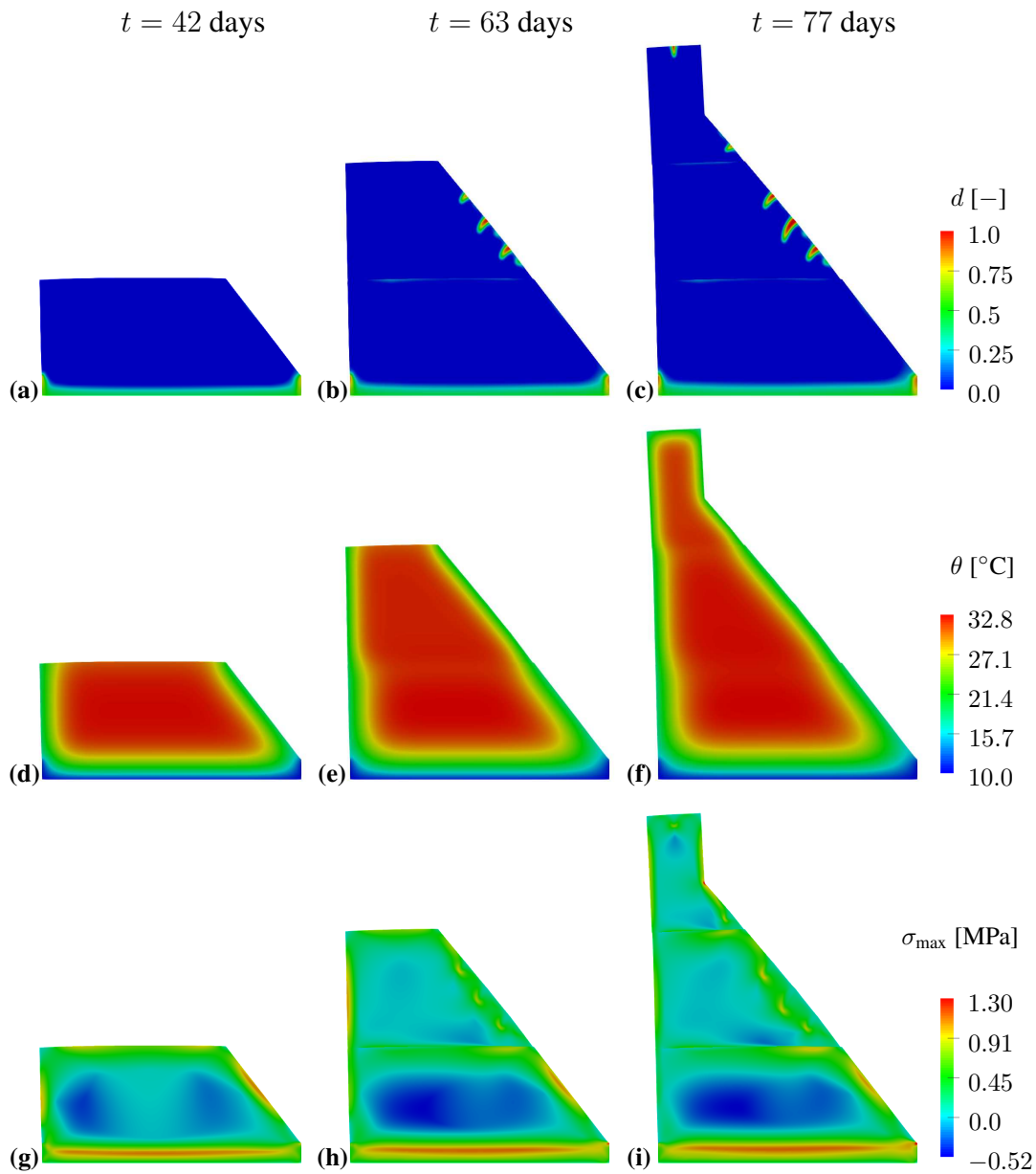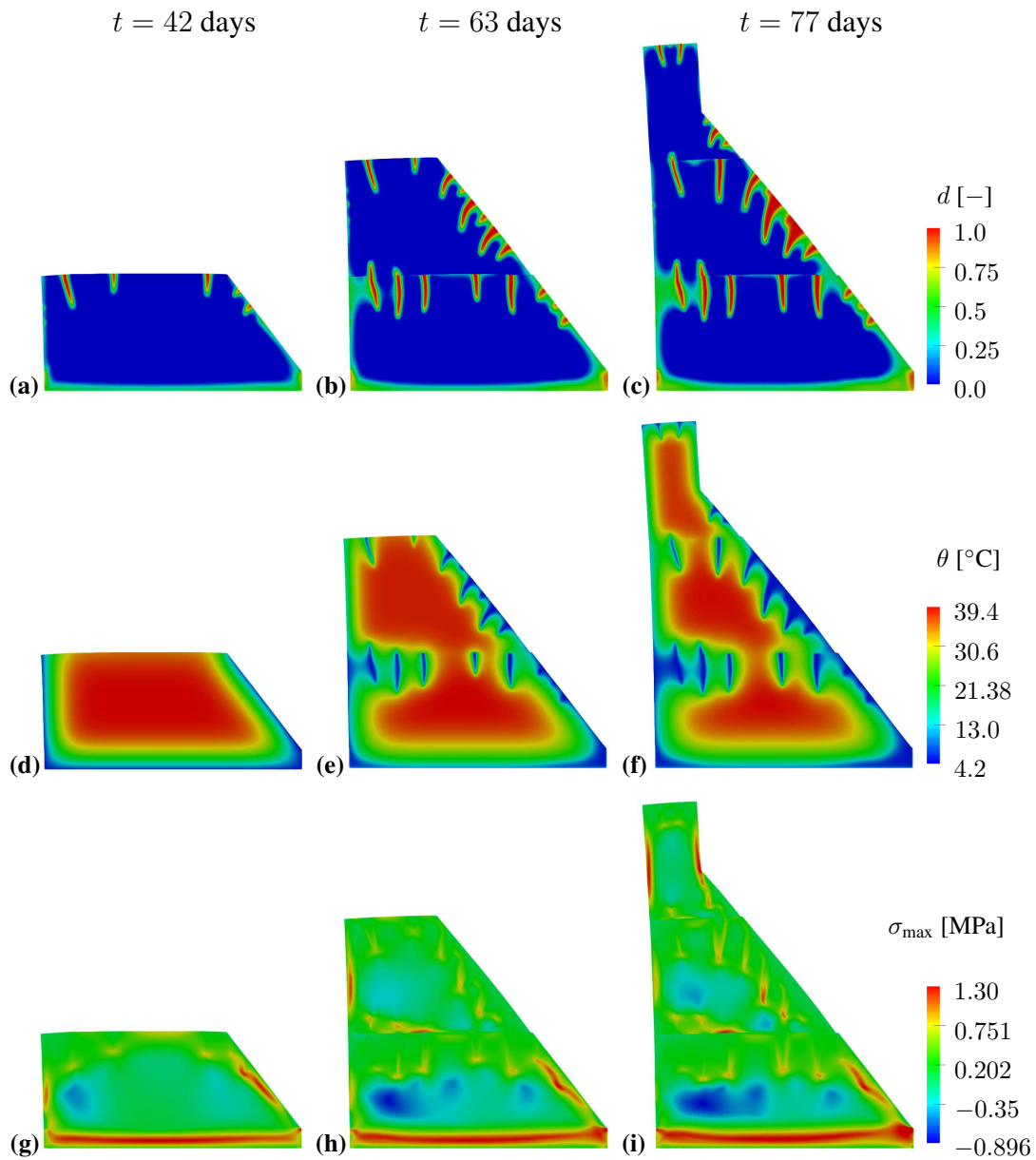Figure 3.12: RCC5: The crack phase-field, the temperature field, and the maximum principal stress distribution with convective heat exchange at the cracks in RCC dam.

observed that at the crack faces due to the convective heat exchange, the body starts to cool down, and both the maximum and minimum temperature decrease. Also, the reduction in thermal conductivity due to degradation can increase the risk of early-age cracking.
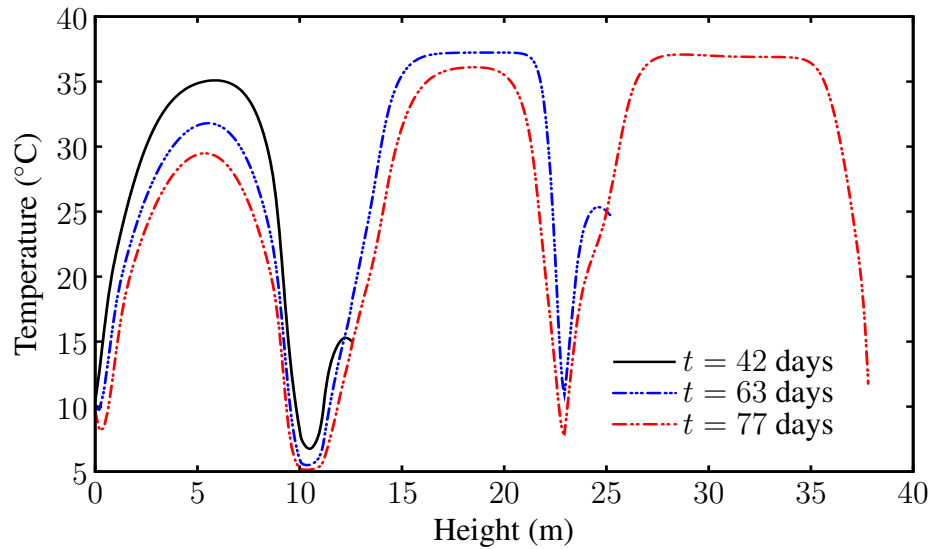
Figure 3.13: `RCC5`: Temperature evolution along Path A at the end of the construction of each part.

3.5 Concluding Remarks

In this study, a coupled chemo-thermo-mechanical model along with the cohesive zone, the phase-field approach is developed for the simulation of early-age cracking of concrete. The proposed coupled chemo-thermo-mechanical model evaluates the evolution of the mechanical properties of concrete during the hydration process. Furthermore, the cohesive zone phase-field approach is applied to predict the possibility of cracking under chemo-thermo-mechanical effects at early ages accounting for the consequence of the ambient temperature and the latent heat of hydration on the temperature, the maximum principal stress, and the crack phase-field distribution in RCC dam. Contrary to the existing phase-field model in the literature which have been developed for the brittle failure in the solids, in this study the cohesive zone phase-field model used for the material like concrete by incorporating a general softening law frequently adopted for quasi-brittle failure.

The capability of this type of phase-field model is illustrated and validated by a number of representative numerical examples. In the phase-field models applied to the brittle crack propagation, the overall global response of the material intrinsically depends on the internal length scale parameter and the mesh size which dominate the

103

maximum load at the time of crack initiation. Adoption of the phase field regularized cohesive zone model decreases the sensitivity of the results to the value of the length scale parameter. This phase field theory is extended to the coupled multi-physics problems in a real structural scale to investigate the bulk material cracking under complex multi-field material response accounting for a chemo-thermomechanically-induced effects involving temperature evolution during the hydration process, heat transport owing to the conduction at the boundaries and convection at the free crack surfaces. In this study, five examples are represented in the case of the RCC dam to investigate the effect of ambient temperature, latent heat of hydration, and convective heat exchange at the crack faces. By decreasing the ambient temperature and increasing the latent heat of hydration a greater part of the dam subjected to cracking. This effect is attributed to the higher temperature gradient between the interior and exterior part of the dam. The convective heat exchange at the crack faces is expressed as an additional heat sink causing heat loss at the crack faces. The results obtained in this study agrees well with the findings reported in the work of Lackner and Mang [23].

CHAPTER 4

A PORO-VISCOELASTIC MODEL FOR DRYING SHRINKAGE AND CREEP IN CONCRETE

4.1 Introduction

This chapter is concerned with the theoretical and computational modeling of drying shrinkage and creep in hardening and mature concrete at early ages and beyond. The associated formulations are conducted by developing a coupled constitutive modeling approach, which is furnished by the robust multi-physics computational tools within the framework of poroviscoelasticity. In the literature, the majority of the relevant works are associated with the determination of shrinkage-induced volumetric strain, based on purely empirical data, through the coefficient of hygral contraction analogous to the coefficient of thermal expansion in the coupled thermo-mechanical problems. The corresponding hygral contraction coefficient is described as a linear, or hyperbolic function of the internal relative humidity [118]. In contrast, we employ a physically motivated technique where the pore pressure is obtained as a function of the water content that is determined using sorption-desorption equations for a given value of the local relative humidity. This equation, which is a fundamental aspect of the drying process, allows us to relate the internal relative humidity and the evaporable water content in pores. Therefore, the proposed model accounts for the hygro-chemo-mechanical cross-coupling effects between the shrinkage-induced strain development due to the pressure evolution through humidity variations and the stress concentrations in hardening and hardened viscoelastic concrete.

At early ages of concrete, several physicochemical phenomena such as hydration, shrinkage, and creep occur at the same time. Therefore, their effects may not be

straightforwardly decoupled. The computational modeling will equip us to investigate the response of the concrete elements individually, subject to the shrinkage and creep phenomenal at early ages and beyond. In contrast to the existing studies in literature, the proposed model provides almost accurate formulations without anymore requirement for any experimentally based and the empirical equation describing the shrinkage-induced volumetric strain. Consequently, the comparison of the numerical examples with experiments demonstrates the excellent predictive capacity of the proposed model.

In a cementitious material, the moisture content is an essential parameter, which strongly governs the full treatment of the physio-chemical aspect of hydration process and aging effect. Therefore, the determination of the moisture distribution mechanism within concrete is practically important to obtain a better investigation of the durability phenomena related to the moisture variation induced by the hydration process itself and the environmental conditions. When concrete comes into a general definition, it is characterized as a multi-phase composite material, consisting of aggregates embedded in a matrix of mortar [119]. The matrix of mortar is composed of fine aggregates embedded in the cement paste. Volume changes in concrete induced by either the thermal or the hygral effects are predominantly dependent on the behavior of the hydrated cement paste. During the course of the hydration process, the capillary pores are formed as a residue of the spaces filled by water. Apart from the capillary pores, the water-filled gel pores form within the cement paste. The total mass of water per unit volume of the material consists of adsorbed water, capillary water, hindered adsorbed water, and a negligible mass of vapor. Therefore, any cementitious material is defined as a hydrophilic porous material that contains a wide range of pores of different and their structures evolving with age. Therefore, the moisture transport within concrete is complicated. Indeed, several physicochemical processes occuring especially at early ages, and also, a long-term state of concrete that govern creep and shrinkage.

In cementitious-based composite materials the recognition of corresponding hygro-chemo-mechanical behavior such as creep and shrinkage, and fracture regarding the initiation and propagation of micro-cracks require a comprehensive theoretical description. This encompasses the coupling between these phenomena occuring simul-

taneously and expresses their effects on concrete behavior in detail. In cementitious materials, shrinkage is generally associated with loss of water in either hardening or hardened state. This moisture transport occurs when concrete is brought into contact with the environment possessing a lower relative humidity than one in its own pore system. On the other hand, creep is another time-dependent phenomenon, observed during short- and long-term state of concrete when it is subjected to a constant mechanical loading, aging effects, and variation of interior water content.

Basic creep and drying creep (Pickett effect) are two extensively used terminologies which particularize creep as the time-dependent deformation that occur when concrete is loaded in a sealed condition while the moisture is not allowed to escape and when concrete under load is allowed to dry in response to the different environmental conditions, respectively. Creep has recoverable and irreversible components, when concrete is unloaded, although the elastic strain is completely recovered, the accumulated creep strain is partially recovered. The composition and type of Portland cement and admixtures, the type of aggregates, the water/cement ratio, the relative humidity of the place where the concrete is stored for curing, temperature, the strength of concrete, state of stress, age, and the size of concrete specimen are of considerable important factors that effect the creep response of concrete [119]. Among these variables, relative humidity and temperature are governed by the environmental conditions. The others can be classified as the intrinsic characteristics of concrete. The effects of the temperature and the humidity variation are investigated both experimentally and numerically.

In the literature, there is a variety of experimental and numerical studies focused on the understanding the creep and shrinkage phenomena. Most of the numerical studies have used the microprestress-solidification theory to investigate the effect of the aging due to continuing cement hydration process and the effects of the environmental conditions such as the temperature and the relative humidity to describe creep response of concrete. The numerical modeling of early age creep of ordinary concrete and its application to tunneling as a coupled creep-chemoplastic problem is addressed in [120, 121]. In these studies, two creep mechanisms are introduced within the framework of closed reactive porous media. These mechanisms are associated with a stress-induced water movement and redistribution, and a relaxation mechanism in

the micropores of cement gel expressing the long-term and short-term creep, respectively. In [122, 123, 19, 31] a micromechanics-based creep model is proposed for a solidifying material to obviate deficiencies of the forms of the creep law with aging to determine the creep strain as a sum of aging and nonaging viscoelastic strain and an aging viscous strain. This proposed formulation was verified by applying it to concrete specimens undergo no significant drying.

In addition to solidification theory, the long-term aging which cannot be described by the volume growth of hydration products, the microprestress theory has been presented [19, 31]. This theory considers the long-term aging as the relaxation of tensile microprestress in the bonds or bridges that cross the micropores in hardened cement gel filled by hindered adsorbed water, see Figure 1.3. The breakage and reformation of the bonds across the micropores resulting in viscous shear between the opposite walls of micropores lead to long-term creep. The relaxation reduces the effective viscosity of the shear slip so the long-term aging comes with the flow term is observed in the creep model. In this manner, the microprestress theory contributes to interpret drying creep or strain-induced shrinkage not due to the volumetric growth of hydration production, but due to the relaxation of tensile microprestress. In [124], the previously proposed microprestress-solidification theory is used to numerically simulate the effect of temperature changes to capture the transitional thermal creep. The results demonstrate that the chemical potential of pore water which is sensitive to both pore humidity and temperature is the key factor governing the creep prediction through the concept of microprestress. This theory is improved in [33, 125, 126] by reformulating the governing equation of the microprestress in terms of viscosity by explicitly considering the effect of relative humidity and temperature variations, and it is verified by applying to the experimental benchmark problems at variable humidity and temperature.

The model, designated as the solidification-microprestress-microplane is developed in [32] to account for the relevant aspects of concrete behavior, such as creep, shrinkage, thermal deformation and cracking initiating from the early ages up to the state of the several years of age. In the latter, a multi-physics framework is introduced to numerically model: (i) the visco-elastic behavior of concrete such as creep/relaxation through the solidification theory, (ii) drying creep, long-term creep and variation of

relative humidity and temperature through the microprestress theory, and (iii) the microplane model [127] to describe cracking and damage under hygrothermal effects in concrete. Furthermore, a hygro-thermo-mechanical model for high performance concrete and its application for self-desiccation and drying tests associated with moisture transport and heat transfer are represented in [12, 128]. Within the scope of this model, diffusion equation is formulated in terms of pore relative humidity, this equation is coupled with the heat balance equation by considering the heat liberated during hydration and silica fume reaction. Moreover, the relative humidity is determined as a function of the amount of evaporable water by adopting adsorption/desoprtion isotherm [129].

A coupled thermo-hygro-mechanical model based on the framework of the microprestress-solidification theory to investigate time-dependent deformation of hardened concrete incorporating aging, creep, drying shrinkage, thermal dilation, and tensile cracking is represented in [130]. This proposed model is also applied to the coupled multi-physics problems at a structural scale. The long-term mechanical behavior of concrete at early ages is studied in [34] by adopting a viscoelastic aging model through the solidification-microprestress theory to reproduce the creep and relaxation phenomena. An improved microprestress-solidification (MPS) theory is proposed in [131] to study the size effect of drying creep and capture the humidity dependence of transient thermal creep effect where the expression related to the evolution of the microprestress and its relation with the viscosity of the flow term is modified. Simulation of creep response of concrete, dealing with non-linearity of the numerical model, the multi-axiality of loading, and temperature and drying effect within the poro-mechanical framework is studied in [132]. The so-called hybrid mixture theory which considers concrete as a multiphase porous visco-elastic material along with the solidification-type model is applied in [133, 134, 135] to develop a numerical model of the hygro-thermo-chemo-mechanical phenomena by focusing on creep and shrinkage.

The early age behavior of massive concrete structures is studied in [136, 137] by conducting a thermal active restrained shrinkage ring test and developing a numerical analysis through a coupled chemo-thermo-elastic-damage model. In the study, the proposed model is used to simulate the active ring test and a concrete nuclear

containment construction to evaluate evolution of mechanical characteristics, autogenous shrinkage, temperature effect and the coupling between creep and damage. A micromechanical model for the cementitious materials, extended to the domain of diffusion-driven phenomena is represented in [138]. Drying shrinkage and the resulting cracking under hygro-mechanical coupled problem is investigated by taking into account the effect of the aggregates and the degree of drying.

Determination of relationship between shrinkage and interior humidity of concrete and its moisture diffusion coefficient as a function of the interior humidity is experimentally investigated in [139, 140] to evaluate shrinkage-induced effects leading to cracking risk in concrete structures. Moreover, an internal humidity based micromechanical model, based on experimental findings, is developed in [141] to study autogenous and drying shrinkage in concrete structures at early-ages. The dry-wet cycle as one of the aggressive environmental conditions is researched through the experiments and theoretical simulations to evaluate the shrinkage behavior of concrete by regarding the variation of the internal humidity [142].

In further studies, the moisture movement in early-age concrete and consequent cement hydration and drying shrinkage induced cracking from ring test to circular column and concrete pavement under the effects of environmental conditions, internal curing and water to cement ratio are investigated in [143, 144, 145, 146]. In the literature, the many other studies examined fluid transport in porous media. The effect of a freely moving pore fluid on the porous media under quasi-static deformation was first developed in 1923 by Terzaghi [147]. Then it was extended the three-dimensional consolidation process of soil which was determined by settlement under water extraction from the voids in response to the gradual application of load variation by Biot [148] in 1941. A new derivation of Biot's theory of linear poroelasticity is developed in a modern thermodynamically consistent framework [149]. This recently developed formulation introduces the fluid-solid mixture as a single homogenized continuum body contrary to the theory of mixture [150] in which the fluid-solid mixture is treated as a multicomponent mixture. Although, there is a variety of works focused on moisture transfer in concrete [151, 152, 153, 154], there has not been any comprehensive work which develops a coupling between the theory of poroelasticity with hygro-chemo-mechanical model to study creep and shrinkage, and their associ-

110

ated hygromechanical effects in concrete.

In this study, a coupled constitutive modeling approach, furnished with a robust computational framework, is developed to address the durability problems that arise from drying shrinkage within the three-dimensional framework of poroviscoelasticity. Hence, the proposed approach accounts for the hygro-chemo-mechanical cross coupling effects between the shrinkage-induced strain development due to the pressure evolution through humidity variations and the stress concentrations in hardening or hardened viscoelastic concrete.

To this end, we additively decompose the stress expression into the effective stress of the viscoelastic concrete skeleton and the pressure developing in pores. The viscoelastic model of the skeleton takes into account short- and long-term creep effects through the well-known microprestress theory. The material parameters related with the rigidity and strength of concrete are assumed to evolve with the degree of hydration. In the proposed model, as opposed to the modeling approaches suggested in the literature, the shrinkage strain is not obtained directly by using an empirical formula involving the hygromechanical expansion coefficient and the change in humidity. Instead, we employ a physically motivated approach where the pore pressure is obtained as a function of water content that is determined using sorption-desorption equations for a given value of the local relative humidity. In addition to the conservation of linear momentum equation, the Darcy-type transient continuity equation is used to calculate the temporal and spatial variation of the relative humidity.

In this chapter, first the governing equations of the hygro-chemo-mechanical model are introduced. Then, the aging effect and the evolution of the mechanical properties of concrete are defined through a physico-chemical model based on the definition of the degree of hydration. In the following, the constitutive equations, including the overall stress tensor, the relative humidity flux and moisture storage are introduced. The total stress tensor is decomposed into the effective stress tensor and the pore pressure. The long-term viscoelastic behavior of concrete is described through the micoprestress theory to define the concrete viscosity as a function of the hygral effects. The moisture storage in the evolution equation of the relative humidity is calculated through the adsorption-desorption isotherm model. Indeed, we define the

water content as the state variable representing the hygral part of the problem, but to model the experiments in the literature, it is required to define the governing equation and the constitutive relations in terms of relative humidity. The adsorption-desorption isotherm model provides us with a relationship between the water content and the relative humidity.

The capability of the proposed three-dimensional model is validated by several representative numerical examples of boundary-value problems. These examples are the experiments performed in the literature, including the basic creep, flexural creep, and drying shrinkage tests.

4.2   Theory

In this section, the principal equations of the coupled boundary value problem of the hygro-chemo-mechanics are developed within the framework of poroviscoelasticity in hardening concrete by presenting the governing differential equations and the constitutive equations.

4.2.1   Geometry and Kinematics

The geometry and kinematics, related to the mechanical part of the problem is presented in Section 3.2.

4.2.2   Thermodynamic State

In the traditional theory of poroelasticity, the related formulations have been presented based on the concept of pore pressure. In this study, we construct our formulation based on the relative humidity as a field variable. Indeed, the pore pressure is implicitly calculated through a relation in which the variation of water content is determined as a function of the relative humidity. But we first formulate the balance law for the diffusing fluid in terms of the mass content of the evaporable fluid. Expressing the mass content of evaporable fluid in terms of the relative humidity through the

112

adsorption-desorption isotherm model, the associated balance law is reformulated for the relative humidity, that the effect of its variation is projected to the stress response in terms of the pore pressure. To this end, we derive the related expressions with regard to the concept of chemical potential, conjugate to the mass content of evaporable water, referring to [149, 155, 156, 157], then we implicitly relate the chemical potential to the relative humidity through the adsorption-desorption isotherm model. As a result of this local simplification, the following governing and constitutive expressions are rewritten as a function of relative humidity.

As is known, when concrete is in the hardening state, a highly exothermic and thermally activated reaction, the so-called hydration process mainly governs the evolution of the mechanical properties and critical fracture energy of the material. Based upon the theory of porous media [158] proposed by Ulm and Coussy [3, 4], at a macroscopic level, the hydration process is specified as a chemical reaction in which the free water is a reactant phase combining with the unhydrated cement to form combined water in the hydrates as a product phase. At the microscopic level, the diffusion of water through the layers of already formed hydrates may be taken into account as the governing mechanism in the kinematics of the reaction [7]. The process of hydration is quantified by the hydration extent through a single variable, known as the degree of hydration ξ.

The degree of hydration, $\xi(\boldsymbol{x}, t)$ is identified to inspect the aging phenomena corresponding to the effect of the hydration process on the coupled chemo-thermomechanical behavior of concrete resulting in the growth of rigidity and strength of hardening concrete. A coupled problem of isothermal hygro-chemo-mechanics within a framework of poroviscoelasticity is formulated in terms of four primary field variables, namely the total strain tensor $\boldsymbol{\varepsilon}(\boldsymbol{x}, t)$, the mass content of evaporable fluid $w_e(\boldsymbol{x}, t)$, the viscous strain $\boldsymbol{\alpha}(\boldsymbol{x}, t)$ and the degree of hydration $\xi(\boldsymbol{x}, t)$. The first two state variables are the external variables and the remaining are the internal variables

$$\text{State}(\boldsymbol{x}, t) := \{\boldsymbol{\varepsilon}(\boldsymbol{x}, t), w_e(\boldsymbol{x}, t), \boldsymbol{\alpha}(\boldsymbol{x}, t), \xi(\boldsymbol{x}, t)\}. \tag{4.1}$$

These state variables govern the volume-specific Helmholtz free energy which defines the coupled hygro-chemomechanical potential

$$\Psi = \hat{\Psi}(\boldsymbol{\varepsilon}, \varphi, \boldsymbol{\alpha}, \xi) \tag{4.2}$$

Moreover, the spatial and temporal evolution of the primary field variables are governed by two fundamental field equations: the balance of linear momentum and the mass balance law for the diffusing fluid. Additionally, the evolution of the degree of hydration can be expressed as a thermally activated process through an Arrhenius-type differential equation, based on the theory of reactive porous media developed by Coussy [158], and its application to (chemoplasticity) concrete as proposed by Ulm and Coussy [3, 4].

4.2.3 Governing Differential Equations

In this section, we introduce the differential equations that govern the evolution of the state variables, given in (4.1). In particular, the balance of linear momentum and the continuity equation of evaporable water content, express the spatio-temporal evolution of external state variables, the displacement field $\boldsymbol{u}(\boldsymbol{x}, t)$ and the evaporable water content $w_e(\boldsymbol{x}, t)$, respectively. The evolution equation of the degree of hydration $\xi(\boldsymbol{x}, t)$ is generally obtained through a thermo-chemo-mechanical model. In addition to this model, we adopt a micro-presrtress theory to determine the viscous strain $\boldsymbol{\alpha}(\boldsymbol{x}, t)$.

The balance of linear momentum that adopts the following well-known local spatial form

$$\operatorname{div} \hat{\boldsymbol{\sigma}} + \bar{\boldsymbol{b}} = \boldsymbol{0}, \tag{4.3}$$

represents the quasi-static stress equilibrium in terms of the total stress tensor $\hat{\boldsymbol{\sigma}}$,
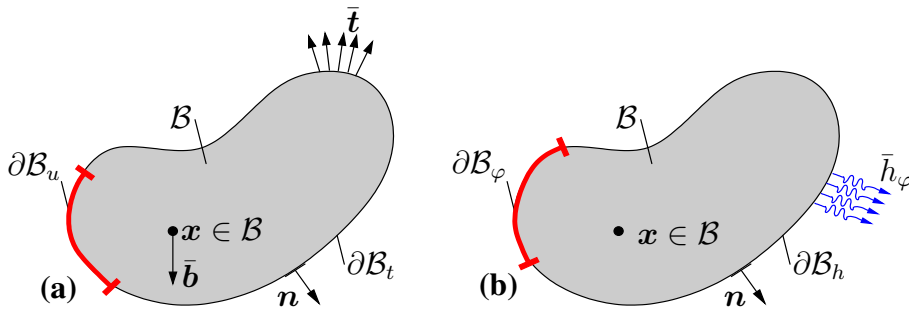
Figure 4.1: Schematic representations of the Dirichlet and Neumann boundary conditions for the **(a)** mechanical and **(b)** hygral problems.

and the volume-specific body forces $\bar{b}$. This expression governs the evolution of the displacement field $u(x, t)$ in conjunction with the Dirichlet boundary $u = \bar{u}$ on $\partial \mathcal{B}_u$ and the Neumann $\sigma n = \bar{t}$ on $\partial \mathcal{B}_u$ boundary conditions where n represents the outward unit surface normal on $\partial \mathcal{B}$. It is obvious that the respective parts of the boundary $\partial \mathcal{B}_u$ and $\partial \mathcal{B}_t$ satisfy $\partial \mathcal{B} = \partial \mathcal{B}_u \cup \partial \mathcal{B}_t$ and $\partial \mathcal{B}_u \cap \partial \mathcal{B}_t = \emptyset$ as demonstrated in Figure 4.1.

The local balance law for the diffusing fluid expressing the temporal and spatial variation of the mass content of the evaporable fluid is given by

$$\dot{w}_e = - \operatorname{div} \hat{\boldsymbol{j}}(w_e, \nabla_x w_e) \tag{4.4}$$

where the flux $\hat{\boldsymbol{j}}(w_e; \nabla_x \mu_\varphi) = -\hat{\boldsymbol{M}}(\boldsymbol{\varepsilon}, w_e) \nabla_x \mu_\varphi$ represents the spatial variation in the mass content of evaporable fluid in a porous medium induced by diffusion across the boundary as a function of the positive-semidefinite fluid mobility tensor $\hat{\boldsymbol{M}}(\boldsymbol{\varepsilon}, w_e)$. For an isothermal process, the balance laws (4.3) and (4.4) are employed to state the temporal changes in free energy of a porous medium $\mathcal{B}$, see Figure 4.1, which is not greater than the power extended on $\mathcal{B}$, plus the flux of energy carried into $\mathcal{B}$. Therefore, the free energy imbalance under isothermal conditions and neglected inertial effects is written as

$$\underbrace{\int_{\mathcal{B}} \dot{\Psi} \, dV}_{\dot{\mathcal{E}}} \leq \underbrace{\int_{\partial \mathcal{B}} \boldsymbol{\sigma} \boldsymbol{n} \cdot \dot{\boldsymbol{u}} + \int_{\mathcal{B}} \bar{\boldsymbol{b}} \cdot \dot{\boldsymbol{u}} \, dV}_{\mathcal{P}_{\text{ext}}} - \underbrace{\int_{\partial \mathcal{B}} \mu_\varphi \boldsymbol{j} \cdot \boldsymbol{n} \, dA}_{\mathcal{Q}_{\text{ext}}} \tag{4.5}$$

where $\dot{\mathcal{E}}$ represents the represents the rate of change of the internal energy of part $\mathcal{B}$, $\mathcal{P}_{\text{ext}}$ is the external mechanical power exerted on part $\mathcal{B}$ by the surface tractions $\boldsymbol{\sigma} \boldsymbol{n}$ and body force $\bar{\boldsymbol{b}}$, and $\mathcal{Q}_{\text{ext}}$ represents the the flux of energy carried into $\mathcal{B}$ by the flux $\boldsymbol{j}$ of diffusing fluid. The energy carried into part $\mathcal{B}$ by fluid transport is characterized by introducing primitive quantity, namely the chemical potential field $\mu_\varphi(\boldsymbol{x}, t)$. The chemical potential or Gibbs function per unit mass of the fluid phase is given by [156, 157, 159]

$$\mu_\varphi = \int_{p_0^w}^{p^w} \frac{dp^w}{\rho^f} \tag{4.6}$$

where p^w is the pore pressure, brought about by the variation of mass content of evaporable fluid inside the porous medium. By applying the divergence theorem to

the integral over $\partial\mathcal{B}$, the inequality in (4.5) becomes is reread as

$$\int_{\mathcal{B}} (\dot{\Psi} - \boldsymbol{\sigma} : \dot{\boldsymbol{\varepsilon}} - (\text{div}\,\boldsymbol{\sigma} + \bar{\boldsymbol{b}}) \cdot \dot{\boldsymbol{u}} + \mu\,\text{div}\,\boldsymbol{j} + \boldsymbol{j} \cdot \nabla_x \mu_\varphi)\, dV \leq 0 \qquad (4.7)$$

Referring (4.3) and (4.4), the local form of the free energy imbalance is given by

$$\dot{\Psi} - \boldsymbol{\sigma} : \dot{\boldsymbol{\varepsilon}} - \mu\dot{w}_e + \boldsymbol{j} \cdot \nabla_x \mu_\varphi \leq 0 \qquad (4.8)$$

According to the first law of thermodynamics $\dot{\omega} = \boldsymbol{\sigma} : \dot{\boldsymbol{\varepsilon}} + Q_{\text{ext}}$ expresses the rate of energy balance in terms of the volume-specific ground canonical internal energy ω, the internal stress $\boldsymbol{\sigma} : \boldsymbol{\varepsilon}$ and the externally supplied hydraulic power $Q_{\text{ext}} = \boldsymbol{j} \cdot \nabla_x \mu_\varphi$. The stress and the chemical potential can be used as independent variables by performing a Legendre transformation $\omega = \Psi - \mu_\mu w_e$ between the internal energy and Helmholtz free energy, we arrive at the following form of the first law

$$-w_e \dot{\mu}_\varphi = \mathcal{D}_{\text{loc}} + Q_{\text{ext}} \qquad (4.9)$$

where $\mathcal{D}_{\text{loc}} := \boldsymbol{\sigma} : \dot{\boldsymbol{\varepsilon}} - \dot{\Psi} + \mu_\varphi \dot{w}_e \geq 0$ denotes the intrinsic dissipation due to the internal dissipative mechanisms. The non-negativeness of $\mathcal{D}_{\text{loc}}$ is dictated by the second law of thermodynamics. Expanding the rate of the free energy $\hat{\Psi}(\boldsymbol{\varepsilon}, w_e, \boldsymbol{\alpha}, \xi)$ in (4.2) in terms of its partial derivatives with respect to the state variables (4.1) and their rates, we obtain the Clausius-Planck Inequality

$$\mathcal{D}_{\text{loc}} := [\boldsymbol{\sigma} - \partial_{\boldsymbol{\varepsilon}}\hat{\Psi}] : \dot{\boldsymbol{\varepsilon}} - [\mu_\varphi - \partial_{w_e}\hat{\Psi}]\dot{w}_e - \partial_\xi\hat{\Psi}\dot{\xi} - \partial_{\boldsymbol{\alpha}}\hat{\Psi} : \dot{\boldsymbol{\alpha}} \geq 0. \qquad (4.10)$$

Based on the Coleman's exploitation method, see e.g. Coleman & Gurtin [109], we demand that the non-negativeness of $\mathcal{D}_{\text{loc}}$ must be fulfilled for arbitrary rates of the controllable external variables $\boldsymbol{\varepsilon}$ and w_e. Based on this argument associated with the thermodynamic restrictions, the expressions in the brackets vanish identically to yield the well-known constitutive definitions of the stress tensor $\boldsymbol{\sigma}$ and the chemical potential μ_φ through

$$\hat{\boldsymbol{\sigma}} = \partial_{\boldsymbol{\varepsilon}}\hat{\Psi}(\boldsymbol{\varepsilon}, w_e, \boldsymbol{\alpha}, \xi) \quad \text{and} \quad \mu_\varphi = \partial_{w_e}\hat{\Psi}(\boldsymbol{\varepsilon}, w_e, \boldsymbol{\alpha}, \xi). \qquad (4.11)$$

In this study, we employ a physically motivated approach, where the pore pressure is implicitly identified as a function of the relative humidity. To this end, we reformulate the balance law for diffusing water, and rewrite the expression with reference to relative humidity. Indeed, the formulation based on the concept of the relative humidity contributes to simulate the behavior of concrete under hygro-chemo-mechanical

effects referring to the experimental studies in the literature. Therefore, the balance equation for diffusing water (4.4) is recast into the general form analogous to (4.3)

$$\text{div}\, \hat{\boldsymbol{q}}_\varphi - \hat{\mathcal{H}}_{\varepsilon - \varphi} + \hat{f}_\varphi = \boldsymbol{0} \tag{4.12}$$

where $\text{div}\, \hat{\boldsymbol{q}}_\varphi$ stands for the humidity flux vector, $\hat{f}_\varphi$ describes the moisture storage, which is defined through the adsorption-desorption isotherm model as a function of the relative humidity field and $\hat{\mathcal{H}}_{\varepsilon - \varphi}$ represents the coupled hygro-mechanical effect, as this effect is not remarkable, it can be neglected. Therefor, (4.12) is rewritten as

$$\text{div}\, \hat{\boldsymbol{q}}_\varphi + \hat{f}_\varphi = \boldsymbol{0}\,. \tag{4.13}$$

The spatio-temporal evolution of the relative humidity field $\varphi(\boldsymbol{x}, t)$ is expressed by the evolution equation of the relative humidity that is accompanied by the Dirichlet boundary condition $\varphi = \bar{\varphi}$ on $\partial \mathcal{B}$, the Neumann boundary condition $\boldsymbol{q}_\varphi \cdot \boldsymbol{n} = \bar{h}_\varphi$ on $\partial \mathcal{B}_\varphi$ and the initial condition $\varphi_0(\boldsymbol{x}) = \varphi(\boldsymbol{x}, t = 0)$ in $\mathcal{B}$, see Figire 4.1. The local dissipation due to the hydration reactions $\mathcal{D}^\xi_{\text{loc}} := -\partial_\xi \hat{\Psi} \dot{\xi} \geq 0$ responsible for the growth of concrete in strength and rigidity can be expressed as a product of the chemical driving force $\hat{A}_\xi$ and the rate of the degree of hydration $\dot{\xi}$; that is,

$$\mathcal{D}^\xi_{\text{loc}} = \hat{A}_\xi \dot{\xi} = -\partial_\xi \hat{\Psi} \dot{\xi} \geq 0 \tag{4.14}$$

where $\hat{A}_\xi := -\partial_\xi \hat{\Psi}(\boldsymbol{\varepsilon}, \varphi,, \boldsymbol{\alpha}\xi)$ presents the chemical affinity, defined as an energy-conjugate variable of the degree of hydration. Since hydration is a thermally activated process, the evolution of the degree of hydration is assumed to be described by the thermodynamically consistent, Arrhenius-type first-order kinetics activated by temperature [7]

$$\dot{\xi} = \frac{\hat{A}_\xi}{\hat{\eta}_\xi} \exp\left(-\frac{E_\text{a}}{R\theta}\right) \tag{4.15}$$

where $\hat{\eta}_\xi$ which represents the microdiffusion of the free water through the already formed hydrates. Since the growth of layers of hydrates increases the diffusion time of the free water to reach the unhydrated cement, it is defined as an increasing function of the degree of hydration ξ [7].

In (4.15), E_a and R denotes the activation energy and the universal constant for ideal gases with $R = 8.315$ J/(mol K) respectively. The ratio E_a/R can be experimentally determined, ranging from 3000 to 8000 K for concrete. According to [110] for many

practical purposes, at least for Portland cement, $E_a = 33500$ J/mol for $\theta \geqslant 293$ K and $E_a = 33500 + 1470 \times (293 - \theta)$ J/mol. Therefore, the aging model based on the definition of the degree of hydration is developed to clarify the variation of the mechanical properties. The ultimate value of the hydration degree is ξ^∞ is always less than one. It means that the complete hydration of concrete is never achieved.

The hydration process was completely attained if the ideal conditions would be accomplished, i.e., an adequate water-cement ratio should be supplied to provide full hydration and absolute contact between water and cement grains [160]. The calculation of ultimate degree of hydration ξ^∞ is proposed by Pantazopoulou & Mills [161] for normal concrete with respect to the referential water-cement ratio w/c as follows

$$\xi^\infty = \frac{1.031 w/c}{0.194 + w/c}. \tag{4.16}$$

In (4.10) the local dissipation origination from the viscous effects is determined as follows

$$\mathcal{D}_{\text{loc}}^\alpha = \boldsymbol{\beta}_\alpha : \dot{\boldsymbol{\alpha}} \quad \text{with} \quad \boldsymbol{\beta}_\alpha = -\partial_\alpha \Psi. \tag{4.17}$$

4.2.4 Constitutive Equations

The governing equations of two main fields, the deformation and relative humidity, the evolution equation of the degree of hydration, and the corresponding boundary and initial conditions introduced in the previous subsection, give a complete description of a coupled boundary-value problem of hygro-chemo-mechanics. In the current subsection, the constitutive equations expressing the total stress tensor $\hat{\boldsymbol{\sigma}}$, the effective stress tensor $\hat{\boldsymbol{\sigma}}_{\text{eff}}$, the pore pressure p_i^w, the relative humidity flux $\hat{\boldsymbol{q}}_\varphi$, the moisture storage f_φ, and the coupled hygro-mechanical force $\mathcal{H}_{\varepsilon-\varphi}$ are manifested.

Stress Response. The total stress tensor is introduced over N Maxwell branches in the rheological model applied for the long term behavior of concrete as

$$\hat{\boldsymbol{\sigma}}(\boldsymbol{\varepsilon}, \varphi, \boldsymbol{\alpha}_i, \xi) = \hat{\boldsymbol{\sigma}}_{\text{eff}} - \sum_{i=1}^{N} \hat{b}_i(\xi) \chi_s^{ws} p_i^w \mathbf{1} \tag{4.18}$$

where the effective stress tensor $\hat{\boldsymbol{\sigma}}_{\text{eff}}$ is defined as

$$\hat{\boldsymbol{\sigma}}_{\text{eff}} = \sum_{i=1}^{N} \hat{K}_i^{\text{dr}}(\xi) \text{tr}(\boldsymbol{\varepsilon}_i^e) \mathbf{1} + 2\hat{\mu}_i(\xi) \text{dev}(\boldsymbol{\varepsilon}_i^e) \tag{4.19}$$

with $\text{dev}(\boldsymbol{\varepsilon}) = \boldsymbol{\varepsilon} - \dfrac{1}{3}\,\text{tr}\,\boldsymbol{\varepsilon}$ and $\hat{K}_i^{\text{dr}}(\xi)$ is the bulk modulus of the porous medium. The latter is calculated as a function of the Biot's effective parameter $\hat{b}_i(\xi)$, the Biot's modulus $\hat{M}_i(\xi)$, the undrained bulk modulus of concrete $\hat{K}_i(\xi)$, and χ_s^{ws}, which indicates the fraction of skeleton area in contact with water

$$\hat{K}_i^{\text{dr}}(\xi) = \hat{K}_i(\xi) - \hat{b}_i^2(\xi)\hat{M}_i(\xi)\chi_s^{ws} \tag{4.20}$$

Pore Pressure. The change in the mass content of fluid per its unit volume ζ causes the pressure in the pores p^w contributing the stress response at the macroscopic scale. Indeed, if we rewrite the volume specific free energy function $\hat{\Psi}$ in terms of the volumetric change of the fluid mass content, the pore pressure is identified as

$$p_i^w := \partial_\zeta \hat{\Psi} = \hat{M}_i(\xi)\zeta - \hat{M}_i(\xi)\hat{b}_i(\xi)\text{tr}(\boldsymbol{\varepsilon}^e) - p_0^w \quad \text{with} \quad \zeta = \frac{\hat{w}_e(\varphi) - w_0}{\rho^f} \tag{4.21}$$

where $\hat{M}_i(\xi) = M_\infty \xi$ and $\hat{b}_i(\xi) = 0.9995 - (1 - b_\infty)\xi$ respectively describe the instant Biot Modulus and Biot coefficient as the functions of their ultimate values and the degree of hydration. In the literature, the storage coefficient of the porous medium is determined as a measure of the amount of water content that can be forced into a porous solid under pressure while the volume of the porous solid is kept constant [148, 162]. Its inverse is defined as the Biot modulus M_∞ described as a ratio of the variation of the pore-pressure to the change in the variation of the water content. The Biot coefficient b_∞ measures the ratio of the water volume squeezed out to the volume change of the porous body if it is compressed while the water is being allowed to escape [148, 162]. The ultimate value of the Biot's effective parameter is constrained between 0 and 1 as $0 \leq b_\infty \leq 1$. If $b_\infty = 0$, the water content in the pores does not vary due to the volume change of the porous medium, in return if $b_\infty = 1$, the change in the water content is equal to the volume change. According to the definitions of the Biot's constants, it is understood that the porosity of concrete is a governing parameter determining the values of these macroscopic poroelastic parameters of concrete.

In general, during the hydration process, the production of the hydrates decreases the porosity of concrete. Therefore, the strength of concrete increases. It means that there fundamentally exists an inverse relationship between the porosity and the concrete strength [163]. In the progress of hydration, the decrease in porosity reduces the ratio of the change in the water content to the volume change of the concrete so

the value of $\hat{b}(\xi)$ decreases from its initial value $\hat{b}(\xi = 0) = 1$ to its ultimate value reached at the hardened state. Also, the decrease in the concrete porosity reduces the moisture capacity so the Biot's modulus $\hat{M}(\xi)$ increases.
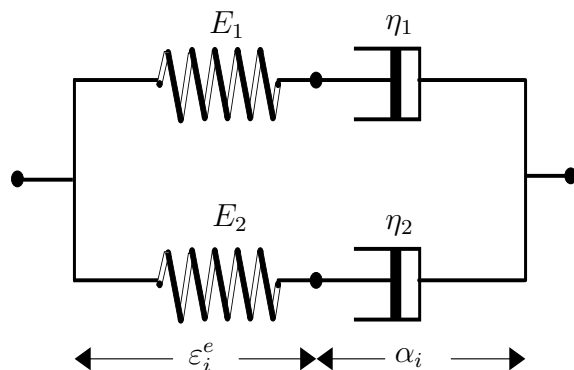
Figure 4.2: Schematic illustration of the rheological model representing the long-term behavior of concrete.

Microprestress Theory. Since the duration of creep response of concrete to a fixed mechanical loading decreases significantly with an increasing age at loading, the aging model founded on the solidification theory is not sufficient to describe the long-term aging of concrete. Therefore, besides the aging model, the microprestress model has been proposed to determine the long-term behavior of concrete [7]. The long-term behavior of concrete refers to the the situations of sustained loading or the straining due to the thermal and chemical effects caused by the hydration process itself. This model is mainly devised to model the creep and shrinkage as the conventional durability phenomena in concrete structures. A viscoelastic aging approach based on a rheological model shown in Figure 4.2 is adopted to simulate the creep and relaxation phenomena.

This rheological model is presented in the form of the Generalized Maxwell Models arranged in parallel. These springs and dashpots have independently varying elastic moduli and viscosities. The proposed solidification theory cannot sufficiently predict the long-term behavior of concrete such as the considerable decrease in creep duration for a fixed load with increasing age at loading, still after many years, so the microprestress theory has been developed [7, 14]. At the micro level of the material,

the so-called microprestress is interpreted as a tensile stress in the cement paste generated by the disjoining pressure of the hindered adsorbed water in the micropores, and by very large and highly localized volume changes in the course of the hydration process. It is presumed to be much bigger than any stress acting on the macroscopic level. The tensile microprestresses are carried by the bonds and bridges crossing the gel pores in the hindered cement gel. The long-term creep is supposed to occur as a result of viscous shear slips between the opposite walls of the micropores in which the bonds, conveying the microprestress, break and reform. The change of relative humidity has a significant effect of the microprestress at the long-term, thereby the nonlinear differential equation is proposed [33, 130] to implicitly calculate the microprestress

$$\dot{S} + \hat{\psi}_s(\varphi)c_0 S^2 = k_1 \left| \frac{\mathrm{d}(\theta_0 \ln \varphi)}{\mathrm{d}t} \right|, \quad \text{and} \quad \hat{\psi}_s(\varphi) = \alpha_s + (1 - \alpha_s)\varphi^2$$

$$\text{with} \quad S(t_0) = \frac{1}{c_0 t_0} \tag{4.22}$$

where c_0 and k_1 are constant parameters, and $\hat{\psi}_s(\varphi)$ is a humidity dependent variable represents the variation rate of microprestress relaxation at different values of humidities with $\alpha_s \approx 0.1$. The factor $\hat{\psi}_s(\varphi)$ is associated with a transformed time which determines the rate of microprestress relaxation. Moreover, $S(t_0)$ represents the initial condition for microprestress and t_0 the time shows the start of humidity variations. This formulation contributes to theoretically determining evolution of flow term viscosity as

$$\hat{\eta}_\mu(S) = \frac{1}{Sc_0 q_4} \quad \text{with} \quad \eta_\mu(t_0) = \frac{t_0}{q_4} \quad \text{and} \quad q_4 = \frac{1}{E_\infty \tau_{\mu_0} c_{\mu_0}} \tag{4.23}$$

here q_4 is a parameter associated with basic creep and $\eta_\mu(t_0)$ presents the initial condition for viscosity. The basic creep parameter, q_4 is correspondingly determined as a function of the ultimate elastic modulus, and two additional parameters τ_{μ_0} and c_{μ_0}. These two parameters express respectively the initial value of relaxation time, and the material constant governing the evolution rate of the viscosity. [34]. The formulation related to viscosity definition is promoted by completely eliminating the microprestress and reformulate the differential equation (4.22) in terms of viscosity. To this end, the microprestress is rewritten as a function of viscosity as $S = 1/\eta_\mu c_0 q_4$ from the combination of (4.22) and (4.23), and its differentiation with respect to time

yields $\dot{S} = -\dot{\eta}_\mu/(\eta_\mu^2 c_0 q_4)$. By substituting S and $\dot{S}$ into (4.22), it leads to a nonlinear first-order differential equation as

$$\dot{\eta}_\mu + \frac{\mu_s}{\theta_0}\left|\theta_0\frac{\dot{\varphi}}{\varphi}\right|\eta_\mu^2 = \frac{\psi_s}{q_4} \tag{4.24}$$

Viscous Strains. The viscous strain tensor is defined by considering the effect of aging and flow term on the retardation time of the dashpots in the rheological model. By assuming a serial combination between these effects, the evolution law for the viscous strain in each Maxwell element is defined as

$$\dot{\boldsymbol{\alpha}}_i = \frac{1}{\hat{\eta}_i}\,\hat{\boldsymbol{\sigma}}_i^{\mathrm{eff}}(\boldsymbol{\varepsilon}_i^e, \xi), \quad \text{with} \quad \frac{1}{\hat{\eta}_i} = \frac{1}{\eta_i} + \frac{1}{\hat{\eta}_a} + \frac{1}{\hat{\eta}_\mu} \quad \text{and} \quad \eta_i = \tau_i\hat{E}_i(\xi) \tag{4.25}$$

where $\hat{\eta}_i$ represents the viscosity of each Maxwell element, and η_i and τ_i are the viscosity of each dashpot, respectively. $\hat{\eta}_a = \hat{\tau}_a\hat{E}_i(\xi)$ represents the effect of aging on the elastic modulus where $\hat{\tau}_a$ denotes the aging-dependent retardation time and $\hat{E}_{i(\xi)}$ is the elastic modulus of the ith spring in the generalized Maxwell model, see Figure 4.2. It is used to show that even though η_i and $\hat{\eta}_\mu$ are large enough, there remains some viscous after even long time passed from the onset of development of mechanical properties. The aging dependent retardation time is given by

$$\hat{\eta}_a(\xi) = \hat{E}_i(\xi)\hat{E}_c(\xi)/\dot{\hat{E}}_c(\xi). \tag{4.26}$$

In (4.24) $\hat{\eta}_\mu$ indicates the viscosity related to the flow term presented. The evolution equation of the flow term viscosity with initial condition is numerically treated by approximating the current value of the viscosity as $\eta_\mu^{n+1} = \eta_\mu^n + \Delta\eta_\mu^n$ at time $t_{n+1} = t_n + \Delta t$. By applying finite differences and approximating η_μ by the average of η_n and η_{n+1}, to this end (4.24) is written as

$$\frac{\Delta\eta_\mu^n}{\Delta t} + \frac{|\Delta(\theta_0\ln\varphi)_n|}{\theta_0\Delta t}\mu_s\left(\eta_\mu^n + 0.5\Delta\eta_\mu^n\right)^{1/2} = \frac{\psi_s}{q_4} \tag{4.27}$$

In this equation, we have,

$$\Delta(\theta_0\ln\varphi)_n = \theta_0\ln\varphi_{n+1} - \theta_0\ln\varphi_n \tag{4.28}$$

Accordingly, (4.24) is simplified in the following form

$$\dot{\eta}_\mu + A^2\eta_\mu^2 = B^2 \tag{4.29}$$

122

where,

$$A = \sqrt{\frac{\mu_s \left| \Delta(\theta_0 \ln \varphi)_n \right|}{\Delta t \theta_0}} \quad \text{and} \quad B = \sqrt{\frac{\psi_s}{q_4}} \tag{4.30}$$

Finally, by considering an analytical solution to (4.29) which are described in details in [33], the viscosity of the flow term is written as

$$\eta_\mu^{n+1} = \eta_\mu^n + \Delta\eta_\mu^n \quad \text{with} \quad \Delta\eta_\mu^n = \frac{(1 - \tilde{e})(B^2 - A^2(\eta_\mu^n)^2)}{A(B(1 + \tilde{e}) + A\eta_\mu^n(1 - \tilde{e}))} \tag{4.31}$$

by expanding $\tilde{e}$ into Taylor series, it is written as

$$\tilde{e} = 1 - 2AB\Delta t + 2A^2 B^2 (\Delta t)^2 \tag{4.32}$$

Adsorption-Desorption Isotherm Model. The pore pressure in concrete is calculated by using the so-called water vapor adsorption-desorption isotherms implicitly. It contributes to building the relationship between the amount of evaporable water and relative humidity. If we investigate one-way drying or one-way wetting, the exact values of the adsorption and desorption curves and their shapes are not of main importance. Also, the comparison of the results presented that the shape of adsorption and desorption curve is almost the same [15, 164].

For this reason, in the following, desorption isotherm is used respecting both adsorption and desorption isotherms. In the literature there are a number of formulations used to determine the desorption isotherm of normal concrete. The best-known isotherm model is the Brunauer-Emmette-Teller (BET) [165] developed from statistical thermodynamics of adsorption. But, the range of validity to the BET equation for cement and concrete ordinarily covers the relative pressure (humidity) from 0.01 to 0.1. Therefore, the common BET theory has been modified in favor of obtaining improved agreement with experimental isotherm data in the multi-layer region. Some of the modified models are: the Brunauer-Deming-Deming-Teller (BDDT) model, derived form statistical thermodynamics of adsorption and the modified form of the BET equation [166], the Hasley's model (FHH) applied for the physical adsorption on non-uniform and heterogeneous surfaces [167], the Hillbors's formula derived by a small modification to the BET theory to promote its application for cylindrical and slit-shaped pores [168], and the Brunauer-Skalny-Bodor (BSB) model applied for the nonporous solids [169].

In this study, the semi-empirical model proposed by Mjörnell [170] is used. According to this model, the content of evaporable water content $\hat{w}_e(\varphi)$ is calculated as

$$\hat{w}_e(\varphi) = c\left[a_1^\varphi(1 - \exp(-a_3^\varphi\varphi)) + a_2(\exp(a_3^\varphi\varphi) - 1)\right]$$

$$a_1^\varphi = \frac{0.15\xi}{1 - \exp(-a_3)}, \quad a_2^\varphi = \frac{w_0/c - 0.33\xi}{\exp(a_3^\varphi) - 1}, \quad \text{and} \quad a_3^\varphi = -(w_0/c)f_1 + f_2$$

$$(4.33)$$

where c is the cement content, a_1^φ, a_2^φ and a_3^φ are the degree of hydration (ξ) dependent parameters, w_0/c is the initial water-cement ratio, and f_1 and f_2 indicate two shape factors. The moisture capacity $\hat{C}(\varphi)$ is consecutively calculated as the derivative of the desorption isotherm,

$$\hat{C}(\varphi) = \hat{w}_e'(\varphi) := c\left[a_1^\varphi a_3^\varphi \exp(-a_3^\varphi\varphi) + a_2^\varphi a_3^\varphi \exp(a_3^\varphi\varphi)\right]. \qquad (4.34)$$

Therefore, the pore pressure is explicitly calculated as a function of the relative humidity presented in (4.21) where the respective solid-phase equilibrium pressure is specified as $p_i^s = \chi_s^{ws}p_i^w$. The temporal and spatial variation of the internal moisture content is implicitly described through the balance equation of relative humidity in terms of the moisture capacity and the humidity flux vector.

Moisture Storage. The moisture storage f_φ is implicitly evaluated by using physically motivated adsoption-desorption dependent expression and the degree of hydration evolution referring (4.15) and (4.34)

$$f = \hat{f}(\varphi; \dot{\varphi}) := \hat{C}(\varphi)\dot{\varphi} + \kappa_\varphi\hat{\mathcal{W}}(\varphi, \dot{\xi}) \quad \text{with} \quad \hat{\mathcal{W}}(\varphi, \dot{\xi}) = \frac{\hat{w}_e(\varphi)}{c}\dot{\xi}. \qquad (4.35)$$

Before the concrete is subjected to drying shrinkage, the variation of water content due to the hydration process may cause the autogenous shrinkage, which is taken into account by $\kappa_\varphi\hat{\mathcal{W}}(\varphi, \dot{\xi})$ in (4.35) where κ_φ is a constant representing the evolution of the autogenous shrinkage. This expression is implicitly determined as a function of the relative humidity and the degree of hydration, which is introduced based on a cross-coupling between the evolution of degree of hydration and the variation of water-cement ratio calculated through the adsorption-desorption isotherm model. Indeed, this additional relation can contribute to obtain a robust prediction of relative humidity variation by considering both the hydration process and environmental effects, and the consequent autogenous and drying shrinkage in concrete structures.

Humidity Flux Vector. The spatial variation of the relative humidity is expressed by the humidity flux vector $\hat{q}$ in terms of the effective diffusivity tensor $\hat{D}_{\text{eff}}(\varphi)$ and the humidity gradient $\nabla\varphi$

$$\hat{q}_\varphi(\varphi; \nabla\varphi) = -\hat{D}_{\text{eff}}(\varphi)\nabla\varphi. \tag{4.36}$$

The effective diffusivity of concrete is strongly dominated by the relative humidity. To this end, the effective diffusivity of concrete, referring [15], is written as

$$\hat{D}_{\text{eff}}(\varphi) = [D_0 + D_1\hat{\varpi}(\varrho, \varphi)]\,\mathbf{1} \tag{4.37}$$

where D_0 and D_1 are constants respectively, defining the values of the effective diffusion coefficient at zero relative humidity and fully saturated states. Owing to the nonlinear relation between the effective diffusivity and the relative humidity, a hyperbolic function $\hat{\varpi}(\varrho, \varphi)$ is justified depending on the relative humidity as

$$\hat{\varpi}(\varrho, \varphi) = 1 - 2^{-10^{\varrho(\varphi-1)}} \tag{4.38}$$

The relation between the effective diffusion coefficient and the relative humidity with respect to the shape factor ϱ, and the variation of the water content and its derivative with respect to the relative humidity are illustrated in Figure 4.3.
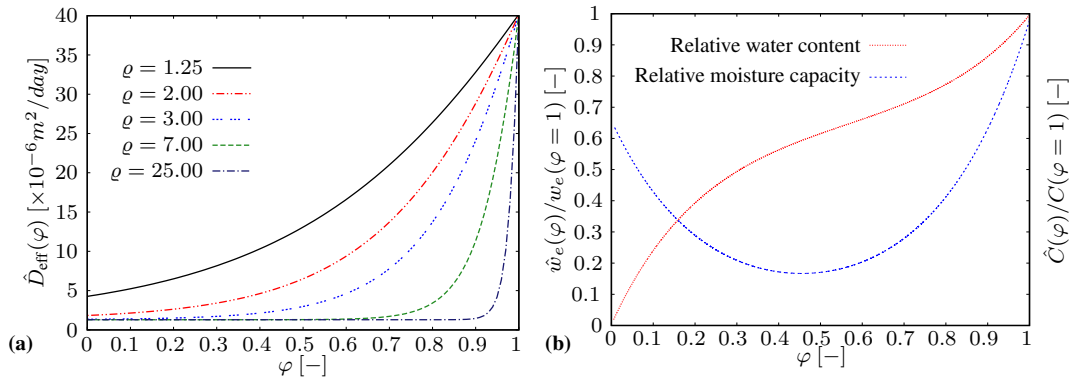
Figure 4.3: **(a)** Effect of the shape factor on the effective diffusion coefficient, and **(b)** the relative water content and its derivative with respect to the relative humidity

Chemical Hydration and Growth in Rigidity and Strength. The chemical affinity $\hat{A}_\xi$ in (4.15) is defined as a function the degree of hydration as [7]

$$\hat{A}_\xi = k_\xi(\xi + \frac{A_{\xi_0}}{\xi^\infty k_\xi})(\xi - \xi^\infty). \tag{4.39}$$

The microdiffusion of the free water through the already formed hydrates is described by introducing the viscosity dependent function $\hat{\eta}_\xi$ in (4.15), as follows

$$\hat{\eta}_\xi = \eta_{\xi_0} \exp(\eta_\xi \frac{\xi}{\xi_\infty}). \tag{4.40}$$

The aging expressions are introduced to model the hydration-induced growth of concrete in rigidity and strength which specify the mechanical properties such as the compressive strength f_c, the tensile strength f_t, the elastic modulus E and the Poisson's ratio ν. The effects of the hydration process and temperature on the mechanical properties of concrete is represented through the introduction of the aging parameter $\chi = \hat{\chi}(\xi, \theta)$. The evolution equation of the aging parameter by considering the thermal and the hydration-induced effects is written as

$$\dot{\chi} = \hat{\lambda}_\theta \hat{\lambda}_\xi \dot{\xi} \tag{4.41}$$

where $\hat{\lambda}_\theta$ and $\hat{\lambda}_\xi$ are respectively formulated as

$$\hat{\lambda}_\theta = \left(\frac{\theta_{\max} - \theta}{\theta_{\max} - \theta_r} \right)^{n_\theta}, \qquad \hat{\lambda}_\xi = A_f \xi + B_f \tag{4.42}$$

in which, $\theta_{\max}$ accounts for the maximum temperature, n_θ is a material parameter regularizing the temperature dependency of the aging model, and A_f and B_f are the constants control the variation of the aging variable with respect to the degree of hydration. To this end, the mechanical properties including the compressive strength f_c, the tensile strength f_t, the elastic modulus E_c and the Poisson's ratio ν of the concrete are respectively defined as

$$
\begin{aligned}
\hat{f}_c(\chi) &= \chi f_c^\infty & \text{[MPa]} \\
\hat{f}_t(\chi) &= 1.40(\hat{f}_c(\chi)/10)^{2/3} & \text{[MPa]} \\
\hat{E}_c(\chi) &= 2.15 \cdot 10^4 (\hat{f}_c(\chi)/10)^{1/3} & \text{[MPa]} \\
\hat{\nu}(\chi) &= 0.18 \sin(\xi\pi/2) + \exp(-10\xi) & \text{[-]}
\end{aligned}
\tag{4.43}
$$

To impose the convective boundary condition, the so-called Robin boundary condition, the humidity transports at the boundaries of the solid bodies are modeled by introducing the humidity flux prescribed as $q_n = \alpha_s(\varphi - \varphi_\infty)$. In which α_s is the

Table 4.1: Governing equations of the hygro-chemo-mechanical model

Field	Problem	Equation	#	BC's / IC's
$\boldsymbol{u}(\boldsymbol{x},t)$	Mechanical	$\operatorname{div} \boldsymbol{\sigma} + \bar{\boldsymbol{b}} = \boldsymbol{0}$	(4.3)	$\boldsymbol{u} = \bar{\boldsymbol{u}}$ on $\partial\mathcal{B}_u$
				$\boldsymbol{\sigma}\boldsymbol{n} = \bar{\boldsymbol{t}}$ on $\partial\mathcal{B}_t$
$\varphi(\boldsymbol{x},t)$	Hygral	$\operatorname{div} \hat{\boldsymbol{q}}_\varphi + \hat{f}_\varphi = 0$	(4.13)	$\varphi = \bar{\varphi}$ on $\partial\mathcal{B}_\varphi$
				$\boldsymbol{q}_\varphi \cdot \boldsymbol{n} = \bar{h}_\varphi$ on $\partial\mathcal{B}_h$
				$\varphi_o(\boldsymbol{x}) = \varphi(\boldsymbol{x}, t=0)$ in $\mathcal{B}$
$\xi(\boldsymbol{x},t)$	Hydration	$\dot{\xi} = \tilde{A}_\xi \exp\left(-\dfrac{E_\mathrm{a}}{R\theta}\right)$	(4.15)	$\xi_o(\boldsymbol{x}) = \xi(\boldsymbol{x}, t=0)$ in $\mathcal{B}$
$\boldsymbol{\alpha}(\boldsymbol{x},t)$	Viscous strain	$\dot{\boldsymbol{\alpha}} = \sigma_\mathrm{eff} \dfrac{1}{\hat{\eta}}\left(\boldsymbol{\varepsilon}, \xi\right)$	(4.25)	$\boldsymbol{\alpha}_o(\boldsymbol{x}) = \boldsymbol{\alpha}(\boldsymbol{x}, t=0)$ in $\mathcal{B}$

convection parameter, also known as the surface emissivity, representing the humidity transfer occur due to the moisture movement over the boundaries of the body, and φ_∞ is the ambient humidity. The governing equations, constitutive relations, and the corresponding Dirichlet boundary and initial conditions related to the problem determined with the framework of the poroviscoelasticity are summarized in Table 4.1.

The material parameters used in the formulation to express the governing equations and constitutive relations corresponding to the hygro-chemo-mechanical model are presented in Table 4.2. These parameters are classified according to the aging formulations of the material properties, poroviscoelastic model and the hygral model including the adsorption-desorption isotherms and the associated constitutive relations.

4.3 Finite Element Formulation

In this section, we construct the compatible linearization of weak integral of the nonlinear governing equations Eq. 4.3 and Eq. 4.12 which are introduced in the preceding section. For this purpose, we employ conventional Galerkin method to the fundamen-

Table 4.2: Material properties of the ordinary Portland cement concrete used in the governing and constitutive expressions related to the hygro-chemo-mechanical model

Parameter	Description	Equation
Hydration and Aging		
E_a/R	Normalized activation energy	(4.15)
ξ^∞	Ultimate degree of hydration	(4.40)
k_ξ/η_{ξ_0}	Hydration parameter	(4.15)
A_ξ/η_{ξ_0}	Hydration parameter	(4.15)
η_{ξ_0}	Reference viscosity	(4.40)
η_ξ	Exponent for viscosity	(4.40)
θ_{max}	Maximum temperature for strength evolution	(4.42$_1$)
θ_r	Reference temperature	(4.42$_1$)
n_θ	Temperature-based exponent for strength evolution	(4.42$_1$)
A_f, B_f	Material properties for aging evolution	(4.42$_2$)
f_c^∞	Final compressive strength	(4.43$_1$)
Poro-visco-mechanical		
c_0, k_1	microprestress based material constants	(4.22), (4.23)
α_r	Transformed time based material constant	(4.22)
q_4	Material constant related to basic creep	(4.23)
τ_{μ_0}	Initial value of relaxation time	(4.23)
c_{μ_0}	Material constant related to evolution rate of viscosity	(4.23)
θ_0	Initial temperature	(4.24)
μ_s	microprestress parameter	(4.24)
η_i	Viscosity of ith dashpot in the Generalized Maxwell Model	(4.25)
τ_i	Retardation time of ith dashpot in the Generalized Maxwell Model	(4.25)
b_∞	Ultimate Biot's coefficient	(4.21)
M_∞	Ultimate Biot's modulus	(4.21)
Hygral		
w_0	Initial water content	(4.33)
c	Cement content	(4.33), (4.34), (4.35)
k_φ	autogenous shrinkage-dependent constant	(4.35)
χ^{ws}	Fraction of skeleton area in contact with water	(4.18)
f_1	shape factor of adsorption-desorption isotherm model	(4.33)
f_2	shape factor of adsorption-desorption isotherm model	(4.33)
D_0	Effective diffusion coefficient at zero relative humidity	(5.17)
D_1	Effective diffusion coefficient at fully saturated state	(5.17)
ϱ	Effective diffusivity shape factor	(5.18), (5.17)

tal field equations by individually multiplying them by the weight functions $\delta\boldsymbol{u} \in \mathscr{U}_0$, $\delta\varphi \in \mathscr{V}_0$ whose square of integrals are finite and they meet the conditions of the homogeneous boundary conditions ($\delta\boldsymbol{u} = \boldsymbol{0}$ over $\partial\mathcal{B}_{\boldsymbol{u}}$, $\delta\varphi = 0$ over $\partial\mathcal{B}_{\varphi}$). The weighted residual equations, integrated over the volume, take the following forms for the conservation of linear momentum and the continuity of relative humidity after integrating by part,

$$
\begin{cases}
G^u(\delta\boldsymbol{u}; \boldsymbol{u}, \varphi) = G^u_{\mathrm{int}}(\delta\boldsymbol{u}; \boldsymbol{u}, \varphi) - G^u_{\mathrm{ext}}(\delta\boldsymbol{u}) = 0\,, \\
G^\varphi(\delta\varphi; \boldsymbol{u}, \varphi) = G^\varphi_{\mathrm{int}}(\delta\varphi; \boldsymbol{u}, \varphi) - G^\varphi_{\mathrm{ext}}(\delta\varphi; \boldsymbol{u}, \varphi) = 0\,.
\end{cases}
\tag{4.44}
$$

It should be noted that since transient evolution of the degree of hydration ξ and the viscous strain $\boldsymbol{\alpha}$ are expressed as the functions of the temperature in (4.15) and the effective stress tensor in (4.25), at a Gauss point, respectively, they are solved only by discretizing in time space as a local history variable. Therefore, in the above equations, the degree of hydration and the viscous strain do not appear as an additional field. Accordingly, in the weak form derived for the conservation of linear momentum ($(4.44)_1$), internal and external Galerkin functions ($G^u_{\mathrm{int}}, G^u_{\mathrm{ext}}$) are demonstrated as follows

$$
G^u_{\mathrm{int}}(\delta\boldsymbol{u}; \boldsymbol{u}, \varphi) := \int_{\mathcal{B}} \delta\boldsymbol{\varepsilon} : \hat{\boldsymbol{\sigma}}\ dV\,,
$$

$$
G^u_{\mathrm{ext}}(\delta\boldsymbol{u}) := \int_{\mathcal{B}} \delta\boldsymbol{u} \cdot \bar{\boldsymbol{b}}\ dV + \int_{\partial\mathcal{B}_t} \delta\boldsymbol{u} \cdot \bar{\boldsymbol{t}}\ dA\,.
\tag{4.45}
$$

where $\bar{\boldsymbol{b}}$ and $\bar{\boldsymbol{t}}$ are respectively specific body forces and surface traction vector. Analogously, for the hygral part of the coupled problem, the internal and external Galerkin functions ($G^\varphi_{\mathrm{int}}, G^\varphi_{\mathrm{ext}}$) are defined as

$$
\begin{aligned}
G^\varphi_{\mathrm{int}}(\delta\varphi; \varphi) &:= \int_{\mathcal{B}} -\nabla_x(\delta\varphi) \cdot \hat{\boldsymbol{q}}_\varphi\ dV\,, \\
G^\varphi_{\mathrm{ext}}(\delta\varphi; \varphi) &:= \int_{\mathcal{B}} \delta\varphi - \hat{f}_\varphi\ dV - \int_{\partial\mathcal{B}_{q_\varphi}} \delta\varphi\ \bar{h}_\varphi\ dA\,.
\end{aligned}
\tag{4.46}
$$

When the governing equations are not linear, the weighted residual functions are the non-linear functions of the field magnitudes. Therefore, the coupled field equations are numerically solved by implementing Finite Element Method, at the same time Newton's method as an iterative technique is applied to solve the coupled problems. In the following, for each iteration step, the weighted Galerkin functions are consistently linearized with respect to the field variables almost their intermediate values $\tilde{\boldsymbol{u}}$

and $\tilde{\varphi}$,

$$\text{Lin}\, G^u(\delta \boldsymbol{u}; \boldsymbol{u}, \varphi)|_{\tilde{\boldsymbol{u}}, \tilde{\varphi}} \quad := \quad G^u(\delta \boldsymbol{u}; \tilde{\boldsymbol{u}}, \tilde{\varphi}) \quad + \quad \Delta G^u(\delta \boldsymbol{u}; \tilde{\boldsymbol{u}}, \tilde{\varphi}; \Delta \boldsymbol{u}, \Delta \varphi) = 0\,,$$

$$\text{Lin}\, G^\varphi(\delta \varphi; \varphi)|_{\tilde{\varphi}} \quad := \quad G^\varphi(\delta \varphi, \tilde{\varphi}) \quad + \quad \Delta G^\varphi(\delta \varphi, \tilde{\varphi}; \Delta \boldsymbol{u}, \Delta \varphi) = 0\,.$$

$$(4.47)$$

The incremental terms ΔG^u and ΔG^φ, derived by Gâteaux derivative are rewritten as functions of the external and internal terms according to Eq. $(4.44)_{1,2,3}$

$$\Delta G^\gamma = \Delta G_{\text{int}}^\gamma - \Delta G_{\text{ext}}^\gamma \quad \text{with} \quad \gamma = u, \varphi\,. \tag{4.48}$$

As stated in Eq. $(4.45)_1$, ΔG_{int}^u is obtained as

$$\Delta G_{\text{int}}^u = \int_{\mathcal{B}} \delta \boldsymbol{\varepsilon} : \Delta \hat{\boldsymbol{\sigma}}\, dV \tag{4.49}$$

In this expression, the total stress increment is specified as

$$\Delta \hat{\boldsymbol{\sigma}} = \mathbb{C}^{uu} : \Delta \boldsymbol{\varepsilon} + \boldsymbol{C}^{u\varphi} \Delta \varphi\,, \tag{4.50}$$

where the fourth order tensor $\mathbb{C}^{uu}$ is determined as the derivative of the total stress tensor with respect to the strain tensor, and the second order tensor $\boldsymbol{C}^{u\varphi}$ are described respectively as the derivative of the total stress tensor with respect to the relative humidity,

$$\mathbb{C}^{uu} := \partial_{\boldsymbol{\varepsilon}} \hat{\boldsymbol{\sigma}}\,, \quad \boldsymbol{C}^{u\varphi} := \partial_\varphi \hat{\boldsymbol{\sigma}} \tag{4.51}$$

Based on the expressions stated above, Eq. (4.49) is rewritten as

$$\Delta G_{\text{int}}^u \quad = \quad \int_{\mathcal{B}} \delta \boldsymbol{\varepsilon} : \mathbb{C}^{uu} : \Delta \boldsymbol{\varepsilon}\, dV + \int_{\mathcal{B}} \delta \boldsymbol{\varepsilon} : \boldsymbol{C}^{u\varphi} \Delta \varphi\, dV \tag{4.52}$$

On the other hand, as regards the hygral part of the coupled problem, the increment of the internal Galerkin function is expressed as

$$\Delta G_{\text{int}}^\varphi = \int_{\mathcal{B}} -\nabla_x(\delta \varphi) \cdot \Delta \hat{\boldsymbol{q}}_\varphi\, dV \tag{4.53}$$

where the increment of the relative humidity flux is stated as

$$\Delta \hat{\boldsymbol{q}}_\varphi = -\hat{\boldsymbol{D}}_{\text{eff}} \cdot \nabla_x(\Delta \varphi) \quad \text{where} \quad \hat{\boldsymbol{D}}_{\text{eff}} := -\partial_{\nabla_x \varphi} \hat{\boldsymbol{q}}_\varphi = D_{\text{eff}}\, \boldsymbol{1} \tag{4.54}$$

The increment of the external Galerkin function in terms of the relative humidity field is also defined as

$$\Delta G_{\text{ext}}^\varphi := \int_{\mathcal{B}} \delta \varphi\, (-\Delta \hat{f}_\varphi)\, dV, \tag{4.55}$$

Isoparametric Gelerkin method will be followed in order to approximate the weak forms Eq. $(4.44)_{1,2,3}$ given in the form of continuous integral equations above. The basic state variables of the coupled problem, the above-introduced generalized displacement $\boldsymbol{u}(\boldsymbol{x}, t)$ and the relative humidity field $\varphi(\boldsymbol{x}, t)$, and the weighted functions associated with these fields are interpolated on each finite element

$$
\begin{aligned}
\delta \boldsymbol{u}_e^h &= \sum_{i=1}^{n_{en}} N^i \delta \boldsymbol{d}_i^e, \quad \delta \varphi_e^h = \sum_{j=1}^{n_{en}} N^j \delta \Phi_k^e, \\
\boldsymbol{u}_e^h &= \sum_{k=1}^{n_{en}} N^l \boldsymbol{d}_l^e, \quad \varphi_e^h = \sum_{l=1}^{n_{en}} N^n \Phi_n^e.
\end{aligned}
\tag{4.56}
$$

where n_{ne} represents the number of nodes on each finite element. Then the spatial gradients of the weighted residual functions are presented as

$$
\begin{aligned}
\nabla_x(\delta \boldsymbol{u}_e^h) &= \sum_{i=1}^{n_{en}} \delta \boldsymbol{d}_i^e \otimes \nabla_x N^i, \\
\nabla_x(\delta \varphi_e^h) &= \sum_{j=1}^{n_{en}} \delta \Phi_j^e \otimes \nabla_x N^j.
\end{aligned}
\tag{4.57}
$$

Likewise, the spatial gradient of the increment of the generalized displacement vector and the relative humidity field are respectively demonstrated as

$$
\begin{aligned}
\nabla_x(\Delta \boldsymbol{u}_e^h) &= \sum_{l=1}^{n_{en}} \Delta \boldsymbol{d}_l^e \otimes \nabla_x N^k, \\
\nabla_x(\Delta \varphi_e^h) &= \sum_{m=1}^{n_{en}} \Delta \Phi_m^e \otimes \nabla_x N^l,
\end{aligned}
\tag{4.58}
$$

Incorporating the discretized representations Eq. 4.56 and (4.57) in $(4.44)_{1,2}$ along (4.45) and (4.46), we end up with the discrete residual vectors

$$
\boldsymbol{R}_I^u = \mathop{\mathbf{A}}_{e=1}^{n_{el}} \left\{ \int_{\mathcal{B}_e^h} \nabla_x N^i \cdot \hat{\boldsymbol{\sigma}} \ dV - \int_{\mathcal{B}_e^h} N^i \bar{\boldsymbol{b}} \ dV - \int_{\partial \mathcal{B}_t^e} N^i \bar{\boldsymbol{t}} \ dA \right\} = \boldsymbol{0},
$$

$$
R_J^\varphi = \mathop{\mathbf{A}}_{e=1}^{n_{el}} \left\{ -\int_{\mathcal{B}_e^h} \nabla_x N^j \cdot \hat{\boldsymbol{q}}_\varphi \ dV - \int_{\mathcal{B}_e^h} N^j (\hat{\mathcal{H}}_\varepsilon - \hat{f}_\varphi) \ dV \right\} = 0,
$$

$$
\tag{4.59}
$$

where the operator $\mathbf{A}$ designates the standard assembly of element contributions at the local element nodes $i, j = 1, ..., n_{en}$ to the global residuals at the global nodes

$I, J = 1, ..., \mathrm{n_{nd}}$ of a mesh with $\mathrm{n_{nd}}$ nodes. Likewise, by means of (4.56), (4.57) and (4.58) along with (4.46) and (4.46), the tangential matrices

$$\boldsymbol{K}_{IL}^{uu} = \underset{e=1}{\overset{\mathrm{n_{el}}}{\mathbf{A}}} \left\{ \int_{\mathcal{B}_e^h} \nabla_x N^i \cdot \hat{\mathbb{C}}^{uu} \cdot \nabla_x N^l \ dV \right\},$$

$$\boldsymbol{K}_{IM}^{u\varphi} = \underset{e=1}{\overset{\mathrm{n_{el}}}{\mathbf{A}}} \left\{ \int_{\mathcal{B}_e^h} (\nabla_x N^i \cdot \hat{\boldsymbol{C}}^{u\varphi}) N^m \ dV \right\},$$

$$\boldsymbol{K}_{JL}^{\varphi u} = \underset{e=1}{\overset{\mathrm{n_{el}}}{\mathbf{A}}} \left\{ \int_{\mathcal{B}_e^h} N^j (\boldsymbol{C}^{u\varphi} \cdot \nabla_x N^l) \ dV \right\},$$

$$K_{JM}^{\varphi\varphi} = \underset{e=1}{\overset{\mathrm{n_{el}}}{\mathbf{A}}} \left\{ \int_{\mathcal{B}_e^h} \nabla_x N^j \cdot \hat{\boldsymbol{D}} \nabla_x N^m \ dV - \int_{\mathcal{B}_e^h} N^j (-\phi_d) N^m \ dV \right\},$$

$$(4.60)$$

To this end the global residual vectors associated with the hygro-chemo-mechanical problems are represented as $\mathcal{R} := [\boldsymbol{R}^u \ \boldsymbol{R}^\varphi]^T$, and the global vectors embracing the mechanical and hygral degrees of freedom (DOFs) are defined as $\mathcal{D} := [\boldsymbol{d} \ \Phi]^T$. Furthermore, the global coupled tangent matrix including the determined tangential matrices are presented as

$$\mathcal{K} := \begin{bmatrix} \boldsymbol{K}^{uu} & \boldsymbol{K}^{u\varphi} \\ \boldsymbol{K}^{\varphi u} & \boldsymbol{K}^{\varphi\varphi} \end{bmatrix}$$

The repetitive solutions of determined mechanical, hygral DOFs at the global nodes of the finite element meshes are obtained through the following equation

$$\mathcal{D} = \bar{\mathcal{D}} - \bar{\mathcal{K}}^{-1} \cdot \bar{\mathcal{R}} \qquad (4.61)$$

where $\bar{\mathcal{R}} := \mathcal{R}(\bar{\mathcal{D}})$, $\bar{\mathcal{K}} := \mathcal{K}(\bar{\mathcal{D}})$ indicates respectively the global residual vectors and global coupled tangent matrix. The solutions related to predefined DOFs are calculated at time $t = t_{n+1}$ for an intermediate repetitive values $\bar{\mathcal{D}}$. This problem is solved with a staggered approach.

4.4 Representative Numerical Examples

In this section, the thermodynamically consistent poroviscoelastic model, proposed in this chapter is validated through the experimental results of creep and shrinkage. The numerical results obtained from the proposed approach are partly presented in [171]. We first investigate the basic creep behavior of concrete consider without considering the drying effects. The intrinsic creep response of concrete accounting for the mechanical loading and the hygral effects is then studied through the flexural deflection test. Drying shrinkage in a concrete ring, slabs and square prismatic specimens is simulated in this section to demonstrate the capability of the proposed model.

In the following representative numerical examples, a generalized Maxwell model with tow elements are used, see Figure 4.2 in which for simplicity, we take the upper branch retardation time as $\tau_1 = \infty$ and its elastic modulus takes the ultimate value $E_1 = E_\infty$. The relation between E_1 and E_2 are assumed to be $3:1$, i.e. the elastic modulus belonging to the upper branch reaches about the 0.33% its ultimate value when the degree of hydration reaches its asymptotic value [34]. Also, for the upper branch we use the ultimate value of the Biot's coefficient $b_1 = b_\infty$ and the Biot's modulus, $M_1 = M_\infty$, as these parameters are determined as function of the degree of hydration for the lower branch.

4.4.1 Basic Creep Tests

The basic creep occurs in a concrete specimen under fixed mechanical loading, while it is completely sealed so that the humidity transfer between the interior and exterior of the solid body is not allowed. In the first example (`BC-C-R120/80`), we investigate the experimental studies reported in [172] consisting of monotonic and cyclic tests. In the monotonic creep experiments, the specimens are subjected to an axial compressive stress 30% of the instant compressive strength at the age of loading. The specimens used in the monotonic and cyclic tests are cylinders whose geometric dimensions are presented in Figure 4.4. In the finite element model, a single eight-node brick element is used to discretize the domain. The cyclic loading scenario, applied on the cylindrical specimen is depicted in Figure 4.5.
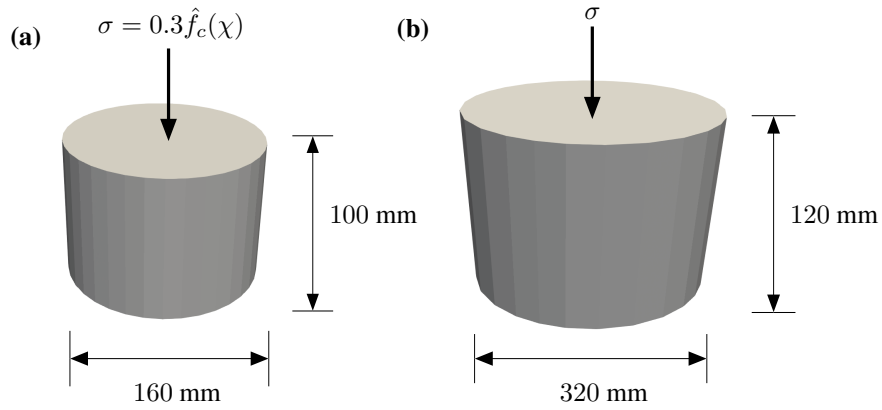
Figure 4.4: Basic creep tests. **(a)** Geometry, dimensions and loading conditions of the cylindrical specimen used in the analysis of monotonic test, and **(b)** Geometry, dimensions and loading conditions of the cylindrical specimen used in the analysis of cyclic test.
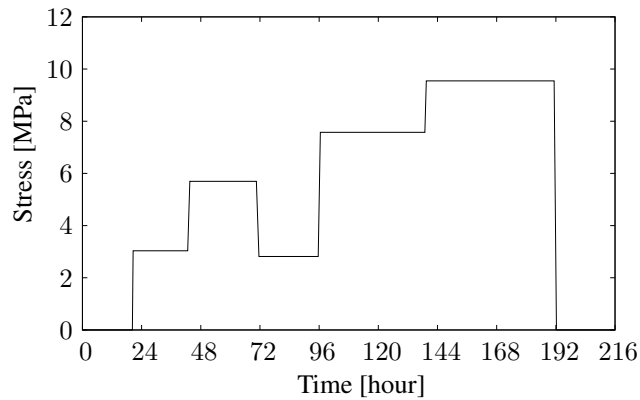
Figure 4.5: Cyclic loading condition applied on the cylindrical concrete specimen

The results obtained through the numerical approach versus the experiments [172] are demonstrated in Figure 4.6. The results represent that the model applied in this study has a good capability of predicting the basic creep response under the cyclic loading. In terms of the monotonic loading, the proposed model presents an accepted prediction capability at $t = 72$ h, $t = 168$ h and $t = 675$ h, however, at the earlier ages ($t = 18$ h and $t = 24$ h), there exist differences between the experimental and numerical results. To obtain improved predictions, it is required to reanalyze the problem with the parameters which control the development of concrete creep response and its strength. The hydration process is a complex phenomenon and the effects of what occurs in the microstructure of the concrete may not be completely considered in the

134

macroscopic model, such as the effect of the variation of the interior humidity due to the self-desiccation phenomenon on the hydration model and the consequences of the aging effect in terms of the development of physicochemical characteristics of concrete. Moreover, the results show that as the applied load is increased with the age at loading, the creep-induced strain increases in the both monotonic and cyclic loading test. The material properties for this example, taken form [34] are given in Table 4.3.
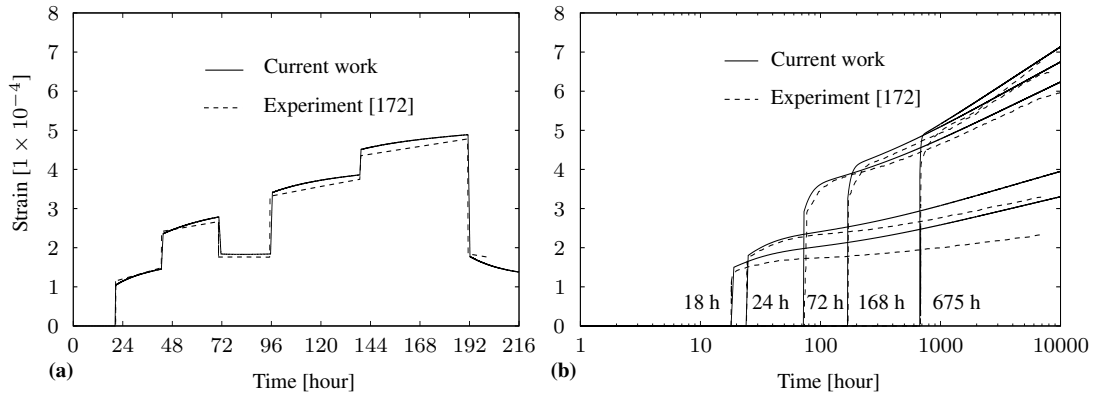
Figure 4.6: Basic creep tests: **(a)** cyclic test on the cylindrical concrete specimen, and **(b)** monotonic test on the cylindrical concrete specimen

In the second example (`BC-P-SQ`), the experimental results associated with the basic creep, reported in [173] are numerically modeled. The study investigated experimentally the effects of creep on the longer span concrete bridges where the effect of loading age on the creep behavior of the concrete specimens is evaluated. The experiments were conducted on the square prismatic concrete specimens. The specimens are completely sealed to observe the basic creep behavior in concrete specimens. They are subjected to a constant value of compressive stress with $\bar{\sigma}_0 = 7$ MPa at different ages of concrete with $t = 8, 14, 21, 28, 84$ and 182 days. The initial temperature is $\theta_0 = 20°$C. The geometric set-up, the dimensions of the specimens and the loading condition are illustrated in Figure 4.7. In the finite element model, a single eight-node brick element is used to discretize the domain. The numerical and experimental results in terms of the longitudinal compressive strain corresponding to the loading at $t = 8, 14, 21, 28, 84$, and 182 days are demonstrated in Figure 4.8.

The results obtained from the proposed model are conforming to the experiments.

135
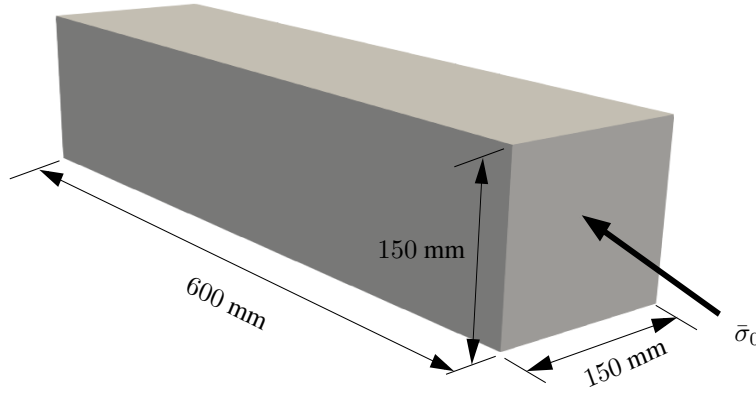
Figure 4.7: Basic creep tests. Geometry, dimensions of the specimens with square cross-section and loading condition.
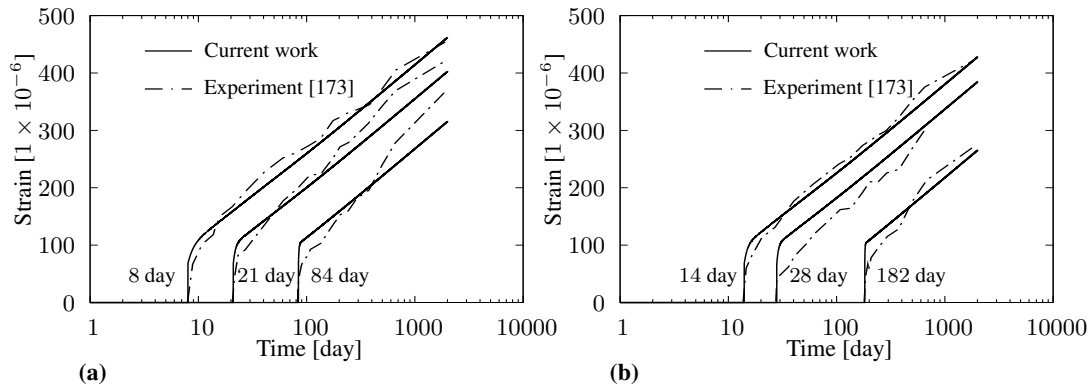
Figure 4.8: Basic creep tests: **(a)** the square prismatic specimens are loaded at the age of 8, 21 and 84 days , and **(b)** the square prismatic specimens are loaded at the age of 14, 28 and 182 days

The results validate the decrease in the creep-induced strain with the increase in the loading age at a constant stressing level. However, there exists small differences between the experiments and the model, as it is observed the model fits the experiments well at $t = 8$ day, $t = 14$ day and $t = 21$ day. To obtain a better match at $t = 28$ day, $t = 84$ day and $t = 182$ day, it may be required to modify the parameters associated with the aging and the microprestress models associated with the development of the mechanical properties and the viscosity of the dashpot that represents long-term viscous flow. The other reason may be related to the ratio of the springs elastic moduli in the Generalized Maxwell Model. In this example, the material properties related to the chemo-mechanical model are derived by fitting the empirical equation, given

in [173] for the evolution of the elastic modulus of the hardening concrete. These parameters are given in Table 4.3.

In the third example (BC-C-R75), the basic creep test is conducted on the cylindrical specimens made up of high-strength concrete which is used in the bridge construction [174]. The study investigated experimentally and numerically the short- and long-term behavior of a prestressed bridge constructed from a high performance concrete. The behavior of long-span continuous box girder bridges made up of prestressed concrete is highly sensitive to the creep and shrinkage phenomena. In [174], the analysis was conducted by applying the solidification-microprestress-microplane model (SMM), proposed in [32].

The specimens are subjected to a constant $\bar{\sigma}_0 = 14$ MPa compressive stress at different concrete ages (2 and 28 days). They are loaded at constant temperature $\theta_0 = 20°$C. The geometry, the dimensions of the concrete specimens and the loading condition are shown in Figure 4.9. To discretize the finite element model, we use a single eight-node brick element. The results of the creep tests comparing to the experimental findings are exhibited in 4.10. The material properties adopted for the numerical studies of the basic creep related to the examples demonstrated above are given in Table 4.3.
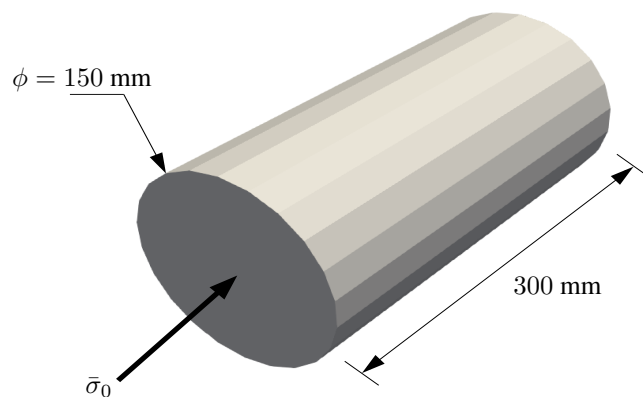
Figure 4.9: Basic creep tests. Geometry, dimensions of cylindrical concrete specimen and loading condition.

The numerically obtained results are consistent with the experiments and ones obtained from the SMM model. Also, it is observed that at the constant level of stressing as the age of concrete increases the creep-induced strain decreases in the specimen. To obtain a better fit, it may be required to redefine the parameters governing the development of the mechanical properties and the ones related to the viscosities of the dashpot such as the constants employed in the microprestress model and the calculation of the viscous trains. The material properties associated with the chemomechanical model for the hardening concrete are obtained by fitting the evolution of elastic modulus and compressive strength reported in [174]. These parameters are presented in Table 4.3.
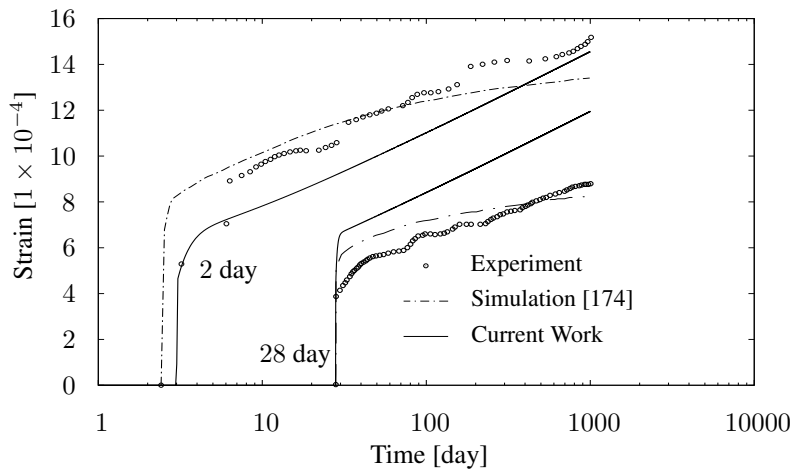
Figure 4.10: Basic creep tests. **(a)** cyclic test on the cylindrical concrete specimen, and **(b)** monotonic test on the cylindrical concrete specimen

4.4.2 Flexural Creep Tests

In the literature, concrete creep response to different environmental conditions is generally measured using the unaxial compressive or tensile test. However, the measurement obtained form a test including the effects of creep and shrinkage, it is required to decouple the creep deformation from the measured total deformation. To quantify the intrinsic creep from the measured deformation, the flexural deflection test is proposed in [175]. The intrinsic creep property of concrete is shrinkage- and size-independent, and it is only dependent on the mixture proportion of concrete. Therefore, the aim of

Table 4.3: Material properties of the Portland cement concrete used for the creep tests analyses

Parameter	Unit	`BC-C-R120/80`	`BC-P-SQ`	`BC-C-R75`
Hydration and Aging				
w_0/c	[–]	0.5	0.47	0.37
θ_0	[K]	294	294	294
E_a/R	[K]	4×10^3	4.45×10^3	4.14×10^3
ξ^∞	[–]	0.75	0.58	0.67
k_ξ/η_{ξ_0}	[1/h]	1×10^6	8×10^6	1×10^6
A_ξ/η_{ξ_0}	[–]	1×10^{-4}	1×10^{-6}	1×10^{-6}
η_ξ	[–]	7.5	6	5.5
A_f, B_f	[–]	2.56, 0.37	3.25, 1.125	2.01, 0.95
f_c^∞	[MPa]	47.5	40	69.5
Poro-visco-mechanical				
μ_s	[1/(MP h)]	—	—	—
α_r	[–]	0.1	0.1	0.1
τ_{μ_0}	[h]	7×10^2	7×10^2	1×10^3
c_{μ_0}	[1/h]	6×10^{-3}	6×10^{-3}	1×10^{-2}
τ_1	[h]	∞	∞	∞
τ_2	[h]	15	15	25
b_∞	[–]	0.4	0.4	0.4
M_∞	[MPa]	6×10^3	6×10^3	6×10^3

this type of test is to reduce the effect of shrinkage on the measured creep, specially for concrete at early ages when the drying condition in not inevitable. The flexural test is conducted based on a four-point bending beam, shown in Figure 4.11. For this purpose, the concrete beams with dimensions of 50 mm in height, 50 mm in width, and 1220 mm in length are used. The deflections of beam at specified points are measured by a linear variable differential transformer (LVDT). The beams are sealed

in all faces for the sealed cases and for the unsealed cases only the top and bottom faces of the specimens are exposed to drying condition, i.e. the environment with the relative humidity of $\varphi = 40\%$.

The locations of the LVDTs to measure the beam deflection are at the mid-span and the 350 mm from the mid-span, see Figure 4.11. The beam specimens are subjected to their weights, and the external loads of 10 kg are symmetrically applied at the points located 200 mm from the supports as illustrated in Figure 4.11. To this end, the time-dependent deflection of the loaded beam is in the main caused by the external load as well as the self-weight of the beam and its deflections under drying creep is calculated based on the approach proposed in this study and the results are compared with the experiments. The geometry, the placement of the measuring devices, the dimensions, the boundary and the loading conditions, and the sealing state of the beam specimens are illustrated in Figure 4.11. The beam is discretized with 4270 eight-node brick elements. The material properties used for analyzing the flexural test of the four-point bending beam `FC-BEAM` are given in Table 4.4.

In the current example, only two Maxwell elements are used, see Figure 4.2, in which for simplicity, we take the upper branch retardation time as $\tau_1 = \infty$ and its elastic modulus takes the ultimate value $E_1 = E_\infty$. The ratio of E_1 to E_2 is assumed to be $3 : 1$, i.e. the elastic modulus belonging to the lower branch reaches about the 0.33% its ultimate value when the degree of hydration reaches its asymptotic value. Also, for the upper branch we use the ultimate value of the Biot's coefficient $b_1 = b_\infty$ and the Biot's modulus $M_1 = M_\infty$, as these parameters are determined as a function of the degree of hydration for the lower branch. The material properties related to the chemo-mechanical model are derived by fitting the evolution of the elastic modulus given in [175]. The parameters related to the viscous and the hygral parts of the model are obtained through the fitting of the experimental results.

The numerically and experimentally measured creep-induced deflection of the concrete beam for the sealed and the drying cases are respectively demonstrated in Figure 4.12. The results obtained through the proposed model in this study are in good agreement with ones are experimentally obtained. In this example, we aim to solve a problem which has a more complex phenomenology involving the cross-effects of the vis-
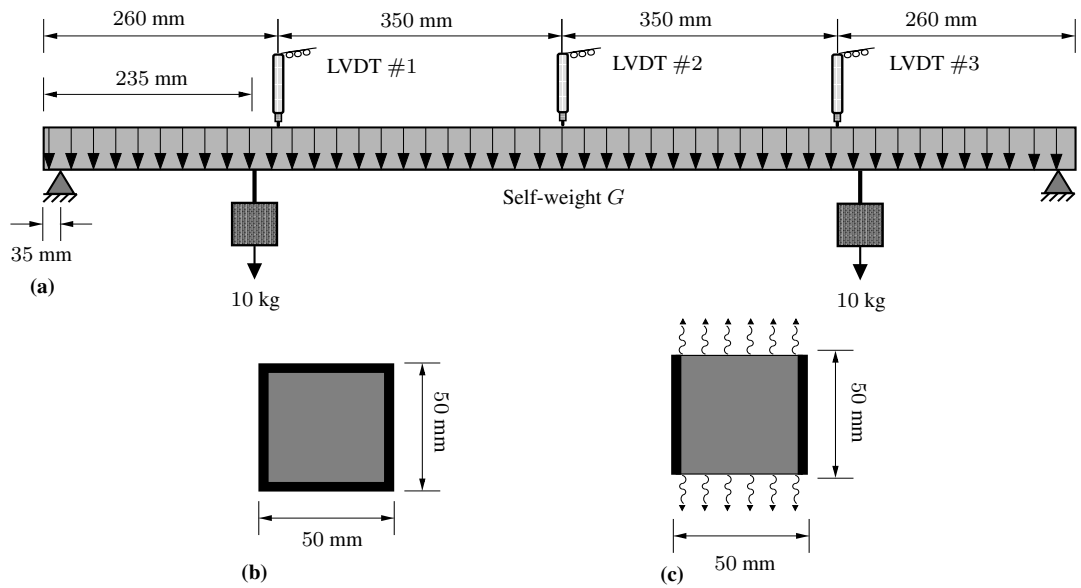
Figure 4.11: Flexural creep test: **(a)** geometric dimensions, boundary and loading conditions of loaded specimens **(b)** condition of sealed specimens and **(c)** condition of unsealed specimens

coelastic and hygral responses. Another point should be considered is the complexity of the physicochemical phenomena occuring during the hydration at the microstructure of the concrete, which may not be completely contemplated in the macroscopic formulation such as the effect of the variation of the internal water content originating from the chemical or autogenous shrinkage at the early ages. Therefore, we can obtain a better prediction of the experiments by modifying the parameters associated with the aging model that is applied to determine the evolution of the mechanical parameters and the determination of the dashpot viscosities used to define the viscous response of concrete. Moreover, redefining the parameters related to the diffusivity of concrete may present an accepted fit in terms of the drying shrinkage. On the other hand, it may be demanded to reformulated the expression dealing with the autogenous shrinkage in (4.35), to have a more robust simulation of the self-desiccation phenomenon at the early ages. The distribution of the beam deflection at the end of the test for the sealed case is represented in Figure 4.13.

The distribution of the relative humidity and the beam deflection at the end of the test for the drying case are depicted in Figure 4.14.
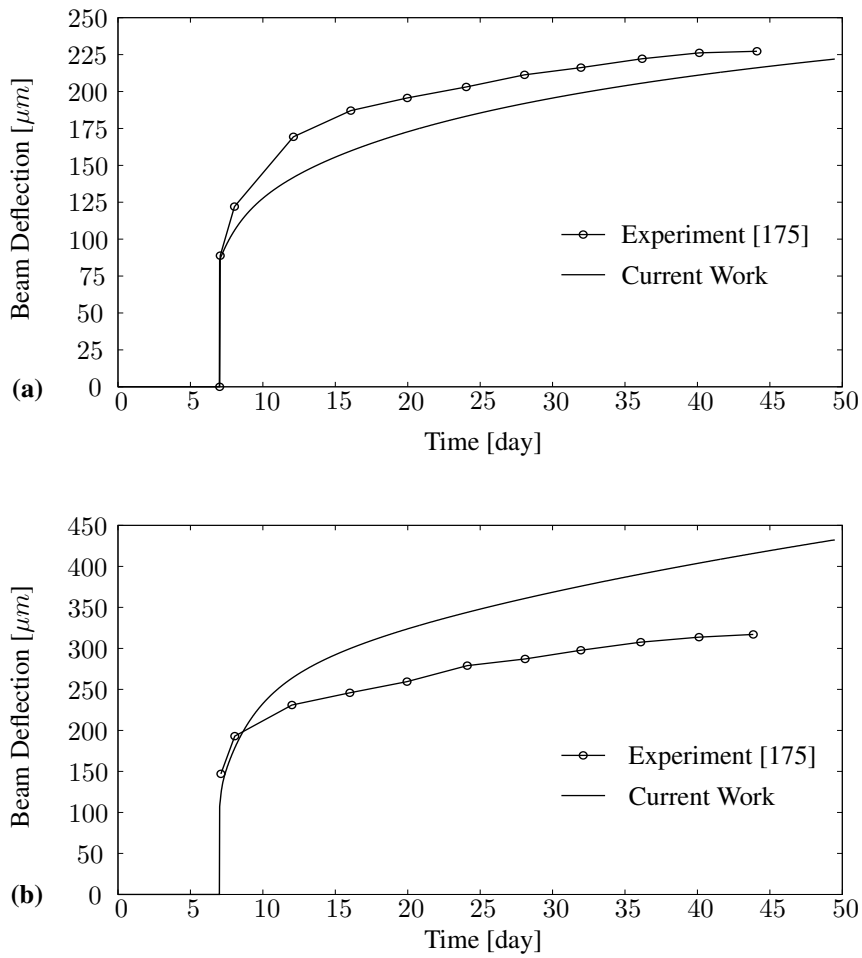
Figure 4.12: Flexural deflection of concrete beam under different conditions: **(a)** sealed curing under self-weight of the beam and **(b)** exposed simultaneously to drying at the age of 7 days under self weight and external loading.
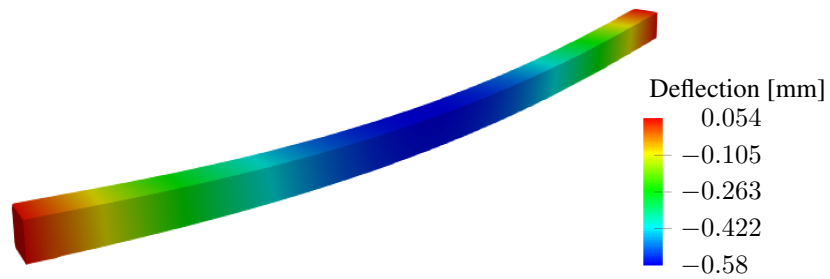
Figure 4.13: Distribution of the creep-induced deflection in the concrete beam under the sealed condition at the end of the test.
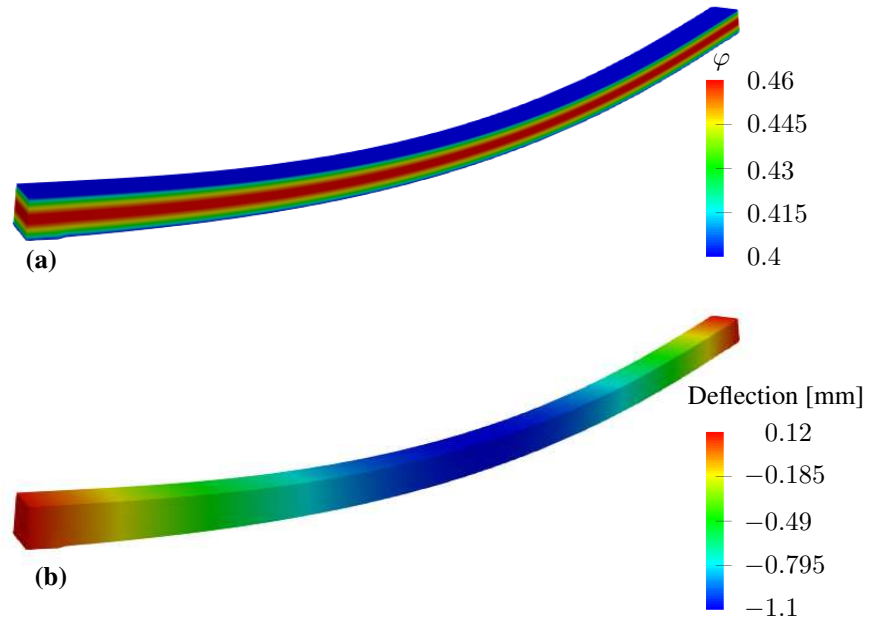
Figure 4.14: Flexural deflection of concrete beam under drying condition. **(a)** Distribution of the relative humidity and **(b)** distribution of the creep-induced deflection, in the concrete beam at the end of the test.

4.4.3 Drying Shrinkage Tests in Concrete Ring Specimens

In the case of drying shrinkage where the concrete structure is subjected to the environment with the humidity lower than the internal one, we study the distribution the internal relative humidity and shrinkage induced effects in steel-concrete composite ring test [145]. A steel ring has the outer diameter $\phi_{\text{out}}^{\text{s}} = 320$ mm and inner diameter $\phi_{\text{in}}^{\text{s}} = 260$ mm, and the outer and inner diameters of the composite ring are respectively $\phi_{\text{out}}^{\text{c}} = 360$ mm and the $\phi_{\text{out}}^{\text{c}} = 320$ mm, i.e. the thickness of concrete is 35 mm used in this study. The height of the specimen is 150 mm. The fresh concrete is cast into the ring mold in two layers and consolidated by a vibrating table. The casting faces are sealed with soft plastic sheet to prevent moisture exchange with its surroundings after finishing the surfaces. After 3 days, the plastic sheet is removed but the top and bottom surfaces are still sealed, so the specimen is subjected to the environmental condition with $\varphi_\infty = 40\%$ from the circumferences. The geometric dimension of the ring specimen and its two-dimensional finite element model is rep-

143

resented in Figure 4.15. The concrete ring domain is discretized with 2400 four-node quadrilateral plain strain elements.

In the literature, the results are obtained in terms of the evolution of internal humidity and shrinkage induced strain, through the micromechanical model proposed in [140]. The micromechanical approach is an analytically derived model, developed on the basis of the capillary tension in capillary pores. According to the model, the shrinkage-induced stress and strain are computed in terms of the radius of meniscus, formed between the capillary pores during the hydration process, the variation of relative humidity and the surface tension of water. The micromechanical approach is fundamentally constructed on a theoretical model including semi-empirical formulation to calculate the shrinkage-induced stress-strain response of concrete. The variation of the relative humidity in terms of the autogenous shrinkage is determined based on a semi-empirical expression, as well. After fitting the experimentally recorded variation of the relative humidity, the shrinkage-induced strain is determined as a function of the the shrinkage coefficient also know as the coefficient of hygral contraction in the literature, which acts in a multiplicative format on the relative humidity. In this study, in contrast to the micromechanical model, we apply the physically based poro-viscoelastic approach to model the drying shrinkage in the concrete ring specimen.
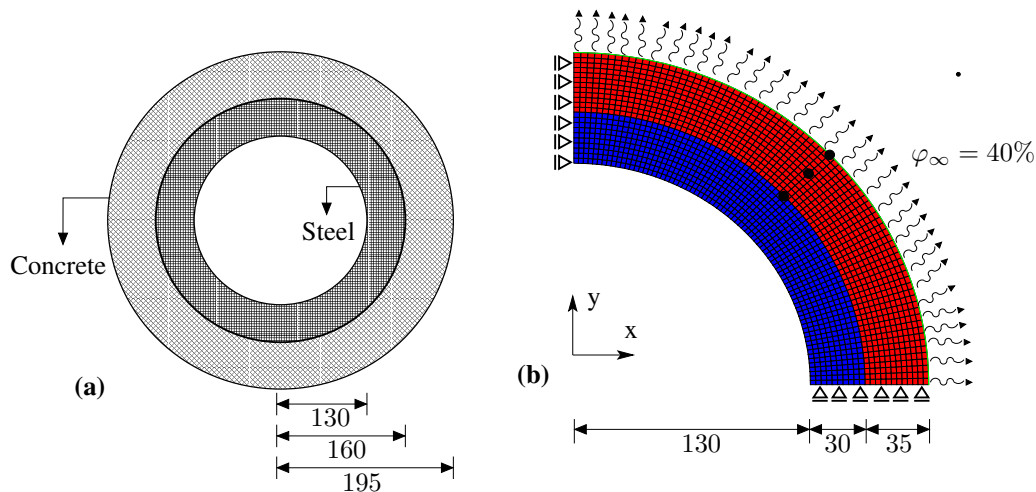
Figure 4.15: Drying shrinkage: **(a)** geometric dimensions of the steel-concrete composite ring, **(b)** FEM model and boundary conditions (all dimensions are in mm)

The results in terms of the evolution of internal relative humidities and shrinkage induced strains at the outer, the central and the internal surfaces of the ring specimen filled with concrete having the characteristic strength of about 50 MPa on the 28th day of its age (C30) are represented in Figure 4.16. Also, the distribution of the shrinkage induced strains in concrete ring are presented in Figure 4.17.
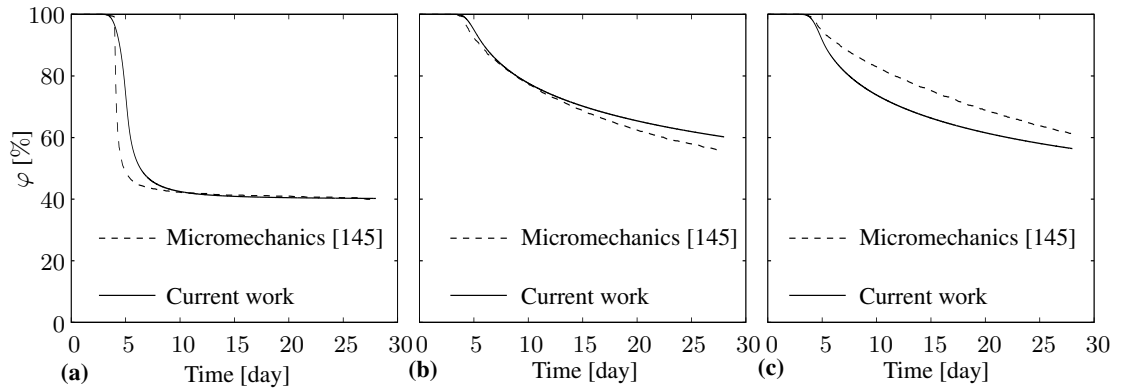
Figure 4.16: Drying shrinkage: the distribution of internal relative humidity **(a)** at the outer surface, **(b)** at the center and **(b)** at the inner surface of the concrete specimen (C30)
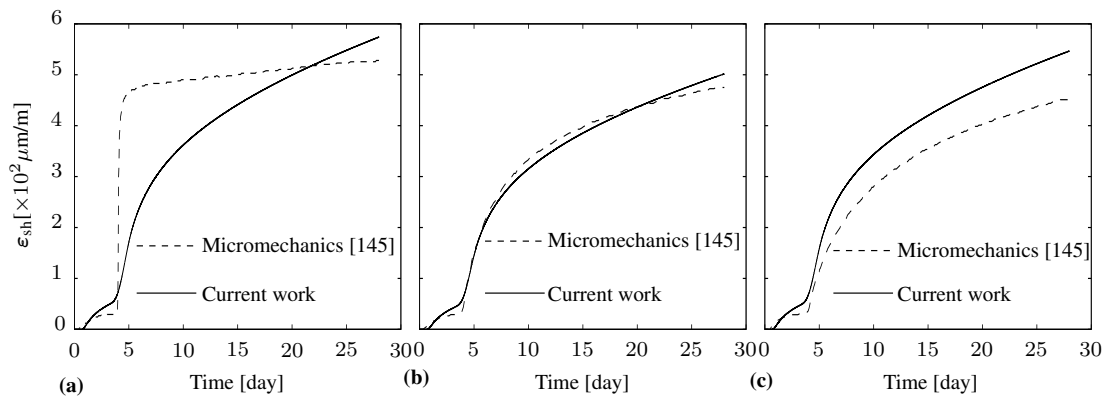
Figure 4.17: Drying shrinkage: the distribution of shrinkage induced strain **(a)** at the outer surface, **(b)** at the center and **(c)** at the inner surface of the concrete specimen (C30)

The capability of the proposed approach in simulating drying shrinkage is represented by further analysis of the steel-concrete ring test filled with the concrete having the characteristic strength of about 50 MPa on the 28th day of its age (C50). The asso-

ciated distribution of the relative humidity and shrinkage induced strain at the outer, central and inner surfaces are respectively demonstrated in Figure 4.18 and Figure 4.19.
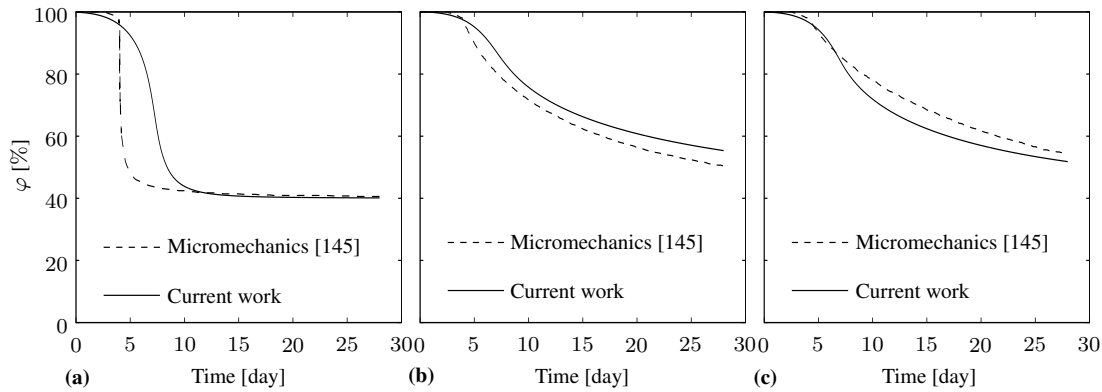
Figure 4.18: Drying shrinkage: the distribution of internal relative humidity at **(a)** outer surface, **(b)** center and **(b)** inner surface of the concrete specimen (C50)
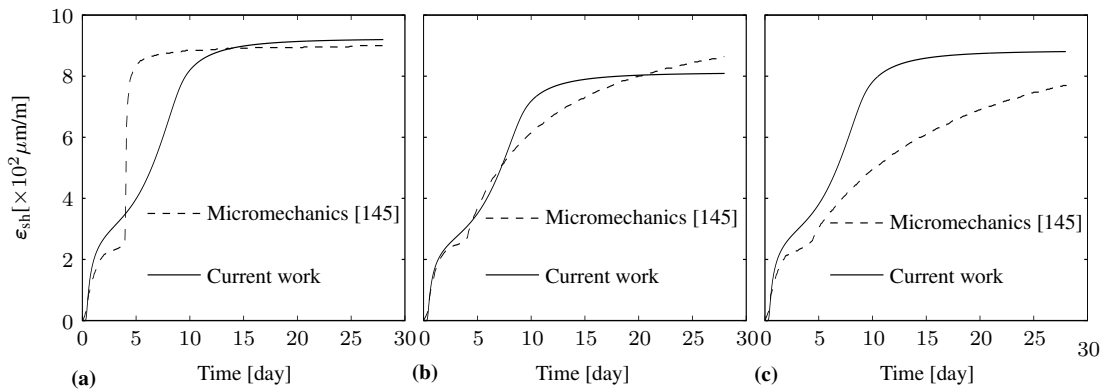
Figure 4.19: Drying shrinkage: the distribution of shrinkage induced strain at **(a)** outer surface, **(b)** center and **(b)** inner surface of the concrete specimen (C50)

The results show that there is a good agreement between the micromechanical model proposed in [145] and the model developed within the poro-viscoelasticity in the current study. However, the small differences observed between the results of these two approaches. These differences may originate from the dissimilarity of the approaches.

The distribution of the relative humidity (φ) and the maximum principal stress (σ_{max}) for the ring specimen with the concrete C30 and C50 are represented in Figure 4.20 and 4.21.
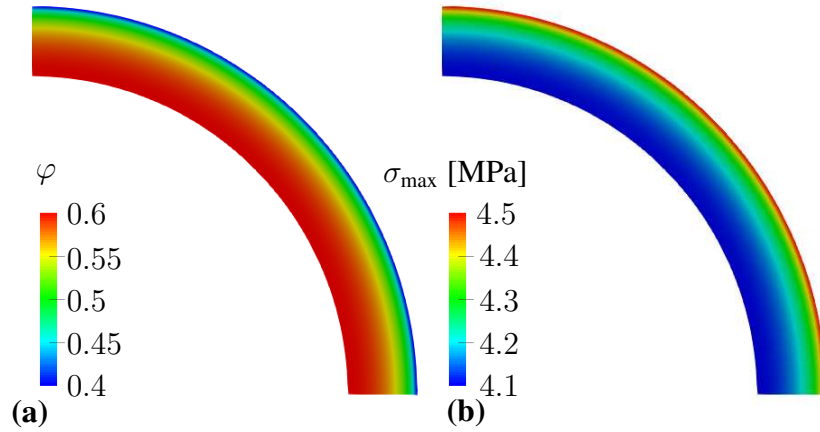
Figure 4.20: Drying shrinkage: **(a)** Distribution of the relative humidity and **(b)** distribution of the maximum principal stress in the concrete ring specimen (C30).
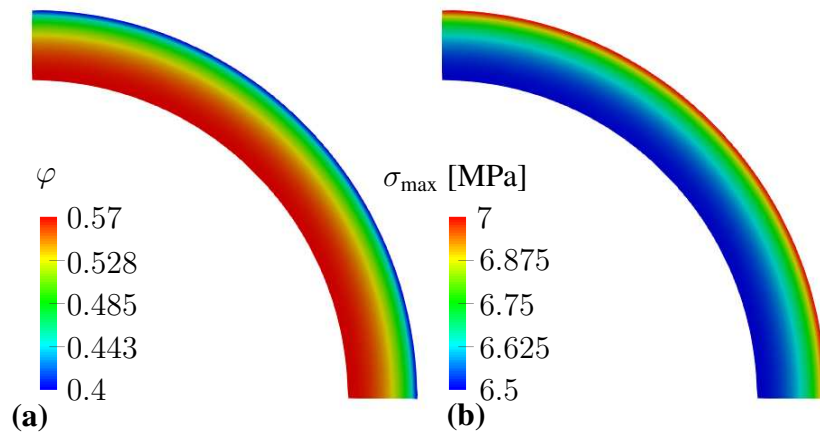
Figure 4.21: Drying shrinkage: **(a)** Distribution of the relative humidity and **(b)** distribution of the maximum principal stress in the concrete ring specimen(C50).

The material properties adopted in the chemo-mechanical model are taken from [145], and the material constants associated with the viscous and the hygral parts are defined by fitting the experimental results in terms of the distribution of relative humidity and shrinkage-induced strain. The material properties of concrete C30 (`DS-R-C30`) and C50 (`DS-R-C50`) used in the related analyses of drying shrinkage in ring specimens are given in Table 4.4.
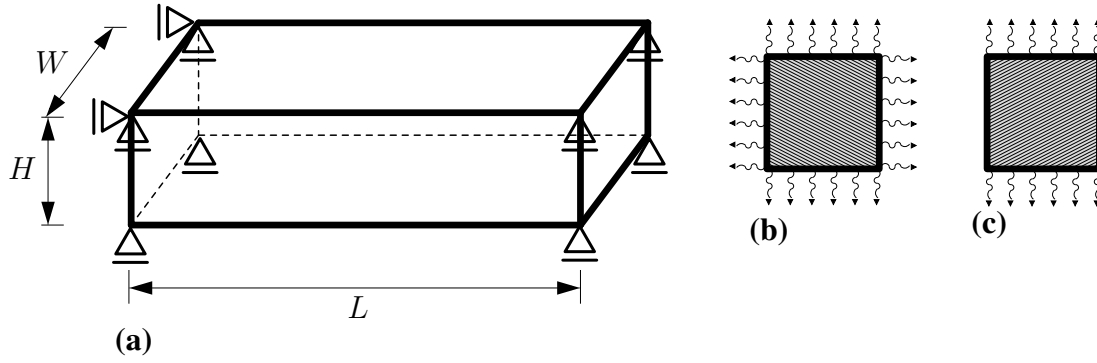
Figure 4.22: Drying shrinkage test. **(a)** Geometry, dimensions and boundary conditions, **(b)** drying condition of square prismatic specimen (`DS-P-SQ`) and **(c)** drying condition of thick slab specimen (`DS-P-TS`).

4.4.4 Drying Shrinkage Tests in Concrete Prismatic Specimens

The proposed poroviscoelasticity approach is applied to simulate the behavior of concrete square columns and thick slabs under drying shrinkage, reported in [173]. This study deals with the experimental investigation, aiming at validating shrinkage prediction methods applied in design of longer span concrete bridges. The specimens, used in this study are the square columns and the thick slabs. The geometric set-up, the dimensions, the boundary conditions of the square prismatic columns (`DS-P-SQ`) and the thick slabs (`DS-P-TS`) with $H = W$ and $L = 4 \times H$ are depicted in Figure 4.22. The domains of the square prismatic columns and the thick slabs are discretized with 6912 eight-node brick elements. In the square prismatic columns (`DS-P-SQ`), the four sides of the concrete specimens are exposed to the environment with ambient relative humidity of $\varphi_\infty = 40\%$, and the ends of the specimens are sealed. In the case of the thick slabs (`DS-P-TS`), the top and the bottom sides of the specimens are exposed to the environment with ambient relative humidity of $\varphi_\infty = 40\%$, and the other sides in addition to the ends of the specimens are sealed.

We analyze the drying shrinkage test in the square prismatic columns and thick slabs with the dimensions of $100 \times 100 \times 400$ mm^3, $150 \times 150 \times 600$ mm^3 and $200 \times 200 \times 800$ mm^3. The results are numerically obtained in terms of the shrinkage-induced strain and compared with the experiments reported in [173]. The shrinkage-induced strain obtained from the analysis conducted using the proposed model for each of the square

148
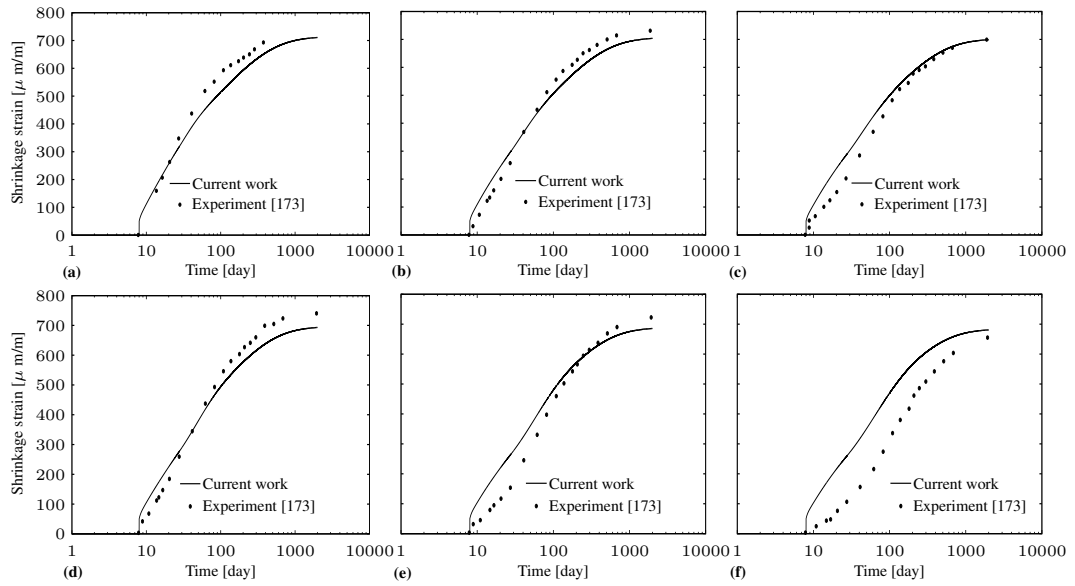
Figure 4.23: Drying shrinkage test. Shrinkage-induced strain for **(a)** 100 mm square prismatic column **(b)** 150 mm square prismatic column, **(c)** 200 mm square prismatic column, **(d)** 100 mm thick slab, **(e)** 150 mm thick slab and **(f)** 200 mm thick slab.

prismatic columns and the thick slabs are presented in Figure 4.23 in comparison with the experiments.

The results show that the proposed model is able to provide a good prediction of the structural response to the shrinkage phenomenon in concrete. The material properties used in the chemo-mechanical model are determined by fitting the empirical expression representing the evolution of elastic modulus, given in [173]. The material constants related to the viscous and the hygral parts are defined by fitting the experimental results in terms of the shrinkage strains numerically.

4.5 Concluding Remarks

In the current study, we address the durability phenomena arise from drying shrinkage and creep in concrete structures. To describe these problem computationally within the three-dimensional thermodynamically consistent framework, we propose a phenomenological approach. This approach accounts for the hygro-chemo-mechanical cross coupling effects between the shrinkage-induced strain development due to the

Table 4.4: Material properties of the Portland cement concrete used for the flexural creep and drying shrinkage analyses

Parameter	Unit	FC-BEAM	DS-R-C30	DS-R-C50	DS-P-SQ/TS
Hydration and Aging					
w_0/c	[–]	0.3	0.62	0.43	0.47
θ_0	[K]	296	294	294	294
E_a/R	[K]	5×10^3	4×10^3	5×10^3	4.45×10^3
ξ_∞	[–]	0.625	0.825	0.75	0.58
k_ξ/η_{ξ_0}	[1/h]	2.5×10^7	5.25×10^5	1×10^5	8×10^6
A_ξ/η_{ξ_0}	[–]	1×10^{-5}	1×10^{-5}	1×10^{-5}	1×10^{-6}
η_ξ	[–]	6.5	7.25	7.25	5.5
A_f, B_f	[–]	1.125, 1.165	0.825, 1.02	0.53, 1.22	3.25, 1.125
f_c^∞	[MPa]	75	34.1	50	40
Poro-visco-mechanical					
μ_s	[1/(MP h)]	7.02×10^{-8}	7.02×10^{-8}	7.08×10^{-8}	7.02×10^{-8}
α_r	[–]	0.1	0.1	0.1	0.1
τ_{μ_0}	[h]	7×10^2	7×10^2	7×10^2	1×10^3
c_{μ_0}	[1/h]	6×10^{-3}	6×10^{-3}	6×10^{-3}	20×10^{-3}
τ_1	[h]	∞	∞	∞	∞
τ_2	[h]	15	15	15	25
b_∞	[–]	0.4	0.4	0.4	0.4
M_∞	[MPa]	6×10^3	6×10^3	6×10^3	6×10^3
Hygral					
c	[kg/m^3]	810	345	445	345
χ^{ws}	[–]	2.85×10^{-2}	1.25×10^{-2}	2.85×10^{-2}	1.35×10^{-2}
f_1	[–]	2	2	2	2
f_2	[–]	7	7	7	7
D_0	[m^2/d]	4.32×10^{-8}	1.296×10^{-6}	1.296×10^{-6}	8.424×10^{-6}
D_1	[m^2/d]	1.512×10^{-4}	9.504×10^{-3}	4.752×10^{-3}	3.681×10^{-4}
ϱ	[–]	4.5	5.95	5.95	5
α_s	[kg/(m^2 s)]	225	57.5	57.5	2.225
ρ^f	[kg/m^3]	1×10^{-6}	1×10^{-6}	1×10^{-6}	1×10^{-6}
ρ^f	[kg/m^3]	997	997	997	997

pressure evolution through humidity variations and the stress concentrations in hardening or hardened viscoelastic concrete. The evolution of mechanical properties of concrete at early ages are described in terms of the hydration and aging phenomena within the chemo-mechanical setting base on the theory of reactive porous media.

We investigate the shrinkage in concrete which results from the variation of the internal water content due to the self-desiccation and the drying shrinkage phenomena. In the literature, the majority of the studies have developed an empirical formulation to compute the shrinkage-induced stress-strain response of concrete based on the experimental results. In these studies, the shrinkage-induced strain is defined as a function of a shrinkage coefficient, the so-called the coefficient of hygral contraction that acts in a multiplicative manner on the variation of the water content or the relative humidity. This coefficient is also determined as a linear or hyperbolic function of the water content or the relative humidity. As opposed to the existing modeling methods, we apply a physically motivated approach within the three-dimensional framework of poroviscoelasticity, in which the general theory of poroelasticity is employed to explain the shrinkage effect on the basis of the pore-pressure variation in the pore-structure of concrete caused by the variation in the water content. The pore-pressure is determined by using the adsorption-desorption isotherm model which defines the water content in terms of the relative humidity. In this sense, the variation of the pore pressure is implicitly computed as a function of the relative humidity. In addition, the viscoelastic behavior of concrete is considered to explain the realistic short- and long-term assessment of creep phenomena in concrete applying the microprestress theory. The viscoelastic response is formulated on the bases of defining the viscosity of concrete originated from the aging phenomenon and the flow term through the well-known microprestress theory. The latter explains the effect of variation of temperature and the relative humidity on the concrete viscoelastic response.

The material parameters used in each numerical example are taken from the related experimental study in the literature. But, in the examples that some of the parameters are not given for the specific type of concrete, I referred to the literature to take the parameters from other studies which use concrete with the mix design close to my cases. Otherwise I have performed the parametric studies until obtaining an acceptable match between the analyses and the experiments considering the lower and upper bound of the parameters.

The capability of the proposed model is then validated by computationally modeling of creep and shrinkage in several representative numerical examples. These examples include the basic creep, flexural creep and drying shrinkage. The obtained results

151

agree well with the experiments. This indicates that the proposed poroviscoelastic model provides a good prediction of concrete response to the creep and shrinkage effects. These problems have complex phenomenology with many material parameters expressing the coupled effects of the autogenous and drying shrinkage, and the viecoelastic behavior. Also, the development of these parameters is defined regarding the aging effect. In addition to the aging model, we use two other local models to determine the viscosity of concrete based on the microprestress theory, and the adsorption-desorption isotherm to implicitly compute the pore-pressure as a function of the relative humidity. However, we can find some physical parameters for the definite type of concrete from the literature, but others are defined through a parametric study in which we keep up analyzing the problems until approximately capturing the experimental results. Therefore, the predictive capability of the proposed model may be improved by redefining the material parameters by following their upper and lower limits. In the next chapter, we extend this model to incorporate the phase-field regularized cohesive zone model in order to investigate the concrete fracture under the hygral effects, especially in the case of the drying shrinkage.

CHAPTER 5

PHASE-FIELD MODELING OF SHRINKAGE-INDUCED CRACKING IN CONCRETE

5.1 Introduction

Concrete structures, in particular at their early ages, may undergo significant deformations due to autogenous and drying shrinkage accompanied by the time-dependent creep phenomenon. Therefore, for any concrete structure, an accurate estimation of the service life necessitates a sound understanding and quantitative prediction of creep and shrinkage-induced deformations, and the associated stress concentrations. The latter is greatly affected by durability-related phenomena that starts to arise due to the initiation of micro-cracks as the principal stresses exceed the instant tensile strength of hardening concrete. The drying shrinkage-induced localization of tensile stresses result from uneven volume changes due to the change in relative humidity through the loss of evaporable water from the surface of concrete, in contact with generally less humid air. In the previous chapter, a coupled poroviscoelastic model is developed to computationally account for the hygro-chemo-mechanical cross-coupling effects in concrete at early ages due to imbalance of the internal and external relative humidity. In this chapter, a further coupling is constructed between the poroviscoelastic model and the cohesive zone phase-field approach to simulate the fracture of a concrete structure subjected to drying shrinkage and creep.

In the literature, there exists a variety of studies investigating the failure mechanism of concrete by accounting for a multi-physics coupling of chemo-thermo-mechanical process. In these works, the effects of several factors such as thermal shrinkage, autogenous and drying shrinkage, basic and thermal transient creep, and fracture are

considered.

The effects of micro-cracking and stress-driven shrinkage on the Picket effects, i.e. the pronounced increase in creep caused by the simultaneous existence of drying effect and mechanical loading are investigated in [176, 177]. In these studies, the shrinkage-induced strain is computed by multiplying a relative-humidity-dependent coefficient of hygral contraction by the obtained relative humidity. This expression is derived by fitting the experimental results. However, it is not implicitly mentioned any fracture methods in these works.

The hydric damage model [178], proposed on the basis of the local elastic damage model in the work of Mazars [179], is examined to analyze drying shrinkage-induced damage in concrete. According to this method, the damage is modeled by introducing two local variables representing the hygral and mechanical effects. These variables describe the mechanical damage effect projected on the tensile and compressive stresses and the effect of the water content variation on the overall response of concrete, respectively.

The effect of drying shrinkage on the mechanical behavior of concrete is examined in [180] through an experimental study and numerical modeling. Within the numerical framework of this study, the hydro-mechanical model is coupled with the elasto-plastic damage model proposed in [181], founded on the mechanics of partially saturated porous media to take into consideration the desiccation-driven mechanical and capillary plastic deformations, and damage evolution.

The aforementioned studies do not point out the effect of the creep relaxation on the structural response of concrete to the cracking caused by the drying shrinkage. The effect is examined by simulating the differential drying induced micro-cracking of concrete in [182] accounting for the basic and the drying creep models. Cracking is investigated by the isotropic elastic damage model [179] and the orthotropic elastic-plastic damage model presented in [183]. The orthotropic elastic-plastic damage model is adopted to describe the interaction between drying shrinkage, creep, and cracking based on a coupling of the hydromechanical model with an orthotropic elasto-plastic damage model. To this end, the damage is presumed to be isotropic while the body is being subjected to the compressive stresses, whereas it is considered

154

to be an orthotropic in tension due to the drying effects. The corresponding drying shrinkage, basic creep, and drying creep strain tensors are determined in the form of the semi-empirical expressions in terms of the functions of the relative humidity, as the drying shrinkage is related to the water content through a linear relationship.

In order to examine behavior of massive concrete structures in terms of cracking during hardening while both autogenous and thermal shrinkage are being constrained, an experimental study related to the thermal actively restrained shrinkage ring test is conducted in [136]. In [137], a numerical model is developed to express several visco-chemo-thermo-mechanical phenomena happen concurrently at early ages, such as hydration and consequent aging effect, thermal shrinkage, creep and fracture. In this study, the evolution of the mechanical properties are expressed within a chemo-thermal model. The autogenous shrinkage is determined as a function of the degree of hydration, defined in the chemo-thermal model. The transient thermal creep is computed in terms of the temperature evolution and a Kelvin-Voigt model is adopted to describe the basic creep. Moreover, an elastic-damage model inspired in the work of Mazars [179], is employed to simulate cracking under these coupling chemo-thermo-mechanical effects. Further study, associated with the autogenous shrinkage and the creep effects on the meso-scale modeling of concrete at an early age, and the consequent evolution of damage field is reported in [184]. In these aforementioned works, drying shrinkage is not addressed, and the autogenous shrinkage and the transient thermal creep are defined as the local variables, reckoned as a function of the degree of hydration and temporal evolution of the temperature.

The phase-field model [26], which has gotten remarkable popularity among the researchers, is applied to investigate the crack propagation in deforming porous media induced by the variation of moisture content. It specially regards to the modeling of hydraulic fracturing, the so-called fracking [71, 72, 73]. In theses studies, the formulations are developed to express a macroscopic Darcy-Biot-type bulk response of hydro-poro-elasticity, an evolution of regularized crack surface in the solid skeleton, induced by the effective stress, modeling of Poiseuille flow in regularized crack considering a deformation-dependent permeability, and modeling of hydraulic fracturing caused by injections of fluid volume in prescribed spatial domains. The total deformation-dependent permeability is defined in terms of both isotropic and

anisotropic forms for unbroken and broken solids, respectively. The anisotropic permeability for the broken solid describes a modification of fluid transport law when cracking initiates and fluid flow inside the crack path increases. This term is defined as function of the total strain tensor and the crack opening. The brittle phase-field model is further extended to model the desiccation-induced cracking in variably saturated porous medium in the case of the compacted soil [185] within the framework of the poromechanics. This work accounts for a coupling between the deformation, the water-pressure, and the crack phase-field.

Intricate fracture behavior in cementitious materials induced by autogenous shrinkage and generated heat during the hydration process is investigated in [29, 28, 30] by applying the brittle phase-field model [26]. In these studies, a coupling is constructed between the phase-field approach and the chemo-thermo-mechanical model. By means of this model, the heat of hydration and the thermal transfer and the aging effect on the mechanical properties are interpreted. The autogenous shrinkage and the transient thermal creep are calculated in terms of the degree of hydration and the development of the temperature, as for the basic creep a Kelvin-Voigt model is used.

The long-term nonlinear and time-dependent deformations, driven by the thermal, shrinkage and creep effects are studied in [186] on the basis of the extension of the localizing gradient enhanced damage model [187] to the extended microprestress-solidification theory [126]. The strains driven by the flow term is determined as a function of the microprestress and the associated viscosity, as the shrinkage-induced strain conjugates the relativity humidity via the hygral contraction coefficient, which is analogous to the thermal expansion coefficient in thermo-mechanical problems. The consequent evolving damage is defined based on the elastic damage model characterizing the nonlocal gradient form. To overcome the deficiencies related to the standard gradient enhanced damage model [55, 188, 189] such as the counterfeit damage initiation and propagation.

Referring to the literature, we notice that, there does not exist any work related to simulating the hygral effect-induced fracture in hardening concrete using the phase-field regularized cohesive zone method. In the current study, we extend the phase-field regularized cohesive zone model, presented in Chapter 2 to the hygro-chemo-mechanical

156

model proposed within the computational framework of the poroviscoelasticity in Chapter 4 of this thesis.

In the following sections of the current chapter, we present the governing equations and the constitutive relations associated with the hygro-chemo-mechanical model coupled with the cohesive zone phase-field model, and the associated finite element formulation. Then the capability of the model is represented by the numerical examples in which the hygral effects, such as shrinkage, induce cracking in hardening concrete.

5.2 Theory

In this section, the principal relations, involving the governing differential and the constitutive equations, of the coupled boundary value problem of the hygro-chemo-mechanics along with the phase-field approximation of quasi-brittke fracture are developed within the framework of poroviscoelasticity in hardening concrete.

5.2.1 Thermodynamic State

In general, the comprehensive response of hardening concrete to chemical, water transport-related hygral, mechanical, and fracture phenomena are coupled at different scales. Therefore, we construct an isothermal hygro-chemo-mechanical model at macro scale within the framework of the theory of reactive porous media, originally proposed by Ulm and Coussy [3, 190, 4, 6]. To this end, the local thermodynamic state of hardening concrete possibly undergoing water transport hygral-induced quasi-brittle fracture is expressed by the following five state variables

$$\text{State}(\boldsymbol{x}, t) = \{\boldsymbol{\varepsilon}(\boldsymbol{x}, t), \varphi(\boldsymbol{x}, t), d(\boldsymbol{x}, t), \xi(\boldsymbol{x}, t), \boldsymbol{\alpha}(\boldsymbol{x}, t)\} \,. \tag{5.1}$$

The strain tensor $\boldsymbol{\varepsilon}(x, t)$ and the crack phase field $d(\boldsymbol{x}, t)$ have already been introduced in Chapter 2. In addition to the latter, we have the relative humidity field $\varphi(\boldsymbol{x}, t)$, the degree of hydration $\xi(\boldsymbol{x}, t)$ and the viscous strain tensor $\boldsymbol{\alpha}(\boldsymbol{x}, t)$ that characterize the hygral, chemical and the viscoelastic behavior of hardening concrete, respectively. A fundamental state function governing the coupled chemo-thermo-mechanical behav-

ior of hardening concrete exhibiting thermal cracking is the Helmholtz free energy function

$$\Psi = \hat{\Psi}\left(\boldsymbol{\varepsilon}, \varphi, d, \boldsymbol{\alpha}, \xi\right), \tag{5.2}$$

formulated in terms of the state variables (5.1).

According to the theory of reactive porous media, the hydration process in hardening concrete is quantified through an evolution equation of the degree of hydration ξ. This variable is an essential field variable indicating the aging effect in terms of the growth of rigidity and strength of hardening concrete [7, 24, 191, 108]. For this purpose, the degree of hydration ξ is considered as an internal state variable whose thermally activated evolution is governed by an Arrhenius-type ordinary differential equation [7]. Considering the viscous effects originating from the effects of mechanical loading and ambient conditions, the elastic strain tensor is defined as $\varepsilon^{\mathrm{e}} := \varepsilon - \boldsymbol{\alpha}$ where the viscous strain tensor is considered as the local state variable. Its evolution equation is obtained referring to the aging effects and the definition of the microprestress theory [33].

5.2.2 Governing Differential Equations
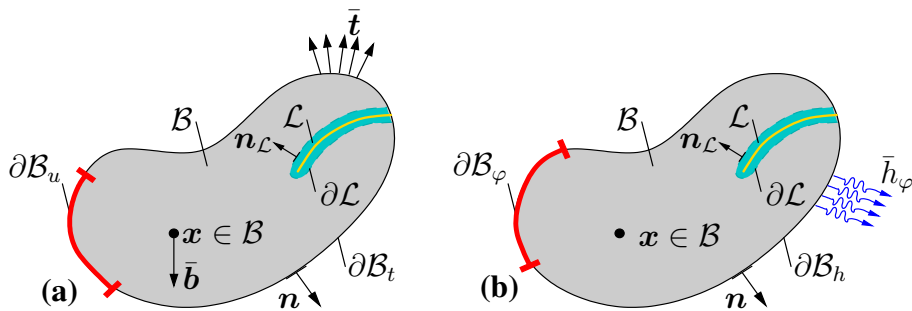
Figure 5.1: Schematic representations of the Dirichlet and Neumann boundary conditions for the **(a)** mechanical and **(b)** hygral problems.

In this section, we introduce the differential equations that govern the evolution of the state variables, given in (5.1). In particular, the balance of linear momentum and the conservation of energy, through the Darcy-type transient continuity equation, describe the spatio-temporal evolution of external state variables, the displacement field

$\boldsymbol{u}(\boldsymbol{x}, t)$ and the relative humidity field $\varphi(\boldsymbol{x}, t)$, respectively. Moreover, the evolution equation of the non-local damage evolution is introduced to express the spatial evolution of the crack phase-field d within the localization zone $\mathcal{L}$. To describe the hydration reaction, and the viscoelastic response of concrete, the evolution equations of the local state variables, i.e. the degree of hydration ξ and α are introduced, respectively.

The balance of linear momentum represents the quasi-static stress equilibrium

$$\operatorname{div} \hat{\boldsymbol{\sigma}} + \bar{\boldsymbol{b}} = \boldsymbol{0}, \tag{5.3}$$

in terms of the total stress tensor $\hat{\boldsymbol{\sigma}}$, and the volume-specific body forces $\bar{\boldsymbol{b}}$. This expression governs the evolution of the displacement field $\boldsymbol{u}(\boldsymbol{x}, t)$ in conjunction with the Dirichlet $\boldsymbol{u} = \bar{\boldsymbol{u}}$ on $\partial \mathcal{B}_u$ and the Neumann $\boldsymbol{\sigma} \boldsymbol{n} = \bar{\boldsymbol{t}}$ on $\partial \mathcal{B}_u$ boundary conditions where $\boldsymbol{n}$ represents the outward unit surface normal on $\partial \mathcal{B}$. It is obvious that the respective parts of the boundary $\partial \mathcal{B}_u$ and $\partial \mathcal{B}_u$ satisfy $\partial \mathcal{B} = \partial \mathcal{B}_u \cup \partial \mathcal{B}_t$ and $\partial \mathcal{B}_u \cap \partial \mathcal{B}_u = \emptyset$ as demonstrated in Figure 5.1.

The the Darcy-type transient equation of the relative humidity is recast into the general form as

$$\operatorname{div} \hat{\boldsymbol{q}}_\varphi + f_\varphi = 0. \tag{5.4}$$

This expression is accompanied by the Dirichlet $\varphi = \bar{\varphi}$ on $\partial \mathcal{B}_\varphi$ and the Neumann $\boldsymbol{q} \cdot \boldsymbol{n} = \bar{h}$ on $\partial \mathcal{B}_h$ boundary conditions and the initial condition $\varphi_0(\boldsymbol{x}) = \varphi(\boldsymbol{x}, t = 0)$ in $\mathcal{B}$. The parts of the boundary, $\partial \mathcal{B}_\varphi$ and $\partial \mathcal{B}_h$ are complementary $\partial \mathcal{B} = \partial \mathcal{B}_\varphi \cup \partial \mathcal{B}_h$ and disjoint $\partial \mathcal{B}_\varphi \cap \partial \mathcal{B}_h = \emptyset$ as shown in Figure 5.1b.

Also, the nonlocal evolution of the crack phase-field d is written as

$$\operatorname{div} \hat{\boldsymbol{q}}_d - \hat{\mathcal{H}}_d + f_d = 0. \tag{5.5}$$

The evolution equation of the degree of hydration ξ is defined by the thermodynamically consistent, Arrhenius-type first-order kinetics activated by temperature

$$\dot{\xi} = \frac{\hat{A}_\xi}{\hat{\eta}_\xi} \exp\left(-\frac{E_a}{R\theta}\right), \tag{5.6}$$

The governing equations corresponding to the coupled hygro-chemo-mechanical phase-field model with the specified boundary and initial conditions are summarized in 5.1.

Table 5.1: Governing equations of the chemo-thermomechanical phase field fracture model

Field	Problem	Equation	#	BC's / IC's	
$\boldsymbol{u}(\boldsymbol{x},t)$	Mechanical	$\text{div}\,\boldsymbol{\sigma} + \bar{\boldsymbol{b}} = \boldsymbol{0}$	(5.3)	$\boldsymbol{u} = \bar{\boldsymbol{u}}$	on $\partial\mathcal{B}_u$
				$\boldsymbol{\sigma}\boldsymbol{n} = \bar{\boldsymbol{t}}$	on $\partial\mathcal{B}_t$
$\boldsymbol{d}(\boldsymbol{x},t)$	Crack Phase Field	$\text{div}\,\hat{\boldsymbol{q}}_d - \hat{\mathcal{H}}_d + \hat{f}_d = 0$	(5.5)	$\boldsymbol{q}_d \cdot \boldsymbol{n} = 0$	on $\partial\mathcal{L}$
$\varphi(\boldsymbol{x},t)$	Hygral	$\text{div}\,\hat{\boldsymbol{q}}_\varphi + \hat{f}_\varphi = 0$	(5.4)	$\varphi = \bar{\varphi}$	on $\partial\mathcal{B}_\varphi$
				$\boldsymbol{q}_\varphi \cdot \boldsymbol{n} = \bar{h}$	on $\partial\mathcal{B}_h$
				$\varphi_o(\boldsymbol{x}) = \varphi(\boldsymbol{x}, t=0)$	in $\mathcal{B}$
$\xi(\boldsymbol{x},t)$	Hydration	$\dot{\xi} = \tilde{A}_\xi \exp\left(-\dfrac{E_\text{a}}{R\varphi}\right)$	(5.6)	$\xi_o(\boldsymbol{x}) = \xi(\boldsymbol{x}, t=0)$	in $\mathcal{B}$

5.2.3 Constitutive Equations

The governing differential equations of the isothermal hygro-chemo-mechanical phase field fracture model are coupled through the constitutive equations for the stress tensor $\hat{\boldsymbol{\sigma}}$ in (5.3), and the crack-driving force $\hat{\mathcal{H}}_d$ in (5.5). In addition to these coupling terms, the moisture capacity f_φ, the relative humidity flux vector $\boldsymbol{q}_\varphi$ in (5.4), the crack resistance term f_φ in (5.4), the chemical affinity A_ξ, and the viscosity function $\hat{\eta}$ representing the microdiffusion of the free water through the already formed hydrates in (5.6) is required to be specified for the hardening concrete to complete the theoretical description of the model. Hence, this section is devoted to the constitutive equations.

Stress Response. To account for the tension-compression asymmetry in the failure behavior of concrete, as discussed in the work of Miehe et al. [68], we decompose the total stress response into the tensile and compressive parts

$$\boldsymbol{\sigma} = \hat{\boldsymbol{\sigma}}(\boldsymbol{\varepsilon}, \varphi, d, \xi, \boldsymbol{\alpha}) = \underbrace{\hat{g}(d)\hat{\boldsymbol{\sigma}}_\text{eff}^+ - \hat{\boldsymbol{\sigma}}_\text{eff}^-}_{\hat{\boldsymbol{\sigma}}_\text{eff}} - \sum_{i=1}^{N} \hat{b}_i(\xi)\chi_s^{ws} p_i^w \mathbf{1} \tag{5.7}$$

where only the tensile part of the stress tensor is affected by damage through the

monotonically decreasing degradation function

$$\hat{g}(d) = \frac{(1-d)^p}{(1-d)^p + Q(d)} \tag{5.8}$$

where following cubic polynomial is assumed for the rigorously positive function $Q(d)$

$$Q(d) = a_1 d + a_1 a_2 d^2 + a_1 a_2 a_3 d^3 \tag{5.9}$$

with $p > 0$ and $Q(d) > 0$ as suggested in the work of Wu [27] being inspired by Lorentz and Godard [86]. The degradation function $\hat{g}(d) \in [0,1]$, a monotonically decreasing function of the crack phase field d, is required to fulfill the following conditions

$$g'(d) < 0, \ g(0) = 1, \ g(1) = 0 \quad \text{and} \quad g'(0) = 0 \quad \text{for all} \quad d \in [0,1] \tag{5.10}$$

In 5.7, the effective stress tensor is defined as

$$\hat{\boldsymbol{\sigma}}_{\text{eff}}^{\pm} = \sum_{i=1}^{N} \hat{K}_i^{\text{dr}}(\xi)\langle \text{tr}\,\boldsymbol{\varepsilon}^e \rangle_{\pm} + 2\hat{\mu}_i(\xi)\,\text{dev}(\boldsymbol{\varepsilon}^e)_{\pm} \quad \text{with} \quad \text{dev}(\boldsymbol{\varepsilon}^e) = \boldsymbol{\varepsilon}^e - \frac{1}{3}\,\text{tr}\,\boldsymbol{\varepsilon}^e \tag{5.11}$$

where $\hat{K}_i^{\text{dr}}(\xi)$ is the instant bulk modulus constant of the porous medium. It is calculated as a function of the Biot's effective parameter $\hat{b}_i(\xi)$, the Biot's modulus $\hat{M}_i^{\text{dr}}(\xi)$, the undrained bulk modulus of concrete $\hat{K}_i(\xi)$, and χ^{ws}, which indicates the fraction of skeleton area in contact with water

$$\hat{K}_i^{\text{dr}}(\xi) = \hat{K}_i(\xi) - \hat{b}_i^2(\xi)\hat{M}_i(\xi)\chi_s^{ws} \tag{5.12}$$

Pore Pressure. For the derivation of the pore pressure, the reader is referred to Chapter 4, Section 4.4.2.

Crack Driving Force. The crack driving force is previously derived in Chapter 3, Section 3.2.4.

Crack Resistance. The definition of the crack resistance is demonstrated in Chapter 3, Section 3.2.4.

Micro-Prestress Theory. The micro-prestress theory which determines the flow term viscosity as a function the temperature and the relative humidity is discussed in detail in Chapter 4, Section 4.4.2.

Viscous Strains. The viscous strains are determined according to the formulations, introduced in Section 4.4.2.

Adsoption-Desorption Isotherm Model. The adsorption-desorption isotherm model which applied to determine the relation between the water content and the relative humidity is discussed in detail in Section 4.4.2.

Moisture Storage. The moisture storage $f_\varphi := \hat{f}_\varphi(\varphi; \dot{\varphi})$ in (5.4) is implicitly evaluated by using physically motivated adsoption-desprption dependent expression and the degree of hydration evolution referring to (5.6) and (4.34)

$$\hat{f}_\varphi(\varphi; \dot{\varphi}) = \hat{C}(\varphi)\dot{\varphi} + \kappa_\varphi \hat{\mathcal{W}}(\varphi, \dot{\xi}) + \hat{\mathcal{R}}_\varphi^c(\varphi, d) \quad \text{with} \quad \hat{\mathcal{W}}(\varphi, \dot{\xi}) = \frac{\hat{w}_e(\varphi)}{c}\dot{\xi}. \quad (5.13)$$

In (5.13), the convective relative humidity exchange is incorporated at crack faces through the additional relative humidity sink $\hat{\mathcal{R}}_\varphi^c(\varphi, d)$. This phenomenon is numerically motivated by presuming that the deformed crack surfaces are in contact with an ambient relative humidity φ^∞ inside the free space induced by the crack opening and shown to be modeled approximately by

$$\hat{\mathcal{R}}_\varphi^c(\varphi, d) := -2\frac{h_c}{\ell}(\varphi - \varphi_\infty)d^2, \quad (5.14)$$

in terms of the convective hygral exchange parameter h_c. This approximation is performed analogous to the convective heat exchange at crack faces induced by an additional heat source per unit volume, described in Miehe et al. [69].

Humidity Flux Vector. The spatial variation of the relative humidity is expressed by the humidity flux vector $\hat{q}_\varphi$ in terms of the effective anisotropic diffusivity tensor $\hat{D}_{\text{eff}}(\varphi, d)$ and the humidity gradient $\nabla \varphi$

$$\hat{q}_\varphi(\varphi; \nabla \varphi) = -\hat{D}_{\text{eff}}(\varphi, d)\nabla \varphi \quad (5.15)$$

where the effective diffusivity of concrete accounting for the effect of the relative humidity and cracking is given by

$$\hat{D}_{\text{eff}}(\varphi, d) = \hat{D}_{\text{eff}}^u(\varphi)(1 - d^2) + d^2 \hat{D}_{\text{eff}}^c(\varphi)(\mathbf{1} - \boldsymbol{n}_\mathcal{L} \otimes \boldsymbol{n}_\mathcal{L}) \quad (5.16)$$

where $\boldsymbol{n}_\mathcal{L} = \frac{\nabla_x d}{\|\nabla_x d\|}$ represents the unit vector orthogonal to the crack plane, $\hat{D}_{\text{eff}}^u(\varphi)$ and $\hat{D}_{\text{eff}}^c(\varphi)$ tensors stand for the effective diffusivity of the undamaged and damaged state of the material, respectively [45].

The effective diffusivity of concrete is strongly dominated by the relative humidity. To this end, the effective diffusivity of concrete, referring [15], is written as

$$\hat{\boldsymbol{D}}_{\text{eff}}^{u}(\varphi) = [D_0 + D_1 \hat{\varpi}(\varrho, \varphi)]\, \mathbf{1} \tag{5.17}$$

where D_0 and D_1 are constants respectively, defining the values of the effective diffusion coefficient at zero relative humidity and fully saturated states. Owing to the nonlinear relation between the effective diffusivity and the relative humidity, a hyperbolic function $\hat{\varpi}(\varrho, \varphi)$ is justified depending on the relative humidity as

$$\hat{\varpi}(\varrho, \varphi) = 1 - 2^{-10^{\varrho(\varphi-1)}} \tag{5.18}$$

Indeed (5.16) demonstrates that the effective anistropic diffusivity $\hat{\boldsymbol{D}}_{\text{eff}}(\varphi, d)$ decreases while the relative humidity is decreasing. In turn, cracking accelerates the diffusivity by generating the entirely connected path for the diffusion process along the crack surfaces, whereas in the direction orthogonal to the crack surface, the effective diffusivity does not change.

Chemical Hydration and Growth in Rigidity and Strength. The determination of the chemical affinity which mathematically expresses the evolution of the chemical hydration, and the definition of the evolution equation of the degree of hydration are given in Section 4.4.2.

The mechanical properties including the compressive strength f_c, the tensile strength f_t, the elastic modulus E_c, the Poisson's ratio ν, the Biot's effective coefficient b, and the Biot's modulus M are determined as function of the degree of hydration ξ in Chapter 4. In addition, the critical energy release rate G_c of the concrete is defined as $\hat{G}_c(\chi) = \chi^{5/6} G_c^{\infty}$.

5.2.4 Finite Element Formulation

In this section, we construct the corresponding weak forms of the governing differential equations, whose strong forms are summarized in Table 5.1, and discretize them both in space and time by using finite element and finite difference methods for the respective cases. Moreover, the system of nonlinear equations obtained through discretization is linearized consistently for the iterative Newton-type solvers.

For the spatial discretization, we employ conventional Galerkin method to the fundamental field equations by individually multiplying them by the weight functions $\delta\boldsymbol{u} \in \mathscr{U}_0$, $\delta d \in \mathscr{V}_0$ and $\delta\varphi \in \mathscr{W}_0$ whose square of integrals are finite and they meet the conditions of the homogeneous boundary conditions ($\delta\boldsymbol{u} = \boldsymbol{0}$ over $\partial\mathcal{B}_{\boldsymbol{u}}$, $\delta d = 0$ over $\partial\mathcal{B}_d$ and $\delta\varphi = 0$ over $\partial\mathcal{B}_\varphi$). The weighted residual equations, integrated over the volume of the object, take the following forms respectively for the conservation of linear momentum, the hygral problem and the evolution of the crack phase-field after integrating by parts,

$$
\begin{cases}
G^u(\delta\boldsymbol{u}; \boldsymbol{u}, d, \varphi) = G^u_{\text{int}}(\delta\boldsymbol{u}; \boldsymbol{u}, d, \varphi) - G^u_{\text{ext}}(\delta\boldsymbol{u}) = 0\,, \\[2mm]
G^\varphi(\delta\varphi; \boldsymbol{u}, d, \varphi) = G^\varphi_{\text{int}}(\delta\varphi; d, \varphi) - G^\varphi_{\text{ext}}(\delta\varphi; d, \varphi) = 0\,, \\[2mm]
G^d(\delta d; \boldsymbol{u}, d, \varphi) = G^d_{\text{int}}(\delta d; d, \varphi) - G^d_{\text{ext}}(\delta d; \boldsymbol{u}, d, \varphi) = 0\,.
\end{cases}
\tag{5.19}
$$

It should be noted that since transient evolution of the degree of hydration ξ and the viscous strain $\boldsymbol{\alpha}$ are expressed as the functions of the relative humidity and the effective stress at the local Gauss point, respectively, so they are solved only by discretizing in time space. Therefore, in the above equations, the degree of hydration and the viscous strain do not appear as the additional fields, instead, they are considered as the internal fields.

Accordingly, in the weak form derived for the conservation of linear momentum $(5.19)_1$, internal and external Galerkin functions (G^u_{int}, G^u_{ext}) are given as follows

$$
G^u_{\text{int}}(\delta\boldsymbol{u}; \boldsymbol{u}, d, \varphi) := \int_{\mathcal{B}} \delta\boldsymbol{\varepsilon} : \hat{\boldsymbol{\sigma}} \ dV\,,
$$
$$
G^u_{\text{ext}}(\delta\boldsymbol{u}) := \int_{\mathcal{B}} \delta\boldsymbol{u} \cdot \bar{\boldsymbol{b}} \ dV + \int_{\partial\mathcal{B}_t} \delta\boldsymbol{u} \cdot \bar{\boldsymbol{t}} \ dA
\tag{5.20}
$$

where $\boldsymbol{b}$ and $\bar{\boldsymbol{t}}$ are the volume specific body forces and surface traction vector, respectively. Analogously, for the hygral part of the coupled problem, the internal and external Galerkin functions (G^φ_{int}, G^φ_{ext}) are defined as

$$
\begin{aligned}
G^\varphi_{\text{int}}(\delta\varphi; \varphi) &:= \int_{\mathcal{B}} -\nabla_x(\delta\varphi) \cdot \hat{\boldsymbol{q}}_\varphi \ dV\,, \\[2mm]
G^\varphi_{\text{ext}}(\delta\varphi; \varphi) &:= \int_{\mathcal{B}} \delta\varphi\,(\hat{\mathcal{H}}_\varphi - \hat{f}_\varphi) \ dV - \int_{\partial\mathcal{B}_h} \delta\varphi\,\bar{q}_\varphi \ dA\,.
\end{aligned}
\tag{5.21}
$$

In the case of the crack phase-field evolution, the internal end external Galerkin functions $(G_{\text{int}}^d, G_{\text{ext}}^d)$ are given by

$$
\begin{aligned}
G_{\text{int}}^d(\delta d; d, \varphi) &:= \int_{\mathcal{B}} -\nabla_x(\delta d) \cdot \hat{\boldsymbol{q}}_d \ dV , \\
G_{\text{ext}}^d(\delta d; \boldsymbol{u}, d, \varphi) &:= \int_{\mathcal{B}} \delta d \, (\hat{\mathcal{H}}_d - \hat{f}_d) \ dV - \int_{\partial \mathcal{B}_{q_d}} \delta d \ \bar{q}_d \ dA .
\end{aligned}
\tag{5.22}
$$

When the governing equations are nonlinear, the weighted residual functions are the non-linear functions of the field magnitudes. Therefore, the coupled field equations are numerically solved by implementing Finite Element Method, at the same time Newton's method as an iterative technique is applied for solving the coupled problems. In the following, for each iteration step, the weighted Galerkin functions are consistently linearized with respect to the field variables around their interval values $\tilde{\boldsymbol{u}}$, $\tilde{d}$ and $\tilde{\varphi}$,

$$
\begin{aligned}
\text{Lin} \, G^u(\delta \boldsymbol{u}; \boldsymbol{u}, d, \varphi)\big|_{\tilde{\boldsymbol{u}},\tilde{d},\tilde{\varphi}} &:= G^u(\delta \boldsymbol{u}; \tilde{\boldsymbol{u}}, \tilde{d}, \tilde{\varphi}) + \Delta G^u(\delta \boldsymbol{u}; \tilde{\boldsymbol{u}}, \tilde{d}, \tilde{\varphi}; \Delta \boldsymbol{u}, \Delta d, \Delta \varphi) = 0 , \\
\text{Lin} \, G^d(\delta d; \boldsymbol{u}, d, \varphi)\big|_{\tilde{\boldsymbol{u}},\tilde{d},\tilde{\varphi}} &:= G^d(\delta d, \tilde{\boldsymbol{u}}, \tilde{d}, \tilde{\varphi}) + \Delta G^d(\delta d, \tilde{\boldsymbol{u}}, \tilde{d}, \tilde{\varphi}; \Delta \boldsymbol{u}, \Delta d, \Delta \varphi) = 0 , \\
\text{Lin} \, G^\varphi(\delta \varphi; \varphi)\big|_{\tilde{\varphi}} &:= G^\varphi(\delta \varphi, \tilde{\varphi}) + \Delta G^\varphi(\delta \varphi, \tilde{\varphi}; \Delta \varphi) = 0 .
\end{aligned}
\tag{5.23}
$$

The incremental terms ΔG^u, ΔG^d and ΔG^φ, derived by Gâteaux derivative are rewritten as functions of the external and internal terms according to $(5.19)_{1,2,5}$

$$
\Delta G^\gamma = \Delta G_{\text{int}}^\gamma - \Delta G_{\text{ext}}^\gamma \quad \text{with} \quad \gamma = u, d, \varphi .
\tag{5.24}
$$

As stated in $((5.20)_1)$, ΔG_{int}^u is obtained as

$$
\Delta G_{\text{int}}^u = \int_{\mathcal{B}} \delta \boldsymbol{\varepsilon} : \Delta \hat{\boldsymbol{\sigma}} \ dV.
\tag{5.25}
$$

In this expression, the total stress increment is specified as

$$
\Delta \hat{\boldsymbol{\sigma}} = \mathbb{C}^{uu} : \Delta \boldsymbol{\varepsilon} + \boldsymbol{C}^{ud} \Delta d + \boldsymbol{C}^{u\varphi} \Delta \varphi ,
\tag{5.26}
$$

where the fourth order tensor $\mathbb{C}^{uu}$ is determined as the derivative of the total stress tensor with respect to the strain tensor, and the second order tensor $\boldsymbol{C}^{u\varphi}$ and $\boldsymbol{C}^{ud}$ are described respectively as the derivative of the total stress tensor with respect to the relative humidity and crack phase-field,

$$
\mathbb{C}^{uu} := \partial_{\boldsymbol{\varepsilon}} \hat{\boldsymbol{\sigma}} , \quad \boldsymbol{C}^{ud} := \partial_d \hat{\boldsymbol{\sigma}} \quad \text{and} \quad \boldsymbol{C}^{u\varphi} := \partial_\varphi \hat{\boldsymbol{\sigma}}
\tag{5.27}
$$

Based on the expressions stated above, ((5.25)) is rewritten as

$$\Delta G_{\text{int}}^u \quad = \quad \int_{\mathcal{B}} \delta\boldsymbol{\varepsilon} : \mathbb{C}^{uu} : \Delta\boldsymbol{\varepsilon} \; dV + \int_{\mathcal{B}} \delta\boldsymbol{\varepsilon} : \boldsymbol{C}^{ud}\Delta d \; dV + \int_{\mathcal{B}} \delta\boldsymbol{\varepsilon} : \boldsymbol{C}^{u\varphi}\Delta\varphi \; dV$$

(5.28)

On the other hand, as regards the hygral part of the coupled problem, the increment of the internal Galerkin function is expressed as

$$\Delta G_{\text{int}}^\varphi = \int_{\mathcal{B}} -\nabla_x(\delta\varphi) \cdot \Delta\hat{\boldsymbol{q}}_\varphi \; dV$$

(5.29)

where the increment of the heat flux is stated as

$$\Delta\hat{\boldsymbol{q}}_\varphi = -\hat{\boldsymbol{K}} \cdot \nabla_x(\Delta\varphi) - \hat{k}(\Delta\varphi)$$

(5.30)

where $\hat{\boldsymbol{K}}$ and $\hat{k}$ are determined as follows

$$\hat{\boldsymbol{K}} := -\partial_{\nabla_x\varphi}\hat{\boldsymbol{q}}_\varphi = k_\varphi\mathbf{1} \quad \text{and} \quad \hat{k} := -\partial_d\hat{\boldsymbol{q}}_\varphi = \partial_d\hat{k}_\varphi(d)\mathbf{1}$$

(5.31)

The increment of the external Galerkin function in terms of the relative humidity field is also defined as

$$\Delta G_{\text{ext}}^\varphi := \int_{\mathcal{B}} \delta\varphi \; (-\Delta\hat{f}_\varphi) \; dV,$$

(5.32)

here, the increment of the thermomechanical heating and viscous thermal resistance are represented as

$$\Delta\hat{f}_\varphi = \partial_\varphi\hat{f}_\varphi \, \Delta\varphi + \partial_d\hat{f}_\varphi \, \Delta d,$$

(5.33)

in which the scalar-valued tangents t_d and t_φ are determined as

$$t_\varphi = \partial_\varphi\hat{f}_\varphi \quad \text{and} \quad t_d = \partial_d\hat{f}_\varphi$$

(5.34)

In the case of the crack phase-field the corresponding increment of the Galerkin function is introduced in the following expression,

$$\Delta G_{\text{int}}^d = \int_{\mathcal{B}} -\nabla_x(\delta d) \cdot \Delta\hat{\boldsymbol{q}}_d \; dV.$$

(5.35)

Here, the increment of the crack phase-field diffusion is determined as

$$\Delta\hat{\boldsymbol{q}}_d = -\hat{\boldsymbol{D}} \cdot \nabla_x(\Delta d) - \hat{d}\Delta\varphi$$

(5.36)

where $\hat{\boldsymbol{D}}$ and $\hat{d}$ are defined as

$$\hat{\boldsymbol{D}} := -\partial_{\nabla_x d}\hat{\boldsymbol{q}}_d = \frac{2\,G_c\,l}{c_0}\mathbf{1} \quad \text{and} \quad \hat{d} := -\partial_\varphi\hat{\boldsymbol{q}}_d = \partial_\varphi\frac{2\,G_c\,l}{c_0}\nabla_x d$$

(5.37)

166

Comparably, the increment of the external Galerkin function for the crack phase-field is formulated as

$$\Delta G_{\text{ext}}^d := \int_{\mathcal{B}} \delta d \left(\Delta \hat{\mathcal{H}}_d - \Delta \hat{f}_d \right) dV \tag{5.38}$$

where the increment of the crack driving force and the viscous crack resistance are introduced in the following form

$$\Delta \hat{\mathcal{H}}_d = -\boldsymbol{C}^{ud} : \Delta \boldsymbol{\varepsilon} + H_d \, \Delta d + H_\varphi \, \Delta \varphi$$
$$\text{and} \quad \Delta \hat{f}_d = h_d \, \Delta d + h_\varphi \, \Delta \varphi \tag{5.39}$$

Here, the tensor- and the scalar-valued tangents are respectively defined as

$$\boldsymbol{C}^{ud} := -\partial_{\boldsymbol{\varepsilon}} \hat{\mathcal{H}}_d = \partial_d \hat{\boldsymbol{\sigma}} \,, \ H_d := \partial_d \hat{\mathcal{H}}_d \,, \ H_\varphi := \partial_\varphi \hat{\mathcal{H}}_d$$
$$\text{and} \quad h_d := \partial_d \hat{f}_d \,, \ h_\varphi := \partial_\varphi \hat{f}_d \tag{5.40}$$

Isoparametric Gelerkin method will be followed in order to approximate the weak forms (5.19) given in the form of continuous integral equations. The basic state variables of the coupled problem, the above-introduced generalized displacement $\boldsymbol{u}(\boldsymbol{x}, t)$, the relative humidity field $\varphi(\boldsymbol{x}, t)$, the crack phase-field $d(\boldsymbol{x}, t)$ and the weighted functions associated with these fields are interpolated on each finite element

$$
\begin{aligned}
\delta \boldsymbol{u}_e^h &= \sum_{i=1}^{n_{en}} N^i \delta \boldsymbol{d}_i^e \,, & \delta d_e^h &= \sum_{j=1}^{n_{en}} N^j \delta D_j^e \,, & \delta \varphi_e^h &= \sum_{k=1}^{n_{en}} N^k \delta \Phi_k^e \,, \\
\boldsymbol{u}_e^h &= \sum_{l=1}^{n_{en}} N^l \boldsymbol{d}_l^e \,, & d_e^h &= \sum_{m=1}^{n_{en}} N^m D_m^e \,, & \varphi_e^h &= \sum_{n=1}^{n_{en}} N^n \Phi_n^e \,.
\end{aligned}
\tag{5.41}
$$

where n_{ne} represents the number of nodes on each finite element. Then the spatial gradients of the weighted residual functions are presented as

$$
\begin{aligned}
\nabla_x (\delta \boldsymbol{u}_e^h) &= \sum_{i=1}^{n_{en}} \delta \boldsymbol{d}_i^e \otimes \nabla_x N^i \,, \\
\nabla_x (\delta d_e^h) &= \sum_{j=1}^{n_{en}} \delta D_j^e \otimes \nabla_x N^j \,, \\
\nabla_x (\delta \varphi_e^h) &= \sum_{k=1}^{n_{en}} \delta \Phi_k^e \otimes \nabla_x N^k \,.
\end{aligned}
\tag{5.42}
$$

Likewise, the spatial gradient of the increment of the generalized displacement vector,

167

the crack phase-field and the relative humidity field are respectively demonstrated as

$$
\begin{aligned}
\nabla_x(\Delta \boldsymbol{u}_e^h) &= \sum_{l=1}^{n_{en}} \Delta \boldsymbol{d}_l^e \otimes \nabla_x N^l \,, \\
\nabla_x(\Delta d_e^h) &= \sum_{m=1}^{n_{en}} \Delta D_m^e \otimes \nabla_x N^m \,, \\
\nabla_x(\Delta \varphi_e^h) &= \sum_{n=1}^{n_{en}} \Delta \Phi_n^e \otimes \nabla_x N^n \,,
\end{aligned}
\tag{5.43}
$$

Incorporating the discretized representations (5.41) and (5.42) in (5.19) along with (5.20), (5.21) and (5.22, we end up with the discrete residual vectors

$$
\begin{aligned}
\boldsymbol{R}_I^u &= \mathop{\mathbf{A}}_{e=1}^{n_{el}} \left\{ \int_{\mathcal{B}_e^h} \nabla_x N^i \cdot \hat{\boldsymbol{\sigma}} \; dV \; - \int_{\mathcal{B}_e^h} N^i \boldsymbol{b} \; dV - \int_{\partial \mathcal{B}_t^e} N^i \bar{\boldsymbol{t}} \; dA \right\} = \boldsymbol{0} \,, \\
R_J^d &= \mathop{\mathbf{A}}_{e=1}^{n_{el}} \left\{ -\int_{\mathcal{B}_e^h} \nabla_x N^j \cdot \hat{\boldsymbol{q}}_d \; dV \; - \int_{\mathcal{B}_e^h} N^j (\hat{\mathcal{H}}_d - \hat{f}_d) \; dV \right\} = 0 \,, \\
R_K^\varphi &= \mathop{\mathbf{A}}_{e=1}^{n_{el}} \left\{ -\int_{\mathcal{B}_e^h} \nabla_x N^k \cdot \hat{\boldsymbol{q}}_\varphi \; dV \; - \int_{\mathcal{B}_e^h} N^k (-\hat{f}_\varphi) \; dV \right\} = 0
\end{aligned}
\tag{5.44}
$$

where the operator $\mathbf{A}$ designates the standard assembly of element contributions at the local element nodes $i, j = 1, ..., n_{en}$ to the global residuals at the global nodes $I, J = 1, ..., n_{nd}$ of a mesh with n_{nd} nodes. Likewise, tangential matrices are defined as

$$
\begin{aligned}
\boldsymbol{K}_{IL}^{uu} &= \mathop{\mathbf{A}}_{e=1}^{n_{el}} \left\{ \int_{\mathcal{B}_e^h} \nabla_x N^i \cdot \hat{\mathbb{C}}^{uu} \cdot \nabla_x N^l \; dV \right\}, \\
\boldsymbol{K}_{IM}^{ud} &= \mathop{\mathbf{A}}_{e=1}^{n_{el}} \left\{ \int_{\mathcal{B}_e^h} (\nabla_x N^i \cdot \hat{\boldsymbol{C}}^{ud}) N^m \; dV \right\}, \\
\boldsymbol{K}_{IN}^{u\varphi} &= \mathop{\mathbf{A}}_{e=1}^{n_{el}} \left\{ \int_{\mathcal{B}_e^h} (\nabla_x N^i \cdot \hat{\boldsymbol{C}}^{u\varphi}) N^n \; dV \right\}, \\
\boldsymbol{K}_{JL}^{du} &= \mathop{\mathbf{A}}_{e=1}^{n_{el}} \left\{ \int_{\mathcal{B}_e^h} N^j (\boldsymbol{C}^{ud} \cdot \nabla_x N^l) \; dV \right\}, \\
K_{JM}^{dd} &= \mathop{\mathbf{A}}_{e=1}^{n_{el}} \left\{ \int_{\mathcal{B}_e^h} \nabla_x N^j \cdot \hat{\boldsymbol{D}} \nabla_x N^m \; dV - \int_{\mathcal{B}_e^h} N^j (H_d - h_d) N^m \; dV \right\}, \\
K_{JN}^{d\varphi} &= \mathop{\mathbf{A}}_{e=1}^{n_{el}} \left\{ \int_{\mathcal{B}_e^h} \nabla_x N^j \cdot \hat{\boldsymbol{d}} N^n \; dV - \int_{\mathcal{B}_e^h} N^j (H_\varphi - h_\varphi) N^n \; dV \right\}, \\
K_{KN}^{\varphi\varphi} &= \mathop{\mathbf{A}}_{e=1}^{n_{el}} \left\{ \int_{\mathcal{B}_e^h} \nabla_x N^k \cdot \hat{\boldsymbol{K}} \nabla_x N^n \; dV - \int_{\mathcal{B}_e^h} N^k (-t_\varphi) N^n \; dV \right\}.
\end{aligned}
\tag{5.45}
$$

To this end the global residual vectors associated with the crack phase-field and thermal problems are represented as $\boldsymbol{\mathcal{R}} := [\boldsymbol{R}^u \, \boldsymbol{R}^d \, \boldsymbol{R}^\varphi]^T$, and the global vectors embracing the mechanical, thermal and crack phase-field degrees of freedom (DOFs) are defined as $\boldsymbol{\mathcal{D}} := [\boldsymbol{d} \; \boldsymbol{D} \; \boldsymbol{T}]^T$. Furthermore, the global coupled tangent matrix including the determined tangential matrices are presented as

$$
\boldsymbol{\mathcal{K}} :=
\begin{bmatrix}
\boldsymbol{K}^{uu} & \boldsymbol{K}^{ud} & \boldsymbol{K}^{u\varphi} \\
\boldsymbol{K}^{du} & K^{dd} & K^{d\varphi} \\
0 & 0 & K^{\varphi\varphi}
\end{bmatrix}
$$

The repetitive solutions of determined mechanical, thermal and crack phase-field DOFs at the global nodes of the finite element meshes are obtained through the following equation

$$
\boldsymbol{\mathcal{D}} = \bar{\boldsymbol{\mathcal{D}}} - \bar{\boldsymbol{\mathcal{K}}}^{-1} \cdot \bar{\boldsymbol{\mathcal{R}}} \tag{5.46}
$$

where $\bar{\boldsymbol{\mathcal{R}}} := \boldsymbol{\mathcal{R}}(\bar{\boldsymbol{\mathcal{D}}})$, $\bar{\boldsymbol{\mathcal{K}}} := \boldsymbol{\mathcal{K}}(\bar{\boldsymbol{\mathcal{D}}})$ indicates respectively the global residual vectors and global coupled tangent matrix. The solutions related to predefined DOFs are calculated at time $t = t_{n+1}$ for an intermediate iterative values $\bar{\boldsymbol{\mathcal{D}}}$.

5.3 Shrinkage-Induced Cracking in Concrete Ring

In this example we investigate the drying shrinkage-induced cracking in a concrete ring. The current example is the same as the one that is considered in Section 4.4.3. The geometry, the boundary conditions and the environmental condition in terms of the ambient relative humidity of the notched concrete ring specimen are demonstrated in Figure 5.2a. The ring specimen is discretized with $15,600$ four-node quadrilateral elements. The finite element model is shown in Figure 5.2b.

The material parameters relate to the hygro-chemo-mechanical model considering the viscoelastic behavior for `DS-R-C30` are given in Table 4.4. Also the material parameters associated with the regularized phase-field cohesive zone model are the critical energy release rate to $G_c^\infty = 150$ J/m^3, the internal length scale parameter $\ell = 5$ mm. The model parameters corresponding to the Cornelissen's model in (5.9), i.e. $a_2 = 1.3868$ and $a_3 = 0.6567$.
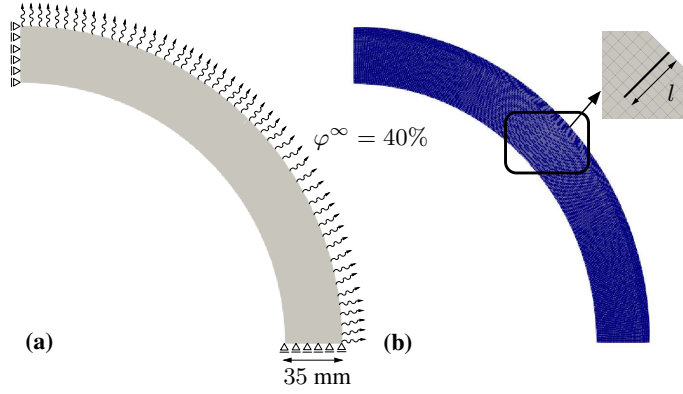
Figure 5.2: Drying shrinkage-induced cracking. **(a)** Geometry, boundary and environmental conditions and **(b)** finite element discretization of the notched concrete ring specimen with the length of notch $l = 5$ mm.

In the first analysis, the additional relative humidity sink in (5.13), and the effect of the crack phase-field on the effective diffusivity tensor in (5.15) are not considered, i.e. $\hat{\mathcal{R}}(\varphi, d) = 0$ and $\hat{\boldsymbol{D}}_{\text{eff}}(\varphi, d) = \hat{\boldsymbol{D}}_{\text{eff}}(d)$. The crack paths induced by the drying shrinkage and the distribution of the relative humidity at $t = 13$, $t = 20$, and $t = 28$ days are shown in Figure 5.3.

The further analysis is conducted to investigate the effect of the additional relative humidity sink $\hat{\mathcal{R}}(\varphi, d)$ in (5.13), and the effective diffusivity is supposed to degrade in the case of fracture by (5.15). The effective diffusivity for the damaged body in (5.15) is assumed to be $\hat{\boldsymbol{D}}_{\text{eff}}^{c}(\varphi) = 100 \hat{\boldsymbol{D}}_{\text{eff}}^{u}(\varphi)$. Also, the convective hygral exchange parameter is set to $h_c = 5.125 \times 10^{-6}$ kg/(s m^2) in (5.14). The results corresponding to the crack path and the distribution of the relative humidity in the specimen are represented in Figure 5.4.

The results show that by applying an additional relative humidity sink, the crack surfaces are exposed to the environmental, therefore the relative humidity exchange occurs along the crack paths. By comparing the distribution of the relative humidity in Figure 5.3 with one in Figure 5.4, we observe that along the crack surfaces, the relative humidity starts to move from the interior of concrete with higher relative humidity to the exterior of concrete of concrete with the lower relative humidity. Hence, a great part of the body may be exposed to the environment.

Figure 5.3: Drying shrinkage-induced cracking without additional hygral sink and the effective diffusivity is not degraded. Crack pattern at **(a)** $t = 13$ days, **(b)** $t = 20$ days and **(c)** $t = 28$ days and temperature distribution at **(d)** $t = 13$ days, **(e)** $t = 20$ days and **(f)** $t = 28$ days.

Using a degrading effective diffusivity reveals this fact that the effective diffusivity of the undamaged material decreases while cracking is growing, in turn the effective diffusivity of the degrading material, which is greater than the the effective diffusivity of the undamaged material increases. Therefore, the diffusion process is intensified in the material.

5.4 Concluding Remarks

In this study, cracking caused by drying shrinkage is modeled. To this end, we extend the hygro-chemo-mechanical model proposed in this study within the three-dimensional framework of poroviscoelasticity by coupling it with the phase-field regularized cohesive zone model. This approach accounts for the hygro-chemo-mechanical cross coupling effects between the shrinkage-induced strain development due to the pressure evolution through humidity variations, the stress concentrations
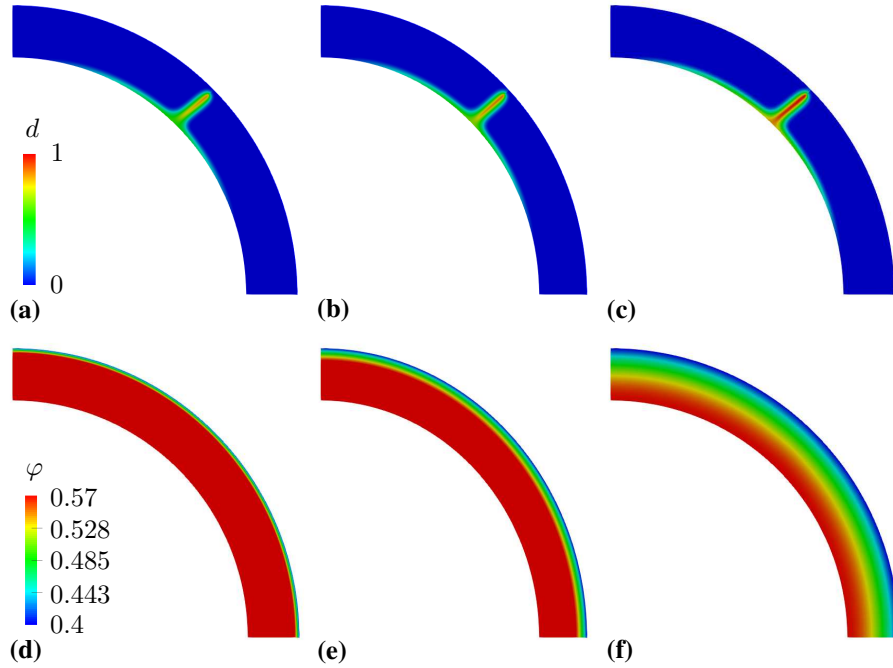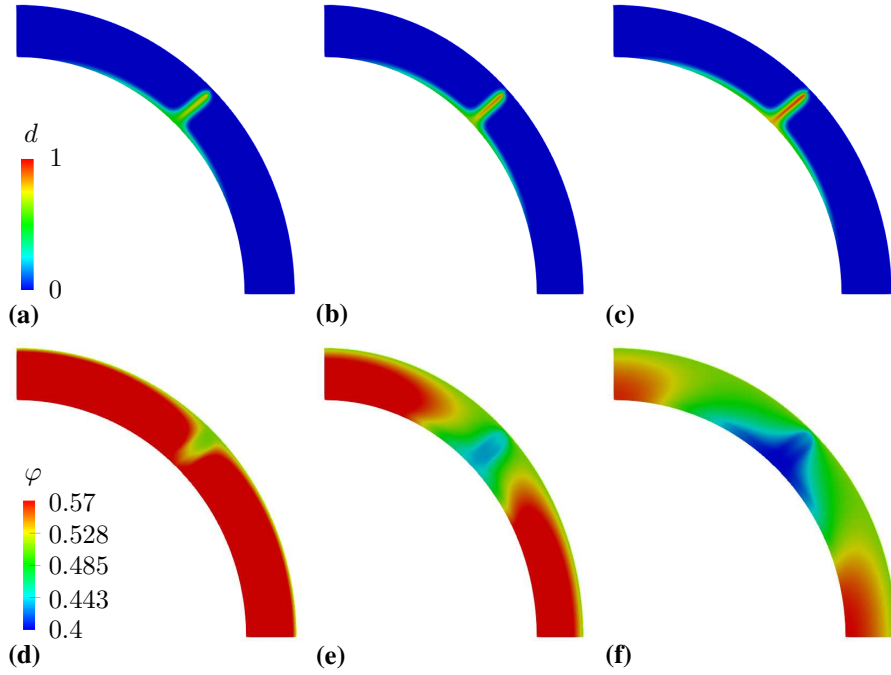
Figure 5.4: Drying shrinkage-induced cracking with additional hygral sink and the effective diffusivity is degraded. Crack pattern at **(a)** $t = 13$ days, **(b)** $t = 20$ days and **(c)** $t = 28$, days and temperature distribution at **(d)** $t = 13$ days, **(e)** $t = 20$ days and **(f)** $t = 28$ days.

in hardening or hardened viscoelastic concrete and crack phase-field. In addition, the evolution of mechanical properties of concrete at early ages are expressed in terms of the hydration and aging phenomena through a chemo-mechanical model based on the theory of reactive porous media.

Although in the literature, there are some works studying the fracture mechanism of concrete subjected to the drying shrinkage, but there exist no work investigating the prediction of crack paths. Also, there is not any work studying the drying shrinkage induced fracture, using the cohesive phase-field model in concrete material.

Moreover, the modeling of crack propagation in concrete caused by drying, we examine the effect of cracking on the moisture capacity and the effective diffusivity of concrete in the current study.

The numerical results demonstrate the capability of the proposed model, employed to conduct predictive crack risk analyses of structures with high area-thickness ratio

where drying shrinkage may be critical.

CHAPTER 6

CONCLUSIONS AND FUTURE WORK

This thesis is concerned with the development of the computational modeling of durability phenomena in both hardening and hardened concrete. In this study, we have specifically modeled cracking in concrete structures considering the cross-effect of the evolution of the temperature, the relative humidity, and the degree of hydration on the durability and mechanical properties of concrete structures. To model the crack initiation and propagation, we have adopted the cohesive zone phase-field model `PF-CZM`. The formulations related to the numerical modeling of fracture through `PF-CZM` have been presented in Chapter 2 where the derivation of the governing equations and the constitutive relations related to the brittle `AT2` and the cohesive phase-field `PF-CZM` models have been represented. Through benchmark problems borrowed from the literature, we have validated our implementation and showed that `PF-CZM` is an appropriate and powerful model to simulate quasi-brittle fracture in concrete.

The constitutive modeling of the chemo-thermo-mechanical approach coupled with `PF-CZM`, dedicated to thermal cracking observed in massive concrete structures has been demonstrated in Chapter 3. To our best knowledge, in the literature, there exist no work where the fracture in hardening concrete especially in the case of massive concrete structures is investigated using `PF-CZM`. However, the few works where the existing phase field-based approaches applied to multi-physics problems, are predominantly restricted to brittle fracture `AT2`. Another novel aspect of the proposed model is that it has, for the first time, incorporated a hardening material in the phase-field framework of fracture. The capabilities of the developed model have been represented through a crack risk analysis of a roller-compacted-concrete dam (RCC) where

the stress concentrations that arise from high temperature gradients are generated by the hydration process and the lower ambient temperature. To account for the casting of concrete dams in successive layers, a new multi-field interface element has been formulated and implemented to ensure the continuity of the displacement and temperature fields across the lifts and to prevent phase-field cracks from propagating artificially through the diffusion term from a previously cast lift to the next one. The results obtained by using the proposed framework for the control case (`RCC1`) favorably agree with the findings reported in the literature. Furthermore, the numerical crack risk analyses conducted through the proposed chemo-thermo-mechanical model coupled with `PF-CZM` underline the importance of controlling the rate of heat generation and monitoring the temperature variations in the ambient temperature. Therefore, the developed computational tool can be utilized to perform crack risk analyses not only in the design stage but also during the construction and service of massive concrete structures.

Furthermore, in Chapter 4, we have developed a coupled constitutive modeling approach that is furnished by robust computational framework to address the durability problems that arise from drying shrinkage and creep within the three-dimensional framework of poro-viscoelasticity. The proposed approach accounts for the hygro-chemo-mechanical cross coupling effects between the shrinkage-induced strain development due to the pressure evolution through humidity variations and the stress concentrations in both hardening and hardened viscoelastic concrete. To this end, we have additively decomposed the stress expression into the effective stress of the viscoelastic concrete skeleton and the pressure developing in the pores. The viscoelastic model of the skeleton takes into account the short- and the long-term creep effects through the well-known micro-prestress theory. The material parameters related to the rigidity and strength of concrete are assumed to evolve with the degree of hydration. The evolution of the material properties due to the aging effects are defined through a chemo-thermo-mechanical model.

In the proposed isothermal hygro-chemo-mechanical model, contrary to the modeling approaches suggested in the literature, the shrinkage strain is not obtained by using an empirical formula involving the hygromechanical expansion coefficient and the change in humidity. Instead, we employ a physically motivated approach where

the pore pressure is obtained as a function of water content that is determined using adsorption-desorption isotherm model for a given value of the local relative humidity. The excellent modeling capacity of the proposed model have been tested through various experimental studies borrowed from literature. These examples cover the basic and flexural creep, and the drying shrinkage in concrete structures.

In Chapter 5, the coupled model of poro-viscoelasticity has been further supplemented by `PF-CZM` to perform the crack risk analysis of concrete structures subjected to the coupled effects of drying shrinkage and creep. Additional representative examples of boundary-value problems have demonstrated the capabilities of the proposed approach predicting cracking due to hygral effects. To our best knowledge, the proposed model is the first one considering the physically motivated approach within the framework of the poroviscoelasticity along with the cohesive zone phase-field model `PF-CZM`.

For the future work, the proposed multi-field formulation supplemented by `PF-CZM` can be extended to simulate the alkali-silica reaction-induced cracking in concrete by developing a micromechanical constitutive model where the standard phase-field model may be used to define the position of the aggregates and the interfacial transition zone. This model would provide a useful tool to investigate the effects of the aggregates reactivity and the interfacial transition zone on the behavior of concrete exposed to the alkali-silica reaction and the induced cracking.

Furthermore, we are planning to extend the hygro-chemo-thermo-mechanical model within the framework of poro-viscoelasticity to account for the cross-effects of temperature and relative humidity on the response of concrete to creep and drying shrinkage, and couple this model with the cohesive phase-field model to perform the crack risk analysis considering the cross-coupling effects due to the shrinkage-induced strain generation arising from pressure evolution through humidity and temperature variations. When striving for this, however, we feel that a more systematic technique for identifying the model parameters should be developed so that the proposed model can be used to describe these volume stability phenomena in various types of concrete to predict potential durability risks before they occur.

REFERENCES

[1] P. C. Taylor, G. F. Voigt, *et al.*, "Integrated materials and construction practices for concrete pavement: A state-of-the-practice manual," tech. rep., United States. Federal Highway Administration. Office of Pavement Technology, 2007.

[2] J. Jacobs, "Concrete for energy-efficient buildings, the benefits of thermal mass," *European Concrete Platform. Brussels: British Cement Association, British Ready-mixed Concrete Association, British Precast Concrete Federation and the Cement Admixtures Association*, 2007.

[3] F. Ulm and O. Coussy, "Modeling of thermochemomechanical couplings of concrete at early ages," *Journal of Engineering Mechanics*, vol. 121, no. 7, pp. 785–794, 1995.

[4] F.-J. Ulm and O. Coussy, "Strength growth as chemo-plastic hardening in early age concrete," *Journal of Engineering Mechanics*, vol. 122, no. 12, pp. 1123–1132, 1996.

[5] E. M. Fairbairn and M. Azenha, *Thermal Cracking of Massive Concrete Structures: State of the Art Report of the RILEM Technical Committee 254-CMS*, vol. 27. Springer, 2018.

[6] F.-J. Ulm and O. Coussy, "Couplings in early-age concrete: From material modeling to structural design," *International Journal of Solids and Structures*, vol. 35, no. 31–32, pp. 4295 – 4311, 1998.

[7] M. Cervera, J. Oliver, and T. Prato, "Thermo-chemo-mechanical model for concrete. I: Hydration and aging," *Journal of Engineering Mechanics*, vol. 125, no. 9, pp. 1018–1027, 1999.

[8] A. M. Neville *et al.*, *Properties of concrete*, vol. 4. Longman London, 1995.

[9] T. C. Powers and T. L. Brownyard, "Studies of the physical properties of hardened portland cement paste," in *ACI Journal Proceedings*, vol. 43, pp. 101–132, 1946.

[10] Z. Bažant, "Constitutive equation for concrete creep and shrinkage based on thermodynamics of multiphase systems," *Matériaux et Constructions*, vol. 3, no. 1, pp. 3–36, 1970.

[11] A. B. Hauggaard, L. Damkilde, and P. F. Hansen, "Transitional thermal creep of early age concrete," *Journal of Engineering Mechanics*, vol. 125, no. 4, pp. 458–465, 1999.

[12] G. Di Luzio and G. Cusatis, "Hygro-thermo-chemical modeling of high performance concrete. I: Theory," *Cement and Concrete Composites*, vol. 31, no. 5, pp. 301–308, 2009.

[13] T. Powers, "The thermodynamics of volume change and creep," *Matériaux et Construction*, vol. 1, no. 6, pp. 487–507, 1968.

[14] Z. P. Bažant, A. B. Hauggaard, S. Baweja, and F.-J. Ulm, "Microprestress-solidification theory for concrete creep. I: Aging and drying effects," *Journal of Engineering Mechanics*, vol. 123, no. 11, pp. 1188–1194, 1997.

[15] Y. Xi, Z. P. Bažant, and H. M. Jennings, "Moisture diffusion in cementitious materials adsorption isotherms," *Advanced Cement Based Materials*, vol. 1, no. 6, pp. 248–257, 1994.

[16] M. Cervera, J. Oliver, and T. Prato, "Simulation of construction of RCC dams. II: stress and damage," *Journal of Structural Engineering*, vol. 126, no. 9, pp. 1062–1069, 2000.

[17] O. Coussy, *Mechanics of porous continua*. Wiley, 1995.

[18] C. Hua, P. Acker, and A. Ehrlacher, "Analyses and models of the autogenous shrinkage of hardening cement paste: I. modelling at macroscopic scale," *Cement and Concrete Research*, vol. 25, no. 7, pp. 1457–1468, 1995.

[19] Z. P. Bažant, A. B. Hauggaard, S. Baweja, and F.-J. Ulm, "Microprestress-solidification theory for concrete creep. I: Aging and drying effects," *Journal Engineering of Mechanics*, vol. 123, no. 11, pp. 1188–1194, 1997.

[20] S. Arrhenius, *Quantitative Laws in Biological Chemistry.* London: G. Bell and Sons, 1915.

[21] E. Rastrup, "Heat of hydration in concrete," *Magazine of Concrete Research*, vol. 6, no. 17, pp. 79–92, 1954.

[22] M. Cervera, J. Oliver, and T. Prato, "Thermo-chemo-mechanical model for concrete. i: Hydration and aging," *Journal of Engineering Mechanics*, vol. 125, no. 9, pp. 1018–1027, 1999.

[23] R. Lackner and H. A. Mang, "Chemoplastic material model for the simulation of early-age cracking: From the constitutive law to numerical analyses of massive concrete structures," *Cement and Concrete Composites*, vol. 26, no. 5, pp. 551–562, 2004.

[24] G. De Schutter and L. Taerwe, "General hydration model for portland cement and blast furnace slag cement," *Cement and Concrete Research*, vol. 25, no. 3, pp. 593–604, 1995.

[25] M. Cervera, J. Oliver, and T. Prato, "Simulation of construction of RCC dams. I: temperature and aging," *Journal of Structural Engineering*, vol. 126, no. 9, pp. 1053–1061, 2000.

[26] C. Miehe, F. Welschinger, and M. Hofacker, "Thermodynamically consistent phase-field models of fracture: Variational principles and multi-field fe implementations," *International Journal for Numerical Methods in Engineering*, vol. 83, no. 10, pp. 1273–1311, 2010.

[27] J.-Y. Wu, "A unified phase-field theory for the mechanics of damage and quasi-brittle failure," *Journal of the Mechanics and Physics of Solids*, vol. 103, pp. 72–99, 2017.

[28] T.-T. Nguyen, D. Waldmann, and T. Q. Bui, "Computational chemo-thermo-mechanical coupling phase-field model for complex fracture induced by early-

181

age shrinkage and hydration heat in cement-based materials," *Computer Methods in Applied Mechanics and Engineering*, vol. 348, pp. 1–28, 2019.

[29] T.-T. Nguyen, M. Weiler, and D. Waldmann, "Experimental and numerical analysis of early age behavior in non-reinforced concrete," *Construction and Building Materials*, vol. 210, pp. 499–513, 2019.

[30] T.-T. Nguyen, D. Waldmann, and T. Q. Bui, "Phase field simulation of early-age fracture in cement-based materials," *International Journal of Solids and Structures*, vol. 191, pp. 157–172, 2020.

[31] Z. P. Bažant, A. B. Hauggaard, and S. Baweja, "Microprestress-solidification theory for concrete creep. II: Algorithm and verification," *Journal of Engineering Mechanics*, vol. 123, no. 11, pp. 1195–1201, 1997.

[32] G. Di Luzio and G. Cusatis, "Solidification–microprestress–microplane (SMM) theory for concrete at early age: Theory, validation and application," *International Journal of Solids and Structures*, vol. 50, no. 6, pp. 957–975, 2013.

[33] M. Jirásek and P. Havlásek, "Microprestress–solidification theory of concrete creep: Reformulation and improvement," *Cement and Concrete Research*, vol. 60, pp. 51–62, 2014.

[34] M. Cervera, J. Oliver, and T. Prato, "Thermo-chemo-mechanical model for concrete. II: Damage and creep," *Journal of Engineering Mechanics*, vol. 125, no. 9, pp. 1028–1039, 1999.

[35] A. A. Griffith, "The phenomena of rupture and flow in solids," *Philosophical Transactions of The Royal Society of London. Series A, Containing Papers of a Mathematical or Physical Character*, vol. 221, pp. 163–198, 1921.

[36] G. R. Irwin, *Fracture*, pp. 551–590. Berlin, Heidelberg: Springer Berlin Heidelberg, 1958.

[37] D. Ngo and A. C. Scordelis, "Finite element analysis of reinforced concrete beams," in *ACI Journal Proceedings*, vol. 64, pp. 152–163, 1967.

[38] Y. Rashid, "Ultimate strength analysis of prestressed concrete pressure vessels," *Nuclear Engineering and Design*, vol. 7, no. 4, pp. 334–344, 1968.

[39] A. Ingraffea and V. Saouma, "Numerical modelling of discrete crack propagation in reinforced and plain concrete," *Fracture Mechanics of Concrete*, pp. 171–225, 1985.

[40] J. Gálvez, J. Červenka, D. Cendon, and V. Saouma, "A discrete crack approach to normal/shear cracking of concrete," *Cement and Concrete Research*, vol. 32, no. 10, pp. 1567–1585, 2002.

[41] M. Jirásek and T. Zimmermann, "Analysis of rotating crack model," *Journal of Engineering Mechanics*, vol. 124, no. 8, pp. 842–851, 1998.

[42] J. Dolbow and T. Belytschko, "A finite element method for crack growth without remeshing," *International Journal for Numerical Methods in Engineering*, vol. 46, no. 1, pp. 131–150, 1999.

[43] F. Liu and R. I. Borja, "A contact algorithm for frictional crack propagation with the extended finite element method," *International Journal for Numerical Methods in Engineering*, vol. 76, no. 10, pp. 1489–1512, 2008.

[44] J. Oliver, A. Huespe, and P. Sanchez, "A comparative study on finite elements for capturing strong discontinuities: E-FEM vs X-FEM," *Computer Methods in Applied Mechanics and Engineering*, vol. 195, no. 37, pp. 4732–4752, 2006.

[45] T. Wu and L. De Lorenzis, "A phase-field approach to fracture coupled with diffusion," *Computer Methods in Applied Mechanics and Engineering*, vol. 312, pp. 196–223, 2016.

[46] G. I. Barenblatt, "The mathematical theory of equilibrium cracks in brittle fracture," *Advances in Applied Mechanics*, vol. 7, pp. 55–129, 1962.

[47] A. Hillerborg, M. Modéer, and P.-E. Petersson, "Analysis of crack formation and crack growth in concrete by means of fracture mechanics and finite elements," *Cement and Concrete Research*, vol. 6, no. 6, pp. 773–781, 1976.

[48] X.-P. Xu and A. Needleman, "Numerical simulations of fast crack growth in

brittle solids," *Journal of the Mechanics and Physics of Solids*, vol. 42, no. 9, pp. 1397–1434, 1994.

[49] T. Wu and P. Wriggers, "Multiscale diffusion–thermal–mechanical cohesive zone model for concrete," *Computational Mechanics*, vol. 55, no. 5, pp. 999–1016, 2015.

[50] E. Schlangen and J. Van Mier, "Simple lattice model for numerical simulation of fracture of concrete materials and structures," *Materials and Structures*, vol. 25, no. 9, pp. 534–542, 1992.

[51] P. Grassl, "A lattice approach to model flow in cracked concrete," *Cement and Concrete Composites*, vol. 31, no. 7, pp. 454–460, 2009.

[52] J. Liu, Z. Zhao, S. Deng, and N. Liang, "Numerical investigation of crack growth in concrete subjected to compression by the generalized beam lattice model," *Computational Mechanics*, vol. 43, no. 2, pp. 277–295, 2009.

[53] B. Šavija, J. Pacheco, and E. Schlangen, "Lattice modeling of chloride diffusion in sound and cracked concrete," *Cement and Concrete Composites*, vol. 42, pp. 30–40, 2013.

[54] L. M. Kachanov, "Time of the rupture process under creep conditions," *Izv. Akad. Nank SSR Otd Tech Nauk*, vol. 8, pp. 26–31, 1958.

[55] R. H. Peerlings, R. de Borst, W. Brekelmans, and M. G. Geers, "Gradient-enhanced damage modelling of concrete fracture," *Mechanics of Cohesive-frictional Materials: An International Journal on Experiments, Modelling and Computation of Materials and Structures*, vol. 3, no. 4, pp. 323–342, 1998.

[56] M. Jirásek, "Mathematical analysis of strain localization," *Revue Européenne de Génie Civil*, vol. 11, no. 7-8, pp. 977–991, 2007.

[57] G. A. Francfort and J.-J. Marigo, "Revisiting brittle fracture as an energy minimization problem," *Journal of the Mechanics and Physics of Solids*, vol. 46, no. 8, pp. 1319–1342, 1998.

[58] B. Bourdin, G. A. Francfort, and J.-J. Marigo, "The variational approach to fracture," *Journal of Elasticity*, vol. 91, no. 1, pp. 5–148, 2008.

[59] G. Dal Maso and R. Toader, "A model for the quasi-static growth of brittle fractures: Existence and approximation results," *Archive for Rational Mechanics and Analysis*, vol. 162, no. 2, pp. 101–135, 2002.

[60] M. Buliga, "Energy minimizing brittle crack propagation," *Journal of Elasticity*, vol. 52, no. 3, pp. 201–238, 1998.

[61] A. Braides, *Approximation of free-discontinuity problems*. No. 1694, Berlin, Germany: Springer Science & Business Media, 1998.

[62] D. B. Mumford and J. Shah, "Optimal approximations by piecewise smooth functions and associated variational problems," *Communications on Pure and Applied Mathematics*, 1989.

[63] L. Ambrosio and V. M. Tortorelli, "Approximation of functional depending on jumps by elliptic functional via Γ-convergence," *Communications on Pure and Applied Mathematics*, vol. 43, no. 8, pp. 999–1036, 1990.

[64] A. Braides, *Gamma-convergence for Beginners*, vol. 22. New York, USA: Clarendon Press, 2002.

[65] V. Hakim and A. Karma, "Laws of crack motion and phase-field models of fracture," *Journal of the Mechanics and Physics of Solids*, vol. 57, no. 2, pp. 342–368, 2009.

[66] A. Karma, D. A. Kessler, and H. Levine, "Phase-field model of mode III dynamic fracture," *Physical Review Letters*, vol. 87, no. 4, p. 045501, 2001.

[67] L. Eastgate, J. P. Sethna, M. Rauscher, T. Cretegny, C.-S. Chen, and C. Myers, "Fracture in mode I using a conserved phase-field model," *Physical Review E*, vol. 65, no. 3, p. 036117, 2002.

[68] C. Miehe, M. Hofacker, and F. Welschinger, "A phase field model for rate-independent crack propagation: Robust algorithmic implementation based on operator splits," *Computer Methods in Applied Mechanics and Engineering*, vol. 199, no. 45, pp. 2765–2778, 2010.

[69] C. Miehe, L.-M. Schänzel, and H. Ulmer, "Phase field modeling of fracture in multi-physics problems. Part I. Balance of crack surface and failure criteria

for brittle crack propagation in thermo-elastic solids," *Computer Methods in Applied Mechanics and Engineering*, vol. 294, pp. 449–485, 2015.

[70] C. Miehe, M. Hofacker, L.-M. Schänzel, and F. Aldakheel, "Phase field modeling of fracture in multi-physics problems. Part II. Coupled brittle-to-ductile failure criteria and crack propagation in thermo-elastic-plastic solids," *Computer Methods in Applied Mechanics and Engineering*, vol. 294, pp. 486–522, 2015.

[71] C. Miehe, S. Mauthe, and S. Teichtmeister, "Minimization principles for the coupled problem of darcy–biot-type fluid transport in porous media linked to phase field modeling of fracture," *Journal of the Mechanics and Physics of Solids*, vol. 82, pp. 186–217, 2015.

[72] C. Miehe and S. Mauthe, "Phase field modeling of fracture in multi-physics problems. Part III. Crack driving forces in hydro-poro-elasticity and hydraulic fracturing of fluid-saturated porous media," *Computer Methods in Applied Mechanics and Engineering*, vol. 304, pp. 619–655, 2016.

[73] S. Mauthe and C. Miehe, "Hydraulic fracture in poro-hydro-elastic media," *Mechanics Research Communications*, vol. 80, pp. 69–83, 2017.

[74] C. V. Verhoosel and R. de Borst, "A phase-field model for cohesive fracture," *International Journal for Numerical Methods in Engineering*, vol. 96, no. 1, pp. 43–62, 2013.

[75] J. Vignollet, S. May, R. De Borst, and C. V. Verhoosel, "Phase-field models for brittle and cohesive fracture," *Meccanica*, vol. 49, no. 11, pp. 2587–2601, 2014.

[76] S. May, J. Vignollet, and R. De Borst, "A numerical assessment of phase-field models for brittle and cohesive fracture: Γ-convergence and stress oscillations," *European Journal of Mechanics-A/Solids*, vol. 52, pp. 72–84, 2015.

[77] H. Cornelissen, D. Hordijk, and H. Reinhardt, "Experimental determination of crack softening characteristics of normalweight and lightweight," *Heron*, vol. 31, p. 45, 1986.

[78] J.-Y. Wu, "A geometrically regularized gradient-damage model with energetic equivalence," *Computer Methods in Applied Mechanics and Engineering*, vol. 328, pp. 612–637, 2018.

[79] J.-Y. Wu and V. P. Nguyen, "A length scale insensitive phase-field damage model for brittle fracture," *Journal of the Mechanics and Physics of Solids*, vol. 119, pp. 20–42, 2018.

[80] J.-Y. Wu, "Robust numerical implementation of non-standard phase-field damage models for failure in solids," *Computer Methods in Applied Mechanics and Engineering*, vol. 340, pp. 767–797, 2018.

[81] V. P. Nguyen and J.-Y. Wu, "Modeling dynamic fracture of solids with a phase-field regularized cohesive zone model," *Computer Methods in Applied Mechanics and Engineering*, vol. 340, pp. 1000–1022, 2018.

[82] K. Pham, H. Amor, J.-J. Marigo, and C. Maurini, "Gradient damage models and their use to approximate brittle fracture," *International Journal of Damage Mechanics*, vol. 20, no. 4, pp. 618–652, 2011.

[83] T. T. Nguyen, J. Yvonnet, M. Bornert, C. Chateau, K. Sab, R. Romani, and R. Le Roy, "On the choice of parameters in the phase field method for simulating crack initiation with experimental validation," *International Journal of Fracture*, vol. 197, no. 2, pp. 213–226, 2016.

[84] E. Tanné, T. Li, B. Bourdin, J.-J. Marigo, and C. Maurini, "Crack nucleation in variational phase-field models of brittle fracture," *Journal of the Mechanics and Physics of Solids*, vol. 110, pp. 80–99, 2018.

[85] B. Bourdin, C. J. Larsen, and C. L. Richardson, "A time-discrete model for dynamic fracture based on crack regularization," *International Journal of Fracture*, vol. 168, no. 2, pp. 133–143, 2011.

[86] E. Lorentz and V. Godard, "Gradient damage models: Toward full-scale computations," *Computer Methods in Applied Mechanics and Engineering*, vol. 200, no. 21-22, pp. 1927–1944, 2011.

[87] B. Bourdin, J.-J. Marigo, C. Maurini, and P. Sicsic, "Morphogenesis and propagation of complex cracks induced by thermal shocks," *Physical Review Letters*, vol. 112, no. 1, p. 014301, 2014.

[88] D.-C. Feng and J.-Y. Wu, "Phase-field regularized cohesive zone model (czm) and size effect of concrete," *Engineering Fracture Mechanics*, vol. 197, pp. 66–79, 2018.

[89] L. Ambrosio and V. M. Tortorelli, "On the approximation of free discontinuity problems," vol. 6B, pp. 105–123, 1992.

[90] T. K. Mandal, V. P. Nguyen, and J.-Y. Wu, "Length scale and mesh bias sensitivity of phase-field models for brittle and cohesive fracture," *Engineering Fracture Mechanics*, vol. 217, p. 106532, 2019.

[91] B. Bourdin, G. A. Francfort, and J.-J. Marigo, "Numerical experiments in revisited brittle fracture," *Journal of the Mechanics and Physics of Solids*, vol. 48, no. 4, pp. 797–826, 2000.

[92] M. J. Borden, C. V. Verhoosel, M. A. Scott, T. J. Hughes, and C. M. Landis, "A phase-field description of dynamic brittle fracture," *Computer Methods in Applied Mechanics and Engineering*, vol. 217, pp. 77–95, 2012.

[93] S. Balay *et al.*, "PETSc users manual," Tech. Rep. ANL-95/11 - Revision 3.14, Argonne National Laboratory, 2020.

[94] R. L. Taylor, "FEAP-a finite element analysis program," 2014.

[95] G. Abaqus, "Abaqus 6.11," *Dassault Systemes Simulia Corp Providence, RI, USA*, 2011.

[96] T. Bittencourt, P. Wawrzynek, A. Ingraffea, and J. Sousa, "Quasi-automatic simulation of crack propagation for 2d lefm problems," *Engineering Fracture Mechanics*, vol. 55, no. 2, pp. 321–334, 1996.

[97] G. N. Wells and L. Sluys, "A new method for modelling cohesive cracks using finite elements," *International Journal for Numerical Methods in Engineering*, vol. 50, no. 12, pp. 2667–2682, 2001.

[98] J. G. Rots, *Computational modeling of concrete fracture*. PhD thesis, Delft University of Technology, The Netherlands., 1988.

[99] B. J. Winkler, *Traglastuntersuchungen von unbewehrten und bewehrten Betonstrukturen auf der Grundlage eines objektiven Werkstoffgesetzes für Beton*. Innsbruck University Press, 2001.

[100] S.-W. Zhou and C.-C. Xia, "Propagation and coalescence of quasi-static cracks in brazilian disks: an insight from a phase field model," *Acta Geotechnica*, vol. 14, no. 4, pp. 1195–1214, 2019.

[101] M. Bahaaddini, M. Serati, H. Masoumi, and E. Rahimi, "Numerical assessment of rupture mechanisms in brazilian test of brittle materials," *International Journal of Solids and Structures*, vol. 180, pp. 1–12, 2019.

[102] "TS-500, Requirements for design and construction of reinforced concrete structures," (Ankara, Turkey), Turkish Standards Institute., 2000.

[103] "ASTM C496/C496M-11, Standard test method for splitting tensile strength of cylindrical concrete specimens," (USA), American Society for Testing and Materials, 2011.

[104] G. De Schutter, "Finite element simulation of thermal cracking in massive hardening concrete elements using degree of hydration based material laws," *Computers & Structures*, vol. 80, no. 27-30, pp. 2035–2042, 2002.

[105] H. Amor, J.-J. Marigo, and C. Maurini, "Regularized formulation of the variational brittle fracture with unilateral contact: Numerical experiments," *Journal of the Mechanics and Physics of Solids*, vol. 57, no. 8, pp. 1209–1229, 2009.

[106] J.-Y. Wu and M. Cervera, "A novel positive/negative projection in energy norm for the damage modeling of quasi-brittle solids," *International Journal of Solids and Structures*, vol. 139, pp. 250–269, 2018.

[107] G. De Schutter and L. Taerwe, "Degree of hydration-based description of mechanical properties of early age concrete," *Materials and Structures*, vol. 29, no. 6, p. 335, 1996.

[108] G. De Schutter and L. Taerwe, "Fracture energy of concrete at early ages," *Materials and Structures*, vol. 30, no. 2, p. 67, 1997.

[109] B. D. Coleman and M. E. Gurtin, "Thermodynamics with internal state variables," *The Journal of Chemical Physics*, vol. 47, no. 2, pp. 597–613, 1967.

[110] K. Van Breugel, "Prediction of temperature development in hardening concrete," in *Prevention of thermal cracking in concrete at early ages. RILEM* (S. R, ed.), vol. 15, pp. 51–75, New York, USA: E & EN SPON, 1998.

[111] Z. P. Bazant, "Thermodynamics of solidifying or melting viscoelastic material," *ASCE J Eng Mech Div*, vol. 105, no. 6, pp. 933–952, 1979.

[112] M. Tokyay, *Cement and concrete mineral admixtures*. CRC Press, 2016.

[113] M. Briffaut, F. Benboudjema, J. M. Torrenti, and G. Nahas, "Numerical analysis of the thermal active restrained shrinkage ring test to study the early age behavior of massive concrete structures," *Engineering Structures*, vol. 33, no. 4, pp. 1390–1401, 2011.

[114] S. Thelandersson, "Modeling of combined thermal and mechanical action in concrete," *Journal of Engineering Mechanics*, vol. 113, no. 6, pp. 893–906, 1987.

[115] T. K. Mandal, A. Gupta, V. P. Nguyen, R. Chowdhury, and A. de Vaucorbeil, "A length scale insensitive phase field model for brittle fracture of hyperelastic solids," *Engineering Fracture Mechanics*, vol. 236, p. 107196, 2020.

[116] "Report on Roller-Compacted Mass Concrete (ACI 207.5R-11)," tech. rep., American Concrete Institute, 2011.

[117] E. Acker, C. Foucrier, and Y. Malier, "Temperature-related mechanical effects in concrete elements and optimization of the manufacturing process," *Special Publication*, vol. 95, pp. 33–48, 1986.

[118] P. Acker and F.-J. Ulm, "Creep and shrinkage of concrete: physical origins and practical measurements," *Nuclear Engineering and Design*, vol. 203, no. 2-3, pp. 143–158, 2001.

[119] A. M. Neville, W. H. Dilger, and J. J. Brooks, "Creep of plain and structural concrete," *Construction Press*, 1983.

[120] J. Sercombe, C. Hellmich, F.-J. Ulm, and H. Mang, "Modeling of early-age creep of shotcrete. I: Model and model parameters," *Journal of Engineering Mechanics*, vol. 126, no. 3, pp. 284–291, 2000.

[121] C. Hellmich, J. Sercombe, F.-J. Ulm, and H. Mang, "Modeling of early-age creep of shotcrete. II: Application to tunneling," *Journal of Engineering Mechanics*, vol. 126, no. 3, pp. 292–299, 2000.

[122] Z. P. Bažant and S. Prasannan, "Solidification theory for concrete creep. I: Formulation," *ASCE Journal of Engineering Mechanics*, vol. 115, no. 8, pp. 1691–1703, 1989.

[123] Z. P. Bažant and S. Prasannan, "Solidification theory for concrete creep. II: Verification and application," *Journal of Engineering Mechanics*, vol. 115, no. 8, pp. 1704–1725, 1989.

[124] Z. P. Bažant, G. Cusatis, and L. Cedolin, "Temperature effect on concrete creep modeled by microprestress-solidification theory," *Journal of engineering mechanics*, vol. 130, no. 6, pp. 691–699, 2004.

[125] P. Havlásek and M. Jirásek, "Multiscale modeling of drying shrinkage and creep of concrete," *Cement and Concrete Research*, vol. 85, pp. 55–74, 2016.

[126] S. Rahimi-Aghdam, Z. P. Bažant, and G. Cusatis, "Extended microprestress-solidification theory for long-term creep with diffusion size effect in concrete at variable environment," *Journal of Engineering Mechanics*, vol. 145, no. 2, p. 04018131, 2018.

[127] G. Di Luzio, "A symmetric over-nonlocal microplane model m4 for fracture in concrete," *International Journal of Solids and Structures*, vol. 44, no. 13, pp. 4418–4441, 2007.

[128] G. Di Luzio and G. Cusatis, "Hygro-thermo-chemical modeling of high-performance concrete. II: Numerical implementation, calibration, and validation," *Cement and Concrete Composites*, vol. 31, no. 5, pp. 309–324, 2009.

[129] K. Norling Mjörnell, "A model on self-desiccation in high performance concrete," in *Proceedings Int. Research Seminar*, (Sweden, Lund), pp. 141–157, 1997.

[130] T. Gasch, R. Malm, and A. Ansell, "A coupled hygro-thermo-mechanical model for concrete subjected to variable environmental conditions," *International Journal of Solids and Structures*, vol. 91, pp. 143–156, 2016.

[131] P. Yu, Y. Duan, Q. Fan, and S. Tang, "Improved mps model for concrete creep under variable humidity and temperature," *Construction and Building Materials*, vol. 243, p. 118183, 2020.

[132] A. Sellier, S. Multon, L. Buffo-Lacarrière, T. Vidal, X. Bourbon, and G. Camps, "Concrete creep modelling for structural applications: non-linearity, multi-axiality, hydration, temperature and drying effects," *Cement and Concrete Research*, vol. 79, pp. 301–315, 2016.

[133] D. Gawin, F. Pesavento, and B. A. Schrefler, "Hygro-thermo-chemo-mechanical modelling of concrete at early ages and beyond. Part I: hydration and hygro-thermal phenomena," *International Journal for Numerical Methods in Engineering*, vol. 67, no. 3, pp. 299–331, 2006.

[134] D. Gawin, F. Pesavento, and B. A. Schrefler, "Hygro-thermo-chemo-mechanical modelling of concrete at early ages and beyond. Part II: shrinkage and creep of concrete," *International Journal for Numerical Methods in Engineering*, vol. 67, no. 3, pp. 332–363, 2006.

[135] D. Gawin, F. Pesavento, and B. Schrefler, "Modelling creep and shrinkage of concrete by means of effective stresses," *Materials and Structures*, vol. 40, no. 6, pp. 579–591, 2007.

[136] M. Briffaut, F. Benboudjema, J. M. Torrenti, and G. Nahas, "A thermal active restrained shrinkage ring test to study the early age concrete behaviour of massive structures," *Cement and Concrete Research*, vol. 41, no. 1, pp. 56–63, 2011.

[137] M. Briffaut, F. Benboudjema, J. M. Torrenti, and G. Nahas, "Numerical analysis of the thermal active restrained shrinkage ring test to study the early age be-

havior of massive concrete structures," *Engineering Structures*, vol. 33, no. 4, pp. 1390–1401, 2011.

[138] A. E. Idiart, C. M. López, and I. Carol, "Modeling of drying shrinkage of concrete specimens at the meso-level," *Materials and structures*, vol. 44, no. 2, pp. 415–435, 2011.

[139] J. Zhang, H. Dongwei, and S. Wei, "Experimental study on the relationship between shrinkage and interior humidity of concrete at early age," *Magazine of Concrete Research*, vol. 62, no. 3, pp. 191–199, 2010.

[140] J. Zhang, D. Hou, Y. Gao, and S. Wei, "Determination of moisture diffusion coefficient of concrete at early age from interior humidity measurements," *Drying Technology*, vol. 29, no. 6, pp. 689–696, 2011.

[141] J. Zhang, D. Hou, and Y. Han, "Micromechanical modeling on autogenous and drying shrinkages of concrete," *Construction and Building Materials*, vol. 29, pp. 230–240, 2012.

[142] J. Zhang, Y. Gao, Y. Han, and W. Sun, "Shrinkage and interior humidity of concrete under dry–wet cycles," *Drying Technology*, vol. 30, no. 6, pp. 583–596, 2012.

[143] J. Zhang, J. Wang, and Y. Gao, "Moisture movement in early-age concrete under cement hydration and environmental drying," *Magazine of Concrete Research*, vol. 68, no. 8, pp. 391–408, 2016.

[144] J. Zhang, Y. Han, and J. Zhang, "Evaluation of shrinkage induced cracking in concrete with impact of internal curing and water to cement ratio," *Journal of Advanced Concrete Technology*, vol. 14, no. 7, pp. 324–334, 2016.

[145] J. Zhang, Y. Gao, Y. Han, and J. Wang, "Evaluation of shrinkage induced cracking in early age concrete: From ring test to circular column," *International Journal of Damage Mechanics*, vol. 26, no. 5, pp. 771–797, 2017.

[146] J. Zhang, J. Wang, and X. Ding, "Calculation of shrinkage stress in concrete structures with impact of internal curing," *Engineering Fracture Mechanics*, vol. 192, pp. 54–76, 2018.

[147] K. Terzaghi, *Erdbaumechanik auf bodenphysikalischer Grundlage*. Leipzig: F. Deuticke, 1925.

[148] M. A. Biot, "General theory of three-dimensional consolidation," *Journal of Applied Physics*, vol. 12, no. 2, pp. 155–164, 1941.

[149] L. Anand, "2014 Drucker medal paper: A derivation of the theory of linear poroelasticity from chemoelasticity," *Journal of Applied Mechanics*, vol. 82, no. 11, p. 111005, 2015.

[150] R. M. Bowen, "The thermochemistry of a reacting mixture of elastic materials with diffusion," *Archive for Rational Mechanics and Analysis*, vol. 34, no. 2, pp. 97–127, 1969.

[151] Z. Bažant and L. Najjar, "Nonlinear water diffusion in nonsaturated concrete," *Matériaux et Construction*, vol. 5, no. 1, pp. 3–20, 1972.

[152] H. Akita, T. Fujiwara, and Y. Ozaka, "A practical procedure for the analysis of moisture transfer within concrete due to drying," *Magazine of Concrete Research*, vol. 49, no. 179, pp. 129–137, 1997.

[153] T. Ayano and F. H. Wittmann, "Drying, moisture distribution, and shrinkage of cement-based materials," *Materials and Structures*, vol. 35, no. 3, pp. 134–140, 2002.

[154] L.-O. Nilsson, "Long-term moisture transport in high performance concrete," *Materials and Structures*, vol. 35, no. 10, pp. 641–649, 2002.

[155] M. A. Biot and G. Temple, "Theory of finite deformations of porous solids," *Indiana University Mathematics Journal*, vol. 21, no. 7, pp. 597–620, 1972.

[156] M. A. Biot, "Nonlinear and semilinear rheology of porous solids," *Journal of Geophysical Research*, vol. 78, no. 23, pp. 4924–4937, 1973.

[157] J. Rudnicki, "Coupled deformation-diffusion effects in the mechanics of faulting and failure of geomaterials ," *Applied Mechanics Reviews*, vol. 54, pp. 483–502, 11 2001.

[158] O. Coussy and F. Ulm, *Mechanics of porous continua*, vol. 1016. Wiley New York, 1995.

194

[159] J. R. Rice, "On the stability of dilatant hardening for saturated rock masses," *Journal of Geophysical Research*, vol. 80, no. 11, pp. 1531–1536, 1975.

[160] T. C. Powers, "Structure and physical properties of hardened portland cement paste," *Journal of the American Ceramic Society*, vol. 41, no. 1, pp. 1–6, 1958.

[161] S. J. Pantazopoulou and R. Mills, "Microstructural aspects of the mechanical response of plain concrete," *Materials Journal*, vol. 92, no. 6, pp. 605–616, 1995.

[162] E. Detournay and A. H.-D. Cheng, "Fundamentals of poroelasticity," in *Analysis and design methods*, pp. 113–171, Elsevier, 1993.

[163] P. K. Mehta and P. J. Monteiro, *Concrete: microstructure, properties, and materials*. New York, USA: McGraw-Hill Education, 2014.

[164] Y. Xi, Z. P. Bažant, L. Molina, and H. M. Jennings, "Moisture diffusion in cementitious materials moisture capacity and diffusivity," *Advanced Cement Based Materials*, vol. 1, no. 6, pp. 258–266, 1994.

[165] S. Brunauer, P. H. Emmett, and E. Teller, "Adsorption of gases in multimolecular layers," *Journal of the American Chemical Society*, vol. 60, no. 2, pp. 309–319, 1938.

[166] S. Brunauer, L. S. Deming, W. E. Deming, and E. Teller, "On a theory of the van der waals adsorption of gases," *Journal of the American Chemical society*, vol. 62, no. 7, pp. 1723–1732, 1940.

[167] G. Halsey, "Physical adsorption on non-uniform surfaces," *The Journal of Chemical Physics*, vol. 16, no. 10, pp. 931–937, 1948.

[168] A. Hillerborg, "A modified absorption theory," *Cement and Concrete Research*, vol. 15, no. 5, pp. 809–816, 1985.

[169] S. Brunauer, J. Skalny, and E. Bodor, "Adsorption on nonporous solids," *Journal of Colloid and Interface Science*, vol. 30, no. 4, pp. 546–552, 1969.

[170] K. N. Mjörnell, "A model on self-desiccation in high-performance concrete," in *Proceedings of the International Research Seminar on Self-desiccation and its Importance in Concrete Technology*, pp. 141–157, 1997.

[171] M. Ghasabeh and S. Göktepe, "Computational modeling of drying shrinkage in early-age concrete," *PAMM*, vol. 19, no. 1, p. e201900415, 2019.

[172] P. Laplante, *Propriétés mécaniques dês bétons durcissants: analyse comparée dês bétons classiques et a très hautes performances*. PhD thesis, École Nationale des Ponts et Chaussées, Paris, 1993.

[173] A. H. Bryant and C. Vadhanavikkit, "Creep, shrinkage-size, and age at loading effects," *ACI Materials Journal*, vol. 84, no. 2, pp. 117–123, 1987.

[174] G. Di Luzio, R. Felicetti, and L. Cedolin, "Numerical and experimental study of creep and shrinkage in a high-performance concrete," in *CONCREEP 10*, pp. 128–137, 2015.

[175] S. Liang and Y. Wei, "Methodology of obtaining intrinsic creep property of concrete by flexural deflection test," *Cement and Concrete Composites*, vol. 97, pp. 288–299, 2019.

[176] Z. P. Bažant and J. Chern, "Concrete creep at variable humidity: constitutive law and mechanism," *Materials and Structures*, vol. 18, no. 1, p. 1, 1985.

[177] Z. P. Bažant and X. Yunping, "Drying creep of concrete: constitutive model and new experiments separating its mechanisms," *Materials and Structures*, vol. 27, no. 1, pp. 3–14, 1994.

[178] F.-X. Hubert, N. Burlion, and J.-F. Shao, "Drying of concrete: modelling of a hydric damage," *Materials and structures*, vol. 36, no. 1, pp. 12–21, 2003.

[179] J. Mazars, "A description of micro-and macroscale damage of concrete structures," *Engineering Fracture Mechanics*, vol. 25, no. 5-6, pp. 729–737, 1986.

[180] N. Burlion, F. Bourgeois, and J.-F. Shao, "Effects of desiccation on mechanical behaviour of concrete," *Cement and Concrete Composites*, vol. 27, no. 3, pp. 367–379, 2005.

[181] F. Bourgeois, N. Burlion, and J.-F. Shao, "Modelling of elastoplastic damage in concrete due to desiccation shrinkage," *International Journal for Numerical and Analytical Methods in Geomechanics*, vol. 26, no. 8, pp. 759–774, 2002.

196

[182] C. de Sa, F. Benboudjema, M. Thiery, and J. Sicard, "Analysis of microcracking induced by differential drying shrinkage," *Cement and Concrete Composites*, vol. 30, no. 10, pp. 947–956, 2008.

[183] F. Benboudjema, F. Meftah, and J.-M. Torrenti, "Interaction between drying, shrinkage, creep and cracking phenomena in concrete," *Engineering Structures*, vol. 27, no. 2, pp. 239–250, 2005.

[184] M. Briffaut, F. Benboudjema, C. Laborderie, and J.-M. Torrenti, "Creep consideration effect on meso-scale modeling of concrete hydration process and consequences on the mechanical behavior," *Journal of Engineering Mechanics*, vol. 139, no. 12, pp. 1808–1817, 2013.

[185] T. Cajuhi, L. Sanavia, and L. De Lorenzis, "Phase-field modeling of fracture in variably saturated porous media," *Computational Mechanics*, vol. 61, no. 3, pp. 299–318, 2018.

[186] T. Tong, G. Hua, Z. Liu, X. Liu, and T. Xu, "Localizing gradient damage model coupled to extended microprestress-solidification theory for long-term nonlinear time-dependent behaviors of concrete structures," *Mechanics of Materials*, p. 103713, 2020.

[187] L. H. Poh and G. Sun, "Localizing gradient damage model with decreasing interactions," *International Journal for Numerical Methods in Engineering*, vol. 110, no. 6, pp. 503–522, 2017.

[188] R. De Borst and H.-B. Mühlhaus, "Gradient-dependent plasticity: formulation and algorithmic aspects," *International Journal for Numerical Methods in Engineering*, vol. 35, no. 3, pp. 521–539, 1992.

[189] R. Peerlings, d. R. R. Borst, W. Brekelmans, and d. J. Vree, "Gradient enhanced damage for quasi-brittle materials," *International Journal for Numerical Methods in Engineering*, vol. 39, no. 19, p. 3391, 1996.

[190] O. Coussy, *Mechanics of porous continua*. Chichester, New York, USA: Wiley, 1995.

197

[191] G. De Schutter and L. Taerwe, "Degree of hydration-based description of mechanical properties of early age concrete," *Materials and Structures*, vol. 29, no. 6, pp. 335–344, 1996.

CURRICULUM VITAE

PERSONAL INFORMATION

Surname, Name: Ghasabeh, Mehran

Nationality: Iranian

Date and Place of Birth: 1984, Urmia, West Azerbaijan Province, Iran

Marital Status: Single

E-Mail Address: mehran.ghasabeh@gmail.com

LANGUAGES

Azerbaijani, Persian, Turkish and Advanced English

EDUCATION

Degree	Institution	Year of Graduation
M.S.	Middle East Technical University	2013
B.S.	Urmia University	2007
High School	Andisheh Borna	2003

PROFESSIONAL EXPERIENCE

- Working as a freelance consulting structural engineer between 2007-2010.

- Working as a teaching assistant for the bachelor and graduated courses, CE

241 (Materials Science), CE 344 (Materials Of Construction) CE 4006 (Introduction to Computational Mechanics of Materials), CE 7018 (Computational Inelasticity) and CE 7026 (Continuum Mechanics) between 2014-2020.

AREAS OF INTEREST

Continuum Solid Mechanics, Coupled Problems, Fracture Mechanics, Computational Modeling of Durability in hardening or hardened state Concrete

PUBLICATIONS

National Conferences

M. Ghasabeh, S. Göktepe, Betonda Kemo-Termo-Mekanik Yükler Altında Çatlak Oluşumunun Hesaplamalı Modellenmesi, XXI. Ulusal Mekanik Kongresi, Niğde, Türkiye, 02-06 Eylül 2019, cilt.21, ss.743-752

M. Ghasabeh, S. Göktepe, Sertleşen Betonda Rötre Çatlaklarının Hesaplamalı Modellenmesi, XXI. Ulusal Mekanik Kongresi, Niğde, Türkiye, 02-06 Eylül 2019, cilt.21, ss.644-653

International Conferences

M. Ghasabeh, S. Göktepe, Computational Modeling of Chemo-Thermo-Mechanical Cracking in Early-Age Concrete, 25th International Congress of Theoretical and Applied Mechanics (ICTAM2021), Italy, Milano, 22-27 August 2021

M. Ghasabeh, S. Göktepe, Computational modeling of drying shrinkage in early-age concrete, PAMM, vol. 19, no. 1, p. e201900415, 2019.

M. Ghasabeh, S. Göktepe, A Coupled Poroviscoelastic Model for Drying Shrinkage-Induced Cracking in Concrete, 6th International Conference on Material Modeling (ICMM2019), Sweden, Lund, 26-28 June, 2019

M. Ghasabeh, S. Göktepe, Computational Modeling of Shrinkage-Induced Cracking in Concrete, Beyond 2019, Ankara, Turkey, 09-11 September 2019, ss.31-32

S. Göktepe, M. Ghasabeh 2018, Computational Modeling of Durability Phenomena in Concrete, 55th Annual Technical Meeting of the Society of Engineering Science (SES2018), Madrid, Spain, 10-12 October 2018

GRANT

Receiving a grant among more than 700 applications for participating in the 25th International Congress of Theoretical and Applied Mechanics (ICTAM2021), Italy, Milano, 22-27 August 2021.

HOBBIES

Literature, Poem, History, Music, Cooking, Sport, Soccer